USE OF SIMULATED STRONG GROUND MOTION RECORDS IN EARTHQUAKE ENGINEERING APPLICATIONS

A THESIS SUBMITTED TO
THE GRADUATE SCHOOL OF NATURAL AND APPLIED SCIENCES
OF
MIDDLE EAST TECHNICAL UNIVERSITY

BY

SHAGHAYEGH KARIMZADEH NAGHSHINEH

IN PARTIAL FULFILLMENT OF THE REQUIREMENTS
FOR
THE DEGREE OF DOCTOR OF PHILOSOPHY
IN
CIVIL ENGINEERING

MARCH 2016

Approval of the thesis:

USE OF SIMULATED STRONG GROUND MOTION RECORDS IN EARTHQUAKE ENGINEERING APPLICATIONS

submitted by **SHAGHAYEGH KARIMZADEH NAGHSHINEH** in partial fulfillment of the requirements for the degree of **Doctor of Philosophy in Civil Engineering Department, Middle East Technical University** by,

Prof. Dr. Mevlüde Gülbin Dural Ünver _____
Dean, Graduate School of **Natural and Applied Sciences**

Prof. Dr. İsmail Özgür Yaman _____
Head of Department, **Civil Engineering**

Assoc. Prof. Dr. Ayşegül Askan Gündoğan _____
Supervisor, **Civil Engineering Dept., METU**

Examining Committee Members:

Prof. Dr. Ahmet Yakut _____
Civil Engineering Dept., METU

Assoc. Prof. Dr. Ayşegül Askan Gündoğan _____
Civil Engineering Dept., METU

Assoc. Prof. Dr. Mustafa Tolga Yılmaz _____
Engineering Science Dept., METU

Assoc. Prof. Dr. Abdurrahman Şahin _____
Civil Engineering Dept., Yıldız Technical University

Assoc. Prof. Dr. Baki Öztürk _____
Civil Engineering Dept., Hacettepe University

Date: March 30, 2016

I hereby declare that all information in this document has been obtained and presented in accordance with academic rules and ethical conduct. I also declare that, as required by these rules and conduct, I have fully cited and referenced all material and results that are not original to this work.

Name, Last name: Shaghayegh Karimzadeh Naghshineh

Signature:

ABSTRACT

USE OF SIMULATED STRONG GROUND MOTION RECORDS IN EARTHQUAKE ENGINEERING APPLICATIONS

Karimzadeh Naghshineh, Shaghayegh
Ph.D., Department of Civil Engineering
Supervisor: Assoc. Prof. Dr. Ayşegül Askan Gündoğan

March 2016, 331 pages

With the recent advances in scientific computing, ground motion simulations have become more common. However, use of simulated motions for earthquake engineering purposes is still not well investigated. In this thesis, the efficiency of records simulated with the stochastic finite-fault technique in seismic demand estimation is studied in two different earthquake engineering applications. First, vulnerability assessment in a selected region, Erzincan (Turkey) is performed with simple single-degree-of-freedom structural models. For this purpose, seismic loss estimation for past and potential events is carried out considering both regional seismicity and local building information. Comparison of the estimated damage with the observed damage during the 1992 Erzincan earthquake reveals that, with well-defined local parameters, realistic ground motions can be simulated and used as input to SDOF models for seismic loss estimation. In the second part, nonlinear time history analyses of reinforced-concrete multi-degree-of-freedom models are performed to compare structural responses to simulated records with those to the corresponding real

records. For this purpose, three case studies are considered: The 1992 Erzincan (Turkey) (Mw=6.6), the 1999 Düzce (Turkey) (Mw=7.1), and the 2009 L'Aquila (Italy) (Mw=6.3) earthquakes. Results show that for Erzincan with predominant basin effects, simulated motions fail to realistically predict real MDOF responses. However, results are promising for Düzce located on a shallow alluvial basin. For L'Aquila located mostly on stiff sites, results vary according to the simulation technique applied. In summary, when the simulated motions match the real records in terms of major seismological features, use of simulations in earthquake engineering seems feasible.

Key words: Ground motion simulations, nonlinear time history analysis, seismic loss, single-degree-of-freedom systems, multi-degree-of-freedom systems

ÖZ

BENZEŞTİRİLMİŞ KUVVETLİ YER HAREKETİ KAYITLARININ DEPREM MÜHENDİSLİĞİ UYGULAMALARINDA KULLANIMI

Karimzadeh Naghshineh, Shaghayegh
Doktora, İnşaat Mühendisliği Bölümü
Tez Yöneticisi: Doç. Dr. Ayşegül Askan Gündoğan

Mart 2016, 331sayfa

Bilimsel hesaplama teknolojilerindeki son gelişmeler ile yer hareketi simülasyonları yaygınlaşmıştır. Ancak sentetik kayitların deprem mühendisliği amaçları için kullanımı hala çok detaylı olarak çalışılmamıştır. Bu tezde, stokastik sonlu-fay yöntemi ile simüle edilmiş kayıtların sismik talep hesaplarındaki kullanımı iki farklı deprem mühendisliği uygulamasında çalışılmıştır. Öncelikle, çalışma bölgesi olan Erzincan'da (Türkiye) basit tek-serbest-dereceli yapı modelleri ile kırılganlık analizi yapılmştır. Bu amaçla, bölgesel sismisite ve yerel yapı bilgileri kullanılarak geçmiş ve potansiyel depremler için sismik kayıp tahminleri yapılmıştır. 1992 Erzincan depremi sırasında gözlemlenen hasar ile tahmin edilen hasarın karşılaştırılması, iyi tanımlanmış yerel parametreler ile gerçekçi yer hareketleri simüle edilebildiğini ve bu hareketlerin kayıp tahminleri için tek-serbestlik-dereceli sistemlere girdi olarak kullanılabileceğini göstermektedir. Ikinci kısımda, sentetik kayıtlarla elde edilen yapısal tepkileri gerçek kayıtlarla elde edilen tepkilerle karşılaştırmak amacıyla çoklu-serbestlik-dereceli betonarme yapı modellerinin doğrusal olmayan zaman tanım alanı

analizleri yapılmıştır. Bu amaçla, üç çalışma yapılmıştır: 1992 Erzincan (Türkiye) (Mw=6.6), 1999 Düzce (Turkey) (Mw=7.1), and the 2009 L'Aquila (İtalya) (Mw=6.3) depremleri. Sonuçlar, berligin basen etkileri olan Erzincan için simüle edilmiş kayıtların çoklu-serbestlik-dereceli modellerin gerçek tepkilerini etkili biçimde tahmin edemediğini göstermektedir. Ancak, sonuçlar daha sığ bir basen üzerinde olan Düzce için ümit vericidir. Çoğunlukla sert zeminler üzerinde olan L'Aquila için ise sonuçlar kullanılan simülasyon tekniğine göre değişmektedir. Özetle, simüle edilmiş kayıtların gerçek kayıtlara temel sismolojik özellikler cinsinden uygunluk göstermeleri durumunda simülasyonların deprem mühendisliğinde kullanımı uygun görülmüştür.

Anahtar kelimeler: Yer hareketi simülasyonları, doğrusal olmayan zaman tanım alanı analizi, sismik kayıp, tek-serbestlik-dereceli sistemleri, çoklu-serbestlik-dereceli sistemleri

To my parents, my brother and sister who always support me in all aspects of my life

To my husband, for his patience and support in my study

ACKNOWLEDGEMENTS

I would like to express my most sincere gratitude to my thesis advisor Assoc. Prof. Dr. Ayşegül Askan Gündoğan for her continuous advice, support and encouragement throughout the course of my Ph.D. program. Despite her busy schedule, she has always been accessible to address my questions and concerns. While regularly providing guidance, she has granted me the freedom to develop my individuality and expand my own ideas. I appreciate her commitment to secure financial support for my studies and my attendance at research conferences during the past five years. She is truly a great advisor and I am extremely honored to have studied under her supervision.

I would like to thank my committee members Prof. Dr. Ahmet Yakut, Assoc. Prof. Dr. Mustafa Tolga Yılmaz, Assoc. Prof. Dr. Abdurrahman Şahin, and Assoc. Prof. Dr. Baki Öztürk for their advice and help during my thesis defense. I am indebted Prof. Dr. Murat Altuğ Erberik, for his continued support and valuable suggestions and concise comments on my education career. I am also most grateful to Dr. Nazan Yılmaz Kılıç and Dr. Gabriele Ameri for their kind support.

My research was financially supported by Turkish National Geodesy and Geophysics Union through the project with grant number of TUJJB-UDP-01-12 as well as METU-YESAP project with grant number of BAP-08-11-KB.2015K120470-2. The financial support of the Turkish National Geodesy and Geophysics Union as well as METU is gratefully acknowledged.

I am highly thankful to my friend Koray Kadaş for providing me valuable feedback, assistance and literature that have broadened my knowledge and have inspired future

research ideas based on the present study. I would also like to give special thanks to Saeideh Nazirzadeh for her kindness and assistance during difficult days.

I appreciate the support and concern of my dear colleagues Bijan Abgarmi, Aida Azari, Nurten Sisman, Sadun Taniser, Kaan Katsız, Alper Özdemir, Nefise Şaban, Vesile Akansel, Ceren Demirci, Mustafa Bilal, and my friends Sinem Pirinççi, Sanam Shojaeipour, Yasmin Frad, Nikou Sarabchi throughout this study. I also would like to thank Askan family for their kind support and friendship.

I am grateful to my beloved mother Effat Mirrazavi and father Jafar Karimzadeh Naghshineh for allowing and encouraging me to pursue my Ph.D. degree in Turkey. I will never be able to make it up to them for what they have done for me. I thank them for the unconditional love.

I am thankful to my brother Ali Karimzadeh Naghshineh, his wife Elnaz Seyedmonir and my cousin Sevil Jahed who were always alongside with me throughout my study in Turkey. I also extend my appreciation to my sister, Shabnam Karimzadeh Naghshineh, her husband Peiman Emamverdizadeh, my grandmother Ezzat Fazelzad, my aunt Mahtab and Rafat Mirrazavi and my cousins Sheida Pirouz, Hesam and Hadi Moslemzadeh, in Tabriz (Iran) for their unconditional love.

Finally, I would like to thank my husband Amir Motevalli for his understanding, support, and seamless love. He is always able to cheer me up and he made me happier than I could imagine. I could not complete my Ph.D. program without him. I also thank his family for their kindness and patience.

Above all, I owe it all to Almighty God for granting me the wisdom, health and strength to undertake this research task and enabling me to its completion.

TABLE OF CONTENTS

ABSTRACT v

ÖZ vii

ACKNOWLEDGEMENTS x

TABLE OF CONTENTS xii

LIST OF TABLES xviii

LIST OF FIGURES xxiii

LIST OF SYMBOLS AND ABBREVIATIONS xxxviii

CHAPTERS 1

1 INTRODUCTION 1

1.1 Background 1

1.2 Literature Survey on Ground Motion Simulation Techniques 2

1.3 Literature Survey on Use of Simulated Records in Earthquake Engineering 6

1.4 Objectives and Scope 8

1.5 Organization of the Thesis 10

2 METHODOLOGY FOR GROUND MOTION SIMULATION: THE STOCHASTIC APPROACH 13

2.1 General 13

2.2 Stochastic Point-Source Method 14

2.2.1 Source spectrum, $E(M_0, f)$ 17
2.2.2 Path effects, $P(R, f)$ 19
2.2.3 Site effects, $G(f)$ 22

2.3 Stochastic Finite-Fault Method 26

3 METHODOLOGY FOR DYNAMIC ANALYSES OF BUILDINGS: NONLINEAR TIME HISTORY ANALYSIS 33

3.1 General 33

3.2 Structural Analysis Program 34

3.3 Nonlinear Time History Analysis 35

3.4 Limitations of Nonlinear Time History Analysis 35

4 APPLICATION OF SIMULATED RECORDS IN SEISMIC LOSS ESTIMATION: A CASE STUDY FOR ERZINCAN (TURKEY) 37

4.1 Introduction 37

4.2 Study Region 43

4.3 Simulated Ground Motion Database 50

4.4 Identification and Idealization of the Regional Building Stock 62

4.4.1 Identification of the Building Stock 62
4.4.2 Idealization based on ESDOF models 63

4.5 Fragility Curve Generation Methodology 69

4.5.1 Ground motion variability 70

4.5.2 Variability in structural properties and response statistics 73
4.5.3 Attainment of limit states..... 76
4.5.4 Generation of fragility curves 78
4.6 Simulation Based Seismic Damage Estimation..... 88
4.6.1 Methodology..... 88
4.6.2 Applications in the study region 93
4.6.2.1 Validation of the estimated damage distribution for the 1992 Erzincan earthquake……..…94
4.6.2.2 Estimated damage for potential earthquakes……..…106
4.7 Uncertainties Involved in the Earthquake Loss Estimation..... 116
4.8 Summary and Main Findings of Chapter 4 118
5 APPLICATION OF SIMULATED RECORDS IN NONLINEAR TIME HISTORY ANALYSES OF MULTI- DEGREE-OF-FREEDOM STRUCTURES..... 121
5.1 Introduction 121
5.2 Description of the Frame Models 124
5.3 First Case Study: Ground Motion Simulation of the 1992 Erzincan (Mw=6.6) Earthquake 129
5.3.1 General 129
5.3.2 Real ground motion data of the 1992 Erzincan earthquake..... 130
5.3.3 Simulated ground motion data for the 1992 Erzincan (Mw=6.6) earthquake..... 132
5.3.3.1 Source model……132
5.3.3.2 Path model……133
5.3.3.3 Site model……...……...……...134
5.3.4 Comparison of simulated and real ground motion data for the 1992 Erzincan (Mw=6.6) earthquake 134

5.3.5 Comparison of dynamic responses of the buildings to observed and simulated records for the 1992 Erzincan earthquake..... 144

5.4 Second Case Study: Ground Motion Simulation of the 1999 Düzce (Mw=7.1) Earthquake..... 160

5.4.1 General 160

5.4.2 Real ground motion data of the 1999 Düzce (Mw=7.1) earthquake 161

5.4.3 Simulated ground motion data for the 1999 Düzce (Mw=7.1) earthquake..... 162

5.4.3.1 Source model……162

5.4.3.2 Path model……164

5.4.3.3 Site model……...……...164

5.4.4 Comparison of simulated and real ground motion data for the 1999 Düzce (Mw=7.1) earthquake 165

5.4.5 Comparison of dynamic responses of the buildings to observed and simulated records for the 1999 Düzce (Mw=7.1) earthquake 174

5.5 Third Case Study: Ground Motion Simulation of the 2009 L'Aquila (Mw=6.3) Earthquake..... 187

5.5.1 General 187

5.5.2 Real ground motion data of the 2009 L'Aquila (Mw=6.3) earthquake... 189

5.5.3 Simulated ground motion data for the 2009 L'Aquila (Mw=6.3) earthquake 191

5.5.3.1 Simulated records from the stochastic finite-fault method……191

5.5.3.1.1 Source model…..……..……..…..…..191

5.5.3.1.2 Path model……..……...…...……192

5.5.3.1.3 Site model……..……...…..…...193

5.5.3.2 Simulated records from the hybrid-integral-composite method……194

5.5.4 Comparison of simulated and real ground motion data for the 2009 L'Aquila (Mw=6.3) earthquake 195

5.5.5 Comparison of dynamic responses of the buildings to observed and simulated records for the 2009 L'Aquila (Mw=6.3) earthquake 207

5.6 Uncertainties Involved in the Nonlinear Time History Analyses of MDOF Structures 225

5.7 Main Findings of Chapter 5 226

6 CONTRIBUTIONS, CONCLUSIONS, AND RECOMMENDATIONS 229

6.1 Main Contributions 229

6.2 Conclusions 231

6.3 Fundamental Limitations of This Study and Related Future Work 233

REFERENCES 235

APPENDICES 253

A DESCRIPTION OF THE SELECTED ESDOF MODELS 253

B SENSITIVITY ANALYSIS FOR DERIVATION OF FRAGILITY CURVES 275

B.1 Sensitivity of Fragility Curves to Ground Motion Records 275

B.2 Sensitivity of Fragility Curves to Methodology 279

C COMPARISON OF DIFFERENT DAMAGE ESTIMATION APPROACHES 283

D DESCRIPTION OF SELECTED FRAMES 285

E COMPARISON OF NONLINEAR STATIC PUSH OVER ANALYSES AGAINST NONLINEAR TIME HISTORY ANALYSES 303

E.1 Comparison of Capacity Curve and Dynamic Responses for the 1992 Erzincan Earthquake (Mw=6.6) 304

E.2 Comparison of Capacity Curve and Dynamic Responses for the 1999 Düzce Earthquake (Mw=7.1) 308

E.3 Comparison of Capacity Curve and Dynamic Responses for the 2009 L'Aquila Earthquake (Mw=6.3) 313

F COMPARISON OF SEISMOLOGICAL MISFITS AGAINST NONLINEAR RESPONSE MISFITS 319

F.1 Comparison of the Seismological Misfits versus Nonlinear Response Misfits for the 1992 Erzincan (Mw=6.6) Earthquake 320

F.2 Comparison of the Seismological Misfits versus Nonlinear Response Misfits for the 1999 Düzce (Mw=7.1) Earthquake 322

F.3 Comparison of the Seismological Misfits versus Nonlinear Response Misfits for the 2009 L'Aquila (Mw=6.3) Earthquake 324

CURRICULUM VITAE 329

LIST OF TABLES

TABLES

Table 2.1 Radiation pattern; $R\theta\emptyset$ (Boore and Boatwright, 1984) 17

Table 4.1 Simulation parameters used in the simulation of scenario earthquakes..... 51

Table 4.2 Vs30 values available at the 9 nodes 53

Table 4.3 Proposed ESDOF parameters for all building sub-classes..... 68

Table 4.4 Limit states in terms of displacement for all sub-classes..... 77

Table 4.5 General form of damage probability matrix given by Gurpinar *et al.* (1978) 90

Table 4.6 Observed MDRs during the 1992 Erzincan earthquake with Mw=6.6..... 95

Table 4.7 Percent distribution of buildings with respect to structural type as well as number of stories in the Erzincan region 96

Table 4.8 Estimated PGA, PGV, and MDR values for the 1992 Erzincan earthquake 102

Table 4.9 Performance of different damage estimation approaches in predicting the observed MDRs during the 1992 Erzincan earthquake..... 104

Table 4.10 Estimated PGA values for all scenario earthquakes 107

Table 4.11 Estimated PGV values for all scenario earthquakes 108

Table 4.12 Estimated MDRs for all scenario earthquakes (DEA3) 109

Table 5.1 Total mass and fundamental period of the selected frames 125

Table 5.2 Information on the strong motion stations that recorded the 1992 Erzincan earthquake 131

Table 5.3 Source parameters of the 1992 Erzincan earthquake 133

Table 5.4 SS misfits in terms of fast Fourier amplitude spectra ($Misfit_{FAS}$) for real and simulated data at the stations for the 1992 Erzincan earthquake 142

Table 5.5 SS misfits in terms of response spectra ($Misfit_{RS}$) for real and simulated data at the stations for the 1992 Erzincan earthquake 142

Table 5.6 NSS misfits for real and simulated data at the stations for the 1992 Erzincan earthquake 143

Table 5.7 Top story displacements of observed and simulated data at the stations for the 1992 Erzincan earthquake 155

Table 5.8 Misfits in terms of nonlinear responses ($Misfit_{NR}$) to real and simulated data at the stations for the 1992 Erzincan earthquake 156

Table 5.9 Information on the strong motion stations that recorded the 1999 Düzce earthquake 161

Table 5.10 Source parameters of the 1999 Düzce earthquake 163

Table 5.11 SS misfits in terms of fast Fourier amplitude spectra ($Misfit_{FAS}$) for real and simulated data at the stations for the 1999 Düzce earthquake 172

Table 5.12 SS misfits in terms of response spectra ($Misfit_{RS}$) for real and simulated data at the stations for the 1999 Düzce earthquake 173

Table 5.13 NSS misfits for real and simulated data at the stations for the 1999 Düzce earthquake 173

Table 5.14 Top story displacements of observed and simulated data at the stations for the 1999 Düzce earthquake 184

Table 5.15 Misfits in terms of nonlinear responses (Misfit$_{NR}$) to real and simulated data at the stations for the 1999 Düzce earthquake 184

Table 5.16 Information on the strong motion stations that recorded the 2009 L'Aquila earthquake 190

Table 5.17 Source parameters of the 2009 L'Aquila earthquake..... 192

Table 5.18 SS misfits in terms of fast Fourier amplitude spectra (Misfit$_{FAS}$) for real and simulated data at the stations for the 2009 L'Aquila earthquake 204

Table 5.19 SS misfits in terms of response spectra (Misfit$_{RS}$) for real and simulated data at the stations for the 2009 L'Aquila earthquake 205

Table 5.20 NSS misfits for real and simulated data at the stations for the 2009 L'Aquila earthquake 206

Table 5.21 Top story displacements of observed and simulated data at the stations for the 2009 L'Aquila earthquake..... 217

Table 5.22 Misfits in terms of nonlinear responses (Misfit$_{NR}$) to real and simulated data at the stations for the 2009 L'Aquila earthquake 219

Table A.1 ESDOF parameters for all 20 buildings of sub-class RF1A 253

Table A.2 ESDOF parameters for all 20 buildings of sub-class RF1B 254

Table A.3 ESDOF parameters for all 20 buildings of sub-class RF1C 255

Table A.4 ESDOF parameters for all 20 buildings of sub-class RF2A 256

Table A.5 ESDOF parameters for all 20 buildings of sub-class RF2B 257

Table A.6 ESDOF parameters for all 20 buildings of sub-class RF2C 258

Table A.7 ESDOF parameters for all 20 buildings of sub-class RW1A 259

Table A.8 ESDOF parameters for all 20 buildings of sub-class RF2A 260

Table A.9 ESDOF parameters for all 20 buildings of sub-class RH1A 261

Table A.10 ESDOF parameters for all 20 buildings of sub-class RH1B..... 262

Table A.11 ESDOF parameters for all 20 buildings of sub-class RH2A 263

Table A.12 ESDOF parameters for all 20 buildings of sub-class RH2B..... 264

Table A.13 ESDOF parameters for all 20 buildings of sub-class MU1A 265

Table A.14 ESDOF parameters for all 20 buildings of sub-class MU1B..... 266

Table A.15 ESDOF parameters for all 20 buildings of sub-class MU1C..... 267

Table A.16 ESDOF parameters for all 20 buildings of sub-class MU2A 268

Table A.17 ESDOF parameters for all 20 buildings of sub-class MU2B..... 269

Table A.18 ESDOF parameters for all 20 buildings of sub-class MU2C..... 270

Table A.19 ESDOF parameters for all 20 buildings of sub-class MU3A 271

Table A.20 ESDOF parameters for all 20 buildings of sub-class MU3B..... 272

Table A.21 ESDOF parameters for all 20 buildings of sub-class MU3C..... 273

Table B.1 SRSS errors for all masonry subclasses as well as the mean values of the errors using alternative ground motion sets 278

Table B.2 SRSS errors for all masonry subclasses as well as the mean values of the errors using alternative fragility curve generation methodologies 280

Table D.1 Sectional properties of frame F1-3S2B 285

Table D.2 Sectional properties of frame F2-3S2B 286

Table D.3 Sectional properties of frame F3-3S3B 287

Table D.4 Sectional properties of frame F4-4S3B 288

Table D.5 Sectional properties of frame F5-4S3B 289

Table D.6 Sectional properties of frame F6-5S2B 290

Table D.7 Sectional properties of frame F7-5S4B 291

Table D.8 Sectional properties of frame F8-7S3B 293

Table D.9 Sectional properties of frame F9-8S3B 294

Table D.10 Material properties of concrete 296

Table D.11 Material properties of reinforcing steel 298

Table D.12 Story masses 299

Table D.13 Beam loading of the frames 300

Table D.14 Modal properties 301

LIST OF FIGURES

FIGURES

Figure 2.1 Step by step stochastic point-source modeling procedure (Adapted from Boore, 2003) 16

Figure 2.2 Wave propagation on a rectangular finite-fault model (Adapted from Hisada, 2008) 27

Figure 4.1 Main steps for simulation-based seismic loss assessment..... 42

Figure 4.2 (a) Major tectonic structures around the Anatolian plate and large earthquakes on the North Anatolian Fault Zone in the last century (b) Seismotectonics in the Erzincan region with the fault systems and the epicenters of the 1939 and 1992 events (Figures 4.2.a and 4.2.b are adapted from Akyüz et. al., 2002 and Askan et al., 2013, respectively)..... 44

Figure 4.3 Spatial distribution of all earthquakes with Mw>=5.0 around Erzincan city center..... 45

Figure 4.4 Spatial distribution of the districts in the Erzincan Province (The blue circle indicates the Erzincan city center) 47

Figure 4.5 Percent distribution of all buildings in different districts of Erzincan 48

Figure 4.6 Percent distribution of the number of stories for all buildings in Erzincan 48

Figure 4.7 Percent distribution of the major structural type of all buildings in Erzincan 49

Figure 4.8 Percent distribution of primary use for all buildings in Erzincan..... 49

Figure 4.9 Distribution of the selected nodes in the study area 52

Figure 4.10 Spatial distribution of the simulated (a) PGA (b) PGV values of the 1992 Erzincan earthquake in Erzincan region 55

Figure 4.11 Spatial distribution of the simulated (a) PGA (b) PGV values of the scenario earthquake with Mw=5.0 in Erzincan region..... 56

Figure 4.12 Spatial distribution of the simulated (a) PGA (b) PGV values of the scenario earthquake with Mw=5.5 in Erzincan region..... 57

Figure 4.13 Spatial distribution of the simulated (a) PGA (b) PGV values of the scenario earthquake with Mw=6.0 in Erzincan region..... 58

Figure 4.14 Spatial distribution of the simulated (a) PGA (b) PGV values of the scenario earthquake with Mw=6.5 in Erzincan region..... 59

Figure 4.15 Spatial distribution of the simulated (a) PGA (b) PGV values of the scenario earthquake with Mw=7.0 in Erzincan region..... 60

Figure 4.16 Spatial distribution of the simulated (a) PGA (b) PGV values of the scenario earthquake with Mw=7.5 in Erzincan region..... 61

Figure 4.17 Backbone curve for hysteresis model (Adapted from Ibarra et al., 2005) 66

Figure 4.18 Individual deterioration modes of Ibarra peak-oriented model: (a) basic strength deterioration; (b) post-capping strength deterioration; (c) unloading stiffness

deterioration; and (d) accelerated reloading stiffness deterioration (Adopted from Ibarra *et al.*, 2005) 67

Figure 4.19 Distribution of the ground motion parameters for the first set of motions 72

Figure 4.20 Distribution of the ground motion parameters for the second set of motions 73

Figure 4.21 Period and strength ratio pairs generated by LHS technique for all sub-classes 74

Figure 4.22 Period and ductility factor pairs generated by LHS technique for all sub-classes 75

Figure 4.23 Distribution of the response parameter in terms of maximum displacement with respect to ground motion intensity parameter for (a) RF1A and (b) MU1A 75

Figure 4.24 Schematic representation of the fragility curve generation procedure ... 79

Figure 4.25 Fragility curves for RF sub-classes using records categorized based on (a) PGA and (b) PGV where the red lines correspond to LS_1, the black lines to LS_2, and the blue lines to LS_3 80

Figure 4.26 Fragility curves for RW sub-classes using records categorized based on (a) PGA and (b) PGV where the red lines correspond to LS_1, the black lines to LS_2, and the blue lines to LS_3 81

Figure 4.27 Fragility curves for RH sub-classes using records categorized based on (a) PGA and (b) PGV where the red lines correspond to LS_1, the black lines to LS_2, and the blue lines to LS_3 82

Figure 4.28 Fragility curves for masonry sub-classes using records categorized based on (a) PGA and (b) PGV where the red lines correspond to LS_1, the black lines to LS_2, and the blue lines to LS_3 83

Figure 4.29 Examples of RC buildings from Erzincan; (a) shear wall RC building (RW) (b) frame RC building (RF) (c) dual RC building (RH) 86

Figure 4.30 Examples of masonry buildings from Erzincan with varying material and construction quality 87

Figure 4.31 Conversion from a set of fragility curves to DPM 92

Figure 4.32 Spatial distribution of the low-rise RC buildings in the districts (Erzincan) 97

Figure 4.33 Spatial distribution of the mid-rise RC buildings in the districts (Erzincan) 97

Figure 4.34 Spatial distribution of the 1-story masonry buildings in the districts (Erzincan) 98

Figure 4.35 Spatial distribution of the 2-story masonry buildings in the districts (Erzincan) 98

Figure 4.36 Spatial distribution of the 3-story masonry buildings in the districts (Erzincan) 99

Figure 4.37 Spatial distribution of the simulated (a) PGA (b) PGV values of the 1992 Erzincan earthquake in the districts (Erzincan) 103

Figure 4.38 Comparison of the estimated MDRs using: (a) DEA1 (b) DEA2, and (c) DEA3, with the observed MDRs during the 1992 Erzincan earthquake 104

Figure 4.39 Spatial distribution of the (a) observed and (b) estimated MDRs in the Erzincan region for the 1992 Erzincan earthquake 105

Figure 4.40 Spatial distribution of the estimated (a) PGA (b) PGV (c) MDR in the Erzincan region for scenario event of Mw=5.0 110

Figure 4.41 Spatial distribution of the estimated (a) PGA (b) PGV (c) MDR in the Erzincan region for scenario event of Mw=5.5 111

Figure 4.42 Spatial distribution of the estimated (a) PGA (b) PGV (c) MDR in the Erzincan region for scenario event of Mw=6.0 112

Figure 4.43 Spatial distribution of the estimated (a) PGA (b) PGV (c) MDR in the Erzincan region for scenario event of Mw=6.5 113

Figure 4.44 Spatial dpatial distribution of the estimated (a) PGA (b) PGV (c) MDR in the Erzincan region for scenario event of Mw=7.0 114

Figure 4.45 Spatial distribution of the estimated (a) PGA (b) PGV (c) MDR in the Erzincan region for scenario event of Mw=7.5 115

Figure 5.1 Main steps for NTHA of MDOF structures used in this study 123

Figure 5.2 Graphical representation of a fiber element (Adopted from Taucer *et al.*, 1991) 127

Figure 5.3 Material models for (a) steel and (b) concrete; (In this figure, f_y is the yield strength, E_0 is the initial elastic tangent, b is the strain-hardening ratio of the steel, f_c is the concrete compressive strength at 28 days, ε_c is the concrete strain at maximum strength, f_u is the concrete crushing strength, ε_u is the concrete strain at crushing strength 128

Figure 5.4 Map showing the fault plane and epicenter of the 1992 Erzincan earthquake with the locations of the stations 131

Figure 5.5 Station ERC; (a) Observed and simulated accelerograms (b) Fourier Amplitude Spectra (c) Response Spectra with 5% damping obtained for observed (NS and EW) and simulated horizontal component (Synthetic with and without directivity effects)..... 136

Figure 5.6 Station REF; (a) Observed and simulated accelerograms (b) Fourier Amplitude Spectra (c) Response Spectra with 5% damping obtained for observed (NS and EW) and simulated horizontal component (Synthetic) 137

Figure 5.7 Station TER; (a) Observed and simulated accelerograms (b) Fourier Amplitude Spectra (c) Response Spectra with 5% damping obtained for observed (NS and EW) and simulated horizontal component (Synthetic) 138

Figure 5.8 Distribution of (a) maximum story displacements and (b) maximum drift ratios due to the real and simulated records of Erzincan Earthquake – F1-3S2B.... 146

Figure 5.9 Distribution of (a) maximum story displacements and (b) maximum drift ratios due to the real and simulated records of Erzincan Earthquake – F2-3S2B.... 147

Figure 5.10 Distribution of (a) maximum story displacements and (b) maximum drift ratios due to the real and simulated records of Erzincan Earthquake – F3-3S3B.... 148

Figure 5.11 Distribution of (a) maximum story displacements and (b) maximum drift ratios due to the real and simulated records of Erzincan Earthquake – F4-4S3B.... 149

Figure 5.12 Distribution of (a) maximum story displacements and (b) maximum drift ratios due to the real and simulated records of Erzincan Earthquake – F5-4S3B.... 150

Figure 5.13 Distribution of (a) maximum story displacements and (b) maximum drift ratios due to the real and simulated records of Erzincan Earthquake – F6-5S2B.... 151

Figure 5.14 Distribution of (a) maximum story displacements and (b) maximum drift ratios due to the real and simulated records of Erzincan Earthquake – F7-5S4B.... 152

Figure 5.15 Distribution of (a) maximum story displacements and (b) maximum drift ratios due to the real and simulated records of Erzincan Earthquake – F8-7S3B.... 153

Figure 5.16 Distribution of (a) maximum story displacements and (b) maximum drift ratios due to the real and simulated records of Erzincan Earthquake – F9-8S3B.... 154

Figure 5.17 Map showing the fault plane and epicenter of the 1999 Düzce earthquake with the locations of the stations..... 162

Figure 5.18 Station DZC; (a) Observed and simulated accelerograms (b) Fourier amplitude spectra (c) Response spectra with 5% damping obtained for observed (NS and EW) and simulated horizontal component (Synthetic) 167

Figure 5.19 Station GYN; (a) Observed and simulated accelerograms (b) Fourier amplitude spectra (c) Response spectra with 5% damping obtained for observed (NS and EW) and simulated horizontal component (Synthetic) 168

Figure 5.20 Station IZN; (a) Observed and simulated accelerograms (b) Fourier amplitude spectra (c) Response spectra with 5% damping obtained for observed (NS and EW) and simulated horizontal component (Synthetic) 169

Figure 5.21 Station IZT; (a) Observed and simulated accelerograms (b) Fourier mplitude spectra (c) Response spectra with 5% damping obtained for observed (NS and EW) and simulated horizontal component (Synthetic) 170

Figure 5.22 Station YPT; (a) Observed and simulated accelerograms (b) Fourier amplitude spectra (c) Response spectra with 5% damping obtained for observed (NS and EW) and simulated horizontal component (Synthetic) 171

Figure 5.23 Distribution of (a): maximum story displacements and (b): maximum drift ratios due to the real and simulated records of Düzce Earthquake – F1-3S2B..... 175

Figure 5.24 Distribution of (a): maximum story displacements and (b): maximum drift ratios due to the real and simulated records of Düzce Earthquake – F2-3S2B..... 176

Figure 5.25 Distribution of (a): maximum story displacements and (b): maximum drift ratios due to the real and simulated records of Düzce Earthquake – F3-3S3B..... 177

Figure 5.26 Distribution of (a): maximum story displacements and (b): maximum drift ratios due to the real and simulated records of Düzce Earthquake – F4-4S3B..... 178

Figure 5.27 Distribution of (a): maximum story displacements and (b): maximum drift ratios due to the real and simulated records of Düzce Earthquake – F5-4S3B..... 179

Figure 5.28 Distribution of (a): maximum story displacements and (b): maximum drift ratios due to the real and simulated records of Düzce Earthquake – F6-5S2B..... 180

Figure 5.29 Distribution of (a): maximum story displacements and (b): maximum drift ratios due to the real and simulated records of Düzce Earthquake – F7-5S4B..... 181

Figure 5.30 Distribution of (a): maximum story displacements and (b): maximum drift ratios due to the real and simulated records of Düzce Earthquake – F8-7S3B..... 182

Figure 5.31 Distribution of (a): maximum story displacements and (b): maximum drift ratios due to the real and simulated records of Düzce Earthquake – F9-8S3B..... 183

Figure 5.32 Map showing the fault plane and epicenter of 2009 L'Aquila earthquake with the locations of the selected stations 190

Figure 5.33 Station AQA; (a) Observed and simulated accelerograms (b) Fourier amplitude spectra (c) Response spectra with 5% damping obtained for observed (NS and EW) and simulated horizontal components (Synthetic-SFF and Synthetic-HIC)..... 196

Figure 5.34 Station CLN; (a) Observed and simulated accelerograms (b) Fourier amplitude spectra (c) Response spectra with 5% damping obtained for observed (NS

and EW) and simulated horizontal components (Synthetic-SFF and Synthetic-HIC) 197

Figure 5.35 Station FMG; (a) Observed and simulated accelerograms (b) Fourier amplitude spectra (c) Response spectra with 5% damping obtained for observed (NS and EW) and simulated horizontal components (Synthetic-SFF and Synthetic-HIC) 198

Figure 5.36 Station GSA; (a) Observed and simulated accelerograms (b) Fourier amplitude spectra (c) Response spectra with 5% damping obtained for observed (NS and EW) and simulated horizontal components (Synthetic-SFF and Synthetic-HIC) 199

Figure 5.37 Station LSS; (a) Observed and simulated accelerograms (b) Fourier amplitude spectra (c) Response spectra with 5% damping obtained for observed (NS and EW) and simulated horizontal components (Synthetic-SFF and Synthetic-HIC) 200

Figure 5.38 Station MTR; (a) Observed and simulated accelerograms (b) Fourier amplitude spectra (c) Response spectra with 5% damping obtained for observed (NS and EW) and simulated horizontal components (Synthetic-SFF and Synthetic-HIC) 201

Figure 5.39 Station SUL; (a) Observed and simulated accelerograms (b) Fourier amplitude spectra (c) Response spectra with 5% damping obtained for observed (NS and EW) and simulated horizontal components (Synthetic-SFF and Synthetic-HIC) 202

Figure 5.40 Distribution of (a): maximum story displacements and (b): maximum drift ratios due to the real and simulated records of L'Aquila Earthquake – F1-3S2B ... 208

Figure 5.41 Distribution of (a): maximum story displacements and (b): maximum drift ratios due to the real and simulated records of L'Aquila Earthquake – F2-3S2B ... 209

Figure 5.42 Distribution of (a): maximum story displacements and (b): maximum drift ratios due to the real and simulated records of L'Aquila Earthquake – F3-3S3B ... 210

Figure 5.43 Distribution of (a): maximum story displacements and (b): maximum drift ratios due to the real and simulated records of L'Aquila Earthquake – F4-4S3B ... 211

Figure 5.44 Distribution of (a): maximum story displacements and (b): maximum drift ratios due to the real and simulated records of L'Aquila Earthquake – F5-4S3B ... 212

Figure 5.45 Distribution of (a): maximum story displacements and (b): maximum drift ratios due to the real and simulated records of L'Aquila Earthquake – F6-5S2B ... 213

Figure 5.46 Distribution of (a): maximum story displacements and (b): maximum drift ratios due to the real and simulated records of L'Aquila Earthquake – F7-5S4B ... 214

Figure 5.47 Distribution of (a): maximum story displacements and (b): maximum drift ratios due to the real and simulated records of L'Aquila Earthquake – F8-7S3B ... 215

Figure 5.48 Distribution of (a): maximum story displacements and (b): maximum drift ratios due to the real and simulated records of L'Aquila Earthquake – F9-8S3B ... 216

Figure B.1 Distribution of the ground motion parameters corresponding to records selected with respect to PGA without considering ground motion variability 276

Figure B.2 Fragility curves developed for all masonry subclasses corresponding to records selected with respect to PGA without considering ground motion variability 277

Figure B.3 Schematic representation of the alternative fragility curve generation procedure 280

Figure B.4 Fragility curves developed for all masonry sub-classes with respect to PGA using new approach 281

Figure C.1 Comparison of the average MDRs for Erzincan presented for three approaches: DEA1, DEA2, and DEA3 284

Figure D.1 Frame F1-3S2B 285

Figure D.2 Frame F2-3S2B 286

Figure D.3 Frame F3-3S3B 287

Figure D.4 Frame F4-4S3B 288

Figure D.5 Frame F5-4S3B 289

Figure D.6 Frame F6-5S2B 290

Figure D.7 Frame F7-5S4B 292

Figure D.8 Frame F8-7S3B 294

Figure D.9 Frame F9-8S3B 295

Figure E.1 Capacity Curve and Dynamic Responses of Erzincan Earthquake for F1-3S2B 304

Figure E.2 Capacity Curve and Dynamic Responses of Erzincan Earthquake for F2-3S2B 304

Figure E.3 Capacity Curve and Dynamic Responses of Erzincan Earthquake for F3-3S3B 305

Figure E.4 Capacity Curve and Dynamic Responses of Erzincan Earthquake for F4-4S3B 305

Figure E.5 Capacity Curve and Dynamic Responses of Erzincan Earthquake for F5-4S3B 306

Figure E.6 Capacity Curve and Dynamic Responses of Erzincan Earthquake for F6-5S2B 306

Figure E.7 Capacity Curve and Dynamic Responses of Erzincan Earthquake for F7-5S4B 307

Figure E.8 Capacity Curve and Dynamic Responses of Erzincan Earthquake for F8-7S3B 307

Figure E.9 Capacity Curve and Dynamic Responses of Erzincan Earthquake for F9-8S3B 308

Figure E.10 Capacity Curve and Dynamic Responses of Düzce Earthquake for F1-3S2B 308

Figure E.11 Capacity Curve and Dynamic Responses of Düzce Earthquake for F2-3S2B 309

Figure E.12 Capacity Curve and Dynamic Responses of Düzce Earthquake for F3-3S3B 309

Figure E.13 Capacity Curve and Dynamic Responses of Düzce Earthquake for F4-4S3B 310

Figure E.14 Capacity Curve and Dynamic Responses of Düzce Earthquake for F5-4S3B 310

Figure E.15 Capacity Curve and Dynamic Responses of Düzce Earthquake for F6-5S2B 311

Figure E.16 Capacity Curve and Dynamic Responses of Düzce Earthquake for F7-5S4B 311

Figure E.17 Capacity Curve and Dynamic Responses of Düzce Earthquake for F8-7S4B 312

Figure E.18 Capacity Curve and Dynamic Responses of Düzce Earthquake for F9-8S3B 312

Figure E.19 Capacity Curve and Dynamic Responses of L'Aquila Earthquake for F1-3S2B 313

Figure E.20 Capacity Curve and Dynamic Responses of L'Aquila Earthquake for F2-3S2B 313

Figure E.21 Capacity Curve and Dynamic Responses of L'Aquila Earthquake for F3-3S3B 314

Figure E.22 Capacity Curve and Dynamic Responses of L'Aquila Earthquake for F4-4S3B 314

Figure E.23 Capacity Curve and Dynamic Responses of L'Aquila Earthquake for F5-4S3B 315

Figure E.24 Capacity Curve and Dynamic Responses of L'Aquila Earthquake for F6-5S2B 315

Figure E.25 Capacity Curve and Dynamic Responses of L'Aquila Earthquake for F7-5S4B 316

Figure E.26 Capacity Curve and Dynamic Responses of L'Aquila Earthquake for F8-7S3B 316

Figure E.27 Capacity Curve and Dynamic Responses of L'Aquila Earthquake for F9-8S3B 317

Figure F.1 Average of residuals over all simulated Erzincan records versus frequency, where residual = log(Predicted FAS) - log(Observed FAS). Standard deviation of residulas are depicted by error bars. 321

Figure F.2 Average of residuals over all simulated Erzincan records versus period, where residual = log(Predicted RS) - log(Observed RS). Standard deviation of residulas are depicted by error bars. 321

Figure F.3 Average of residuals over all simulated Erzincan records versus period of frames, where residual = log(Predicted NR) - log(Observed NR). Standard deviation of residulas are depicted by error bars. 322

Figure F.4 Average of residuals over all simulated Düzce records versus frequency, where residual = log(Predicted FAS) - log(Observed FAS). Standard deviation of residulas are depicted by error bars. 323

Figure F.5 Average of residuals over all simulated Düzce records versus period, where residual = log(Predicted RS) - log(Observed RS). Standard deviation of residulas are depicted by error bars. 323

Figure F.6 Average of residuals over all simulated Düzce records versus period of frames, where residual = log(Predicted NR) - log(Observed NR). Standard deviation of residulas are depicted by error bars. 324

Figure F.7 Average of residuals using (a) Synthetic-SFF and (b) Synthetic-HIC methods over all simulated L'Aquila records versus frequency, where residual = log(Predicted FAS) - log(Observed FAS). Standard deviation of residulas are depicted by error bars. 326

Figure F.8 Average of residuals using (a) Synthetic-SFF and (b) Synthetic-HIC methods over all simulated L'Aquila records versus period, where residual = log(Predicted RS) - log(Observed RS). Standard deviation of residulas are depicted by error bars. 327

Figure F.9 Average of residuals using (a) Synthetic-SFF and (b) Synthetic-HIC methods over all simulated L'Aquila records versus period of frames, where residual = log(Predicted NR) - log(Observed NR). Standard deviation of residulas are depicted by error bars. 328

LIST OF SYMBOLS AND ABBREVIATIONS

μ:	Ductility factor
1D:	One-dimensional
2D:	Two-dimensional
3D:	Three-dimensional
b:	Strain-hardening ratio
C:	Collapse
CAV:	Cumulative Absolute Velocity
CDR:	Central Damage Ratio
DEA:	Damage Estimation Approach
DPM:	Damage Probability Matrix
DR:	Damage Ratio
DS:	Damage State
DS_1:	None damage
DS_2:	Light damage
DS_3:	Moderate damage

DS_4: Severe damage

DSHA: Deterministic Seismic Hazard Assessment

E_0: Initial elastic tangent

EERI: Earthquake Engineering Research Institute

EMS: European Microseismic Scale

ERD: Earthquake Research Department

ESDOF: Equivalent Single Degree Of Freedom

EW: East-West

f: Frequency

FAS: Fourier Amplitude Spectrum

f_c: Concrete compressive strength at 28 days

F-K: Frequency-wavenumber

F_r: Residual strength

f_u: Concrete crushing strength

f_y: Yield strength

H/V: Horizontal-to-Vertical

H: Heavy damage

HI: Housner intensity

HIC: Hybrid-Integral-Composite

I_a: Arias intensity

IL: Intensity Level

INGV: Institute of Geophysics and Volcanology

K_e: Elastic (initial) stiffness

K_s: Pre-capping stiffness

L: Light damage

LHS: Latin Hypercube Sampling

LS_1: Immediate Occupancy

LS_2: Life Safety

LS_3: Collapse Prevention

M: Moderate damage

M_0: Seismic moment

MASW: Multi-Channel Array Surface Waves

MDOF: Multi-Degree-Of-Freedom

MDR: Mean Damage Ratio

MMI: Modified Mercalli Intensity scale

MSK: Medvedev–Sponheuer–Karnik

Mw: Moment magnitude

N: No damage

NAF: North Anatolian Fault

NAFZ: North Anatolian Fault Zone

NEHRP: National Earthquake Hazards Reduction Program

NLTHA: Nonlinear Time History Analysis

NR: Nonlinear Response

NS: North-South

NSS: Non-Spectral Seismological

PBEE: Performance-Based Earthquake Engineering

PGA: Peak Ground Acceleration

PGV: Peak Ground Velocity

PSA: Elastic response spectra with 5% damping

PSHA: Probabilistic Seismic Hazard Assessment

PSI: Parameterless Scale of Seismic Intensity

PSV: Pseudo-Spectral Velocity

R: Source-to-site-distance

RC: Reinforced-Concrete

ReMi: Refraction Microtremor

R_{epi}: Epicentral distance

R_{JB}: Joyner-Boore distance

RMS: Root Mean Square

RMSE: Root Mean Square Error

RS: Response Spectra

SASW: Spectral Analysis of Surface Waves

SDOF: Single-Degree-Of-Freedom

SFF: Stochastic Finite-Fault

SPAC: Spatially Averaged Coherency

SRSS: Square Root of the Sum of the Squares

SS: Spectral Seismological

SSR: Standard Spectral Ratio

T: Period

T_1: Fundamental period

t_{eff}: Significant duration

Vs30: The 30m-average shear wave velocity in units of m/s

α_c: Post-capping to elastic stiffness ratio

α_s: Strain hardening ratio

β: Crustal shear wave velocity

γ: Hysteretic energy dissipation parameter

δ_c: Cap deformation

δ_r: Residual strength deformation

δ_y: Yield deformation

$\Delta\sigma$: Stress drop

ε_c: Concrete strain at maximum strength

ε_u: Concrete strain at crushing strength

η: Strength ratio

κ_0: Zero-distance Kappa

λ: Ratio of residual strength to yield strength

ξ: Viscous damping ratio

CHAPTER 1

INTRODUCTION

1.1 Background

Amplitudes, durations, and frequency content are the major characteristics of strong ground motion records that influence seismic behavior of structures. Peak ground motion parameters are commonly used to represent ground motion characteristics. Yet, whenever detailed response analyses of structures are required, full time histories become necessary. Nonlinear Time History Analysis (NLTHA) is a detailed dynamic analysis that provides valuable information by taking into account the material and geometric nonlinearity as well as complexity of the ground motion time series. For accurate estimations of inelastic seismic demand of structures, the use of nonlinear time history analysis is recommended by many recent seismic design codes such as the current Turkish Earthquake Code (2007).

To conduct nonlinear time history analysis, majority of the previous studies used either past strong ground motion records or employed modified/scaled ground motion records that match a target ground motion intensity or a spectrum (e.g.: Iervolino and Cornell, 2005; Baker and Cornell, 2006). However, past records within the Instrumental era are not always sufficient in terms of variability in seismic parameters such as fault type, magnitude, source-to-site-distance, or soil properties. In regions

with sparse ground motion data or large earthquakes with long return periods, as an alternative, simulated ground motions may be utilized. The use of ground motions from alternative simulation techniques has recently been of particular interest in earthquake engineering as the simulated motions can practically be obtained and they reflect the physics of the earthquakes, the faulting mechanisms, and the regional seismic parameters. International building codes (e.g.: EC8, 2004; ASCE Standard ASCE/SEI 7-10, 2010) specify that simulated strong ground motion time histories may be used to represent the seismic excitations.

Next, a brief summary of past studies on ground motion simulation methods and use of simulated motions for engineering purposes are presented separately.

1.2 Literature Survey on Ground Motion Simulation Techniques

With respect to the modeling assumptions and solution techniques, strong ground motion simulation methods can be divided into three main groups: Deterministic, stochastic, and hybrid simulations. Deterministic approaches mostly employ numerical solutions of the partial differential equations of wave propagation and require well-defined seismic sources as well as detailed spatial variation of material properties of the Earth (e.g.: Bouchon, 1981; Frankel, 1993; Olsen *et al.*, 1995; Komatitsch *et al.*, 2004; Aagaard *et al.*, 2010). Despite their accuracy, they are practical for relatively lower frequencies due to the computational and physical constraints related to the minimum wavelength. There are different numerical methods to solve the equation of motion corresponding to seismic wave propagation through a three-dimensional heterogeneous medium. These methods are the boundary-element method (e.g.: Kawase, 1988; Luco *et al.*, 1990; Pedersen *et al.*, 1994), the finite difference method (e.g.: Frankel and Vidale, 1992; Frankel, 1993; Yomogida and Egten, 1993; Olsen *et al.*, 1995; Olsen and Archuleta, 1996; Moczo *et al.*, 2002), the finite element method (e.g.: Li *et al.*, 1992; Rial *et al.*, 1992; Toshinawa and Ohmachi, 1992; Bao, 1998), the spectral element method (e.g.: Cohen *et al.*, 1993; Priolo *et al.*, 1994; Komatitsch, 1997; Komatitsch and Vilotte, 1998; Komatitsch and Tromp, 1999; Komatitsch *et al.*, 2004), the theoretical Green's function method (e.g.: Bouchon,

1981; Hisada, 1994; Chen and Zhang, 2001), and the empirical Green‘s function method (e.g.: Hartzell ,1978; Irikura, 1986).

Stochastic methods mainly simulate high frequency portion of ground motion records that are random and incoherent in nature. The earliest efforts that have considered stochastic character of ground motion records in simulation process are the classical works of Housner (1947), Housner (1955), and Thomson (1959). The mentioned studies have assumed the source as a random sequence of short impulses to model time histories. Other early representative works in this area are the studies by Haskell (1966) and Aki (1967): Two alternative dislocation models of an earthquake source were introduced in these studies. First, Haskell (1966) proposed a ω^{-3} model by fitting an exponentially decaying function to the autocorrelation function of the dislocation acceleration. Later, Aki (1967) concluded that the ω^{-2} model is in better agreement with the decay of the observed amplitude spectrum compared to the ω^{-3} model. Among these two theories, the one proposed by Aki (1967) was later verified by the other authors (e.g.: Brune, 1970; Hanks, 1979).

To improve the original stochastic method, several authors worked on the source-time function including the studies by Haskell (1964), Aki (1968), Brune (1970 and 1971), Hanks (1979), and Hanks and McGuire (1981). The findings of these studies demonstrated that the randomness in high frequency portion of seismic waves can be represented with white Gaussian noise. Boore (1983) proposed a new methodology for generation of time-domain synthetic time histories where the fault is represented as a stochastic point-source by combining the source spectrum of Aki (1967) and Brune (1971) with the findings of Hanks and McGuire (1981). The stochastic point-source technique by Boore (1983) is based on the deterministic far-field S-wave Fourier amplitude spectrum of acceleration with random phase angles through a simple seismological model.

Later, in order to include the finite-fault effects in the synthetic records of near-field events, Beresnev and Atkinson (1997) proposed the Stochastic Finite-Fault (SFF) method. The stochastic finite-fault method is an extension of the stochastic point-

source model of Boore (1983) to finite-faults: The fault plane is discretized into smaller sub-faults, and the contributions of the sub-faults are summed in the time domain where every sub-fault is treated as a stochastic point-source. The most recent version of the stochastic method uses a dynamic corner frequency approach (Motazedian and Atkinson, 2005) to model the high frequency content of the shear wave portion of ground motion records. In the dynamic corner frequency approach, the corner frequency at any time is defined to be inversely proportional to the area of the sub-faults that have ruptured up to that time (Motazedian and Atkinson, 2005).

All of stochastic methods combine the deterministic far-field S-wave spectrum with random phases and yield an average horizontal component of ground motion records (Boore, 1983, 2003, 2009; Beresnev and Atkinson, 1997; Motazedian and Atkinson, 2005). They have an inherent limitation due to lack of full wave propagation effects, yet they are employed effectively for several seismic regions in the world for both point-source and finite-fault modeling (e.g.: Atkinson, 1984; Hanks and Boore, 1984; Toro and McGuire, 1987; Beresnev and Atkinson, 1997; Atkinson and Silva, 2000; Castro *et al.*, 2001 and 2008; Erdik and Durukal, 2001; Durukal, 2002; Roumelioti *et al.*, 2004; Motazedian and Atkinson, 2005; Yalcinkaya, 2005; Motazedian and Moinfar, 2006; Shoja-Taheri and Ghofrani, 2007; Galuzzo *et al.*, 2008; Atkinson *et al.*, 2009; Boore, 2009; Raghukanth and Somala, 2009, Ugurhan and Askan, 2010; Ugurhan *et al.*, 2012; Ghofrani *et al.*, 2013; Askan *et al.*, 2013; Askan *et al.*, 2015b; Askan *et al.*, 2016). Stochastic finite-fault method needs less computational efforts and also is more practical when compared to deterministic technique. Yet, the low frequency content simulated with first method is not as accurate as the latter due to the lack of full wave propagation. To represent the entire frequency band accurately, hybrid methods are developed by combining deterministic and stochastic approaches for simulation of low and high frequency components, respectively (e.g.: Kamae *et al.*, 1998; Hartzell et *al.*, 1999; Pitarka *et al.*, 2000; Hisada, 2008; Frankel, 2009; Halldorsson , 2010; Mai *et al.*, 2010). It should be noted that the alternative ground motion simulation methods mentioned involve different computing costs and provide different levels of accuracy. Thus, several measures are introduced to evaluate the

goodness of fit between the measured and the simulated records (e.g.: Anderson, 2004; Olsen and Mayhew, 2010).

To assess the deterministic seismic hazard of a region for earthquake engineering applications, the use of simulation techniques is preferred to the Ground Motion Prediction Equations (GMPEs) for many reasons. Not only the simulation techniques provide full time histories compatible with the regional seismicity rather than the peak ground motion parameters, but also synthetic records take into account the azimuthal variability in the region. Among different methods of simulation, the use of stochastic methods for engineering applications becomes valuable as they are practical and effective in simulating a wide range of frequencies including those that influence the built environment. Among the stochastic methods, the point-source method is useful for simulation of far-field events, whereas, the stochastic finite-fault technique can produce similar time histories at sites located in close vicinity of the earthquake source for large events. Both point-source and finite-fault methods have been utilized in engineering seismology field, especially for regions with insufficient records, such as the development of the hybrid Ground Motion Prediction Equation (GMPE) (Atkinson and Boore, 2006; Atkinson and Macias, 2009). Modeling and simulation of ground motion records based on stochastic methods can be performed using two simulation packages, FINSIM and EXSIM (http://daveboore.com/software_online.html).

Although it is important to reach seismically acceptable synthetic records (from a seismological point of view), one important need is to investigate the likely impact and consequences of synthetic records on the built environment (from an engineering point of view). The above-mentioned studies on simulating strong ground motion records have progressed extensively and provided satisfactory research results. However a major research field remains open which is concerned with the use of simulated time histories for structural and earthquake engineering applications.

Next, limited number of studies that employ simulated motions for earthquake engineering purposes is discussed.

1.3 Literature Survey on Use of Simulated Records in Earthquake Engineering

A major application in earthquake engineering practice is estimation of seismic damage to existing structures under potential earthquakes. In spite of efforts for dense seismic networks all over the world, there are still areas located in the vicinity of fault planes with sparsely-distributed or no seismic stations. In addition, even regions that are continuously monitored may lack records from some potential large earthquakes with long return periods. For such regions, a full range of recorded ground motions compatible with the regional seismicity is not possible. As an alternative, simulated ground motions can significantly expand the understanding of potential earthquakes and help to mitigate their outcomes on built environment. Existing studies on loss and damage estimations employ generic (instead of local) ground motion information (e.g.: Porter and Kiremidjian, 2001; Kwon and Elnashai, 2005; Erberik, 2008a; Erberik, 2008b; Askan and Yucemen, 2010; Mazılıgüney *et al.*, 2013; Salami and Goda, 2013; Tesfamariam and Goda, 2015).

To assess seismic loss in any region, it is required to obtain information on ground motion characteristics as well as building data. Through these data, building fragility and distribution of damage in the study area are obtained. There is a limited number of studies in the literature that used records obtained from ground motion simulation techniques for seismic loss assessment. Sucuoğlu *et al.* (2003), studied the 1995 Dinar (Turkey) earthquake with M_w=6.4 to investigate the capability of synthetic records generated from Green's functions for estimation of the structural damage in the region of interest. For the sake of urban seismic hazard mitigation, Zhao *et al.* (2007) simulated seismic wave propagation of the 1995 Hyogoken-Nanbu (Kobe) metropolitan earthquake (M_L=7.2). Through comparison of the distribution of hazard levels in terms of peak ground acceleration with the observed building collapse ratios, an excellent agreement was observed. Similarly, Ansal *et al.* (2009) carried out a study on seismic loss estimation in Istanbul (Turkey), using a hybrid-stochastic deterministic approach introduced by Pacor *et al.* (2005). Later, Ugurhan *et al.* (2011) developed a methodology for seismic loss estimation where existing fragility curves are combined

with a synthetic ground motion dataset prepared for a magnitude range of 5.5 to 7.5. Recently, Sørensen *et al.* (2015) investigated the use of synthetic records generated from stochastic finite-fault methodology versus ground motion prediction equations in seismic vulnerability assessment of the 1991 Uttarkashi earthquake (Mw=6.8). In all these studies, there is a limitation in terms regional data use: Either the local building data is not employed, or existing generic fragility curves are used, or variability in regional seismic hazard is not assessed.

Another significant research problem is to further validate the simulated full time series in detailed dynamic response analyses of structures. For this purpose, Heaton *et al.* (1995) generated a hypothetical Mw=7.0 blind thrust earthquake by using a broadband ground motion simulation technique for Los Angeles basin with the aim of evaluating the responses of a 20-story steel-frame building and a 3-story base-isolated structure. In another study, Bazzurro *et al.* (2004) compared post-elastic response of nonlinear Single-Degree-Of-Freedom (SDOF) oscillators for seven simulation techniques against the "true" response provided by observed accelerograms of the 1994 Northridge earthquake. Later, Krishnan *et al.* (2006a) and (2006b) simulated ground motion records of two hypothetical Mw=7.9 earthquakes with a deterministic method on the San Andreas fault to determine the damage to tall steel moment-frame buildings in southern California. In another study, Atkinson and Goda (2010) compared peak nonlinear responses of inelastic SDOF systems under stochastically-simulated records, slightly-modified observed records, and scaled-observed records. Later, Atkinson *et al.* (2011) compared the peak ductility demand of inelastic SDOF systems under accelerograms simulated with the stochastic finite-fault and the hybrid broadband method. Later, Galasso Zareian (2012) compared the elastic and post-elastic seismic responses of SDOF systems subjected to simulated and recorded ground motions of four historical earthquakes: The synthetic records were generated with the hybrid broadband approach by Graves and Pitarka (2010). Later, Galasso *et al.* (2013) conducted a similar study to the one in 2012 by considering the same simulation technique but generalized elastic Multi-Degree-Of-Freedom (MDOF) systems. In another study, Galasso and Zareian (2014) investigated if synthetic time

histories generated from the hybrid broadband approach are systematically biased in terms of median engineering demand parameters of either SDOF or MDOF systems in comparison to real ground motions. Recently, Goda *et al.* (2015) compared the nonlinear seismic responses of generic inelastic SDOF systems subjected to both real and synthetic time histories of the 2011 Tohoku main shock, by using two alternative ground motion simulation techniques. In these studies either SDOF structures are investigated or MDOF structures are assessed with records from only a limited number of events.

Until now, simulated time histories have not been commonly used in practical engineering applications since they have not been sufficiently verified compared to observed records in terms of predicting structural demands. Furthermore, synthetic records are still not fully open to the use of engineering community. So far, studies that incorporate the use of simulated records in local vulnerability models for seismic loss assessment are missing. Similarly, studies on detailed structural responses of multi-degree-of-freedom systems under simulated motions are quite few. To fill these gaps in the literature, it is believed that investigating capability of simulated records in seismic loss estimation and seismic demand evaluation of MDOF structures could be valuable.

1.4 Objectives and Scope

The long-term goal of this thesis, in the light of the detailed literature survey presented, is to extend the knowledge on the use of simulated ground motions for earthquake engineering purposes.

To attain the mentioned long-term goal, the fundamental purpose of this study is to apply the stochastic finite-fault method with the use of well-defined local parameters to model time histories of past and potential seismic events. These records are employed for two major earthquake engineering applications to compare the responses due to real and simulated records. .

The objectives of the thesis can be summarized as follows:

1) To apply the stochastic finite-fault methodology to model observed time histories of past and potential earthquakes
2) To propose the use of simulated ground motion records in earthquake engineering practice by implementing the simulated time histories in two applications which are:
   a) Seismic loss estimation with simple SDOF models
   b) Dynamic response analysis of detailed MDOF frame buildings
3) To investigate and evaluate the efficiency of the simulated motions by comparison of the results against the corresponding results with the real records for two applications mentioned previously

The scope of the thesis in order to accomplish the above mentioned objectives are listed as follows:

- For the first part which is seismic loss estimation with simple SDOF models:

1. Determination of regional seismicity parameters for simulation of time histories
2. Generation of simulated time histories for different scenarios
3. Collection of structural data corresponding to the local building stock
4. Development of fragility curves
5. Seismic damage assessment in the study area
6. Validation of the estimated damage states through comparisons against the observed damages
7. Predictions for the spatial distribution of damage for alternative scenarios in the study area

- For the second part which is dynamic response analysis of detailed MDOF frame buildings:

1. Collection of existing ground motion data for three different case studies
2. Determination of regional seismicity parameters for simulation of time histories

3. Generation of synthetic records for the existing earthquakes for two of the case studies; compilation of the existing simulated motions for the third case study
4. Collection of structural parameters corresponding to typical MDOF frame buildings
5. Performing NLTHA using both real and simulated records to assess the dynamic responses of the MDOF structures
6. Validation of the simulated records for each case study through comparison of the real and simulated structural responses

It must be noted that the main findings of each application is presented at the end of the corresponding Chapter.

1.5 Organization of the Thesis

In this thesis, the following chapters are discussed in the order that they are presented.

Chapter 2 presents the theoretical background of the simulation methodology with a brief explanation of its components.

Chapter 3 briefly describes the NLTHA method which is used as the main method of dynamic structural analysis in this study.

Chapter 4 includes the first application of simulated time histories in earthquake engineering practice: Seismic damage assessment using simulated records with simple SDOF models for a case study. This chapter includes details about the simulated records in the respective area, classification of local building stock, fragility analyses and estimation of damage. Finally, the estimated losses for potential scenarios and a discussion on the results are presented.

Chapter 5 presents the second application of simulated time histories in earthquake engineering practice: Dynamic response analysis of detailed MDOF frame buildings. In this chapter, dynamic analyses of detailed MDOF structures are investigated for both observed and simulated records of three case studies. Discussion of the results for each case study is presented separately.

Finally, in Chapter 6 conclusions are provided on the efficiency of the simulated time histories for two approaches used in this thesis. Recommendations for future studies are also presented.

CHAPTER 2

METHODOLOGY FOR GROUND MOTION SIMULATION: THE STOCHASTIC APPROACH

2.1 General

Simulation methods, both stochastic and deterministic, are introduced to physically model the amplitude and frequency content of ground motions generated during earthquakes that occur on active faults. Deterministic methods require accurate source representations and wave velocity models to model the low frequencies of ground motions (< 1 Hz) which are mostly coherent in nature. High frequencies (>1 Hz) on the other hand, have stochastic nature consisting of random phase angles (Hanks and McGuire, 1981). Stochastic approach is particularly developed in order to account for this incoherency in phase angles. There are two major stochastic methods: point-source and finite-fault methods. The simplest stochastic approach is stochastic point-source method developed by Boore 1983. This technique considers the source as a single point with a ω^{-2} spectrum (Brune 1970, Boore 1983). It is practical for mostly modeling far-field ground motions and small to moderate size earthquakes. However, for larger events or stations located in closer

distances to the sources where the effects of fault geometry, slip distribution on the fault plane, and directivity are of concern, stochastic finite-fault method yields more accurate ground motion amplitudes (e.g.: Hartzell, 1978; Irikura, 1983; Joyner and Boore, 1986; Heaton and Hartzell, 1986; Zeng *et al.*, 1994; Beresnev and Atkinson, 1998a).

The higher frequencies are of major concern for typical residential structures due to the fundamental periods involved. Thus, in this thesis, higher frequencies are mostly investigated where the stochastic finite-fault technique is employed as the main ground motion simulation method. For the completeness of the theory, in the following sections, the fundamental hypotheses of stochastic point-source and stochastic finite-fault technique are represented.

2.2 Stochastic Point-Source Method

Stochastic point-source method is fundamentally based on the original studies of Hanks and McGuire (1981) who proposed that high frequencies of shear waves in time histories can be represented as finite duration, band-limited and white Gaussian noise (Hanks, 1979; McGuire and Hanks, 1980; Hanks and McGuire, 1981). This method assumes stationary behavior for frequency content of ground motion records and considers only the contribution of S-waves. Yet, from structural point of view, shear waves contain most of the energy related to hazard and damage (e.g.: Su and Ye, 2009). In addition, S-waves are mostly sufficient to model the significant features of ground motions, especially of the horizontal components.

The objective of stochastic point-source methodology is to generate a completely stochastic time series whose spectrum represents a target deterministic spectrum for a specified point-source. To generate the time series, first a band-limited Gaussian white noise with zero mean and variance for duration related to the earthquake magnitude and source-to-site-distance is generated. Then the generated noise is windowed and transformed to the frequency domain. For this purpose mostly Saragoni-Hart and boxcar windows are applied. Spectrum of the windowed noise is normalized by the

square root of its mean square amplitude spectrum. The normalized spectrum is multiplied by the theoretical S-wave amplitude spectrum. Finally, the resulted spectrum is transformed back to the time domain that yields the final ground motion time series. These steps for simulation of ground motion records accomplish two main conditions: (a) simulation of time series with a finite duration (b) a specified amplitude spectrum resulting in a physical representation of the fault rupture, path and site effects (Boore, 1983). These steps are shown in Figure 2.1.

The ground motion amplitude spectrum in stochastic point-source model as introduced by Boore (1983) is given in Equation 2.1. It is the product of the source spectrum, E path effect filter, P site effect filter, G and the type of motion parameter, I:

$$Y(M_0, R, f) = E(M_0, f) * P(R, f) * G(f) * I(f) \tag{2.1}$$

where M_0 is the seismic moment, R is the source-to-site-distance, f is the frequency, and $I(f) = (2\pi f i)^n$ indicates the type of time series as it can be ground displacement; $(n = 0)$, ground velocity; $(n = 1)$, or ground acceleration; $(n = 2)$.

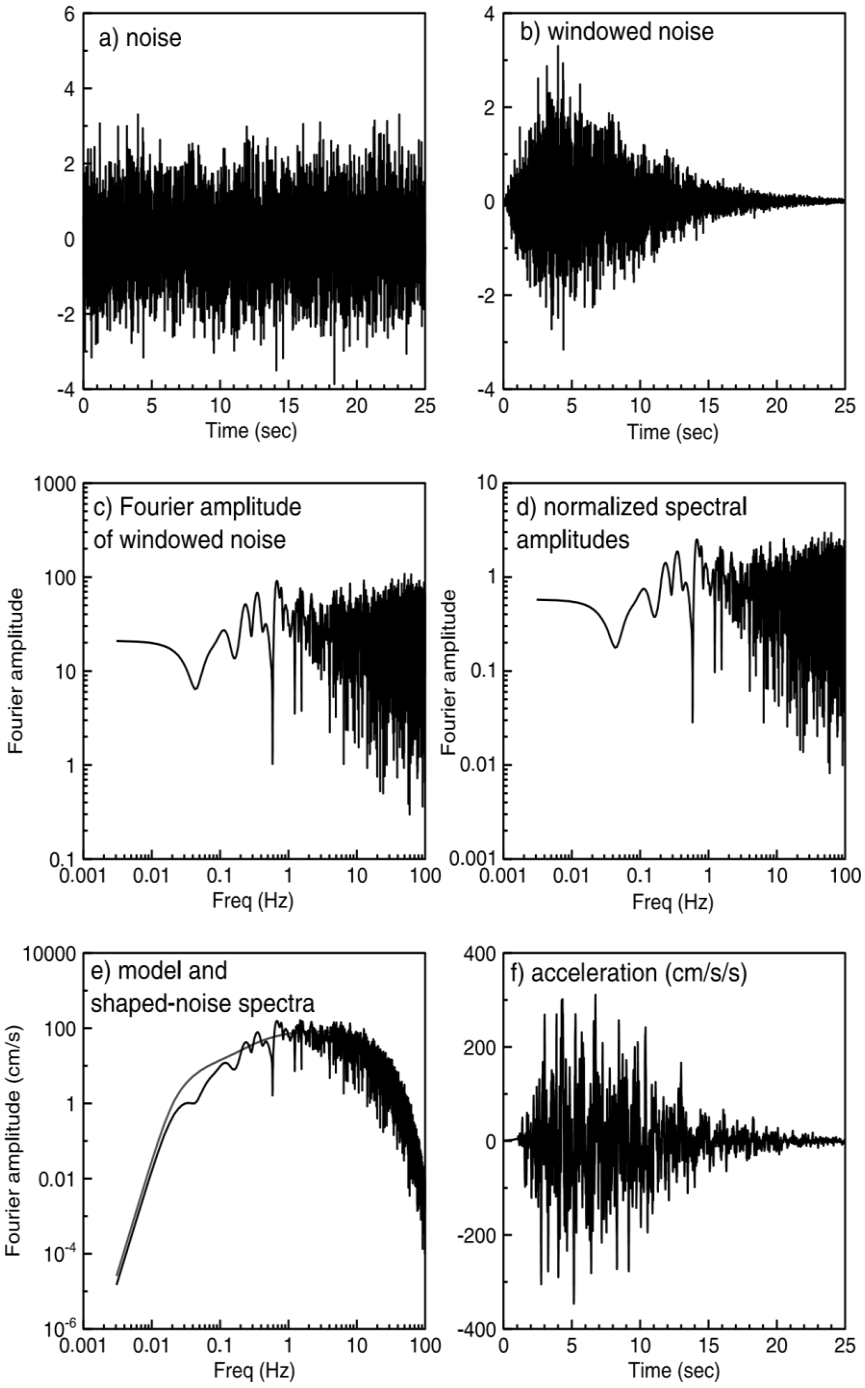

Figure 2.1 Step by step stochastic point-source modeling procedure (Adapted from Boore, 2003)

2.2.1 Source spectrum, $E(M_0, f)$

Source spectrum demonstrates the Fourier amplitude spectrum of the displacements developed at the source due to the shear wave radiation. Majority of the theoretical source spectrum models developed in the literature has the following functional form:

$$E(M_0, f) = C.M_0.S(f) \tag{2.2}$$

where $C = (R_{\theta\emptyset}.FS.PRTITN)/(4\pi\rho_s\beta_s^3\ R_0)$ represents a scaling constant, such that $R_{\theta\emptyset}$ denotes the radiation pattern as a function of style of faulting and Joyner-Boore distance (R_{JB}: The shortest distance from a site to the surface projection of the rupture surface) (Table 2.1). FS accounts for the amplification on the free surface and is assumed to be 2. $PRTITN$ is a reduction factor taken as $1/\sqrt{2}$, which reflects the partitioning of the total energy into two horizontal components. ρ_s and β_s is the density and shear wave velocity, respectively. M_0 is the seismic moment of earthquake generally given by $\mu\bar{u}A$ where μ is the shear modulus or rigidity, $\bar{u}$ accounts for the average slip and A is the fault area.

Table 2.1 Radiation pattern; $R_{\theta\emptyset}$ (Boore and Boatwright, 1984)

Distance	Shallow dipping	Strike-Slip
1 km≤ R_{JB}<25km	0.64	0.50
25 km≤ R_{JB}≤100km	0.48	0.60

To define a relationship between seismic moment (M_0) and moment magnitude (M), Equation 2.3 is developed by Hanks and Kanamori (1979) as follows:

$$M = \frac{2}{3}\log(M_0) - 10.73 \tag{2.3}$$

In Equation 2.2, $S(f)$ accounts for the displacement source function as the most important component used for establishing the source spectrum. There exists variety of functions for source spectrum in the literature. One of the well-known models is Brune (1970) spectrum model in which radiation of shear waves initiates from a point-source located at the center of a fault plane. This model is controlled by two main parameters; the first parameter is seismic moment, M_0 expresses the size of the earthquake. The second one is constant stress drop, $\Delta\sigma$ that represents the total released energy during an earthquake which controls the high frequency amplitudes of the earthquakes. Brune spectrum as a ω-squared model was chosen due to the success of Hanks and McGuire (1981) with it in explaining observed peak and Root Mean Square (RMS) accelerations (Boore, 1983). The source spectrum of Brune (1970) is defined as follows:

$$S(f, f_c) = \frac{1}{1+(\frac{f}{f_c})^2} \tag{2.4}$$

where f_c accounts for the corner frequency defined by Brune (1970, 1971) as follows:

$$f_c = 4.9 \times 10^6 \beta_s (\frac{\Delta\sigma}{M_0})^{1/3} \tag{2.5}$$

where f_c is in Hz, β_s is shear wave velocity in km/s, $\Delta\sigma$ is stress drop in bars, and M_0 is in dyne-cm.

Brune spectrum can estimate the higher frequency ground motion amplitudes effectively for most stochastic simulations. Yet, since this model assumes a circular fault rupture, it can fail to model large magnitude events where fault geometry becomes significant. Therefore, this model can overestimate the ground motion amplitudes at lower frequencies for moderate to high magnitude earthquakes. Indeed, alternative finite-fault models are developed for large events as described in Section 2.3.

To model finite-fault ruptures using point-source methods, another source function alternative to Brune model was later introduced by Atkinson and Silva (2000). This

later model mimics the salient effects of finite-fault ruptures by presenting an equivalent point-source spectrum generated from the finite-fault modeling. The following expression represents the Atkinson and Silva (2000) source model:

$$S(f, f_c) = \frac{1-\varepsilon}{1+(\frac{f}{f_a})^2} + \frac{\varepsilon}{1+(\frac{f}{f_b})^2} \tag{2.6}$$

where f_a is the lower corner frequency which represents the size of the finite-fault and correlates with the source duration, f_b is related to the sub-fault size and represents the higher corner frequency, and ε is a relative weighting parameter which lies between 0 and 1. The following formulae are the empirical equations represented by Atkinson and Silva (2000) for the pre-mentioned parameters:

$$\log(f_a) = 2.181 - 0.496M_w$$

$$\log(f_b) = 2.41 - 0.408M_w \tag{2.7}$$

$$\log(\varepsilon) = 0.605 - 0.255M_w$$

It should be noted that Brune approach with assumption of single corner frequency is applied in the original stochastic finite-fault method. Later, a dynamic corner frequency approach where corner frequency is a function of time has been introduced to be used for generation of ground motions. Details of this concept are presented in Section 2.3.

2.2.2 Path effects, *P(R, f)*

The second significant factor that influences the characteristics of ground motion records is the path effects. The amplitude spectrum along with the frequency content of ground motions change as a result of seismic wave propagation through the crust. These path propagation effects can be categorized into two groups: elastic and anelastic processes known as geometric and anelastic attenuation, respectively. Geometric spreading expresses the reduction of ground motion amplitudes due to spreading of seismic wave energy over a continuously increasing area as a result of

expansion of wave fronts. The anelastic attenuation expresses dissipation of seismic energy in the form of heat energy, commonly because of particle interaction (Romero and Rix, 2001). It is worth to mention that geometric spreading is an elastic process in which seismic energy is conserved, whereas anelastic attenuation is an inelastic process where seismic energy is lost.

The total path effect filter, expressed as a product of both geometrical and anelastic attenuations in the frequency domain is as follows:

$$P(R,f) = Z(R).\exp\left(-\frac{\pi.f.R}{Q(f).c_Q}\right) \tag{2.8}$$

where $Z(R)$ is geometrical spreading function, R denotes source-to-site-distance, $Q(f)$ is a frequency-dependent quality factor and c_Q accounts for the S wave velocity used in the derivation of Q.

Geometrical spreading function (Z), describes the attenuation of ground motion amplitudes due to the source-to-site distance along with the regional thickness of the Earth crust. For cases where distances are close to intermediate, ground motions are governed by the directly arriving seismic waves, whereas at far distances, ground motions are influenced by several reflections of body waves travelling through the Earth crust. These two cases result in spherical and cylindrical distribution of seismic waves at close and far distances, respectively (Atkinson and Mereu, 1992; Lam *et al.*, 2000).Therefore, geometrical spreading is usually expressed as distance-dependent piecewise continuous series of functions. The following functions are introduced by Boore (2003):

$$\mathrm{Z(R)} = \begin{cases} \dfrac{R_0}{R} & R \le R_1 \\ Z(R_1)\left(\dfrac{R_1}{R}\right)^{p_1} & R_1 \le R \le R_2 \\ \vdots & \vdots \\ Z(R_n)\left(\dfrac{R_n}{R}\right)^{p_n} & R \le R_n \end{cases} \tag{2.9}$$

where R is generally assumed to be the closest distance to the rupture surface.

Anelastic attenuation, the exponential term in Equation 2.8, is the other part of path effects which accounts for the exponential decay of ground motion amplitudes with number of wave cycles. In this term, Q is the quality factor which indicates the regional wave transmission quality of the propagation medium (Lam *et al.*, 2000). For determination of quality factor, Q, two prevalent methods based on the analysis of weak motion data are Spectral ratio and Coda wave approaches (Atkinson and Mereu, 1992). It must be noted that Q is inversely proportional to the damping factor, ζ, of the Earth materials.

In stochastic point-source method for generation of simulated ground motion records, there is critical trade-off between the geometrical spreading and anelastic attenuation requiring careful selection of the corresponding parameters.

Even though it is not expressed in the frequency domain representation given in Equation 2.1, ground motion duration is another significant path factor which is affected by the source kinematics as well as the source-to-site-distance. Within the context of the stochastic approach, it is used in the time domain definition of the simulated time series as the summation of source duration, T_0 and distance dependent duration, bR (Atkinson and Boore, 1995; Atkinson and Silva, 2000; Boore, 2003) as follows:

$$T = T_0 + bR \tag{2.10}$$

During the fault rupturing process, the total time needed for the release of accumulated strain energy is defined as the source duration. It should be noted that T_0 increases as the size of an earthquake increases. Therefore, this parameter is inversely proportional to the corner frequency of the source model ($T_0 = 1/(2f_a)$ Atkinson and Silva, 2000). The other term, bR which is distance-dependent increases as the source-to-site distance increases; b is a region-dependent parameter, which is defined either as a constant or a distance-dependent parameter (Atkinson and Boore, 1995).

2.2.3 Site effects, *G(f)*

Characteristics of ground motion records like amplitude, frequency content, and duration are considerably affected by the local site conditions. Due to the inhomogeneity of soil layers in terms of seismic impedance (wave propagation velocity multiplied by the density), traveling of seismic waves from bedrock with higher velocities up to the surface with lower velocities cause their nature to change. The simulation method proposed by Boore (2003) considers the modifications of the seismic waves by the surface soils overlying bedrock separately as the local site effects. One of the drawbacks of Boore's method is that it does not consider nonlinear site effects. Instead, this method computes rock motions by using a linear model and accounts for nonlinear site effects as part of an additional site response analysis.

Site effects on the ground motion amplitude spectrum, $G(f)$ is described as the product of two terms, the amplification, $A(f)$ and diminution, $D(f)$ factors as follows:

$$G(f) = A(f)D(f) \tag{2.11}$$

where $A(f)$ is the unattenuated amplification of seismic waves relative to the source and $D(f)$ is the path-independent loss of high-frequency seismic energy.

i: Computation of A(f):

Amplification of seismic waves due to their transmission from a high-impedance medium to a lower impedance, *A(f)* is commonly assessed from the wave-calculation solutions which explain the impedance differences specified from shear wave velocity variations with depth. The most well-known techniques for derivation of seismic wave velocity profiles are seismic reflection, refraction, and borehole drilling. After determining seismic wave velocity profiles, one can assess the amplification factors by applying theoretical transfer functions. These transfer functions can be computed once the One-Dimensional (1D) (Haskell, 1960; Kennett, 1983), Two-Dimensional (2D) (Sanchez-Sesma, 1987) or Three-Dimensional (3D) (Pitarka *et al.*, 1998) models of the soil medium are specified.

The above-mentioned methods for the construction of seismic wave velocity profiles, particularly in cases where deep basins are of concern, become complicated and costly. Alternatively, to assess the shear wave velocity profiles, surface waves including a wide range of frequencies can be measured and evaluated. In this approach by referring to the higher and the lower frequency portions of the surface wave measurements, velocity profile of the both shallower and also deeper layers of soil can be estimated, respectively. Sources of these surface waves can be either active or passive. Hammers, electromechanical shakers, seismic vibrators, weight drops, and bulldozers are samples of active sources to generate seismic surface wave energies. Two well-known active-source methodologies for derivation of shear wave velocity profiles are Spectral Analysis of Surface Waves (SASW) (Stokoe *et al.*, 1994) and Multi-Channel Array Surface Waves (MASW) (Park *et al.*, 1999). In these techniques, the shear wave dispersion curves are iteratively developed by matching to the measured dispersion curves (e.g.: Rosenblad and Li, 2009).

The alternative approaches to estimate shallow shear velocities for assessment of earthquake site response are the passive-source methods. In these techniques, first the ambient vibrations within the Earth is measured and then analyzed to obtain the shear wave velocity of the soil profile. Microtremors and ambient noise are two examples of passive sources of seismic wave velocities. The most recently-developed passive techniques for determining shallow shear-wave velocity can be listed as Refraction Microtremor, or ReMi (Louie, 2001), Frequency-wavenumber (F-K) (Schmidt, 1986), and Spatially Averaged Coherency (SPAC) (Asten *et al.*, 2003). For the estimation of the thickness and shear wave velocity of the sediments in sites of interest SPAC technique can be useful. In SPAC approach which relies on the findings of Aki (1957), first kind and zero order Bessel function is assumed for the shape of the averaged coherency spectrum. Then, iterations are performed in order to match the theoretical coherency curves with the observed coherency curves to yield the shear wave velocities and thicknesses of the soil layers at a site of interest (Claprood and Asten, 2007).

Another technique to determine *A(f)* is quarter wavelength approximation method. In this method, the amplification of a particular frequency is specified as the square root of the ratio of the seismic impedance at the source to the seismic impedance averaged over a depth that is equivalent to the quarter wavelength of the corresponding frequency (Joyner and Fumal, 1985; Boore and Joyner, 1997). The amplification factor is given as follows:

$$A\big(f(z)\big) = \sqrt{\frac{\rho_s V_{S,s}}{\bar{\rho}(z)\,\bar{V}_s(z)}} \tag{2.12}$$

where $f(z) = \frac{1}{4S_{tt}(z)}$ is frequency corresponding to depth z where $S_{tt}(z)$ represents S-wave travel time from depth z to the ground surface; ρ_s and $V_{S,s}$ explains the density and S-wave velocity in the proximity of the source, respectively; $\bar{\rho}(z)$ and $\bar{V}_s(z)$ is travel-time-weighted average of density and S-wave velocity to depth z, respectively.

The approximate amplification factors of quarter wavelength theory have been compared with the exact theoretical amplifications and it has been validated that this method provides a close estimation (e.g.: Boore and Joyner, 1991; Silva and Darragh, 1995; Boore and Joyner, 1997). However, this method ignores the soil nonlinearity effects. One way to account for the effects of softer soils in amplification factors is to simulate motions at very hard rock sites and afterwards modify them to produce the surface motions at soils with various S-wave velocity profiles (Boore and Joyner, 1997).

Horizontal-to-Vertical (H/V) spectral ratio method (Nakamura, 1989) is another approach to determine the local site amplification factors. The fundamental assumption of this empirical approach is that only the horizontal components of ground motion records are subjected to local site effects while the vertical ones are not. In other words, the vertical components in each site are assumed to be similar to the motions measured at the bedrock layer beneath the site. Therefore, ground amplification factors for a specified site can be determined as the spectral acceleration ratio between the horizontal and vertical components of motions (H/V ratio) at the

corresponding site. This approach has been validated as a successful method for assessing the site amplification factors by many studies (e.g.: Lermo and Cháves-García, 1994; Suzuki *et al.*, 1995; Huang and Teng, 1999; Raghukanth and Somala, 2009).

There is another empirical approach named as Standard Spectral Ratio (SSR) method where the soil amplification factors are determined by dividing the Fourier amplitude spectrum of each site of interest to the Fourier amplitude spectrum of a specified site with very hard rock soil condition chosen as the reference site for all calculations (Borcherdt, 1970). Since it is very difficult to find sites with hard rock conditions at the surface to be used as reference site, this technique is applied less commonly compared to the others. In this work, two of the abovementioned methods are used to consider local site effects during simulation processes with stochastic finite-fault technique. Boore and Joyner (1997) amplification method is selected for the case of L'Aquila and Erzincan regions; while, both H/V and Boore and Joyner (1997) approaches are applied for Düzce case.

ii: Computation of D(f):

Diminution factor, $D(f)$ describes the path-independent loss of high-frequency energy due to the existence of mediums with lower impedance at top of the Earth crust. In some studies, this decay of energy is attributed to not only the site effects but also the source effects or an association of both. Among several studies, Papageorgiou and Aki (1983) considers only source attribution to diminution function; while Hanks (1982) and Atkinson (2004) express that this attenuation comes from soil quality variance in the vicinity of the site. There exist two common filter types referred as f_{max} and κ_0 that account for the decay of higher frequency motions. The diminution function also known as f_{max} filter developed by Hanks (1982) is as follows:

$$D(f) = \left[1 + \left(\frac{f}{f_{max}}\right)^8\right]^{-0.5} \tag{2.13}$$

where f_{max} is defined as the high-cut filter frequency.

The alternative diminution factor is introduced in Equation 2.14 (Anderson and Hough, 1984). It is an exponential function of κ_0 , where κ_0 is the zero-distance intercept of the high-frequency decay parameter, expressed as follows:

$$D(f) = \exp(-\pi\kappa_0 f) \tag{2.14}$$

2.3 Stochastic Finite-Fault Method

Beresnev and Atkinson (1997) introduced the original stochastic finite-fault model for simulation of ground motion records of near-source receiver sites. In this method, the rectangular fault plane is divided into smaller sub-faults with specified width and length sizes to consider the effects of finite dimension of fault plane on ground motion records at stations located in closer distances to sources. Next, the contribution of each sub-fault is summed in time domain to reach the final response by considering the behavior of each sub-fault as a single point-source model (as introduced by Hartzell, 1978). In this technique, it is assumed that the hypocenter is located on the center of one of the sub-faults. Then, the rupture starts to propagate radially from the hypocenter by a constant shear wave velocity and kinematically reaches the other sub-faults. Therefore, to calculate the final ground motion from the entire fault at a receiver, contribution of all sub-faults are summed in time domain by considering time delay of each sub-fault. The final response of the entire fault plane is as follows:

$$a(t) = \sum_{i=1}^{nl} \sum_{j=1}^{nw} a_{ij}\,(t + \Delta t_{ij}) \tag{2.15}$$

where $a(t)$ is the ground motion acceleration at time t, nl and nw is the number of sub-faults along the length and width of the main fault, respectively; Δt_{ij} is the delayed time of the radiated seismic wave from ij^{th} sub-fault to achieve the observation point; $a_{ij}(t)$ is the ground motion acceleration of ij^{th} sub-fault modeled as a point-source as described by Boore (1983). The general outline of the stochastic finite-fault methodology in the form of rupture propagation on the fault plane is presented in Figure 2.2.

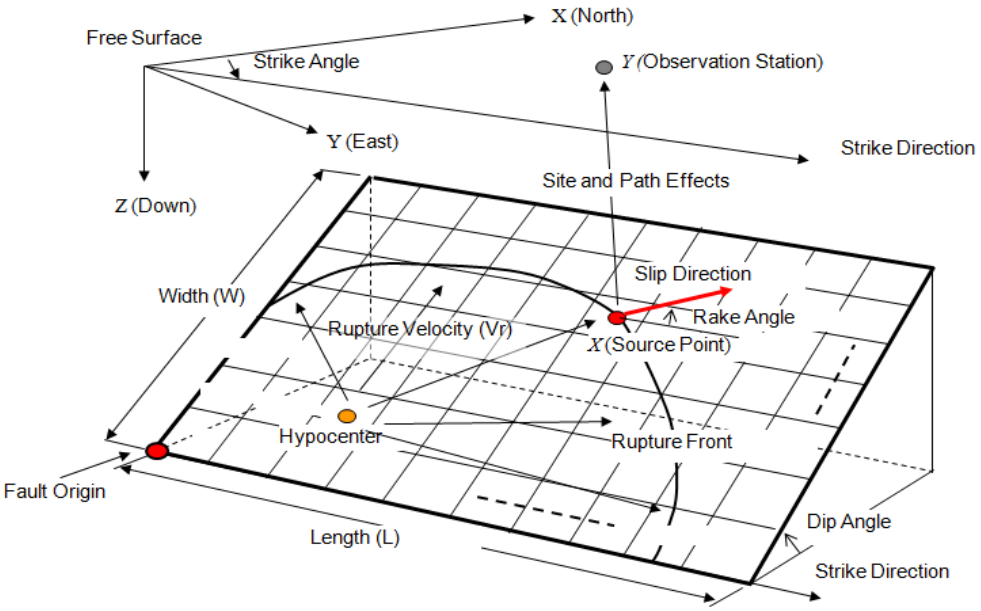

Figure 2.2 Wave propagation on a rectangular finite-fault model
(Adapted from Hisada, 2008)

In stochastic finite-fault model, shear wave acceleration spectrum of each sub-fault is attributed as a point-source located at distance R_{ij}. The acceleration spectrum of each sub-fault was originally modeled with the assumption of an ω^{-2} shape as follows (Aki, 1967; Brune, 1970; Boore, 1983; Beresnev and Atkinson 1997):

$$A_{ij}(f) = CM_{0ij}\frac{(2\pi f)^2}{\left[1+(f_{0ij})^2\right]}\frac{1}{R_{ij}}exp\left(-\frac{\pi f R_{ij}}{Q(f)\beta}\right)exp(-\pi f\kappa)A(f) \qquad (2.16)$$

where M_{0ij}, f_{0ij}, and R_{ij} is the seismic moment, corner frequency, and distance from the observation point of the ijth sub-fault, respectively. The constant C is given by $C = \Re^{\theta\varphi}FV/(4\pi\rho\beta^3)$, where $\Re^{\theta\varphi}$ is radiation pattern of shear waves with average value of 0.55, F is free surface amplification equal to 2, V is partition into two horizontal components as 0.71, ρ is density, and finally β is shear wave velocity. $f_{0ij} =$

$4.9E^{+6}\beta(\frac{\Delta\sigma}{M_{0ij}})^{1/3}$, where $\Delta\sigma$ is stress drop in bars, M_{0ij} is ijth sub-fault seismic moment in dyne-cm, and β is shear wave velocity in km/s. The next term $1/R$ shows the effects of geometric attenuation. The term $exp\left(-\frac{\pi f R_{ij}}{Q\beta}\right)$ represents the anelastic attenuation where Q is the quality factor. The term $exp(-\pi f\kappa)$ represents a high-cut filter resulted from the influences of near-surface kappa in reducing the higher frequency contents of spectral acceleration (Anderson and Hough, 1984). $A(f)$ presents the amplification factor.

The computer program utilizing the original form of the stochastic finite-fault methodology as mentioned above is FINSIM (Beresnev and Atkinson, 1998a and 1998b).

In the finite-fault method, the seismic moment of each sub-fault depends on the ratio of its area to the entire area of the fault plane. If faults are identical, to assess the seismic moment of each sub-fault, total moment of the fault plane will be divided by the number of the sub-faults as follows:

$$M_{0ij} = M_0/N \tag{2.17}$$

where N is the total number of the sub-faults, M_0 is the entire seismic moment of the fault plane, and M_{0ij} is the seismic moment of the ij^{th} sub-fault.

When the sub-fault sizes are not equal, the corresponding seismic moment of each sub-fault is expressed as follows:

$$M_{0ij} = \frac{M_0 S_{ij}}{\sum_{l=1}^{nl}\sum_{k=1}^{nw} S_{kl}} \tag{2.18}$$

where S_{ij} is the relative slip weight of the ij^{th} sub-fault.

There are some weaknesses related to the original form of the stochastic finite-fault methodology with assumption of constant corner frequency approach. In this classical approach, total radiated energy of a particular event depends on the assumption of the sub-fault sizes. This weakness was demonstrated by Motazedian and Atkinson (2005),

as they examined the effect of various sub-fault sizes on the entire radiated energy from a fault. Results showed that as the number of sub-faults increases, energy at low frequencies descends while it ascends at high frequencies. They concluded that even for far stations in which all the simulation parameters have been taken similar, as the size of sub-faults decreases, the total received energy at the observation point increases. Therefore, the total radiated energy is not conserved for a given fault and varies according to sub-fault dimensions, which is not physically correct.

There exist some constraints on the number of sub-faults in the earliest form of stochastic finite-fault method. Also, such kinematic model neglects to model the phasing of different seismic wave arrivals in the signal at far distances as body waves arrive faster than surface waves. At near fault stations, this classical approach does not effectively simulate long-period velocity pulses caused by forward rupture directivity of the source which can affect the frequency, duration, and amplitude content of ground motion records at low frequencies (approximately smaller than 1 Hz).

To handle these limitations, Motazedian and Atkinson (2005) modified the original method by introducing the dynamic corner frequency approach, in which the total radiated energy at high frequencies is independent of sub-fault sizes. It has been investigated by many researchers that corner frequency in stochastic point-source method is inversely proportional to the entire duration or total ruptured area, explicitly or implicitly (e.g.: Hirasawa and Stauder, 1965; Boore, 1983; Boatwright and Choy 1992; Hough and Dreger, 1995). In finite-fault modeling, total area of rupture is a function of time, and consequently the corner frequency. Therefore, to account for the dependency of corner frequency on rupture time, the following expression was developed by Motazedian and Atkinson (2005):

$$f_{0ij}(t) = N_R(t)^{-1/3}\ 4.9 \times 10^6 \beta \left(\frac{\Delta\sigma}{M_{0ave}}\right)^{1/3} \tag{2.19}$$

where $N_R(t)$ is the cumulative number of ruptured subsaults at time t, β is shear wave velocity in km/s, $\Delta\sigma$ is stress drop in bars, and M_{0ave} is the average seismic moment of sub-faults equal to M_0/N.

Besides the corner frequency computations, a second significant difference between the original version (Beresnev and Atkinson, 1997) and the modified version (Motazedian and Atkinson, 2005) of stochastic finite-fault methods is the definition of pulsing sub-fault concept in the latter approach. The modified model divides the sub-fault area into two sections: passive and active rupture areas. The parameter that controls the percentage of the maximum ruptured (active) area is called pulsing area percentage. This new model considers the contribution of only the active part to the dynamic corner frequency. In each time step, the corner frequency of the ijth sub-fault is determined as a function of total number of sub-faults, total number of ruptured sub-faults at that time, stress drop and seismic moment, as given in Equation 2.19. Thus, this feature results in reduction of dynamic corner frequency along with radiated energy at higher frequencies until a specified percentage of pulsing area is attained. After that, the dynamic corner frequency becomes constant. The maximum percentage of pulsing area is named as pulsing area percentage. In order to handle the descending radiated energy problem, a scaling factor H_{ij} for balancing the high frequency spectral level of the sub-faults is specified as follows (Motazedian and Atkinson, 2005):

$$H_{ij} = \left\{ N \frac{\sum\left[\frac{f^2}{1+(\frac{f}{f_0})^2}\right]}{\sum\left[\frac{f^2}{1+\left(\frac{f}{f_{0ij}}\right)^2}\right]} \right\}^{1/2} \tag{2.20}$$

Among different parameters of simulation, pulsing area percentage and stress drop are the two main parameters with significant effects to the final amplitudes of the total amplitude spectra of ground acceleration. The first factor affects mostly the amplitudes of lower frequency part of the generated ground motion records. Boore (1996) explored the effects of pulsing area percentages on the generated ground motions: It was shown that as the pulsing area percentage for a stochastic point-source model decreases, the total radiated energy as well as the relative amplitudes of the response spectra at low frequencies descends. On the other hand, stress drop changes the

amplitudes of spectra at high frequencies. For smaller values of stress drop, smaller amplitudes of response spectra at high frequencies are expected. Therefore, by calibrating both pulsing area percentage and stress drop, it is possible to generate various amplitudes of ground motion records at high and low frequency parts. Yet, this calibration is not randomly performed and the values of these parameters should be consistent with the physical properties of the simulated earthquake.

The other advantages of the modified version of the finite-fault method are the application of this method for earthquakes with a wider magnitude range (M=3.0 to M= 8.0) as well as no restriction on the ratios of amplitudes at high frequencies versus low ones. In addition, to better model forward directivity effects of near fault stations, among different methods, Motazedian and Atkinson (2005) selected the approach of Mavroeidis and Papageorgiou (2003), in which a novel mathematical model for considering this impulsive behavior has been introduced. Within that mathematical model, it is shown that the waveform characteristics of near-fault velocity pulses can be modeled by definition of four parameters: the pulse duration, pulse amplitude, number and phase of half cycles. Therefore, the recent stochastic finite-fault methodology has the capability to combine both analytical and stochastic approaches for cases where directivity effects govern the ground motions.

In the most recent finite-fault method introduced by Motazedian and Atkinson (2005), the final amplitude of acceleration from each sub-fault by considering all source, site and path effects is calculated by the following equation:

$$A_{ij}(f) = CM_{0ij}H_{ij}\frac{(2\pi f)^2}{\left[1+(f_{0ij})^2\right]}\frac{1}{R_{ij}}exp\left(\frac{-\pi f R_{ij}}{Q\beta}\right)exp(-\pi f\kappa)A(f) \qquad (2.21)$$

where the terms are as described earlier.

It must be noted that, other than the major differences in source definitions, the simulation process of the finite-fault approach is identical with the stochastic point-source method as described in Section 2.2 and displayed in Figure 2.1.

In this study, stochastic finite-fault method as introduced by Motazedian and Atkinson (2005) is employed for the simulation of acceleration time histories. This method is selected because stochastic finite-fault method can model the higher frequency contents of ground motion records (>1 Hz) efficiently and these frequencies are along the range of frequencies of engineering interest. Despite its inherent limitations due to the absence of full wave propagation, this approach has been used for simulating several major earthquakes in previous studies (e.g.: Motazedian and Moinfar, 2006; Castro *et al.*, 2008; Ugurhan and Askan, 2010). Thus, this method can be used for engineering purposes in seismically active regions with sparse ground motion data. For simulation purposes, the EXSIM program is utilized. This program which is freely available is widely used and validated by many researchers (e.g.: Motazedian and Atkinson, 2005; Atkinson *et al.*, 2009; Boore, 2009).

The fundamentals of the theory and model parameters are presented in this Chapter. The corresponding values of the input parameters regarding the source, path and site effects will be presented and discussed whenever necessary for each case in the following chapters.

CHAPTER 3

METHODOLOGY FOR DYNAMIC ANALYSES OF BUILDINGS: NONLINEAR TIME HISTORY ANALYSIS

3.1 General

One of the main steps in seismic performance evaluation of structures is to use an accurate dynamic analysis approach in order to determine seismic demands in terms of various structural parameters such as story displacement, inter-story drift, forces and etc. A major point to take into account in structural modeling is that structures may experience severe inelastic deformation under earthquake excitations and as a result their dynamic properties change.

In this study, nonlinear time history analysis is selected in order to investigate the efficiency of simulated ground motion records in earthquake engineering practice in predicting real structural demands. This method is chosen due to the fact that it estimates the inelastic behavior of structures in detail accurately. Therefore, for simulation of structural performance subjected to severe earthquakes, nonlinear time history analysis is more suitable than other analysis techniques. By using this method of analysis, the failure modes as well as the potential for progressive collapse of structures can be identified.

Nonlinear time history analysis is a step by step analysis of dynamic response of a structure under a loading as a function of time, which in this thesis is a ground motion record: Real, simulated, or both.

In the following brief sections, first the structural program used for nonlinear time history analysis in this thesis along with the fundamental equation of motion for NLTHA will be presented. Finally, the limitations of the methodology will be discussed concisely. Modeling details, assumptions along with the related parameters will be presented and discussed in the following chapters, whenever necessary.

3.2 Structural Analysis Program

In this study, as the main structural analysis tool for seismic response estimation, the well-known open-source software platform OpenSees (http://opensees.berkeley.edu) developed by the University of California at Berkeley is selected. This software is based on the concept of finite element analysis in order to simulate the performance of structural systems subjected to earthquake ground motions. The library of materials, elements, and analysis models makes this software a powerful tool for numerical simulation of inelastic structural systems. The OpenSees interface relies on a user-friendly command-driven scripting language. Since this software has various modeling as well as analysis options, different types of analyses including nonlinear time history analysis, can be conducted on this platform.

All structures are expected to experience nonlinear effects throughout their structural components under earthquake excitations where different cyclic degradation modes in their stiffness and strength may be observed. These features can be crucial for seismic response evaluation. In this thesis, the main reasons for selecting OpenSees software are the variability of material models which enables us to consider different cyclic deterioration properties along with its ability to simulate the effects of nonlinearity throughout the structural components (e.g.: Kadaş, 2006; Gavali and Shah, 2008; Girgin *et al.*, 2013).

3.3 Nonlinear Time History Analysis

To identify the detailed dynamic responses of structures under ground shaking, nonlinear time history analyses are performed where the inelastic characteristics of the structures are considered as part of a time domain analysis. Nonlinear time history analysis, as the most reliable method to analyze a structure under severe earthquakes, is used worldwide for direct assessment of seismic performance at member and structural levels. This method of analysis has the ability to model an extensive types of inelastic material behaviors, geometric nonlinearities (including large displacement effects), non-classical damping, and spatial and temporal distributions of inelasticity.

In this thesis, NLTHA involves the full numerical solution to either scalar SDOF (Chapter 3) or vectorial MDOF (Chapter 4) equation of motion under the horizontal-components of the synthetic time histories. The corresponding general (vectorial) form of the differential equation of motion is given as follows:

$$\mathbf{M}\ddot{\underline{u}} + \mathbf{C}\dot{\underline{u}} + \boldsymbol{Fs}(\underline{u}) = -\mathbf{M}\ddot{\underline{u}}_g \tag{3.1}$$

where $\underline{u}$ is the nodal displacement vector, **M** is the mass matrix, **C** is the damping matrix, **Fs(**$\underline{u}$) is the resisting force, and $\ddot{\underline{u}}_g$ is the ground acceleration vector.

3.4 Limitations of Nonlinear Time History Analysis

Although nonlinear time history analysis has advantages over the other methods of seismic analyses, it also involves certain uncertainties arising from different sources. Some of these uncertainties can be summarized as follows:

1. To develop the numerical model for nonlinear time history analysis, the required time and effort increase.
2. Nonlinear time history analysis uses ground motions records as input. The inelastic behavior estimated by NLTHA is much more sensitive to the input ground motion records. Small changes in the content of time histories may result in large variations in nonlinear dynamic responses. Thus, the inelastic

dynamic responses completely depend on the character of input ground motion records.

3. Depending on the modeling assumptions for material properties, beam-column elements and structural capacities made by engineers, various levels of accuracy can be obtained. Structural responses are completely dependent on the strength and stiffness of each component involved and since it is impossible to exactly model the real characteristics of the structures, there are generally uncertainties in the models.
4. In nonlinear time history analysis, the equation of motion is nonlinear, and as a result it is not possible to solve it exactly yielding a variety of numerical approximations. Depending on the numerical integration methods and initial assumptions used for numerical solution of the differential equation of motions, the solutions may involve uncertainties.
5. Final results which are represented for each time step yield a large amount of data by the end of analysis. Therefore, post-processing of the results is time-consuming.

Despite the given limitations, NLTHA is employed in this thesis with the awareness of the assumptions made during the model constructions and analyses. It must be noted that for each SDOF and MDOF model used in this study, material models, modeling details, and the corresponding structural parameters will be presented in detail in the following chapters.

CHAPTER 4

APPLICATION OF SIMULATED RECORDS IN SEISMIC LOSS ESTIMATION: A CASE STUDY FOR ERZINCAN (TURKEY)

4.1 Introduction

Earthquake risk assessment is commonly performed to anticipate the potential structural, social, or economic consequences of an earthquake to a society, a region, or an individual facility. Risk analysis is a multidisciplinary approach which combines a number of research areas such as seismology, geology, geotechnical structural engineering, disaster management, and insurance industry. A basic definition of seismic risk was made by the Earthquake Engineering Research Institute (EERI) Committee on Seismic Risk in 1984, according to which "seismic risk is the probability that social and economic consequences of earthquakes will equal or exceed specified values at a site, at several sites, or in an area during a specified exposure time" (EERI, 1984).

Risk assessment involves estimation of losses in the form of either deterministic or probabilistic framework depending on the definition of seismic hazard. The fundamental objective of every earthquake loss estimation application is to objectively quantify and measure potential physical damage, economic, or social losses. Through earthquake loss estimation studies, future earthquake damages can be reduced in

several ways such as strengthening of existing buildings, establishing codes and provisions for construction of new buildings, compulsory insurance, preparedness and prevention measures (social awareness). There are generally three major components in seismic damage assessment: Seismic hazard, vulnerability of buildings in the study area, and computation of the expected damages or losses. Details about each component are presented as follows:

The first step in any earthquake loss estimation study is to determine seismic hazard level. To predict the seismic hazard in any region, two alternative seismic hazard assessment methodologies are available: Deterministic Seismic Hazard Assessment (DSHA) and Probabilistic Seismic Hazard Assessment (PSHA). DSHA is commonly applied for scenario assessments with given magnitude levels and source-to-site distances. On the other hand, PSHA approach considers all possible earthquakes that can take place in the area of interest as a contribution of all seismic source zones.

The second step involves collection of vulnerability information corresponding to the local building stock of the respective area. For this purpose, data including geographical location, purpose of use, structural properties such as number of stories, material, level of compliance with any seismic design code, and lateral force resisting system is gathered.

Finally, structural losses are estimated based on various ground motion-damage relationships. For this purpose, all building stock in the study area is classified into groups with identical structural characteristics where it is believed that the buildings of each group have similar seismic performance under earthquake excitation. Then, seismic damages of all building prototypes are assessed through ground motion-damage relationships.

Earthquake loss assessment is generally based on traditional (empirical) or analytical (theoretical) approach (Calvi *et al.*, 2006). Traditional approaches (Sandi, 1982) are mostly intensity based and use microseismic intensities including MMI (Modified Mercalli Intensity scale), MSK (Medvedev–Sponheuer–Karnik), EMS–98 (European

Microseismic Scale), and PSI (Parameterless Scale of Seismic Intensity); whereas analytical approaches are based on engineering parameters and employ physical ground motion parameters such as PGA, Peak Ground Velocity (PGV), spectral acceleration, spectral displacement (e.g.: Barbat *et al.*, 1996; Coburn and Spence, 2002). Traditional approaches are based on damage observations from previous earthquakes, while analytical approaches are based on theoretical prediction of structural damages under various levels of ground shaking, using nonlinear structural analyses. The other approach is named as Hybrid method in which damage distribution of any region is assessed through the results of both empirical and theoretical methods (e.g.: Dolce *et al.*, 1994; Kappos *et al.*, 1998; Kappos *et al.*, 2002). Each of the above mentioned methods rely on expert opinion to some extent. Therefore, they include inherent uncertainty arising from a certain number of assumptions.

Results from any of these damage assessment approaches may be represented in the form of either Damage Probability Matrices (DPMs) or fragility curves relying on the type of methodology and availability of the input data. DPMs, originally developed by Whitman *et al.* (1973) denote the discrete probabilities of a certain building class to suffer a certain level of damage at a specified ground motion intensity. On the other hand, fragility curves of a certain building class are continuous functions representing the probability of being in or exceeding a certain damage state at a specified ground motion intensity. There are empirical relationships to convert a DPM into a set of fragility curves which are either dependent on microseismic intensities or physical ground motion parameters (e.g.: Reitherman, 1986).

Loss estimation frameworks are deterministic or probabilistic depending on the definition of seismic hazard. In the deterministic framework, damage or loss outputs are in the form of damage or loss maps representing spatial distribution of damage that are conditional on a given earthquake. In contrast, probabilistic framework involves probabilistic hazard maps or curves for a suit of seismic sources and rupture scenarios where the loss outputs will be in the form of loss maps that are conditional on the hazard with a given return period. Literature surveys show that majority of the loss

studies are deterministic rather than probabilistic. The reason behind is that the results of deterministic-based approaches are presented in a more tangible way such that the variation of the expected losses for a certain event to different ground motion input parameters can be visualized. Another reason is to assess a crucial potential scenario event and the consequences on the nearby critical structures. Compared to deterministic-based earthquake loss estimation approaches, probabilistic-based ones are in general more theoretical such that it may not be possible to directly relate the (input) hazard to (output) loss. In general, probabilistic-based studies are key input to the earthquake insurance industry while deterministic-based approaches can be valuable for emergency planning, post-earthquake rapid loss assessment, or handling the aftermath of an earthquake.

For deterministic seismic loss estimation studies, ground motion levels are employed in the form of hazard input. It is worth to note that ground motion content at any location is influenced by various parameters including earthquake source parameters such as magnitude and fault system, path parameters such as distance and Earth properties (damping and geometrical spreading), and finally effects of local site conditions. Such a detailed consideration is not provided in the classical DSHA (via ground motion prediction equations). Yet, it is possible to include these physical constraints into hazard modeling through either real datasets or ground motion simulations. Real ground motion datasets are inherently incomplete even at the most seismically-active regions due to the natural scarcity of large events. Thus, ground motion simulations provide alternative time histories accounting for the specific features of the fault and the kinematics of the rupture process.

The second critical input is certainly the building dataset used in the loss assessment. Considering potential deficiencies and variations in regional construction practice, local building data is of particular interest to physically model the building damage and consequent losses. In short, it is critical to investigate the seismic loss of any region of interest by considering the regional ground motions and local building stock.

In this study, deterministic-based earthquake loss assessment using simulated ground motions is applied on local building datasets for a case study. Deterministic approach is particularly selected since the aim is to investigate the efficiency of synthetic ground motions in loss calculations generated from a certain well-known fault in eastern of Turkey. To generate the input ground motions, the stochastic finite-fault ground motion simulation approach as described in Chapter 2 is employed due to its versatile implementation. In addition, stochastic method is effective in simulating the frequency content of interest to residential buildings.

The main objective of this chapter is to apply the stochastic finite-fault ground motion simulation technique for generation of synthetic time histories that match the seismotectonic setting of a specified region, and to investigate the effect of using both simulated time histories and locally derived building dataset on the seismic loss of that region. Figure 4.1 illustrates the main steps included in the proposed approach. The scope of this Chapter is as follows: In Section 4.2, general information related to the study area is presented. Next, the generated synthetic ground motion records for the region of interest are presented and discussed in Section 4.3. In Section 4.4, information on the local buildings is gathered. Section 4.5 involves the procedures used for generation of fragility curves. This section includes definition of the methodology, limit state, and ground motion set applied for generation of fragility curves. In Section 4.6, the methodology used for damage estimation is presented followed by a verification exercise where the estimated damage levels for the 1992 Erzincan earthquake (Mw=6.6) is compared with the observed ones. Then, seismic damage assessment is conducted for scenario events with six levels of magnitude as Mw=5.0, 5.5, 6.0, 6.5, 7.0, 7.5, in order to cover the possible scenarios in the study area. Finally, in Sections 4.7 and 4.8, the main findings and uncertainties involved in this research are discussed, respectively.

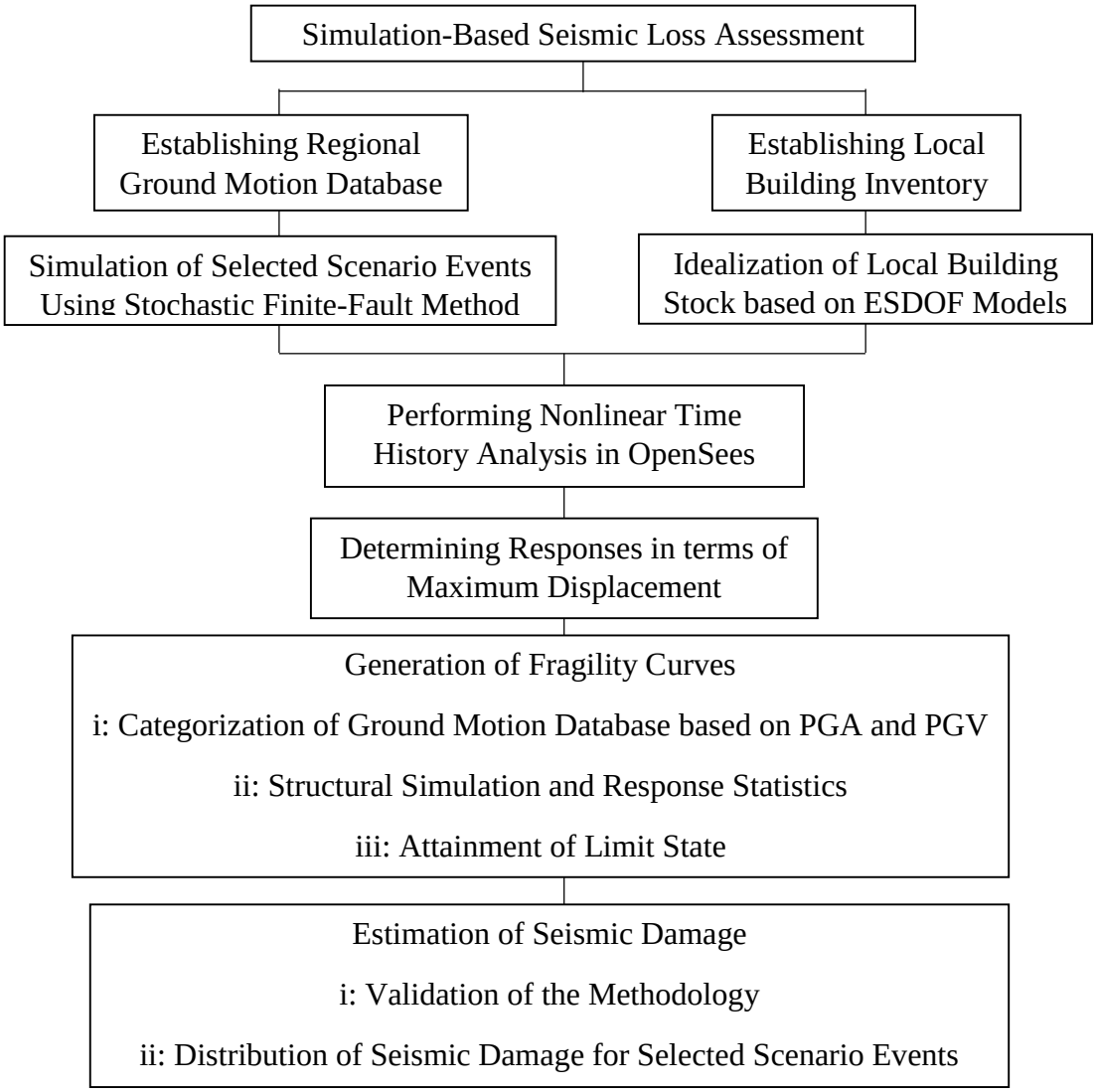

Figure 4.1 Main steps for simulation-based seismic loss assessment

4.2 Study Region

North Anatolian Fault Zone (NAFZ) is an active right-lateral strike-slip fault zone that lies in Northern Turkey and is one of the most active fault zones in the world. In the last century, NAFZ led to the most destructive events in Turkey such as the 1939 Erzincan (Ms~8.0) event in the eastern part (Figure 4.2.a) as well as the 1999 Kocaeli (Mw=7.4) and 1999 Düzce (Mw=7.2) earthquakes in the western part close to Istanbul. Since, majority of the industrial facilities as well as population of Turkey are located in the western sections of the country, there are many studies focusing on these parts. However, in spite of the critical seismic activity, Erzincan area in Eastern Turkey is not as much studied as the western sections of NAFZ. Erzincan is one of the most hazardous cities in Eastern Turkey located on a deep alluvial basin within a tectonically complicated area, at the conjunction of three strike-slip faults: the right lateral North Anatolian Fault, the left lateral North East Anatolian Fault (NEAF), and the left lateral Ovacik fault (Figure 4.2.b). Historical records demonstrate around twenty large earthquakes in the proximity of Erzincan during the past 1000 years (Barka, 1993). In addition to the 1939 event, Erzincan suffered from another destructive earthquake in 1992 (Mw=6.6) that led to significant structural damage as well as mortalities. Figure 4.3 shows the spatial distribution of all events with Mw>=5.0 that occurred within the region of interest. Finally, the city center has a relatively sparse ground motion network despite the seismic activity. Therefore, Erzincan is an ideal location as a case study for the seismic damage assessment method proposed herein because the city center constitutes a region with high seismicity and few real records along with vulnerable building stock.

(a)

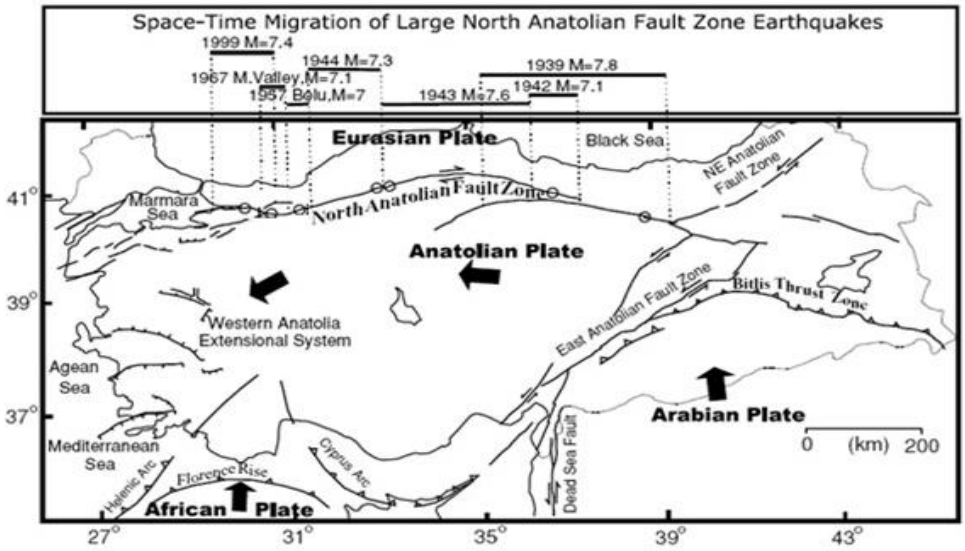

(b)

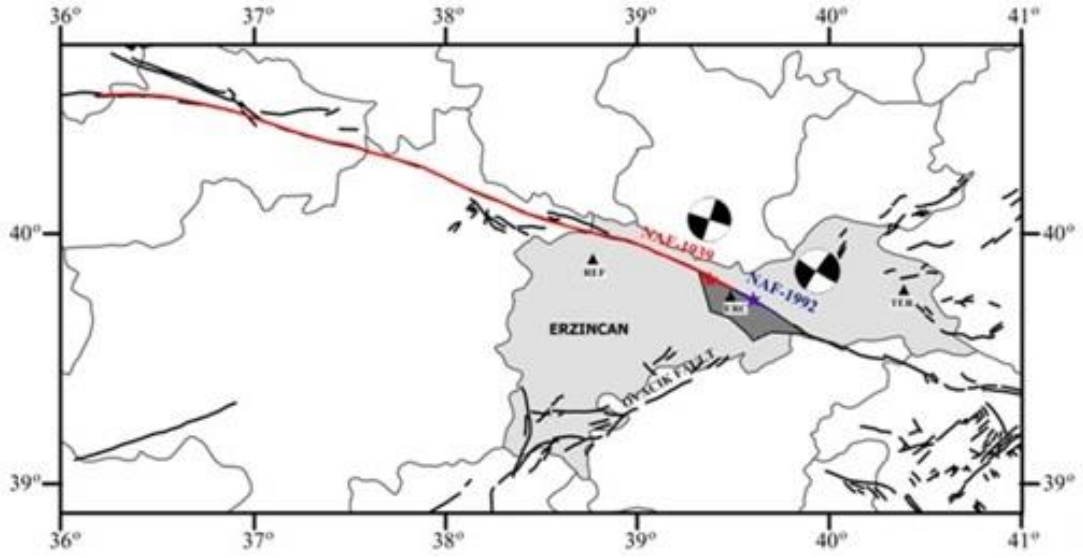

Figure 4.2 (a) Major tectonic structures around the Anatolian plate and large earthquakes on the North Anatolian Fault Zone in the last century (b) Seismotectonics in the Erzincan region with the fault systems and the epicenters of the 1939 and 1992 events (Figures 4.2.a and 4.2.b are adapted from Akyüz *et. al.*, 2002 and Askan *et al*., 2013, respectively)

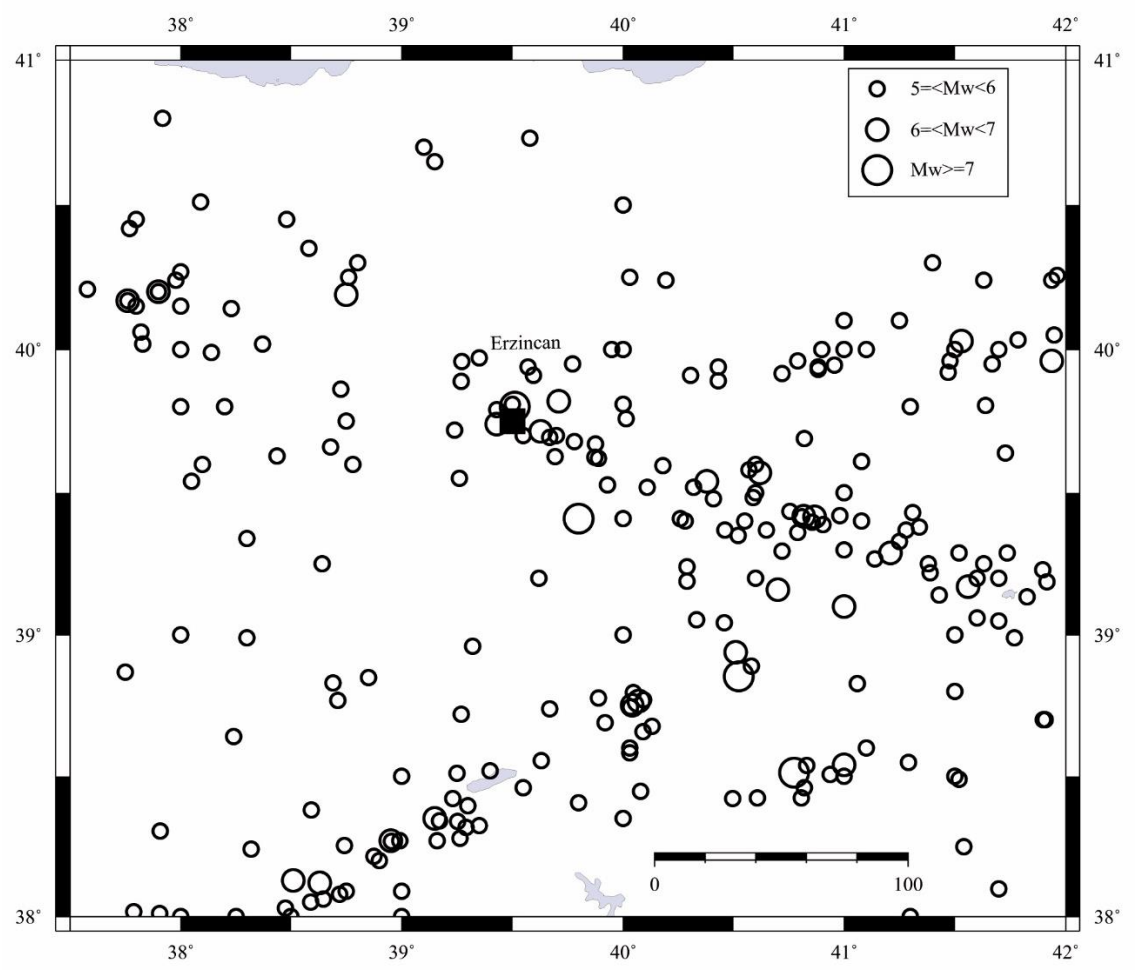

Figure 4.3 Spatial distribution of all earthquakes with Mw>=5.0 around Erzincan city center

Within a regional seismic loss assessment study, a detailed and realistic building inventory database is necessary. In this study, initially some general information including distribution of all building stock in the region of interest with respect to different districts, number of stories, structural type, lateral force resisting system, and primary use are collected from the General Statistic Agency in Turkey (TÜİK). Then, a walk-down survey is also performed as discussed in Section 4.4. The studied locations as well as district names in Erzincan are presented in Figure 4.4.

Figure 4.5 summarizes the percent distribution of buildings in different districts of the city according to the TÜİK database. It is observed that almost 22% of the total number of buildings is located in İnönü and İzzetpaşa districts. Figures 4.6, 4.7, and 4.8 show the percent distribution of all buildings according to the number of stories, structural type, and primary use, respectively. The values in Figure 4.6 demonstrate that more than half of the buildings (53%) are listed as single-story buildings in Erzincan province. It is also observed that approximately half of the remaining buildings are two-story buildings (24%). The rest of the stock consists of three-story or four-story buildings. Few buildings in the city center have higher number of stories than four. Current Turkish seismic design code (2007) has some limitations for construction of buildings in seismic zone 1 especially for masonry buildings. Erzincan is located in seismic zone 1; therefore, the maximum number of stories allowed for masonry buildings in residential areas is two. Available data for masonry structures located in Erzincan shows that this limitation is not neglected excessively.

Figure 4.7 shows the percent distribution of the structural type in Erzincan. It is observed that more than half of the constructed buildings in Erzincan (57%) are masonry buildings. Nowadays, the design and construction of masonry buildings is not common; therefore, it is clear that most of these buildings are old structures distributed in older residential districts such as İzzetpaşa, Halitpaşa, and Hocabey. In contrast, the condition is slightly different for RC building type. A significant number of RC buildings were damaged or destroyed during the 1992 Erzincan earthquake. Therefore, in some districts such as Mimar Sinan, Ergenekon, Yavuz Selim, and

Arslanlı these structures are replaced with newly constructed structures designed according to code. However, this does not guarantee the seismic safety of all RC buildings against future earthquakes and there still exist deficient RC buildings. The percent distribution of primary use of existing buildings is presented in Figure 4.8. According to the values presented in Figure 4.8, majority of the buildings in Erzincan (79%) are residential structures. Within the scope of this study, seismic damage estimation of only residential buildings is assessed. Not included in the study are the remaining buildings including commercial, industrial, architectural, official, religious, and cultural buildings as well as health centers which make up less than 21% of the total buildings in Erzincan city center.

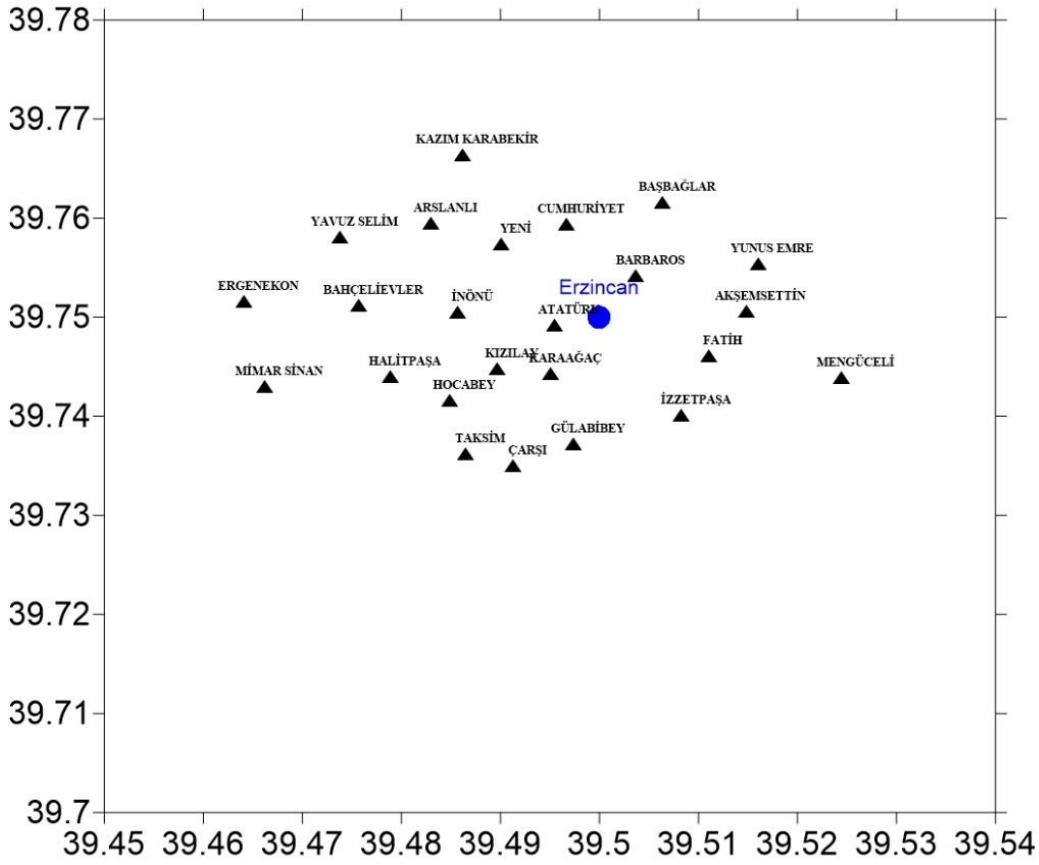

Figure 4.4 Spatial distribution of the districts in the Erzincan Province
(The blue circle indicates the Erzincan city center)

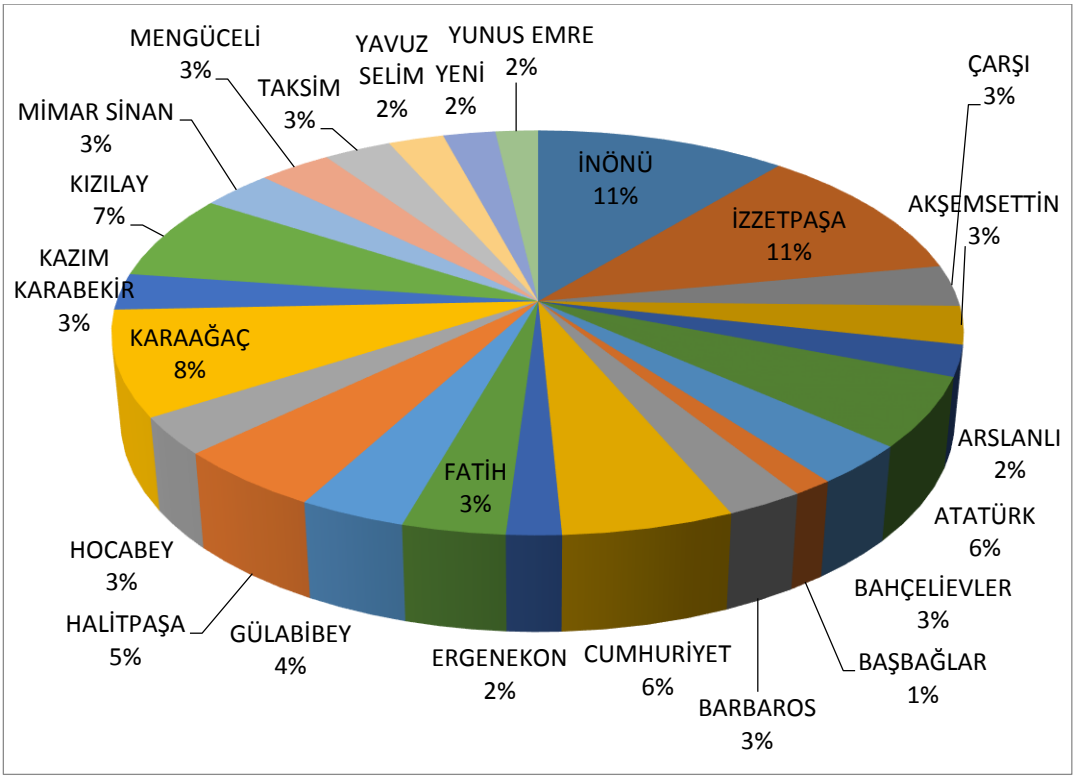

Figure 4.5 Percent distribution of all buildings in different districts of Erzincan

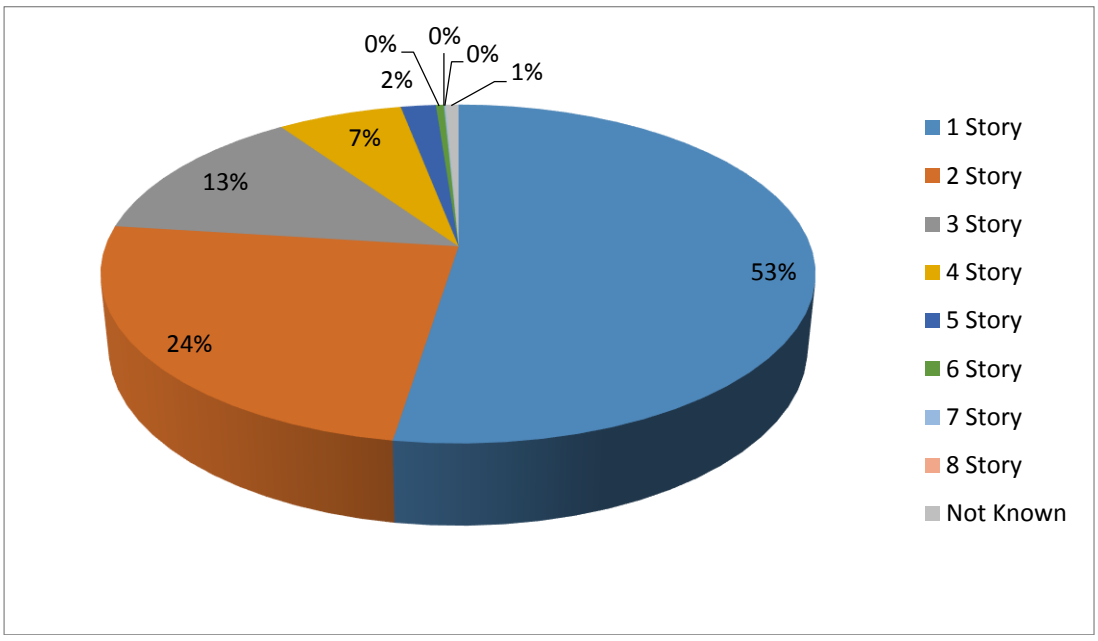

Figure 4.6 Percent distribution of the number of stories for all buildings in Erzincan

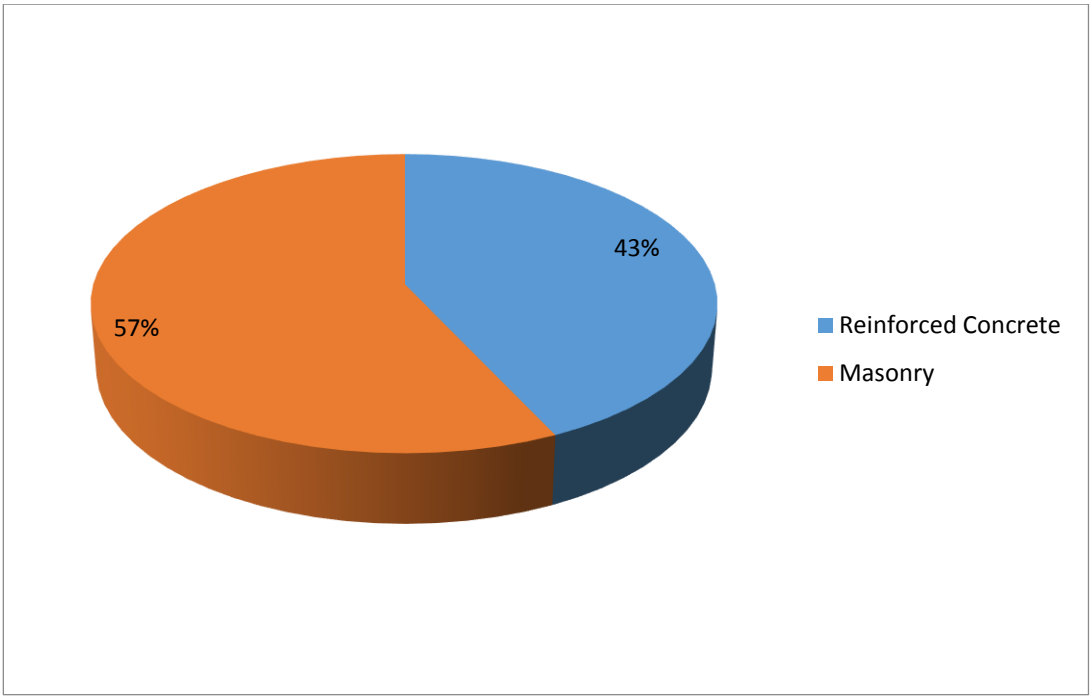

Figure 4.7 Percent distribution of the major structural type of all buildings in Erzincan

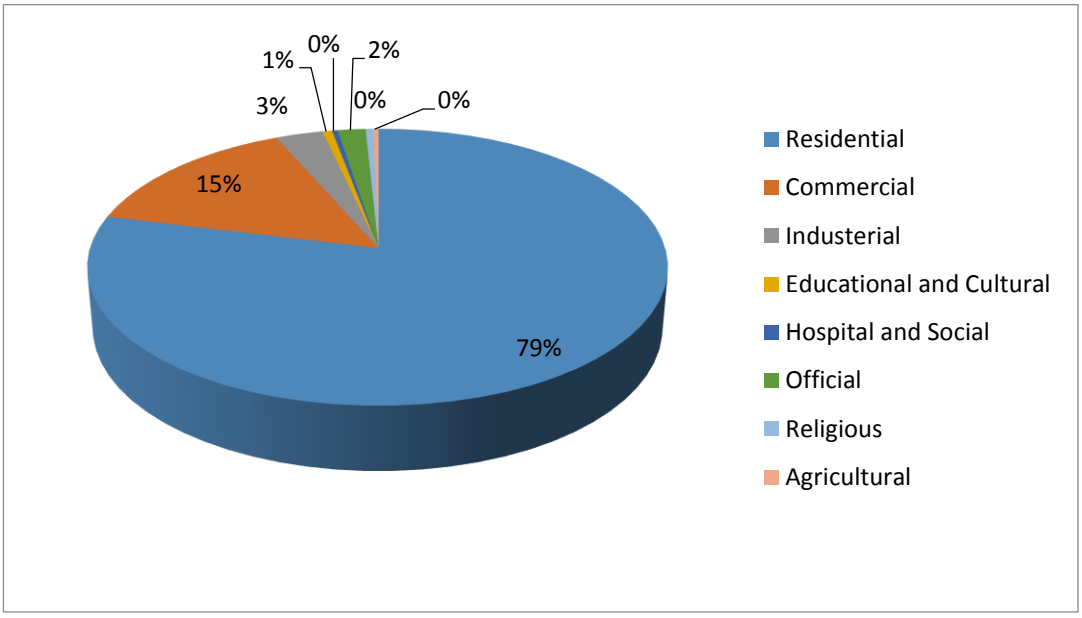

Figure 4.8 Percent distribution of primary use for all buildings in Erzincan

4.3 Simulated Ground Motion Database

In this section, ground motion simulations are performed for scenario earthquakes of size Mw=5.0, 5.5, 6.0, 6.5, 7.0, and 7.5 as well as the 1992 event using stochastic finite-fault methodology as implemented in the computer program EXSIM (Motazedian and Atkinson, 2005). The details of this methodology were introduced in Section 2.3 and therefore will not be repeated herein. It should be noted that all of these scenario events are generated on the same fault where the 1992 Erzincan event (Mw=6.6) occurred (Figure 2.b). During simulation process, the epicenter of all scenario earthquakes is kept the same as the epicenter of the 1992 earthquake. The reason behind this assumption is that the epicenter of the 1992 earthquake is located at a critical point in terms of its close distance to the city center.

The source, path, and site parameters for the simulations are adapted from a previous study by Askan *et al.* (2013) and Askan *et al.* (2015b). In that study, the validity of these parameters was obtained by comparing the generated ground motion time histories with those observed during the 1992 Erzincan earthquake. Therefore, the use of these parameters is believed to provide us accurate results in terms of special distribution of PGA and PGV values for the other scenarios as long as the region of interest and geological features of the fault plane does not change. Since there is no information related to the slip distribution of the scenario events, a random slip distribution model, which is available inside of the EXSIM software, is assumed for all scenarios. Table 4.1 displays the input parameters for the simulations. Among the all source parameters, stress drop and fault dimensions are two parameters that take different values for each Mw.

Table 4.1 Simulation parameters used in the simulation of scenario earthquakes

Parameter	**Value**
Hypocenter Location	39.716ºN, 39.629ºE
Hypocenter Depth	9 km
Depth to the Top of the Fault Plane	2 km
Fault Orientation	Strike: 125º, Dip: 90º
Fault Dimensions	Wells and Coppersmith (1994)
Crustal Shear Wave Velocity	3700 m/s
Rupture Velocity	3000 m/s
Crustal Density	2800 kg/m^3
Stress Drop	Mohammadioun and Serva (2001)
Quality Factor	$Q = 122 f^{0.68}$
Geometrical Spreading	$R^{-1.1}, \quad R \le 25\ km$ $R^{-0.5}, \quad R > 25\ km$
Duration Model	$T = T_0 + 0.05R$
Windowing Function	Saragoni-Hart
Kappa Factor	Regional kappa model (κ_0=0.066)
Site Amplification Factors	Local model at each station (Askan *et al.*, 2015b)

In the present study, the region of interest is defined as a rectangular box bounded by 39.45°-39.54° Eastern longitudes, 39.70°-39.78° Northern latitudes. In order to simulate full time series of ground motions, a total of 123 grid points are selected inside of this region. Figure 4.9 shows the distribution of these 123 nodes in the study area. Among 123 nodes, ninety of them represented by red circle symbols, are selected with a distance of approximately 1 km from each other; twenty-four of them shown by black triangular symbols, correspond to the coordinates of all districts in the Erzincan region; and finally nine of them represented with green rectangular symbols are the stations detailed shear wave velocity soil profiles are available. Since the local soil conditions affect the ground motion amplitudes on the soil surface, local soil profiles are significant in simulations. The existing shear wave velocity profiles at 9

nodes were obtained by a microtremor array method as explained in detail in Askan *et al.* (2015b). Table 4.2 lists the Vs30 (the 30m-average shear wave velocity in units of m/s) values obtained for these 9 nodes within the city center. However, there is no information related to soil conditions at the other nodes. Therefore, the Vs30 of the closest station is assigned to each grid point. Although these assumptions introduce uncertainty to the simulation process, considering the short distances between the nodes, the final error is believed to be negligible.

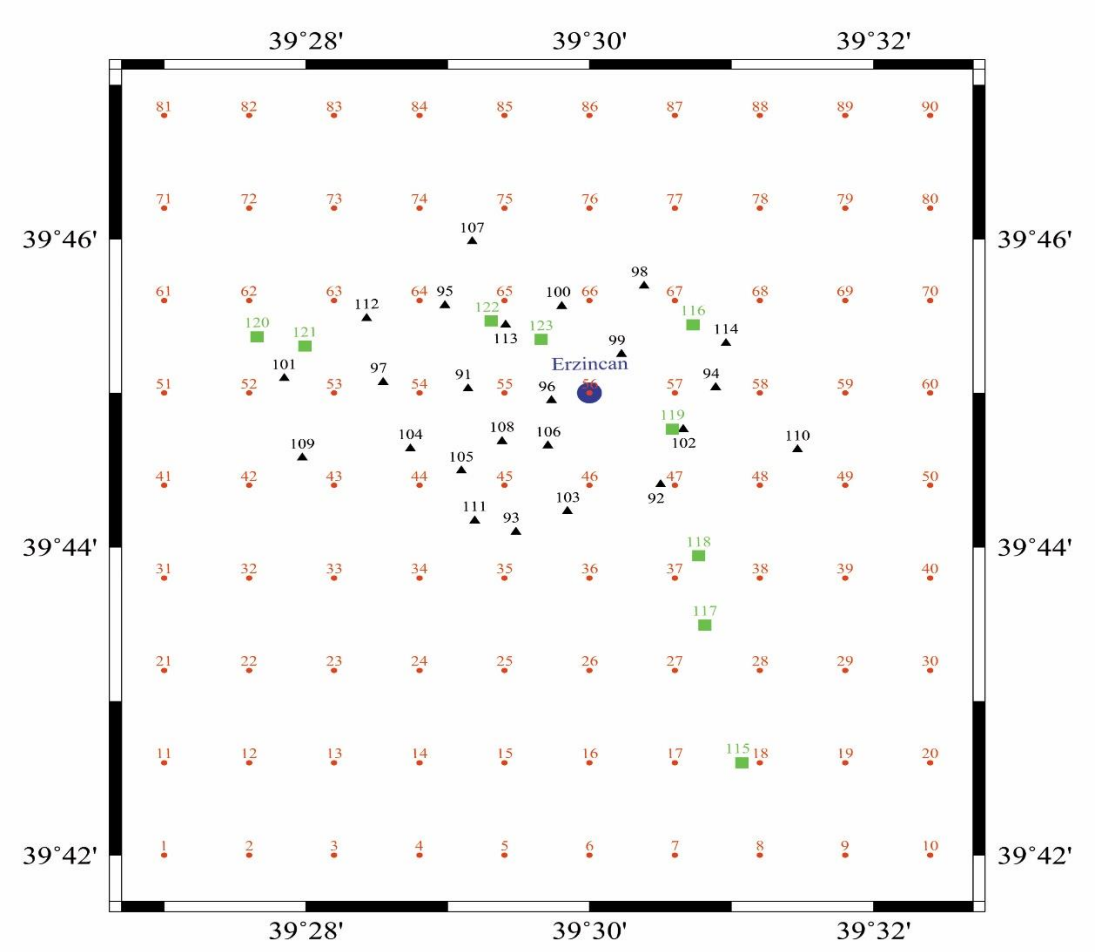

Figure 4.9 Distribution of the selected nodes in the study area

Table 4.2 Vs30 values available at the 9 nodes

Node Number	**115**	**116**	**117**	**118**	**119**	**120**	**121**	**122**	**123**
Site Number	1	2	3	4	5	6	7	8	9
Vs30 (m / s)	256	569	304	287	267	336	348	427	387

Figures 4.10-4.16 illustrate the spatial distribution of PGA and PGV within the city center for the simulation of 1992 Erzincan earthquake (Mw=6.6) as well as scenario events. It is noted that all simulated records are baseline corrected and 4^{th}-order bandpass filtered between 0.25-25 Hz. When the results of scenario events are studied, it is observed that for the generated scenario events with Mw=5.0, 5.5, 6.0, 6.5, 7.0, and 7.5, the maximum values of PGA is anticipated as 0.07g, 0.17g, 0.35g, 0.82g, 1.44g, and 3.05g, respectively. These higher ground motion amplitudes especially for the larger size of events can be explained by very close distances from the fault plane, the soft soil deposits within Erzincan basin, or the numerical errors in computational process due to zero distance effects. Although the Northern part of the study area has stiffer soil conditions, due to the close vicinity of those nodes from the fault plane, they are also subjected to higher amplitudes of ground motions. Similarly, the distribution of PGV values in the city center indicates that as the magnitude of the scenario event increases, the city experiences higher values of PGV. The scenario events with Mw=7.0 and 7.5 point to significant destruction potential in the city center.

The simulation results for the 1992 Erzincan earthquake demonstrate that the city center experiences maximum PGA and PGV values of around 1g and 85 cm/s, respectively. It is believed that these high ground motion levels are observed due to the critical location of the epicenter directly to the North of the city center, soft soil conditions, and overall the close distances of the districts from the fault plane. These values in addition to the poor building stock explain why the residential structures in the city center suffered from significant levels of damage during the moderate size 1992 earthquake. It must be noted that the 1992 Erzincan earthquake was recorded

only at three strong motion stations: ERC, REF, and TER. Among them, the coordinates of station ERC corresponds to the grid point number 54 in this thesis. The observed PGA at this station was recorded as 0.47g while the simulated PGA at this point is 0.44g. In terms of PGV again the estimated and observed values are 68.32 cm/s and 55.73 cm/s, respectively. This quick observation verifies the accuracy of the selected input parameters for simulation process.

(a)

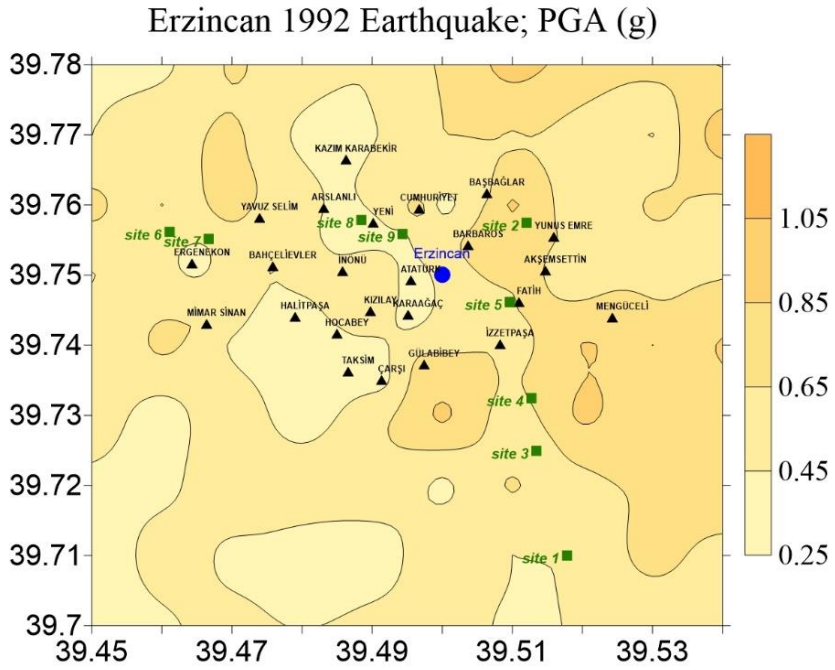

(b)

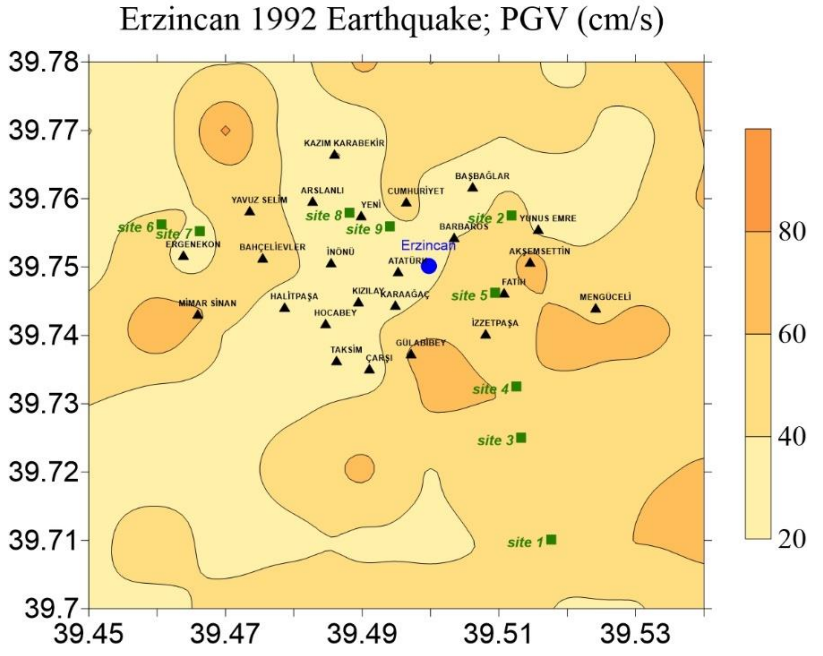

Figure 4.10 Spatial distribution of the simulated (a) PGA (b) PGV values of the 1992 Erzincan earthquake in Erzincan region

(a)

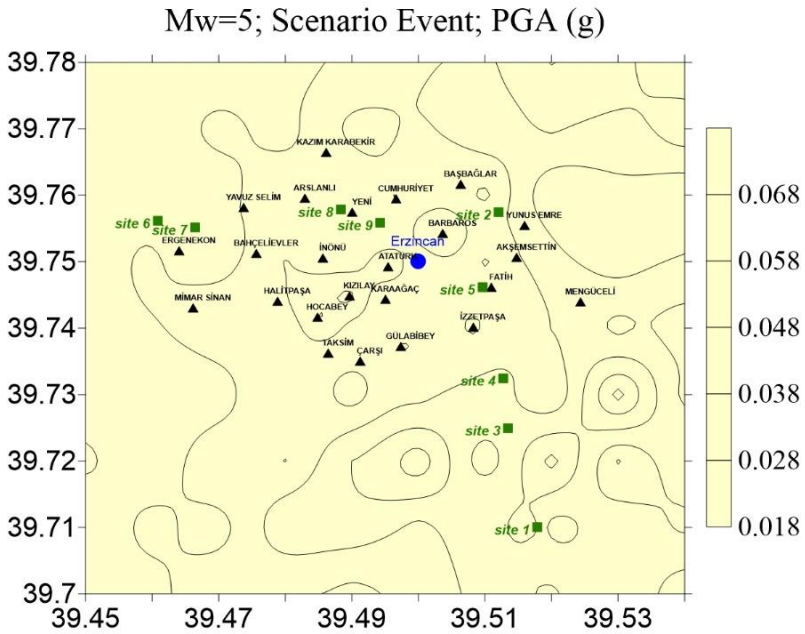

(b)

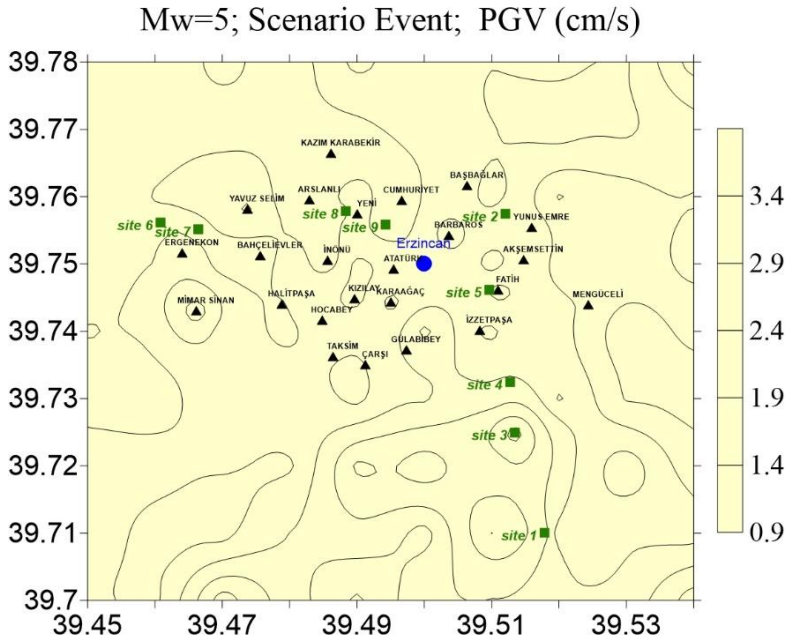

Figure 4.11 Spatial distribution of the simulated (a) PGA (b) PGV values of the scenario earthquake with Mw=5.0 in Erzincan region

(a)

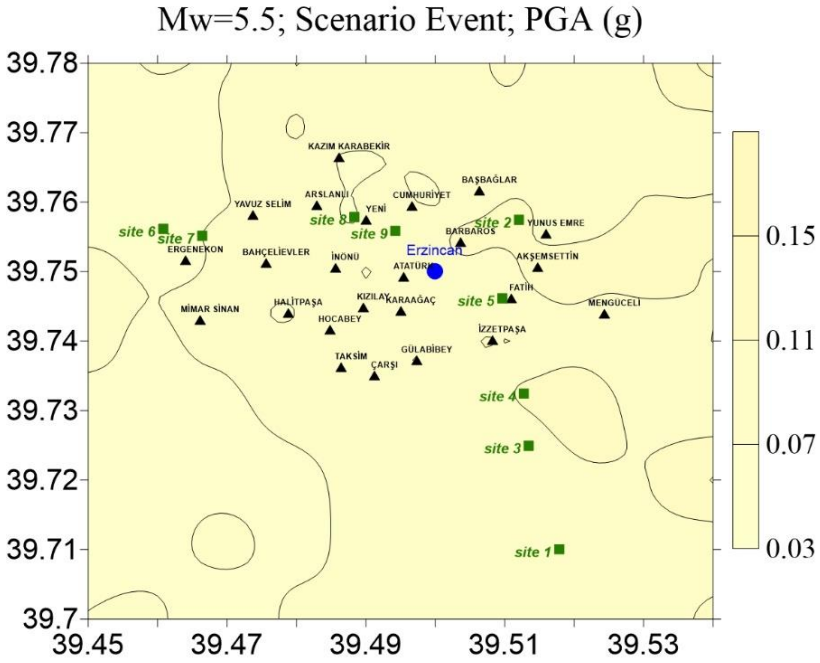

(b)

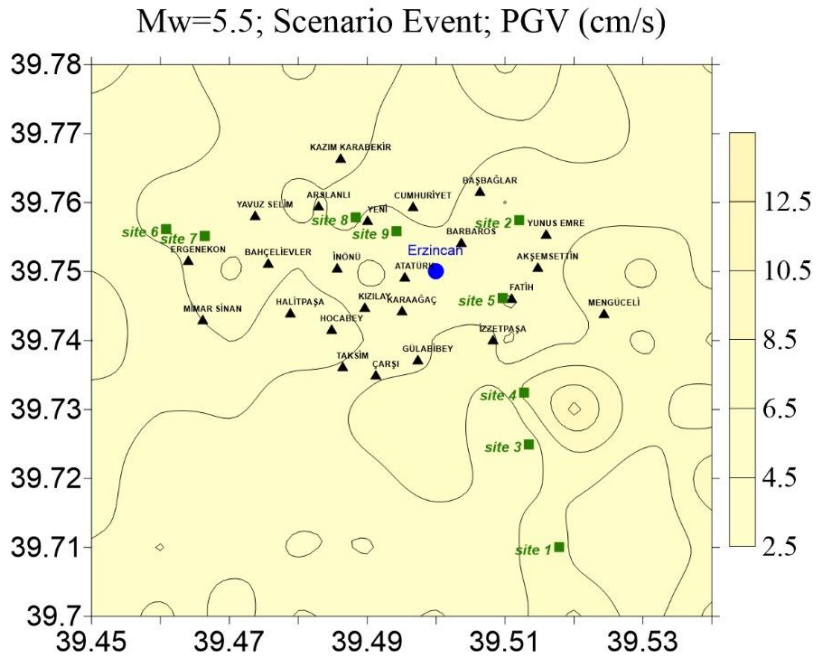

Figure 4.12 Spatial distribution of the simulated (a) PGA (b) PGV values of the scenario earthquake with Mw=5.5 in Erzincan region

(a)

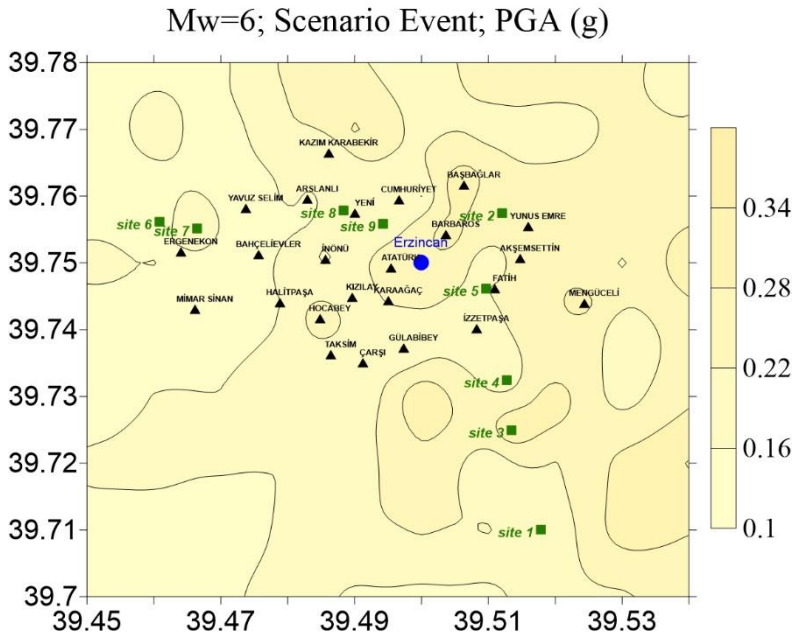

(b)

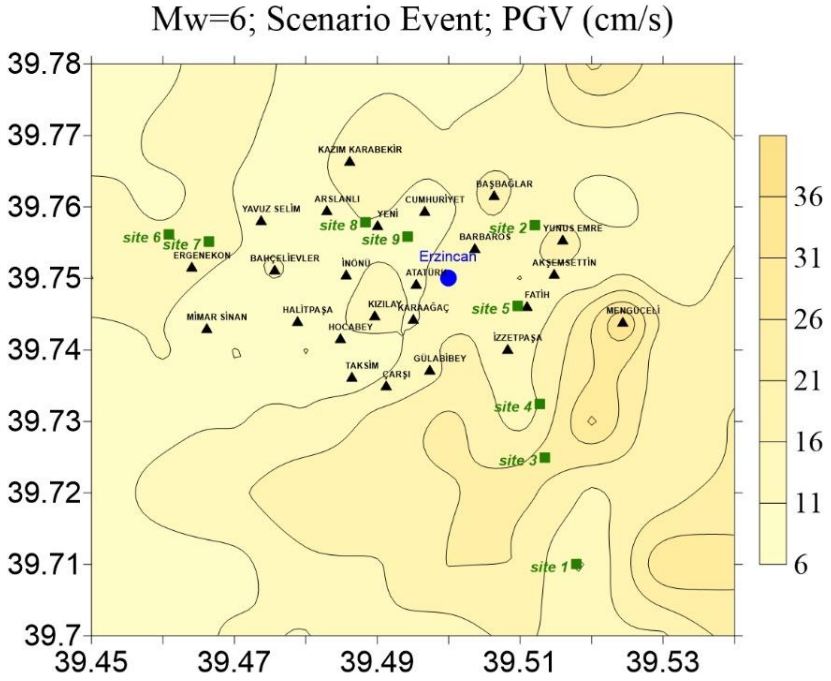

Figure 4.13 Spatial distribution of the simulated (a) PGA (b) PGV values of the scenario earthquake with Mw=6.0 in Erzincan region

(a)

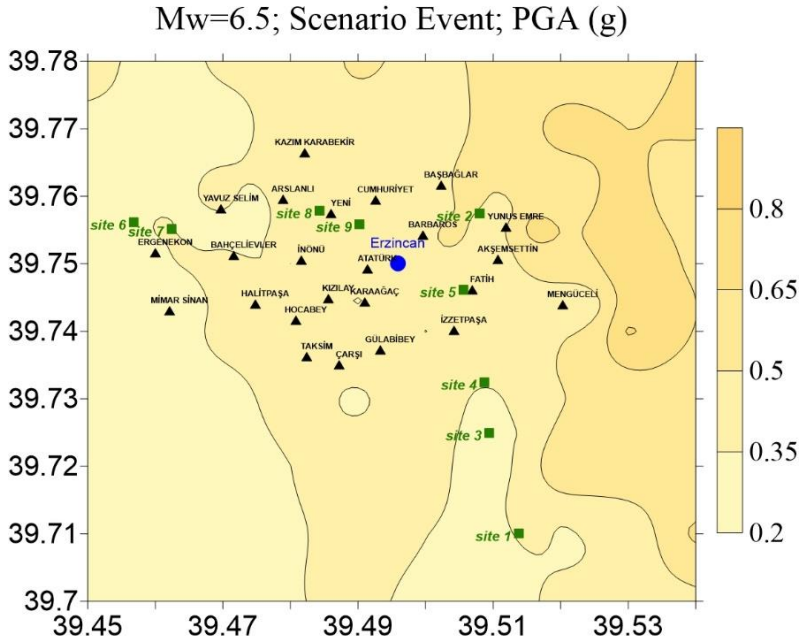

(b)

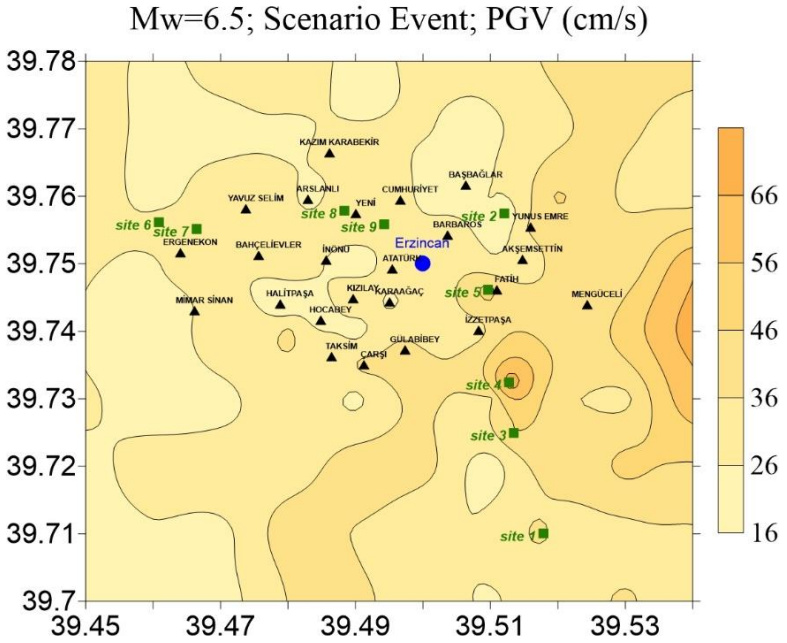

Figure 4.14 Spatial distribution of the simulated (a) PGA (b) PGV values of the scenario earthquake with Mw=6.5 in Erzincan region

(a)

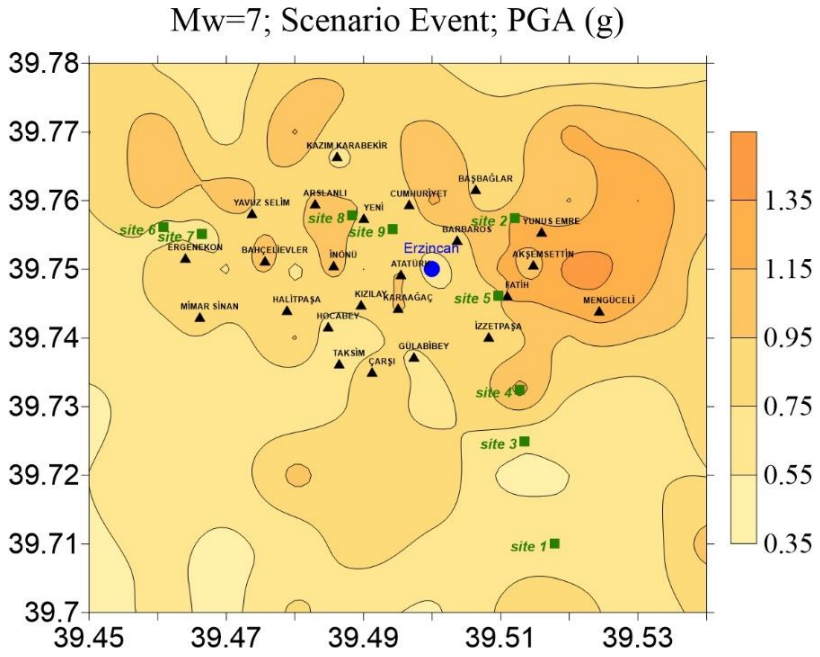

(b)

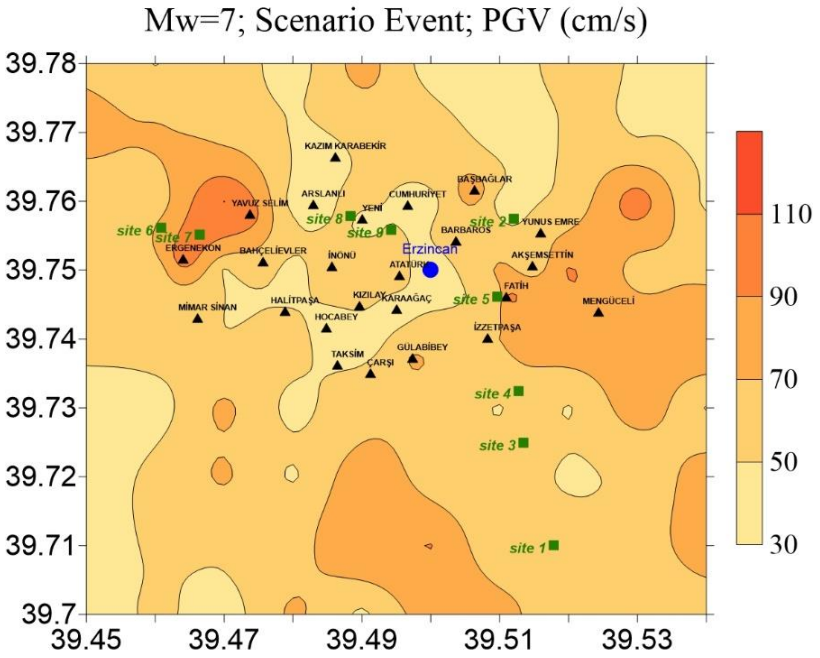

Figure 4.15 Spatial distribution of the simulated (a) PGA (b) PGV values of the scenario earthquake with Mw=7.0 in Erzincan region

(a)

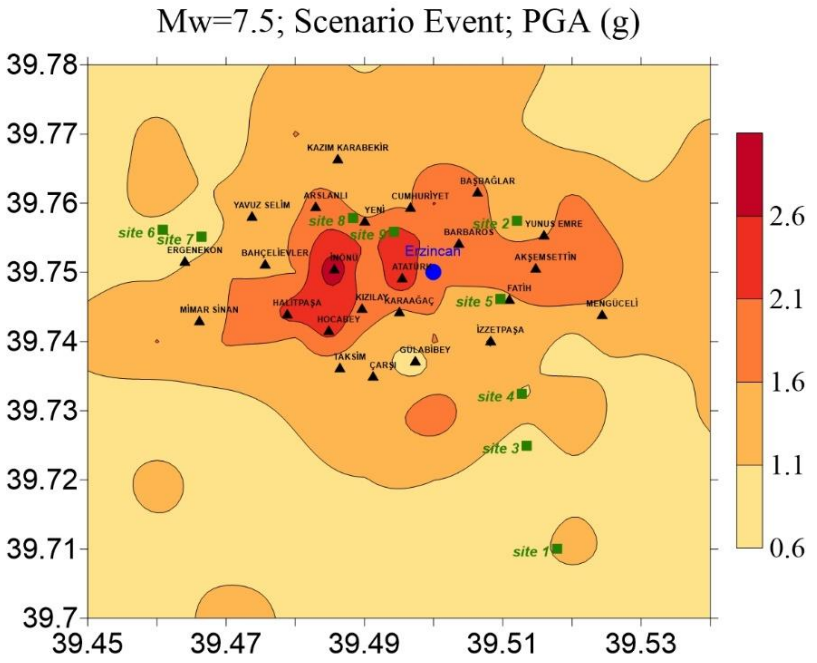

(b)

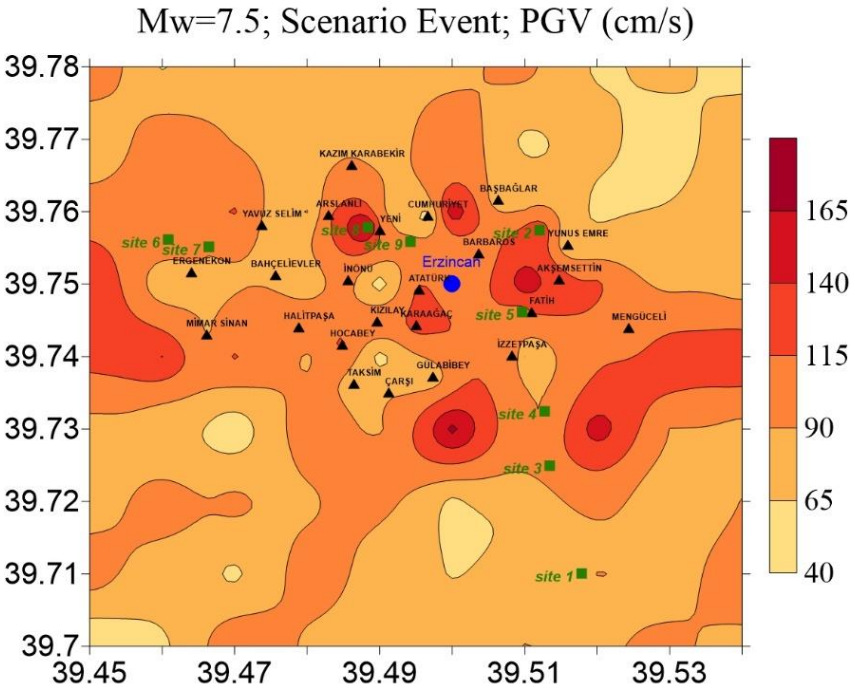

Figure 4.16 Spatial distribution of the simulated (a) PGA (b) PGV values of the scenario earthquake with Mw=7.5 in Erzincan region

4.4 Identification and Idealization of the Regional Building Stock

To perform regional seismic loss assessment, it is required to develop broad building inventory databases. These databases involve the name, address, year of construction, primary use, number of stories, structural material, lateral force resisting system, and soil class at the building site. There are a number of resources that provide this sort of information. However, for areas with insufficient data, walk-down surveys can be conducted. In this study, some of the building data are gathered from the TÜİK and the rest are collected by a side-walk survey in the respective area.

This section deals with the identification and idealization of the building stock in the study region. In Subsection 4.4.1, the classification and the distribution of the building stock are determined based on the available building census data from TÜİK and the observed data obtained during the field survey. In Subsection 4.4.2, the structural characteristics of the existing construction types in the region are idealized by equivalent single degree of freedom models. A well-known hysteresis model is used in order to obtain the response statistics of the ESDOF models through nonlinear time-history analyses. In the Section 4.5, this information will be used to derive fragility curve sets of the ESDOF models corresponding to different building sub-classes.

4.4.1 Identification of the Building Stock

The building census data obtained from TÜİK provides general information regarding the building inventory in the region in terms of the major construction types. However, this is not an up-to-date information and too broad in order to classify the buildings according to their local characteristics for estimating the regional seismic damage distribution. Hence, a site-survey was conducted in Erzincan city center by a technical team in order to update the available building data and to identify the local construction types with their specific characteristics in the field. Based on the results of this site-survey in Erzincan city center, the residential building stock is classified into 21 groups including 12 RC and 9 masonry sub-classes. This means that the buildings within each sub-class are believed to display, on average, similar damage behavior under same

ground shaking levels. Among these sub-classes, RC buildings are considered as either frame type, shear wall type (actually tunnel form), or dual type (frame with shear walls). Of the highly predominant reinforced-concrete and masonry buildings, the most common prototypes are low-rise and mid-rise concrete buildings as well as one-story, two-story, and three-story masonry buildings. Structural parameters used in the classification of buildings are structural type, number of stories, and level of compliance with the seismic design and construction principles. In classification of all sub-classes, the first two letters in the abbreviated names account for the type of structural system, where 'RF' stands for RC frame buildings, 'RW' for RC tunnel-form, 'RH' for RC dual-type, and 'MU' for masonry sub-classes. The number in the next digit indicates the number of stories, where for masonry classes '1', '2', or '3' represents 1 story, 2 story, or 3 story, and for all three RC groups, '1' or '2' indicates whether the building is low-rise (number of stories is between 1 and 3) or mid-rise (number of stories is between 4 and 8), respectively. The letter in the last digit 'A', 'B', or 'C' denotes the high, moderate, and low level of compliance with seismic design codes and construction principles, respectively. For instance, RF2A represents earthquake-resistant mid-rise RC frame buildings whereas MU2C represents deficient 2 story masonry buildings.

4.4.2 Idealization based on ESDOF models

In regional damage estimation, for the sake of computational efficiency, it is generally preferred to use simplified and idealized structural models to simulate the seismic response statistics of large building populations. Accordingly, in this study, each building sub-class is represented through an idealized ESDOF model by specifying three basic structural parameters; period (T), strength ratio (η), and ductility factor (μ). This simplified approach have been employed in earthquake engineering since the early work of Biggs (1964), followed by many remarkable studies (e.g.: Saiidi and Sozen, 1981; Fajfar and Fischinger, 1988; Qi and Moehle, 1991; Aschheim and Black, 2000). The ESDOF approach was also employed in the well-known guidance documents such as ATC-40 (1996) and FEMA 273 (1997). There are two gross

assumptions while using ESDOF systems: First, the global response of a MDOF system is assumed to be represented by a single deformed shape, which is eventually the fundamental mode shape. Second, this deformed shape is assumed to remain constant during the entire response history. In this study, it is considered that the use of ESDOF models, and in turn, these two assumptions are justifiable since the study deals with a population of ordinary residential buildings instead of individual and specific buildings, in which there should be a trade-off between precision and computational effort. Furthermore, the field observations in Erzincan revealed that the surveyed residential buildings are generally regular in plan and elevation with nearly homogeneous distribution of floor mass and stiffness, which are in favor of the above assumptions for ESDOF systems.

Since nonlinear time history analyses are conducted to obtain the response statistics of ESDOF models, a robust hysteresis model is required to simulate the inherent cyclic characteristics of each building sub-class under earthquake excitations. There are many hysteresis models in the literature that take into account the possible deterioration modes such as reloading and unloading stiffness degrading, capping, cyclic strength degrading, and pinching (Takeda *et al.*, 1970; Roufaiel and Meyer, 1987; Park *et al.*, 1987; Otani, 1993; Stojadinovic and Thewalt, 1996; Sivaselvan and Reinhorn, 1999; Sucuoğlu and Erberik, 2004). Structures are generally subjected to significant strength and stiffness deterioration while they approach collapse. As a matter of fact, newer and well-constructed structures are expected to exhibit almost none or slight degradation. However, most existing buildings in Turkey exhibit many structural deficiencies which result in rapid degradation of stiffness and strength along with decreased energy dissipation capacity. Therefore, the most accurate hysteresis models are the ones which include strength and stiffness deterioration features that are critical for demand predictions during major earthquakes. Few of the hysteresis models integrate various modes of cyclic deterioration in strength and stiffness such as basic strength, post-capping strength, uploading stiffness, and reloading stiffness deterioration that may be observed in the real inelastic behavior. In this study, to assess the effect of deterioration characteristics of structural systems on the final fragility

curves, among different hysteresis models, the one proposed by Ibarra *et al.* (2005), named as "Modified Ibarra –Medina-Krawinker Deterioration Model", is applied. Ibarra *et al.* (2005) verified that their hysteresis peak-oriented deterioration model is able to predict the inelastic dynamic response of reinforced-concrete structures during collapse with an acceptable degree of accuracy. The proposed deterioration model has then been used in various studies and for different structural types (e.g.: Ibarra and Krawinkler, 2005; Lignos and Krawinkler, 2010; Lignos and Krawinkler, 2012). The results of these studies seem to be promising.

Figure 4.17 illustrates the backbone curve of the modified Ibarra-Medina-Krawinkler deterioration model with peak-oriented hysteretic response. The model is based on the fundamental hysteretic rules suggested by Clough and Johnston (1966). However, the modified Ibarra-Medina-Krawinker deterioration model contains strength capping as well as residual strength compared to the one proposed by Clough and Johnston. The force-deformation curve of this model starts with monotonically increment of the deformation response. In the backbone curve, parameters K_e, F_y and α_s correspond to the elastic (initial) stiffness, the yield strength and the strain hardening ratio ($\alpha_s=K_s/K_e$), respectively. Here, K_s describes the pre-capping stiffness. In this model, deterioration of the backbone curve initiates by a softening branch with a cap deformation of δ_c that corresponds to the deformation of the peak strength of the force-deformation curve. The ratio of the cap deformation (δ_c) to the yield deformation (δ_y) is denoted as the ductility capacity ($\mu=\delta_c/\delta_y$). The parameter α_c is the ratio of the post-capping stiffness to the elastic stiffness which has generally a negative value ($\alpha_c=K_c/K_e$). Residual strength is represented by F_r which is considered as a fraction of the yield strength ($F_r=\lambda F_y$). Finally, the deformation corresponding to the residual strength is abbreviated as δ_r.

In addition to a post-capping negative stiffness branch of the backbone curve to capture cyclic deterioration, the modified Ibarra-Medina-Krawinkler peak-oriented hysteretic model includes cyclic modes of strength and stiffness deterioration based on the cumulative hysteresis energy dissipation. Four individual cyclic deterioration

modes are basic strength, post-capping strength, unloading stiffness, and reloading stiffness deterioration that may be activated beyond the elastic limit at least in one direction. Figure 4.18 illustrates four cyclic modes. Defining the hysteretic energy dissipation parameter γ, it is possible to simulate different levels of cyclic degradation for the ESDOF models. Further details about the cyclic deterioration modes can be found in Ibarra *et al.* (2005).

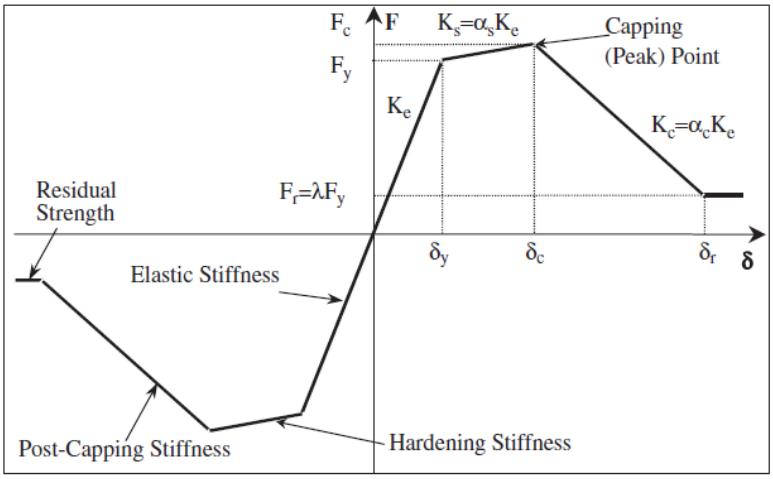

Figure 4.17 Backbone curve for hysteresis model (Adapted from Ibarra *et al.*, 2005)

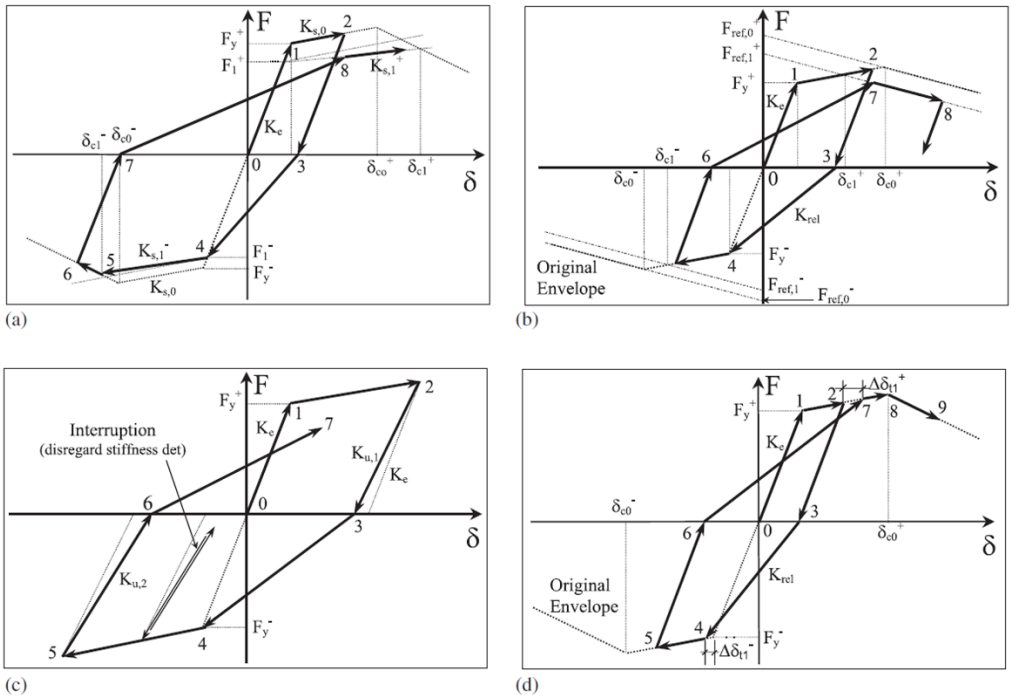

Figure 4.18 Individual deterioration modes of Ibarra peak-oriented model: (a) basic strength deterioration; (b) post-capping strength deterioration; (c) unloading stiffness deterioration; and (d) accelerated reloading stiffness deterioration (Adopted from Ibarra *et al.*, 2005)

In this study, the three major structural parameters (T, η and μ) are considered as random variables with mean and standard deviation values whereas the other hysteretic model parameters (α_s, α_c, λ and γ) are taken to be constant with a single value. Hence, all values of the considered ESDOF parameters for each sub-class are listed in Table 4.3. These parameter values are obtained from various sources: literature (for Turkish residential buildings), analytical computations (from idealized capacity curves of MDOF models), and also expert judgment. The further details for obtaining these ESDOF parameters are provided in Askan *et al.* (2015a) and Karimzadeh *et al.* 2015.

It is observed that the period of each sub-class is dependent on the type of structural system and number of stories. However, period is independent of the level of compliance of a structure with seismic design codes. Therefore, for sub-classes with similar number of stories and structural types but with different levels of compliance with seismic design codes (e.g.: RF1A, RF1B, RF1C), period is considered to be constant. In contrast, strength ratio and ductility factor are two parameters that are mostly influenced by structural type, number of stories, and the level of compliance with seismic design codes.

Table 4.3 Proposed ESDOF parameters for all building sub-classes

Frame ID	T (s)		η		μ		α_s (%)	α_c (%)	λ	γ
	Mean	St.D.	Mean	St.D.	Mean	St.D.				
RF1A	0.38	0.18	0.40	0.08	9.00	3.12	4	-20	0.20	800
RF1B			0.30	0.11	7.30	2.02	4	-25	0.20	400
RF1C			0.23	0.06	4.90	1.47	4	-30	0.20	200
RF2A	0.70	0.27	0.34	0.11	7.10	2.25	4	-20	0.20	800
RF2B			0.26	0.09	6.10	1.75	4	-25	0.20	400
RF2C			0.17	0.06	5.10	1.38	4	-30	0.20	200
RW1A	0.05	0.02	1.95	0.55	3.00	1.10	8	-20	0.20	1200
RW2A	0.15	0.05	1.30	0.36	2.70	0.90	8	-20	0.20	1200
RH1A	0.08	0.04	0.93	0.31	5.40	1.70	4	-20	0.20	1000
RH1B			0.77	0.25	4.50	1.40	4	-25	0.20	500
RH2A	0.43	0.18	0.59	0.17	4.90	1.40	4	-20	0.20	1000
RH2B			0.47	0.13	4.00	1.20	4	-25	0.20	500
MU1A	0.06	0.02	0.86	0.17	3.53	0.71	0	-20	0.20	600
MU1B			0.64	0.13	3.43	0.69	0	-25	0.20	300
MU1C			0.38	0.08	3.32	0.66	0	-30	0.20	150
MU2A	0.12	0.03	0.69	0.17	2.75	0.69	0	-20	0.20	600
MU2B			0.43	0.11	2.62	0.66	0	-25	0.20	300
MU2C			0.23	0.06	2.56	0.64	0	-30	0.20	150
MU3A	0.17	0.05	0.43	0.13	2.20	0.66	0	-20	0.20	600
MU3B			0.27	0.08	2.12	0.64	0	-25	0.20	300
MU3C			0.14	0.04	2.05	0.62	0	-30	0.20	150

4.5 Fragility Curve Generation Methodology

Fragility curve for a certain class of structural system is a continuous function describing the probability of exceeding a predefined damage level for specific levels of ground motion intensity. In this study, the classification system used for building stock includes 21 prototypes formed with respect to the construction practices in the region of interest. The main goal of this section is to generate fragility curves for all 21 building sub-classes with respect to both PGV and PGA as the main ground motion intensity parameter. To derive the fragility curve sets for each building sub-class, ESDOF models with the parameter values given in Table 4.3 are used in NLTHA. Section 4.5.1 describes the selected set of synthetic ground motion records that are employed in the NLTHA. The approach for performing the fragility analysis can be summarized as the following five steps:

- The first step is to conduct NLTHA for the ESDOF systems defined in the previous section by using a selected set of synthetic ground motion records. In this study, OpenSees platform is used for NLTHA as mentioned in Chapter 3. During the analysis, variability both in capacity (in terms of random variables T, η and μ) and demand (record-to-record variability) are considered.

- In the second step, response statistics of the ESDOF models are obtained from the results of NLTHA. For this purpose, ESDOF displacement is selected to be the seismic demand parameter for the considered building types. Next, for each building sub-class and seismic intensity level, the overall responses of ESDOF systems are collected.

- In the third step, limit states are defined for each sub-class in terms of maximum displacements. In this study, the following three performance levels are considered: Immediate Occupancy (LS_1), Life Safety (LS_2) and Collapse Prevention (LS_3).

- In the final step, fragility curves are constructed by using the response statistics and the limit states. First, the responses of all structures are compared with the

predefined limit state values at each hazard intensity level. Then, the probability of the attainment or exceedance of a predefined limit state at each ground motion intensity level is calculated. The conditional probabilities with respect to the intensity level of ground motion records are plotted. The curve obtained is the fragility curve of a certain sub-class derived for a specified performance level. This process is repeated for all limit states and building sub-classes to obtain the complete set.

Details of the fragility curve generation methodology are given in the following sections.

4.5.1 Ground motion variability

Characteristics of the ground motion set have large impact in derivation of the fragility curves. Until now, most of the fragility curves in the literature have been derived based on global ground motion databases with records from different parts of the world. Especially in areas with higher seismicity, regional characteristics of input ground motions can affect the generated fragility curves significantly. Therefore, in this study, fragility curves are developed for local building stock of Erzincan region based on regional ground motion database. This is the first application in the literature where the fragility curves are entirely formed with simulated motions. To consider the regional effects, the input ground motions are particularly taken from the synthetic ground motion dataset generated by the stochastic finite-fault methodology as explained in Section 4.3.

In this study, to investigate the effect of ground motion intensity parameter in seismic damage assessment, two alternative ground motion intensity parameters are considered. For this purpose, earthquake ground motions are separated into two groups: The first group is categorized according to PGV and the second group is classified with respect to PGA as intensity parameter. Overall, the selected synthetic records cover a broad range of magnitudes (Mw=5.0, 5.5, 6.0, 6.5, 7.0, and 7.5). The closest distance to the fault plane varies between 0.26-17.55 km. In order to have an even distribution for responses of the structures, each ground motion set is subdivided

into 20 intensity levels by considering intervals of ΔPGV=5 cm/s and ΔPGA=0.05g. The reason for selection of PGA=1g and PGV=100 cm/s as maximum ground motion intensities for generation of fragility curves is that these values cover the limits for most of the selected districts and scenario events.

While generating the fragility curves, to account for the variability in demand, for each ground motion set, a total of 200 records are selected such that for each intensity level there are 10 region-specific time histories with different soil conditions, distance and magnitude values. To have an idea about the characteristics of the selected time histories, in addition to PGA and PGV, for all records some other ground motion parameters such as Housner intensity (*HI*), Arias intensity (I_a), and significant duration are calculated. Housner intensity is the integral of the pseudo-spectral velocity over the period range of 0.1-2.5 seconds for 5% of viscous damping as given by the following expression:

$$HI = \int_{0.1}^{2.5} PSV(\xi = 0.05, T)dT \tag{4.1}$$

where HI represents Housner intensity, PSV is the pseudo-spectral velocity, T is period, and ξ corresponds to the viscous damping.

Arias intensity is defined as the time-integral of the square of the ground acceleration represents the strength of a ground motion. The following equation represents the Arias intensity (I_a) where T_d is the duration of record above threshold and $a(t)$ is the ground acceleration at time t:

$$I_a = \frac{\pi}{2g}\int_0^{T_d}[a(t)]^2 dt \tag{4.2}$$

Finally, significant duration is defined as the interval of time in between the 5% and 95% of the accumulated Arias intensity.

Figure 4.19 represents the distribution of four ground motion parameters; PGA, significant duration, Housner intensity, and Arias intensity for the first set of records where PGV is considered as the main intensity measure. Figure 4.20 demonstrates the

corresponding distribution for the second set of records where PGA is considered as the main intensity measure. These scattered plots for these two sets of ground motions demonstrate that in the ground motion simulation and selection process, even for a certain intensity level, the regional variability of ground motion parameters is taken into account.

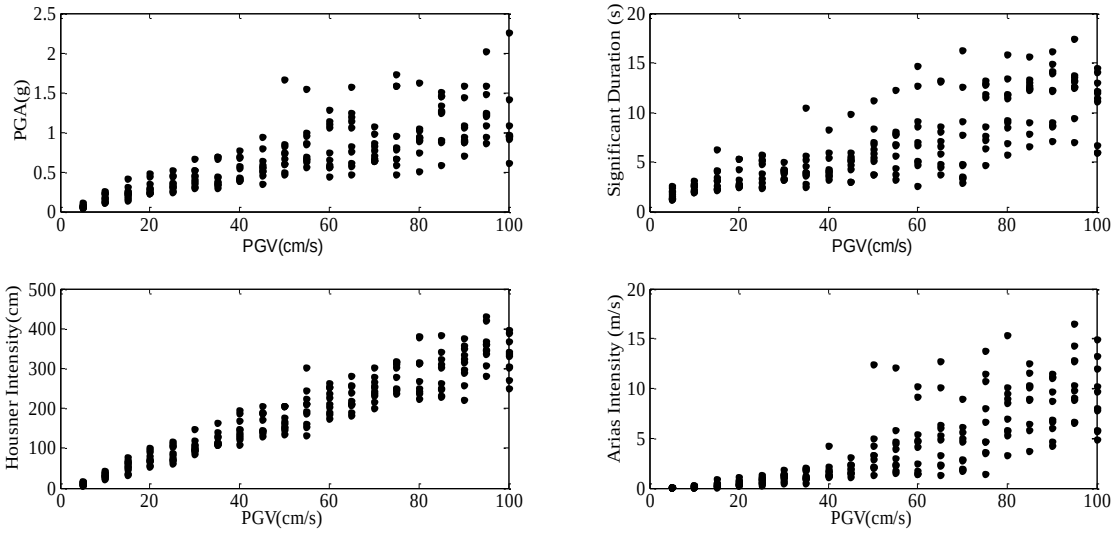

Figure 4.19 Distribution of the ground motion parameters for the first set of motions

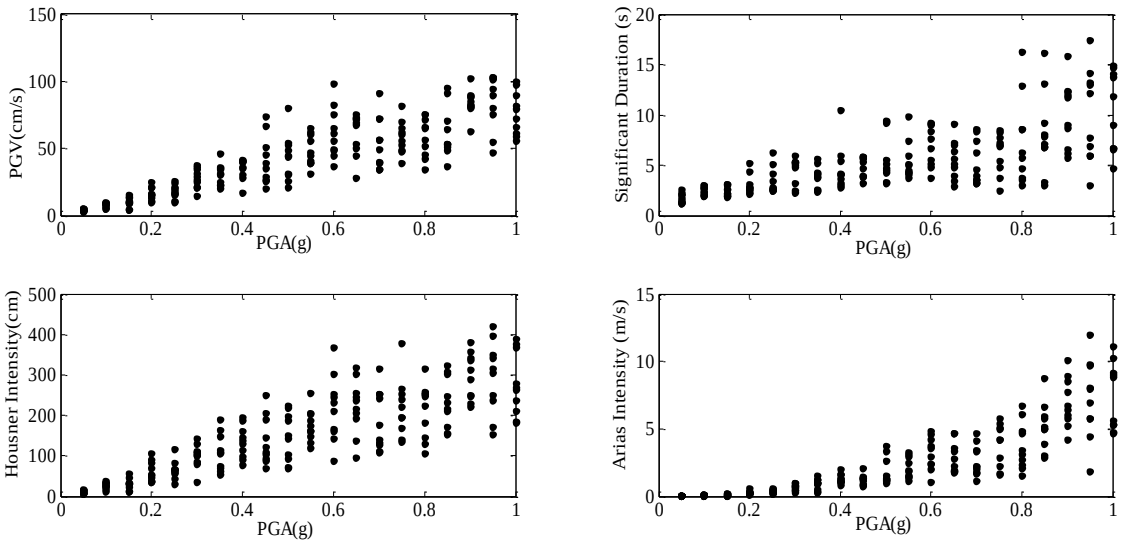

Figure 4.20 Distribution of the ground motion parameters for the second set of motions

4.5.2 Variability in structural properties and response statistics

In this study, the structural parameters T, η, and μ are considered as random variables. Selection of the most suitable probability distribution function for these random variables is not straightforward. However, it is observed that both normal and lognormal distributions have been intensively used for this purpose in the literature. In this study, for the sake of simplicity and physical accuracy (only positive values for the samples), lognormal distribution is selected. For sampling, Latin Hypercube Sampling (LHS) method, which can be regarded as a constrained Monte-Carlo method, is selected (Olsson *et al.*, 2003; Erberik 2008a; Erberik, 2008b). By using the LHS method, 20 samples are generated for each of the random variables (T, η, and μ). Figure 4.21 shows the variation of η with respect to T for all sub-classes. Next, the variation of μ with respect to T for all sub-classes is illustrated in Figure 4.22. The remaining model parameters including α_s, α_c, λ, and γ are assumed to be constant for all 20 simulated buildings from each sub-class. Detailed descriptions of all simulated buildings are available in Appendix A.

For each sub-class with a specified limit state and ground motion intensity, the following number of analyses is performed: for every sub-class since there are 20 building model simulations, and there are 10 records at each specified intensity level (either PGV or PGA), the number of response data points for every intensity level adds up to 200. Since there are a total of 20 intensity levels, the total number of required NLTHA on ESDOF models to obtain the response statistics becomes 4000.

Two samples of the NLTHA results in the form of scattered data are represented in Figure 4.23. In Figures 4.23.a and 4.23.b, the horizontal axis shows the ground motion intensity level for each sub-class where PGV is expressed in cm/s and PGA in cm/s^2, respectively. The vertical axis illustrates response of structures which is considered as maximum displacement in cm. Therefore, each vertical strip corresponds to a specified value of PGV or PGA. The responses of the other sub-classes are found to be similar.

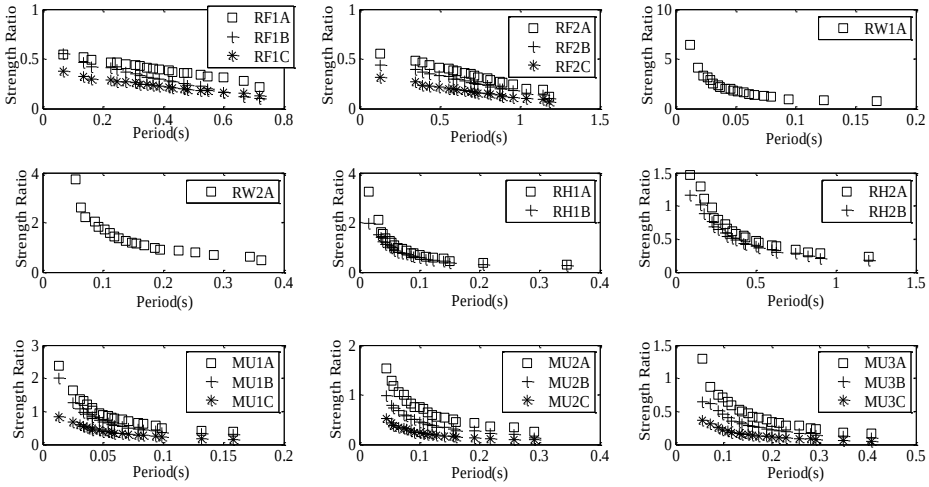

Figure 4.21 Period and strength ratio pairs generated by LHS technique for all sub-classes

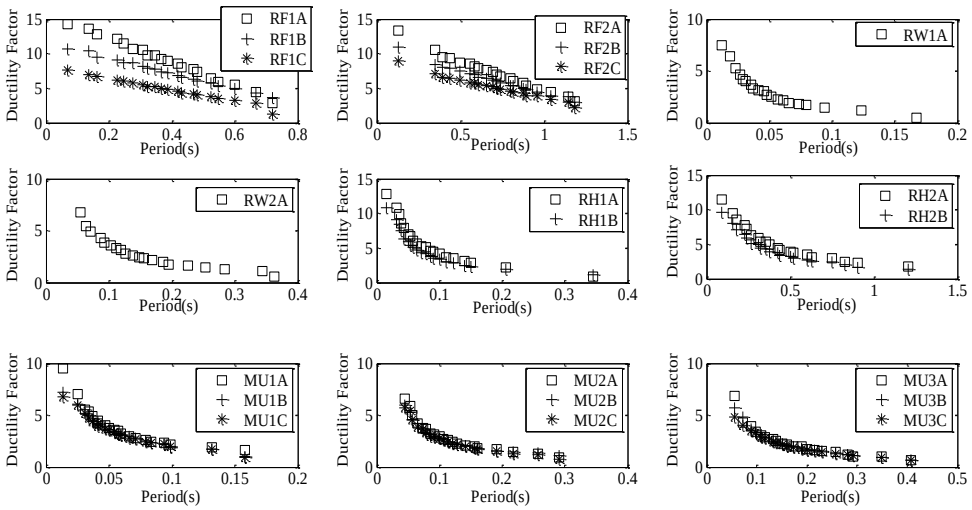

Figure 4.22 Period and ductility factor pairs generated by LHS technique for all sub-classes

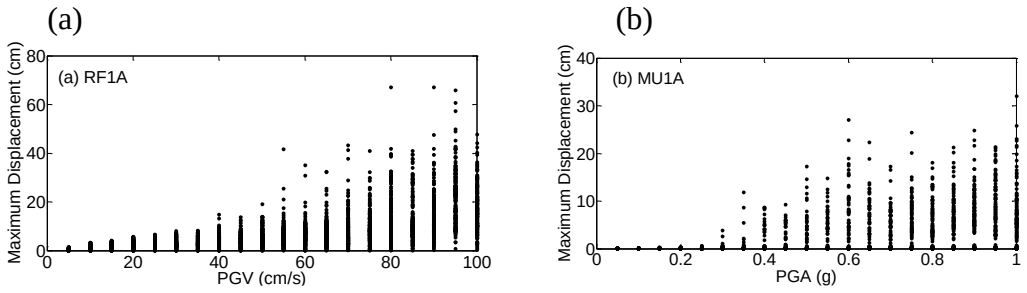

Figure 4.23 Distribution of the response parameter in terms of maximum displacement with respect to ground motion intensity parameter for (a) RF1A and (b) MU1A

4.5.3 Attainment of limit states

Limit states are defined as the performance levels of structures at some predefined thresholds. The attainment of these limit states is a significant part of fragility analysis. Previous studies demonstrate that limit states affect the resulting fragility curves considerably (e.g.: Wasti and Ozcebe, 2003; Erberik, 2008b). Therefore, they should be established with special care.

As it is mentioned previously, three limit states are considered in this study which are Immediate Occupancy, Life Safety, and Collapse Prevention. Immediate Occupancy limit state or shortly LS_1 is generally related to the stiffness of the structure. Life Safety limit state or LS_2 is determined by strength and deformation of the structure. Finally, in Collapse Prevention limit state or LS_3 major degradation in the stiffness and strength of the lateral-force resisting system as well as large permanent lateral deformation occurs. Deformation is the most common parameter that determines this limit state.

Complicated approaches for quantifying the limit states based on detailed behavior of members are more suitable for the analysis of individual or specific buildings. In contrast, this thesis is focused on a building population composed of numerous sub-classes, thus constant (deterministic) values are assigned to the limit states defined above. While determining the limit state values of building sub-classes, previous studies concerning the fragility of Turkish buildings are taken into consideration (e.g.: Akkar *et al.*, 2005; Kircil and Polat, 2006; Erberik, 2008a; Erberik, 2008b; Ucar and Duzgun, 2013). The values corresponding to the predefined limit states in terms of displacement for all sub-classes are listed in Table 4.4. While generating the fragility curves, these values are employed.

Table 4.4 Limit states in terms of displacement for all sub-classes

Frame ID	LS_1 (cm)	LS_2 (cm)	LS_3 (cm)
RF1A	1.55	6.70	12.40
RF1B	1.40	6.30	11.60
RF1C	1.32	5.80	10.70
RF2A	2.40	8.55	16.10
RF2B	2.00	8.10	15.20
RF2C	1.65	7.11	14.30
RW1A	0.40	1.00	3.30
RW2A	0.80	1.90	4.50
RH1A	0.40	1.80	5.50
RH1B	0.28	1.40	3.10
RH2A	1.60	5.90	9.50
RH2B	1.20	4.80	8.80
MU1A	0.07	0.25	1.54
MU1B	0.05	0.18	1.13
MU1C	0.03	0.10	0.87
MU2A	0.23	0.63	2.08
MU2B	0.14	0.37	1.67
MU2C	0.08	0.29	1.45
MU3A	0.32	0.954	3.125
MU3B	0.20	0.63	2.50
MU3C	0.11	0.52	1.88

4.5.4 Generation of fragility curves

Figure 4.24 shows the schematic representation of the applied procedure for generation of fragility curves. In Figure 4.24.a, distribution of a sample response statistics is plotted. In this figure, the horizontal axis shows the ground motion intensity and the vertical axis presents the response parameter. The horizontal line labeled as LS_i represents the target limit state. The scattered data of the j^{th} ground motion intensity level (GMI_j) is selected and shown in Figure 4.24.b. The conditional probability of attainment or exceedance of the i^{th} limit state (LS_i) at the j^{th} ground motion intensity level is calculated by the following formula:

$$P[D \geq LS_i | GMI_j] = \frac{n_A}{n_T} \tag{4.3}$$

where n_A is the sum of responses equal or above the i^{th} limit state, and n_T stands for the total number of responses, both at the j^{th} ground motion intensity level. After repeating this process for all intensity levels, the discrete fragility information presented in Figure 4.24.c can be obtained for a certain limit state. A cumulative lognormal distribution function is fitted to the obtained data with least squares technique as illustrated in Figure 4.24.d. To derive the fragility curves for all building types, this process is repeated for three limit states and all 21 sub-classes.

Figures 4.25-4.28 show the final smooth fragility curves for all building sub-classes. Comparison of the results show that for a given seismic intensity level, as the number of stories increases, the potential of damage also increases for all building types. In addition, for all cases, as the level of compliance with seismic design and construction codes gets poorer, the probability of exceeding LS_3 (or in other words experiencing collapse) increases. This trend verifies that the failure of the buildings which do not comply with the earthquake resistant design principles will be much more brittle than those which satisfy these principles. For LS_1, regardless of the level of compliance of structures with seismic design codes, the results of sub-classes with the same number of stories and structural system are close to each other. This trend is also physically meaningful in the sense that LS_1 depends mainly on the stiffness of the structure.

However, for LS_2 and especially for LS_3, the results deviate from each other, since these limit states are significantly affected by strength and deformation behavior of the structure.

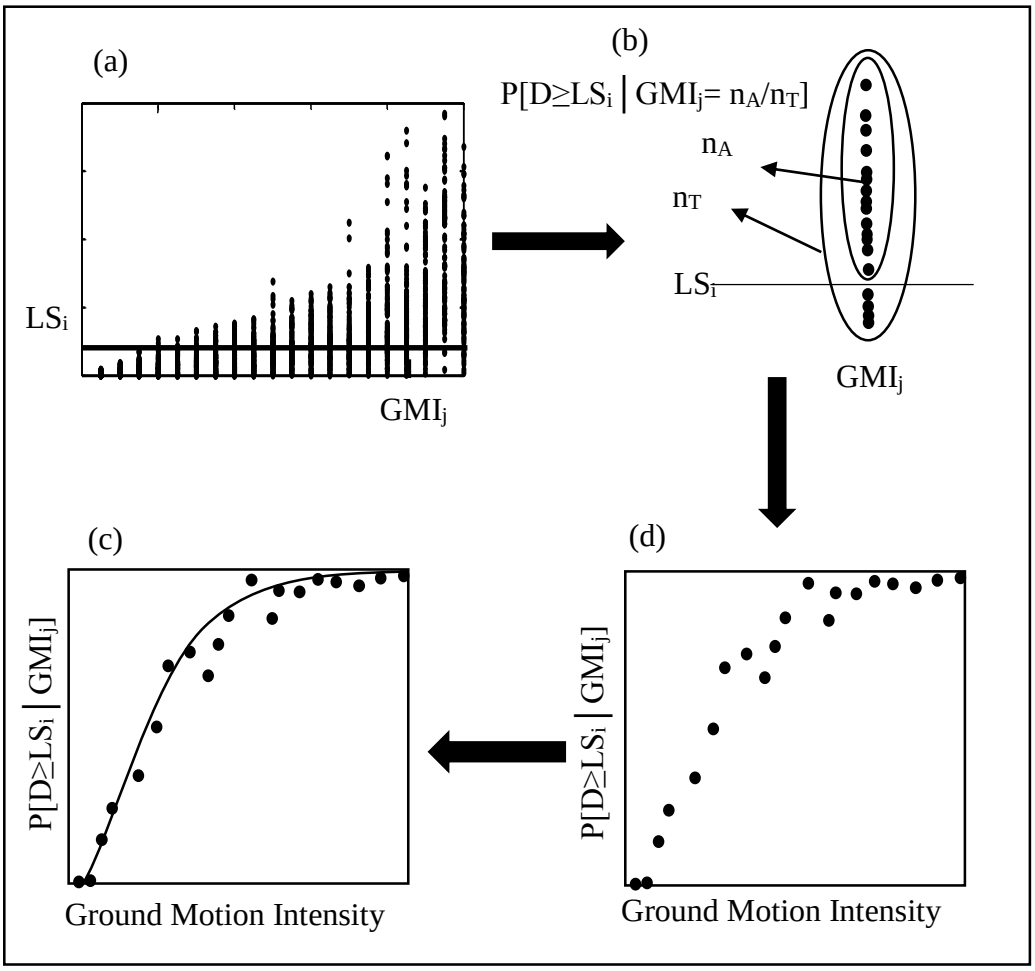

Figure 4.24 Schematic representation of the fragility curve generation procedure

(a)

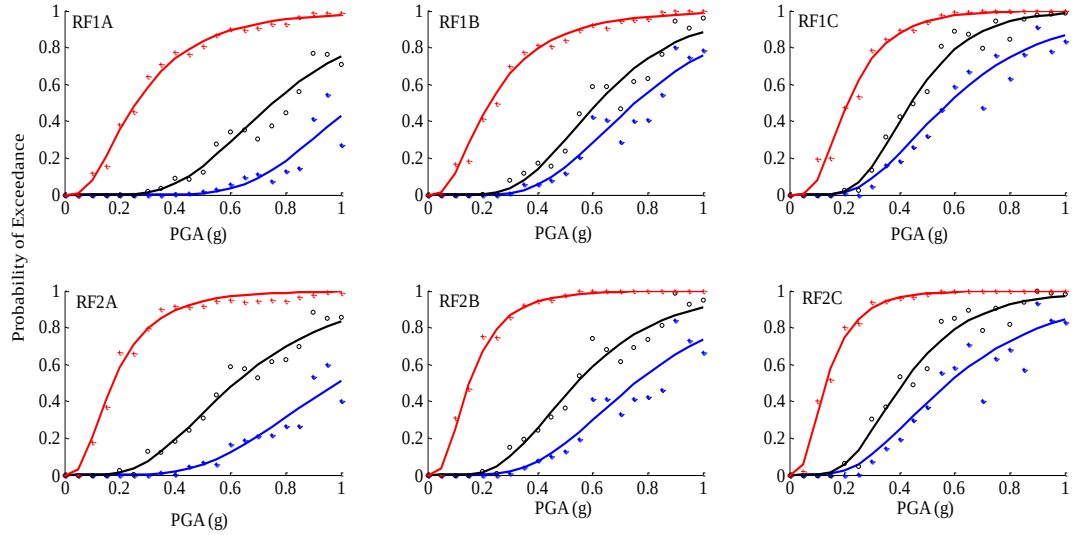

(b)

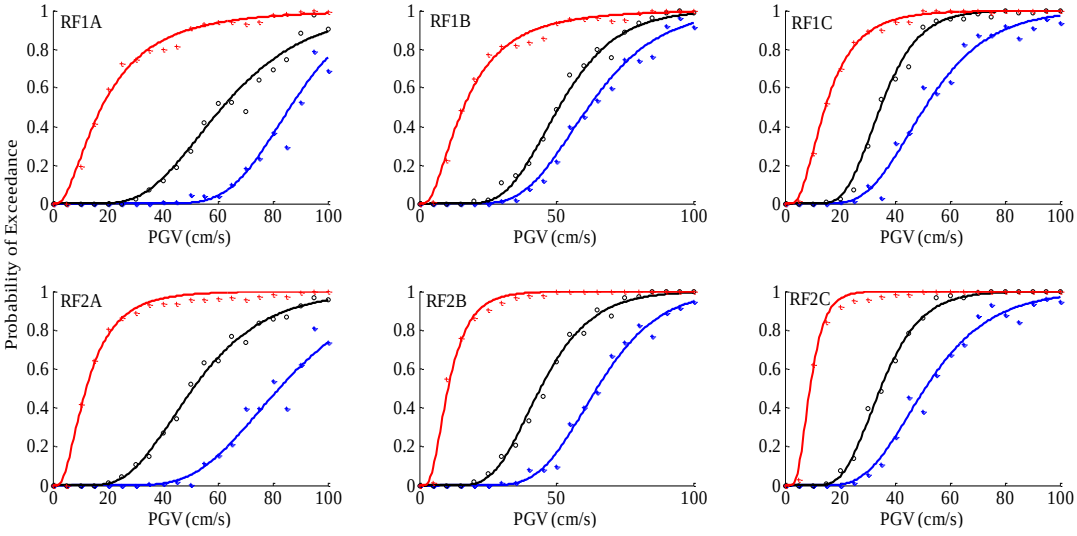

Figure 4.25 Fragility curves for RF sub-classes using records categorized based on (a) PGA and (b) PGV where the red lines correspond to LS_1, the black lines to LS_2, and the blue lines to LS_3

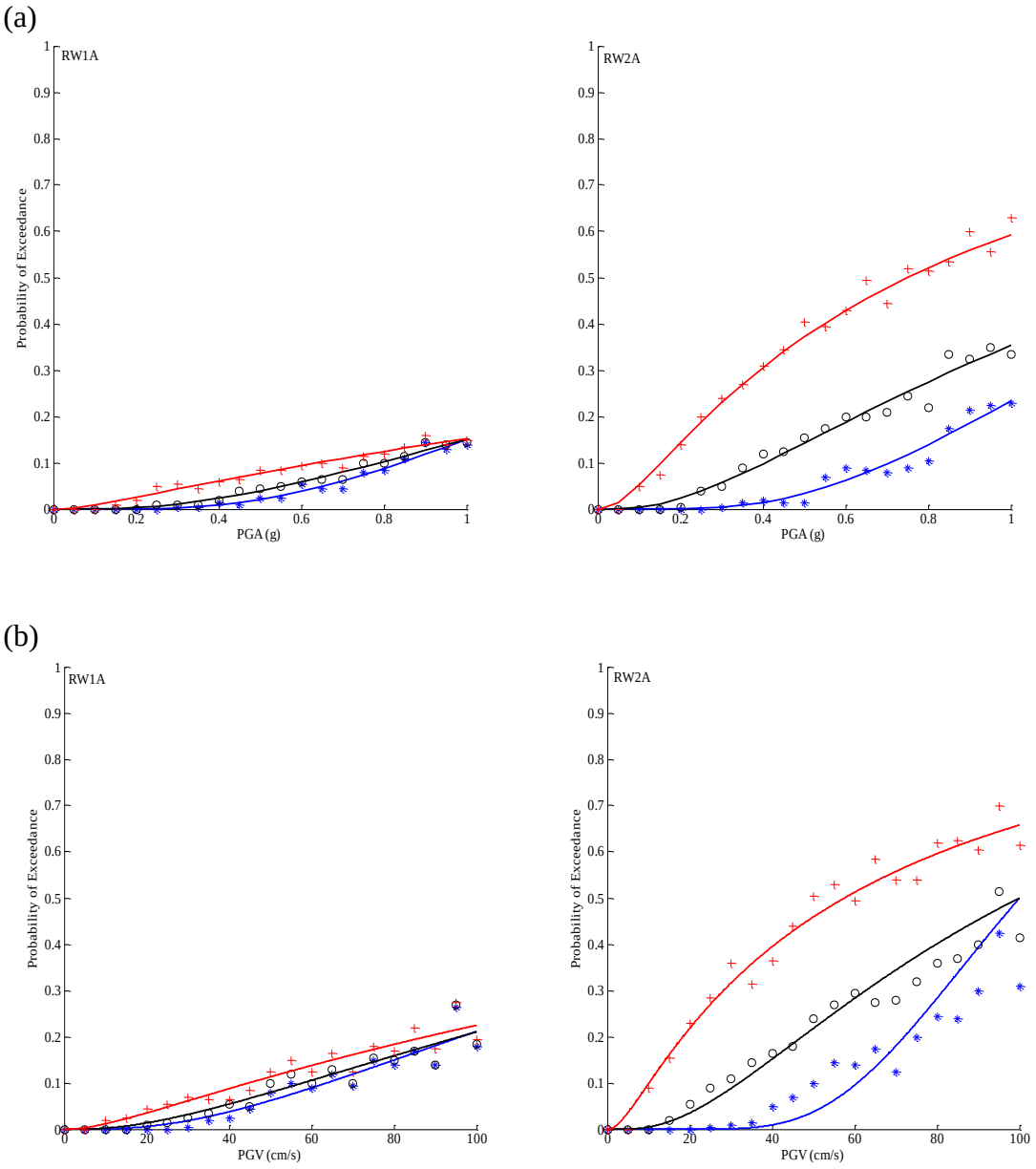

Figure 4.26 Fragility curves for RW sub-classes using records categorized based on (a) PGA and (b) PGV where the red lines correspond to LS_1, the black lines to LS_2, and the blue lines to LS_3

(a)

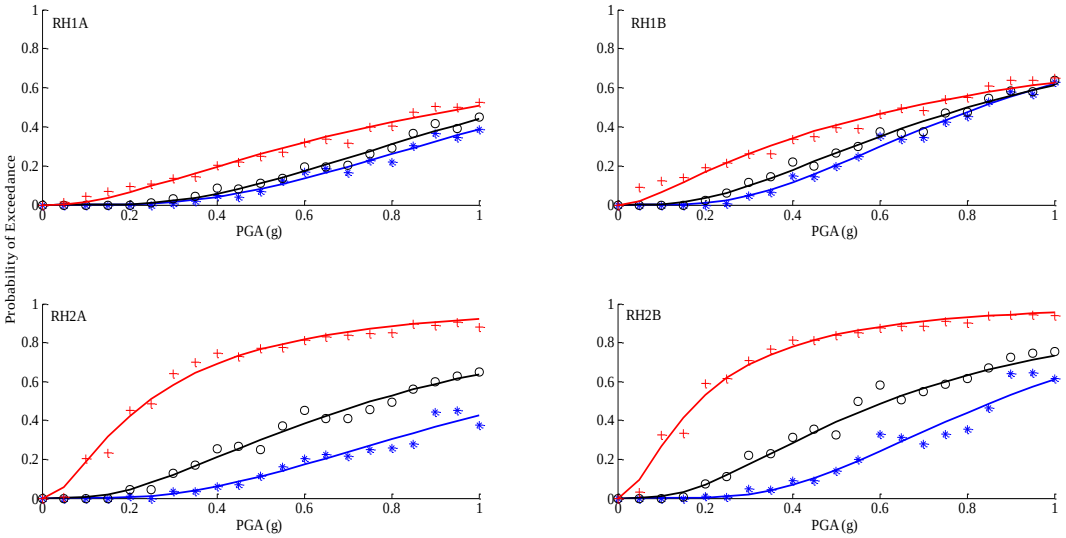

(b)

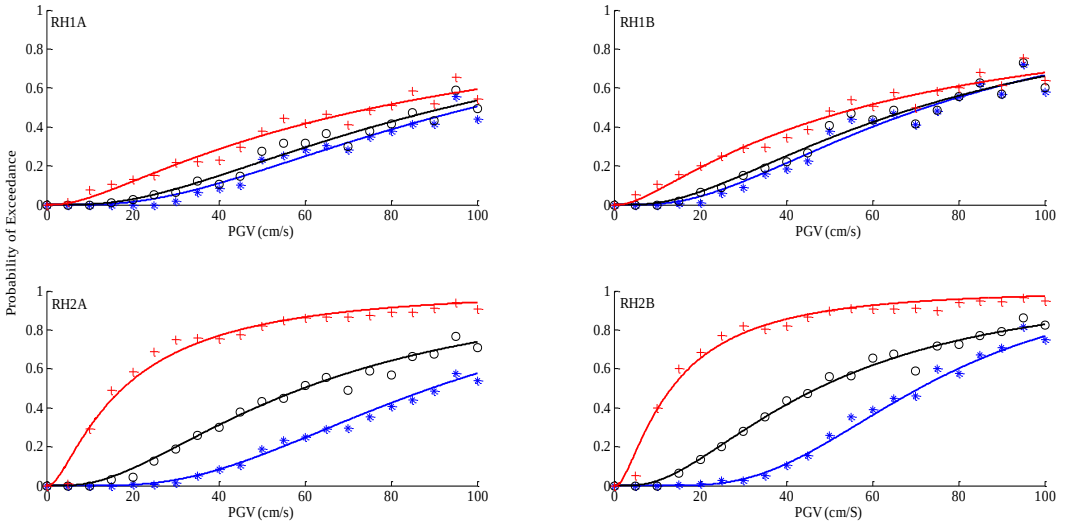

Figure 4.27 Fragility curves for RH sub-classes using records categorized based on (a) PGA and (b) PGV where the red lines correspond to LS_1, the black lines to LS_2, and the blue lines to LS_3

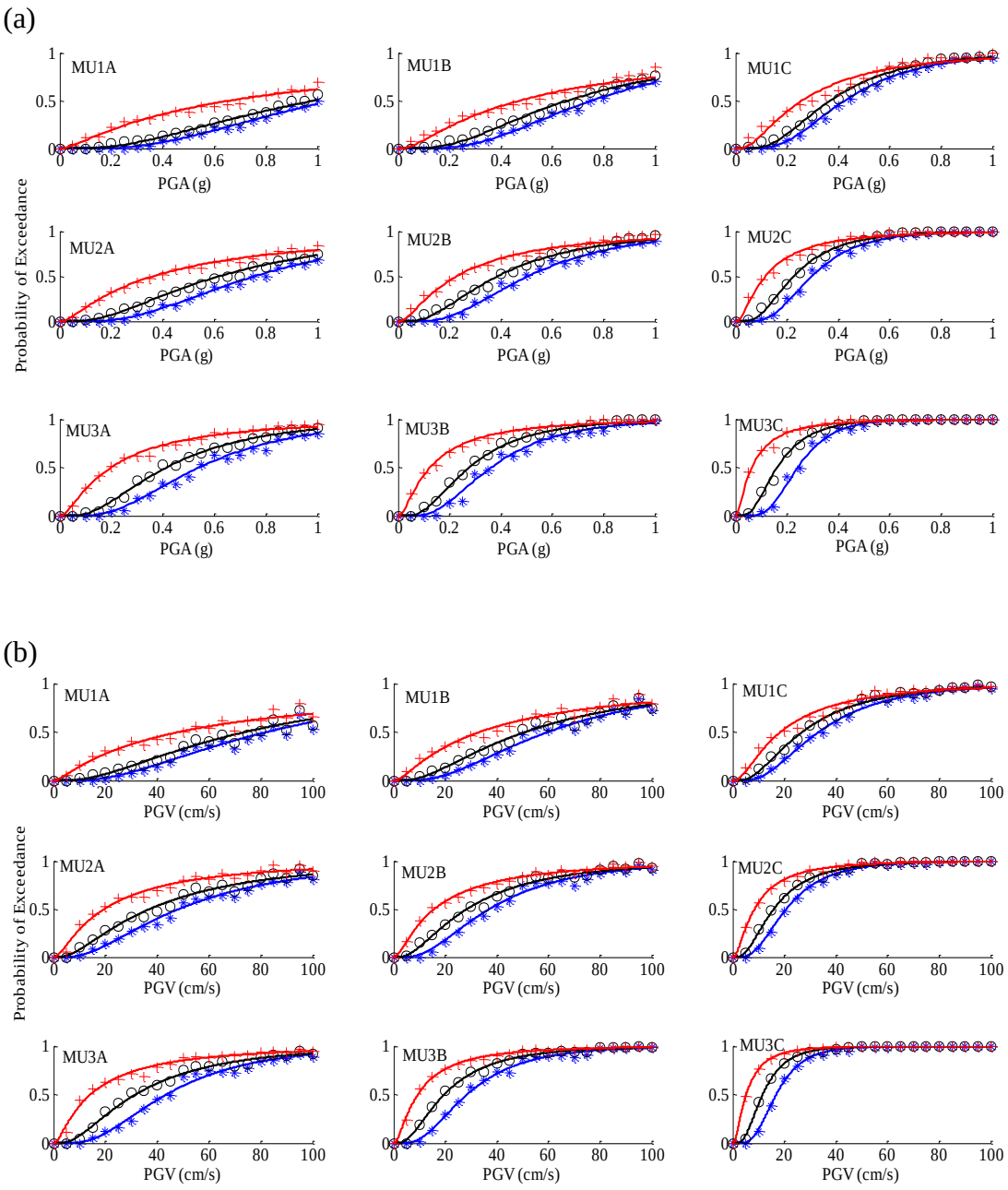

Figure 4.28 Fragility curves for masonry sub-classes using records categorized based on (a) PGA and (b) PGV where the red lines correspond to LS_1, the black lines to LS_2, and the blue lines to LS_3

If the curves are compared with respect to the building types considered, it is observed that among RC buildings, RW sub-classes have the best seismic performance followed by RH sub-classes (Figures 4.26 and 4.27). This is not surprising since these shear-wall (or specifically tunnel-form) buildings (i.e. RW sub-classes) have been built in Erzincan city after the 1992 earthquake as permanent housing for the survivors (Figure 4.29.a). They have been designed and constructed to exhibit superior seismic performance and until now, they have achieved this task during the previous major earthquakes in Turkey. They have a very high strength capacity; however they do not show a very ductile global behavior due to the presence of rigid shear walls and the connections in between. This point is reflected in the fragility curves such that all limit states are very close to each other, especially for RW1A indicating a narrow margin of inelastic behavior for this building type.

The RC frame buildings seem to exhibit different levels of performance depending on the specific characteristics of each sub-class. As the two limiting cases; low-rise RC frame buildings that conform to the modern earthquake resistant design principles (i.e. RF1A sub-class) seem to perform well whereas high-rise RC frame buildings that have structural deficiencies regarding seismic design principles (i.e. RF2C) exhibit poor performance under the same levels of seismic action (Figure 4.25). All the other RF sub-classes have seismic performance levels in between these two limiting cases as observed from the fragility curves. These trends are on justifiable grounds when compared to the field observations after recent major earthquakes in Turkey in the sense that the seismic performances of RC frame buildings are significantly dependent on the number of stories, structural details, and ground motion characteristics (e.g.: Akkar *et al.*, 2011; Akansel *et al.*, 2014). This is due to the fact that all the lateral resistance comes from the frame system without any additional mechanism. A typical mid-rise RC frame building in Erzincan city that was observed during the field survey is demonstrated in Figure 4.29.b.

The dual RC buildings with frames and walls (i.e. RH sub-classes) also seem to show good seismic performance. Low-rise types are eventually more rigid where the

behavior of shear wall dominates. Therefore the fragility curves for RH1A and RH1B are similar to the ones that belong to RW sub-classes. In mid-rise types, the effect of frame behavior seems to be much more pronounced where the fragility curves get apart from each other; an indication of relatively a more ductile behavior with a limited range of inelastic response. This type of RC buildings had been built in some districts after the 1992 earthquake in Erzincan city (Figure 4.29.c). Dual RC buildings are known to exhibit adequate behavior in previous major earthquakes in Turkey, which is also reflected in the corresponding fragility curves.

Masonry sub-classes seem to exhibit a wide range of seismic response such as the RC frame buildings since they are generally non-engineered structures without any standards regarding the material quality and the construction technique. Figure 4.30 shows two masonry buildings from Erzincan city with varying material and construction quality. The best seismic performance is observed for single-story masonry buildings with high level of compliance with the seismic regulations (i.e. MU1A sub-class) whereas the worst seismic performance belongs to three story masonry buildings with low level of compliance with the seismic regulations (i.e. MU3C sub-class). For all MU sub-classes, the fragility curves are found to be close to each other, indicating that the ductility capacities of these structures are limited (Figure 4.28). According to the field observations after major earthquakes in Turkey, when masonry buildings sustain some damage during the earthquake, the propagation of damage is very rapid, causing brittle failure of the structures without showing adequate capacity for inelastic action (e.g.: Akkar *et al.*, 2011; Akansel *et al.*, 2014).

(a)

(b)

(c)

Figure 4.29 Examples of RC buildings from Erzincan; (a) shear wall RC building (RW) (b) frame RC building (RF) (c) dual RC building (RH)

Figure 4.30 Examples of masonry buildings from Erzincan with varying material and construction quality

Above observations show that the fragility curve sets of building sub-classes can simulate the inherent characteristics of the buildings in the study region in justifiable terms. It is thus stated that the use of this fragility information for seismic damage estimation in Erzincan is valid.

Next, in this thesis, sensitivity analyses have been conducted in order to investigate the influences of modeling demand variability and alternative ways to calculate exceedance probabilities in derivation of fragility curves. For this purpose, only masonry building sub-classes which account for majority of the existing structures in Erzincan (almost 75%) are studied. The previous studies have revealed that PGA correlates well with inelastic response of masonry structures (Erberik, 2008b). Therefore, to provide a strong correlation in between hazard parameter as well as nonlinear responses of masonry building stock, only fragility curves derived with respect to PGA (as intensity measure of seismic loading) are compared in sensitivity analyses. Details of these analyses are discussed in Appendix B.

4.6 Simulation Based Seismic Damage Estimation

In this section, first the methodology used for damage assessment is described. Then, for verification purposes, observed damage distribution of the 1992 Erzincan earthquake is compared against the corresponding estimations obtained with the proposed method. Finally, the potential seismic damage distributions for the scenario events of Mw=5.0, 5.5, 6.0, 6.5, 7.0, and 7.5 are presented.

4.6.1 Methodology

Most of the parameters existing in the literature representing damage states are in the form of disaggregated numbers which makes a straight evaluation of damage difficult (Lang *et al*., 2008; Bal *et al*., 2010). However, damage estimates converted into total economic loss, casualty estimates, or mean damage ratio are the most appropriate parameters representing damage levels corresponding to a region. Estimation of total economic loss and casualties involves reliable data on replacement, structural damage, and population in the building. Thus, these parameters require detailed information

and involve noticeable uncertainties otherwise. As a result, in the present study, Mean Damage Ratio (MDR) that expresses the disaggregated damage estimates with a single value as implemented by Askan and Yücemen (2010) is selected.

For computation of MDR, a Damage Probability Matrix (DPM) is required. Introduced by Whitman in 1973, a DPM is constructed for each building class expressing the distribution of discrete damage probabilities for various intensity levels. Each column of DPM expresses a constant level of ground motion intensity, while each row of this matrix stands for the occurrence probability of being in a certain damage state. Therefore, each element of this matrix, P(DS,I) denotes the probability of experiencing a certain Damage State (DS) when the structure type under consideration is subjected to a specified ground motion with intensity level of I. It is noted that in any column of this matrix, the sum of the occurrence probabilities is equal to 1. In a damage probability matrix, the ground motion intensity parameter is defined either in the form of a felt intensity scale (such as the MMI scale) or in the form of quantitative ground motion intensity parameters such as PGA or PGV. The general form of a DPM proposed for Turkey by Gurpinar *et al.* (1978) is given in Table 4.5. In this table, the damage states are separated into 5 different groups as No Damage (N), Light Damage (L), Moderate Damage (M), Heavy Damage, and Collapse (H, C). Each damage state corresponds to the degree of structural or nonstructural damage for the building type and intensity level of interest. Damage Ratio (DR) is defined as the ratio of the cost of repairing to the cost of replacement for a certain type of building. This parameter takes values in between 0%-100%. Even for the same building type under similar seismic excitations it may differ due to variation in soil properties, material conditions, and duration of ground shaking. Therefore, for the sake of simplicity in MDR calculations from DPMs, a single quantitative value named as Central Damage Ratio (CDR) for each damage state is assigned. The corresponding DRs and CDRs for the five damage states are listed in Table 4.5. Each element of DPM is computed as follows:

$$P_k(DS, I) = \frac{N(DS,I)}{N(I)} \tag{4.4}$$

where N(I) is the number of k^{th}-type of buildings in the area subjected to a ground motion of intensity I and N(DS, I) is the number of structures in damage state (DS), among the N(I) buildings.

It must be noted that a DPM can be constructed empirically with damage data in the field or computed from theoretical models such as the method proposed herein.

Table 4.5 General form of damage probability matrix given by Gurpinar *et al*. (1978)

Damage state (DS)	**Damage Ratio (DR%)**	**Central Damage Ratio (CDR%)**	**Ground Motion Intensity Parameter, I (MMI, PGA, PGV, etc.)**
None	0-1	0	Damage State Probabilities, P(DS, I)
Light	1-10	5	
Moderate	10-50	30	
Heavy	50-90	70	
Collapse	90-100	100	

There is a close relationship in between fragility curves and DPMs such that the information provided by a fragility curve can be converted to build a DPM. Figure 4.31 represents the procedure for conversion of a fragility curve to a DPM. The damage information corresponding to each column of the DPM are obtained by intersecting the fragility curve set with vertical lines (dashed lines in Figure 4.31) at particular intensity levels. Then, to determine the damage state probabilities, the portions between any two limit states in these vertical alignments are calculated. For the present study, Intensity Level (IL) takes values corresponding to the intensity parameters of PGV and PGA which are estimated at each district center for each scenario event. In this study, since a certain fragility curve set corresponding to a specified building class is derived for three limit states of Life Safety, Immediate Occupancy, and Collapse Prevention, the constructed DPM will have 4 damage states

as none (DS_1), light (DS_2), moderate (DS_3), and severe (DS_4) states. Every damage grade for each building type refers to the level of damage experienced by a structure due to earthquake ground motions. Damage grade 1 represents none damage which is applicable for structures with no signs of damage; damage grade 2 represents light damage which accounts for structures requiring minor nonstructural repairs; damage grade 3 represents moderate damage where buildings need structural and nonstructural repairs; and damage grade 4 describes heavy damage for buildings which encountered severe and not repairable damage during earthquake. For three of these damage states (DS_1, DS_2, and DS_3) the values corresponding to CDR in Table 4.5 are applied. However, both heavy and collapse damage states of Table 4.5 are considered as a single damage state (severe) for this thesis. The range of damage ratio for the severe damage state is considered to be in between 50%-100%. Also, CDR of this damage state is assumed as 85% which is the mean value of the CDRs for Heavy and Collapse damage states as proposed by Gurpinar *et al.* (1978).

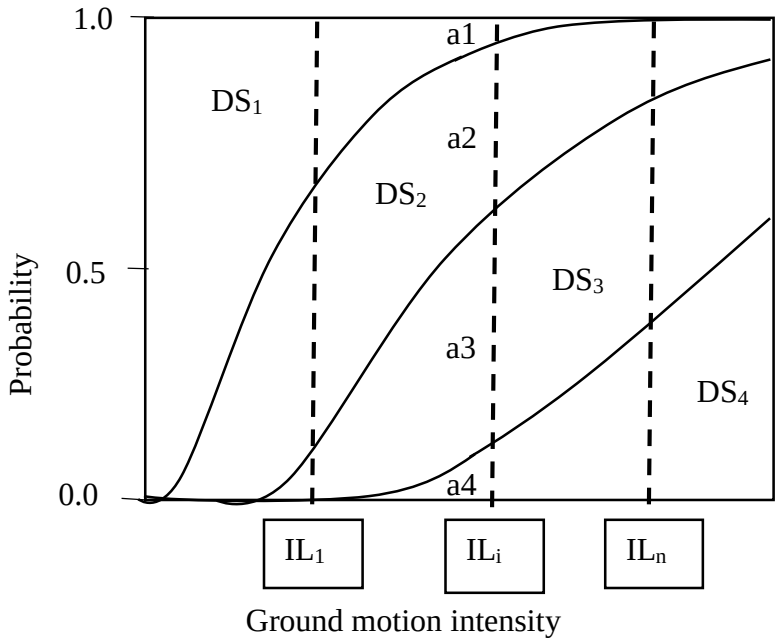

Damage State	**IL_i**
DS_1	a1
DS_2	a2
DS_3	a3
DS_4	a4

Figure 4.31 Conversion from a set of fragility curves to DPM

To express the damage probability matrix in a brief quantitative manner, the discrete values corresponding to each intensity level in a particular column of DPM are converted to a single value as MDR. Equation 4.5 defines MDR based on damage probabilities and CDR values:

$$MDR(I) = \sum_{DS} P_k(DS, I).CDR(DS) \quad (4.5)$$

4.6.2 Applications in the study region

In this part, first it is aimed to evaluate the efficiency of the proposed methodology in predicting actual damage distribution of a past event in the study area. For this purpose, in Subsection 4.6.2.1 distribution of the observed damage for the 1992 Erzincan earthquake is obtained. Then, the proposed method is applied for the 1992 Erzincan earthquake and the estimated damage levels in districts are compared with the corresponding observed damage levels. In Subsection 4.6.2.2, the method is used for prediction of potential losses where the seismic damage for scenario events of Mw=5.0, 5.5, 6.0, 6.5, 7.0, and 7.5 are calculated. For the estimation of damage in both validation and predictions, a total of 16 residential districts in Erzincan city with available building data are selected. The algorithm for damage assessment is summarized as follows:

a) For scenario events of Mw=5.0, 5.5, 6.0, 6.5, 7.0, and 7.5 as well as the 1992 Erzincan earthquake, simulated records for the selected residential areas are collected.

b) Both PGA and PGV values corresponding to centroid of each considered district are obtained from the synthetic ground motion database.

c) For the selected districts, percent distribution of the buildings with respect to the structural type as well as number of stories is compiled.

d) Using the fragility curves derived in Section 4.5.4, in each district DPMs for all of the existing building types under the given ground motions are developed.

e) Finally, the DMPs are combined according to percent distribution of building types in the selected districts. For each residential area and scenario event, a single MDR is calculated.

4.6.2.1 Validation of the estimated damage distribution for the 1992 Erzincan earthquake

There are only few studies on the spatial distribution of the observed damage levels during the 1992 Erzincan earthquake (Sucuoğlu and Tokyay, 1992; Şengezer, 1993; Erdik *et al.*, 1994). The data provided by these studies were obtained through expert-opinion surveys in the field immediately after the earthquake. In total, damage information corresponding to twelve of the selected sixteen residential areas is available. The observed MDRs in the study region are presented in Table 4.6, where N/A corresponds to the residential districts with no damage data. The values presented in Table 4.6 reveal that in spite of moderate size of the 1992 Erzincan earthquake, residential structures in the city center suffered from higher levels of damage during the earthquake, while ten of the residential areas experience moderate damage (10%<=MDR<=50%). However, the estimated damage in the rest of the residential areas are in between 1% to 10%. Therefore, the observed damage levels for the 1992 Erzincan earthquake show that the Erzincan city center is subjected to the moderate damage levels in majority of the residential areas. It is worth to mention that the results presented herein may contain error arising from subjectivity in assigning damage states for the buildings in the field.

Table 4.6 Observed MDRs during the 1992 Erzincan earthquake with Mw=6.6

Node No.	District	Latitude (°)	Longitude (°)	Observed MDR (%)
91	İnönü	39.7505	39.4857	16.78
92	İzzetpaşa	39.7401	39.5083	N/A
94	Akşemsettin	39.7506	39.5148	39.00
95	Arslanlı	39.7595	39.4830	20.84
96	Atatürk	39.7492	39.4955	5.89
97	Bahçelievler	39.7512	39.4757	9.00
99	Barbaros	39.7542	39.5037	15.00
100	Cumhuriyet	39.7594	39.4967	35.00
101	Ergenekon	39.7516	39.4641	N/A
104	Halitpaşa	39.7440	39.4789	13.54
105	Hocabey	39.7416	39.4849	13.83
108	Kızılay	39.7448	39.4897	29.65
109	Mimar sinan	39.7430	39.4662	N/A
112	Yavuz selim	39.7581	39.4738	35.10
113	Yenimahalle	39.7574	39.4901	N/A
102	Fatih	39.7461	39.5110	31.22

Next, efficiency of the proposed method is evaluated in predicting real damage states of the city center. Data for building stock is only provided on the level of sixteen city sectors from a walk-down survey in the study region. Thus, the variations in building distribution within a single geounit are not considered. The collected data involves the percent distribution of buildings with respect to structural type and number of stories as presented in Table 4.7. The spatial distribution of these data in the selected districts are also illustrated in Figures 32-36. It is worth noting that, the information is gathered in 2013. However, comparison of the estimated damage levels are accomplished against observed ones gathered in 1992 after the earthquake. The error arising from this assumption is believed to be negligible since only limited number of districts (Yavuz Selim, Mimar Sinan, Ergenekon, and Arslanlı) include newly constructed reinforced-concrete structures after the 1992.

Table 4.7 Percent distribution of buildings with respect to structural type as well as number of stories in the Erzincan region

District	Latitude (°)	Longitude (°)	RC (%)	MU (%)	Low-Rise RC (%)	Mid-Rise RC (%)	1-Story MU (%)	2-Story MU (%)	3-Story MU (%)
İnönü	39.751	39.486	43	57	90	10	40	44	16
İzzetpaşa	39.7401	39.5083	16	84	99	1	84	14	2
Akşemsettin	39.7506	39.5148	10	90	92	8	90	8	2
Arslanlı	39.7595	39.483	50	50	81	19	45	25	30
Atatürk	39.7492	39.4955	40	60	86	14	25	39	36
Bahçelievler	39.7512	39.4757	49	51	90	10	24	35	41
Barbaros	39.7542	39.5037	20	80	100	0	41	34	25
Cumhuriyet	39.7594	39.4967	15	85	90	10	40	44	16
Ergenekon	39.7516	39.4641	89	11	16	84	40	34	26
Halitpaşa	39.744	39.4789	6	94	97	3	65	25	10
Hocabey	39.7416	39.4849	4	96	99	1	74	19	7
Kızılay	39.7448	39.4897	10	90	99	1	95	2	3
Mimar Sinan	39.743	39.4662	78	22	84	16	48	35	17
Yavuz Selim	39.7581	39.4738	70	30	69	31	23	34	43
Yenimahalle	39.7574	39.4901	27	73	91	9	59	26	15
Fatih	39.7461	39.511	16	84	88	12	86	7	7

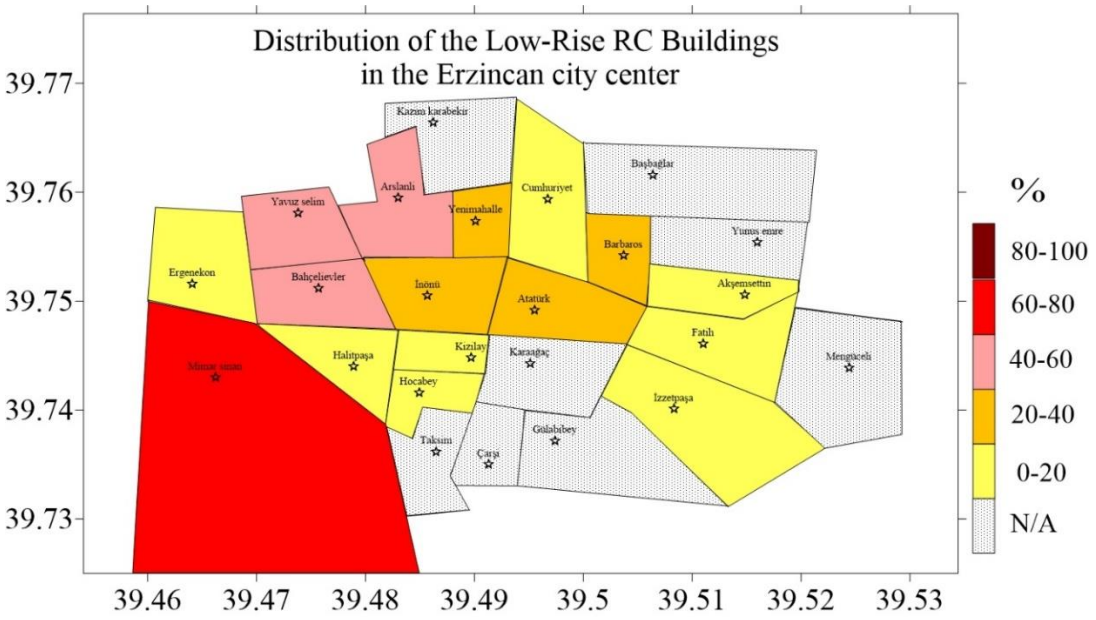

Figure 4.32 Spatial distribution of the low-rise RC buildings in the districts (Erzincan)

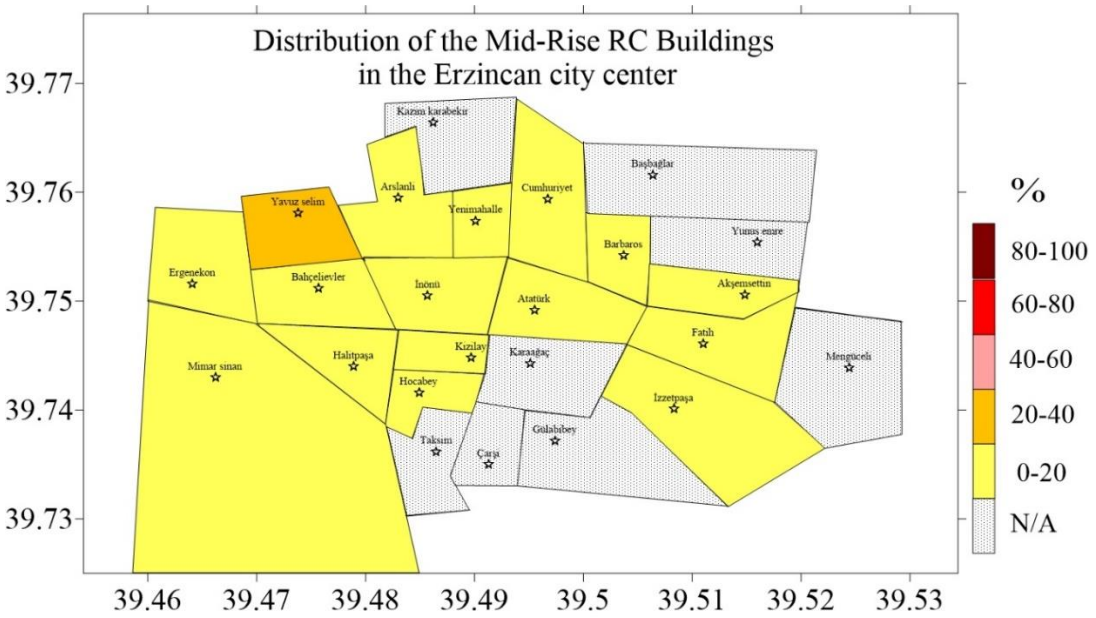

Figure 4.33 Spatial distribution of the mid-rise RC buildings in the districts (Erzincan)

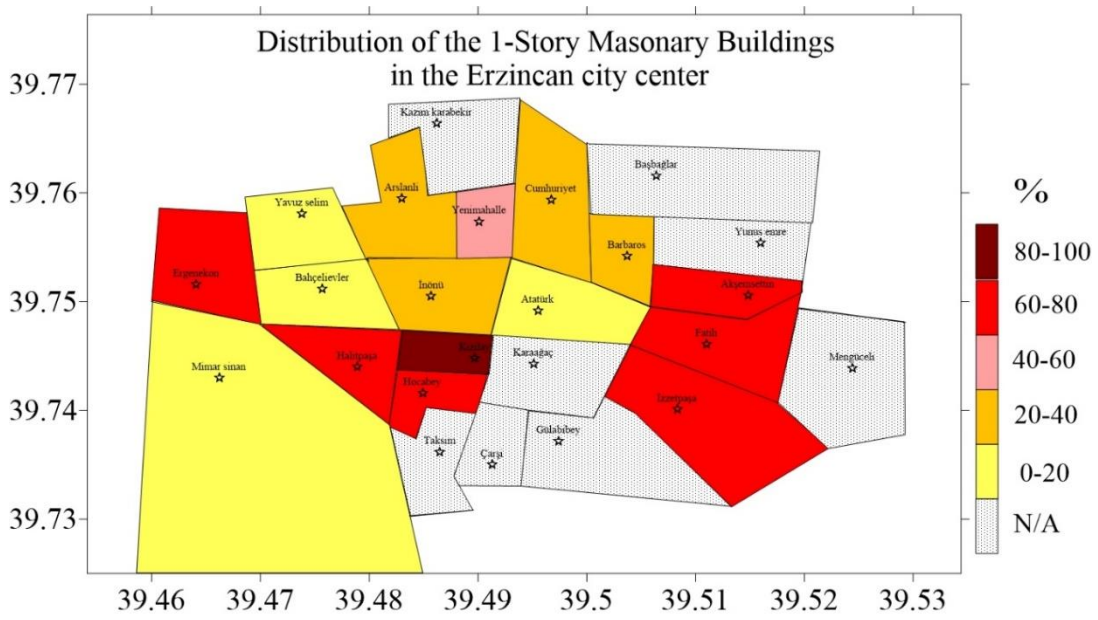

Figure 4.34 Spatial distribution of the 1-story masonry buildings in the districts (Erzincan)

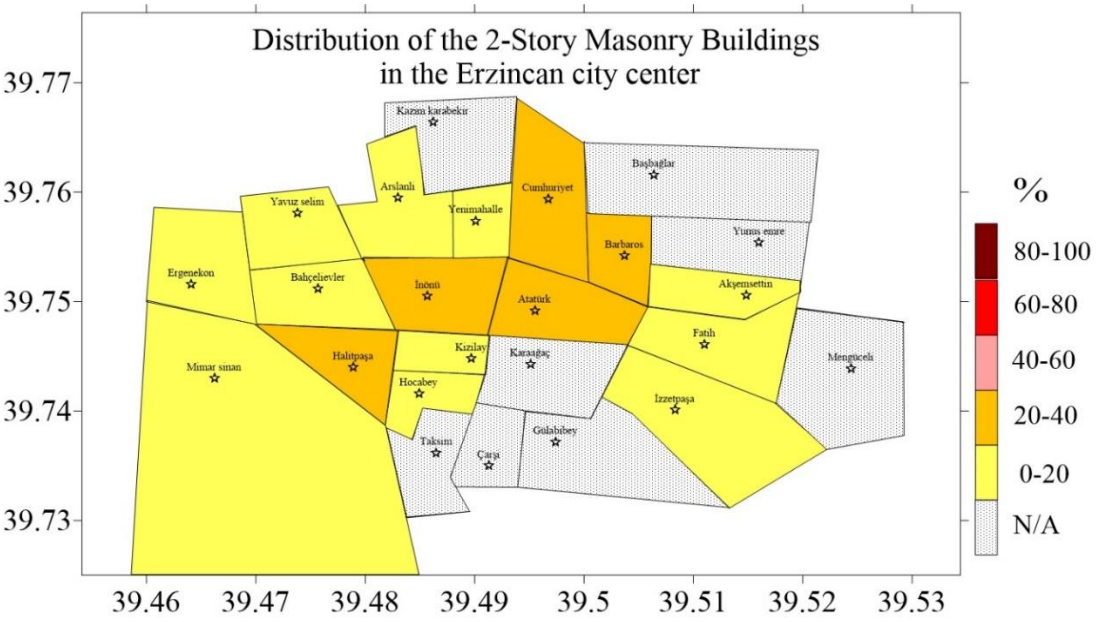

Figure 4.35 Spatial distribution of the 2-story masonry buildings in the districts (Erzincan)

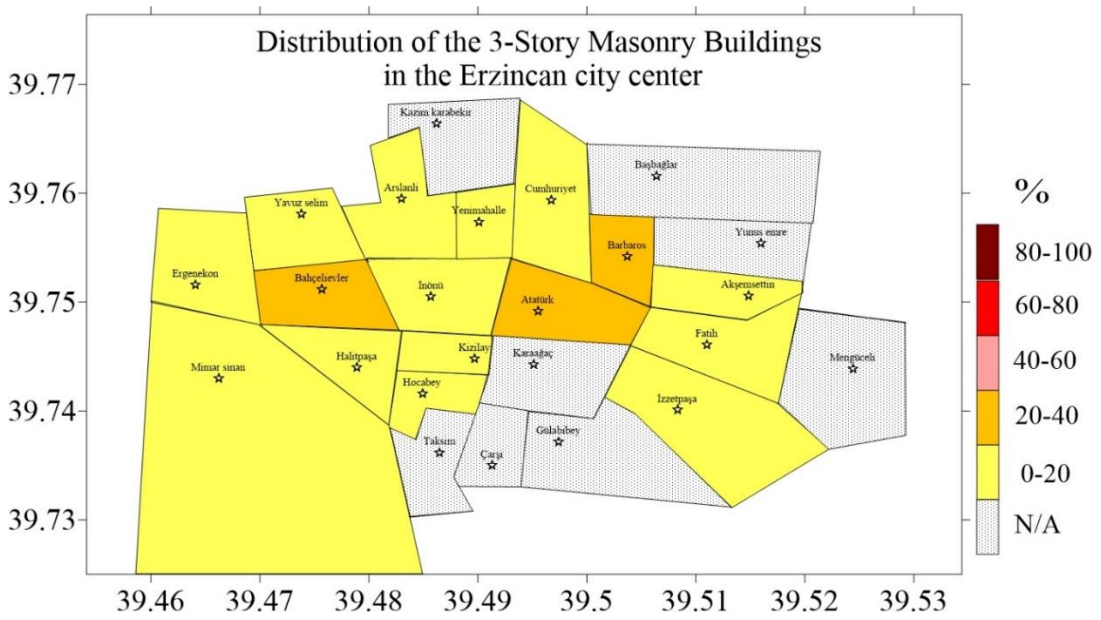

Figure 4.36 Spatial distribution of the 3-story masonry buildings in the districts (Erzincan)

The simulated PGA and PGV values of the 1992 earthquake at the district centers are presented in Table 4.8 and Figure 37. To develop the DPMs, three alternative approaches are evaluated while the major difference between these approaches is the main ground motion intensity parameter in the fragility curves. The first Damage Estimation Approach (DEA1) uses the information obtained by fragility curves in terms of PGA whereas the second approach (DEA2) uses PGV. Damage patterns monitored in the past events revealed that PGV and PGA correlate well with inelastic response of flexible structures (RC) and stiff structures (masonry), respectively (Akkar and Ozen, 2005; Erberik, 2008a; 2008.b). Therefore, in the third approach (DEA3), for reinforced-concrete and masonry structures, information obtained by fragility curves in terms of PGV and PGA, respectively, are used. Then, MDRs for the selected residential areas from all of the mentioned approaches are obtained. The predicted results are presented in Table 4.8. Figure 4.38 compares the estimated MDRs using three different approaches with the observed ones during the 1992 Erzincan

earthquake. In this figure, the horizontal axis represents the observed MDRs whereas the vertical axis shows the estimated MDRs. A Root Mean Square Error (RMSE) function is defined to measure the goodness of match between the estimated damage and observed damage as follows:

$$RMSE = (\frac{1}{N}\sum_{i=1}^{N}(MDR(est)_i - MDR(obs)_i)^2)^{1/2} \quad (4.6)$$

where N is the number of residential districts with available real MDRs, which is equal to 12 herein, $MDR(est)_i$ and $MDR(obs)_i$ is the estimated and observed MDRs at i^{th} residential district, respectively. Also, the correlation coefficients in between the estimated (by implementing three different methods) and the observed MDRs are calculated. Table 4.9 summarizes the calculated correlation coefficients and the corresponding error values. Comparison of these values reveals that among three approaches, the MDRs estimated using the third approach (DEA3) has the largest correlation with the observed MDRs with a correlation coefficient of 0.86 along with the minimum RMSE (2.10). Therefore, the estimated MDRs from the DEA3 better correlates with the observed damage ratios during the 1992 Erzincan earthquake. A further analysis of these approaches is provided in Appendix C. In this study, among the three approaches proposed for estimation of MDR, the third approach (DEA3) is implemented. Figure 4.39.a and 4.39.b shows the percent distribution of the observed MDRs during the 1992 event and the corresponding estimated MDRs using the third approach (DEA3), respectively. In these figures, N/A corresponds to the residential districts where either the observed damage or the building information for modeling is unavailable. Comparison of the observed and estimated damage levels for the 1992 Erzincan earthquake demonstrates that for almost 75% of the residential areas, the results are in good agreement. For the other residential districts, the estimated damage levels are slightly larger than the observed ones. The small differences may be attributed to the uncertainties involved with the loss estimations process or the subjectivity in assigning damage states for the buildings in the field. When the spatial distribution of buildings (Figure 32-36) as well as ground motion intensity parameters (Figure 37) in terms of either PGA or PGV is compared with the spatial distribution

of the estimated MDRs for the 1992 Erzincan earthquake (Figure 39.b), it is observed that all of them are in agreement. For instance, districts such as Fatih, İzzetpaşa, Akşemsettin, Cumhuriyet, Barbaros including mostly unreinforced masonry structures along with highest levels of PGA, have larger MDRs (in between 30%-50%) compared to the other districts. In contrast, for districts such as Atatürk and Halitpaşa, the estimated PGA values are lower in spite of existence of the highest percentage of masonry buildings. As a result, the estimated MDRs are in between 10%-30%, less than the previously mentioned stations. At station Yavuz selim although most of the buildings are newly constructed RC types, larger values of PGV result in larger MDRs (30%-50%). The minimum estimated MDR corresponds to Ergenekon (1%-10%). This is logical since Ergenekon has highest percentage of RC structures along with lowest PGV. Overall, it is believed that fragility information derived from locally simulated ground motions yields reliable damage distributions.

Table 4.8 Estimated PGA, PGV, and MDR values for the 1992 Erzincan earthquake

District	Latitude (°)	Longitude (°)	PGA (g)	PGV (cm/s)	Estimated MDR (%)		
					DEA1	DEA2	DEA3
İnönü	39.7505	39.4857	0.48	22.12	11.05	23.09	18.86
İzzetpaşa	39.7401	39.5083	0.65	53.51	43.18	40.49	40.29
Akşemsettin	39.7506	39.5148	0.64	72.19	56.71	38.4	40.15
Arslanli	39.7595	39.483	0.45	25.5	15.69	26.61	20.84
Atatürk	39.7492	39.4955	0.39	23.79	11.61	14.2	13.47
Bahçelievler	39.7512	39.4757	0.44	50.34	30.9	16.62	20.89
Barbaros	39.7542	39.5037	0.71	40.37	26.92	36.59	34.22
Cumhuriyet	39.7594	39.4967	0.74	55.97	40.25	38.55	37.81
Ergenekon	39.7516	39.4641	0.35	23.06	5.58	8.07	5.6
Halitpaşa	39.744	39.4789	0.37	29.13	19.52	15.64	15.57
Hocabey	39.7416	39.4849	0.42	29.27	18.21	17.94	17.79
Kizilay	39.7448	39.4897	0.64	37.29	20.63	30.03	28.36
Mimar Sinan	39.743	39.4662	0.65	62.97	31.53	21.58	28.66
Yavuz Selim	39.7581	39.4738	0.56	61.75	45.14	28.76	38.43
Yenimahalle	39.7574	39.4901	0.4	30.39	22.5	21.98	20.74
Fatih	39.7461	39.511	0.7	50.94	31.06	32.36	32.36

(a)

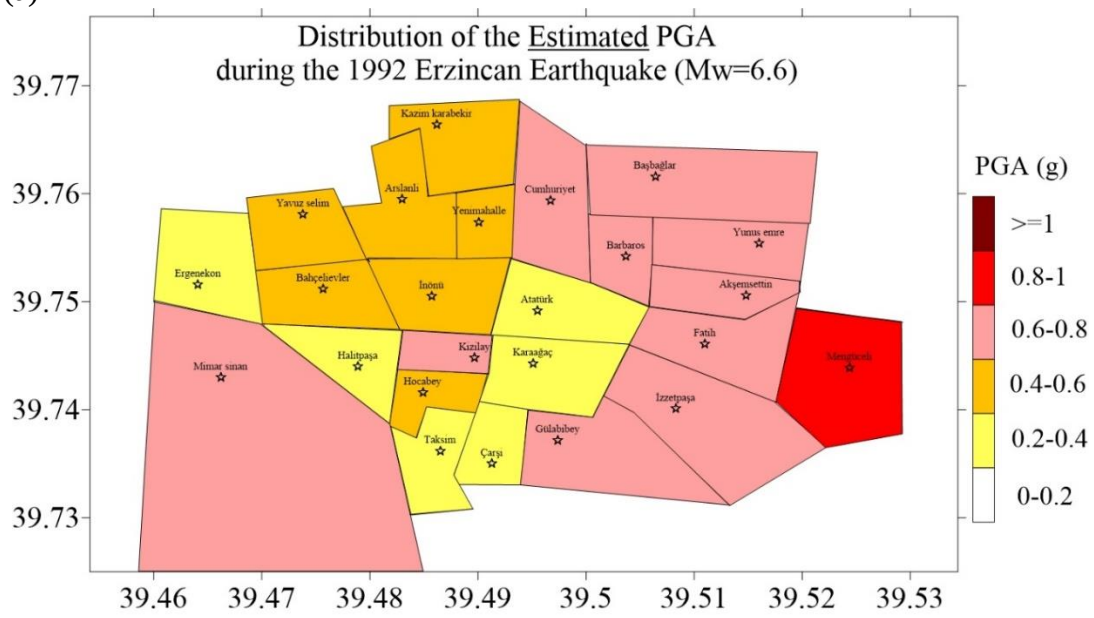

(b)

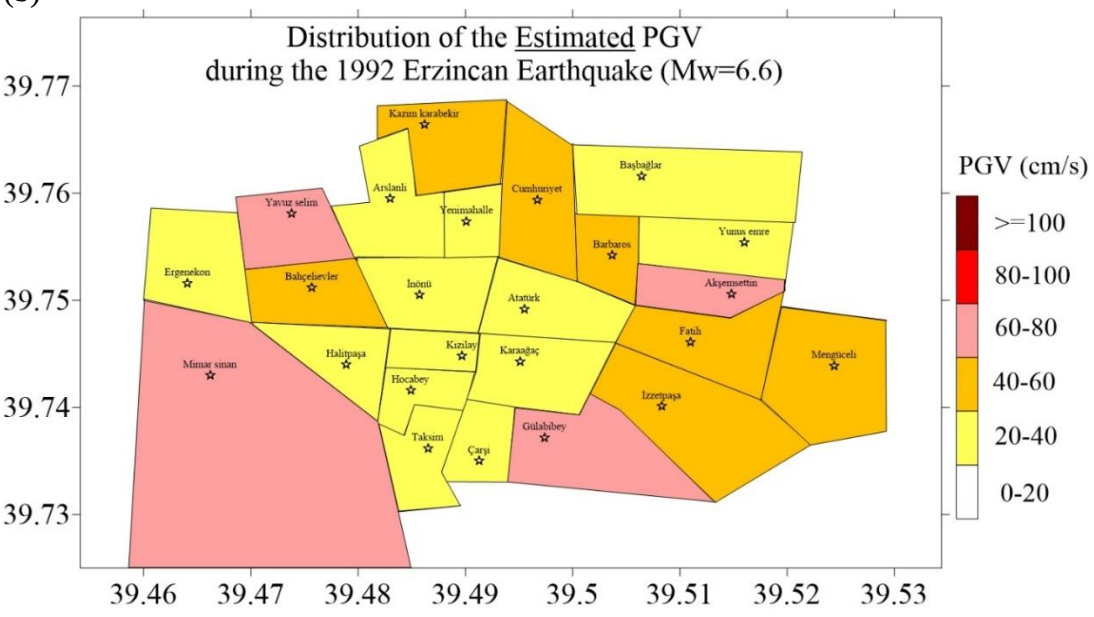

Figure 4.37 Spatial distribution of the simulated (a) PGA (b) PGV values of the 1992 Erzincan earthquake in the districts (Erzincan)

Table 4.9 Performance of different damage estimation approaches in predicting the observed MDRs during the 1992 Erzincan earthquake

Damage Estimation Approach	Error (RMSE)	Coefficient of Correlation
DEA1	2.99	0.75
DEA2	2.27	0.80
DEA3	2.10	0.86

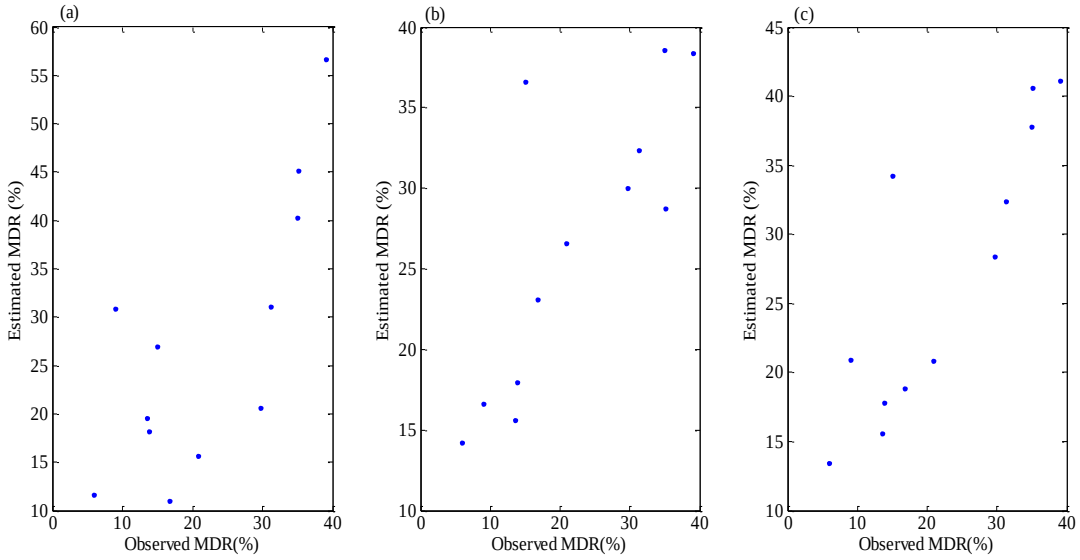

Figure 4.38 Comparison of the estimated MDRs using: (a) DEA1 (b) DEA2, and (c) DEA3, with the observed MDRs during the 1992 Erzincan earthquake

(a)

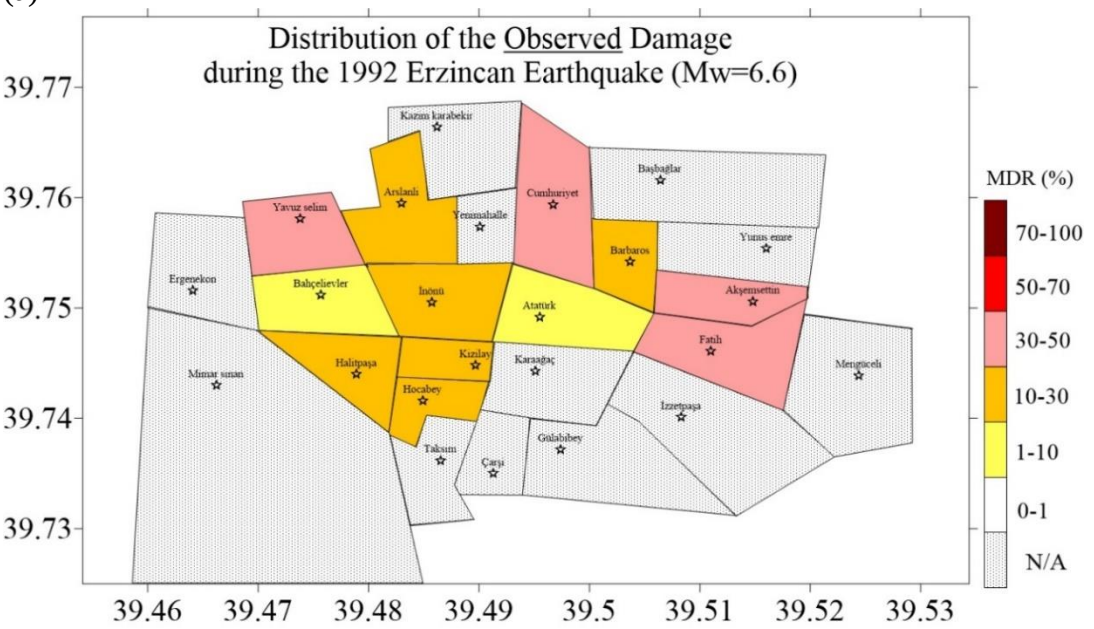

(b)

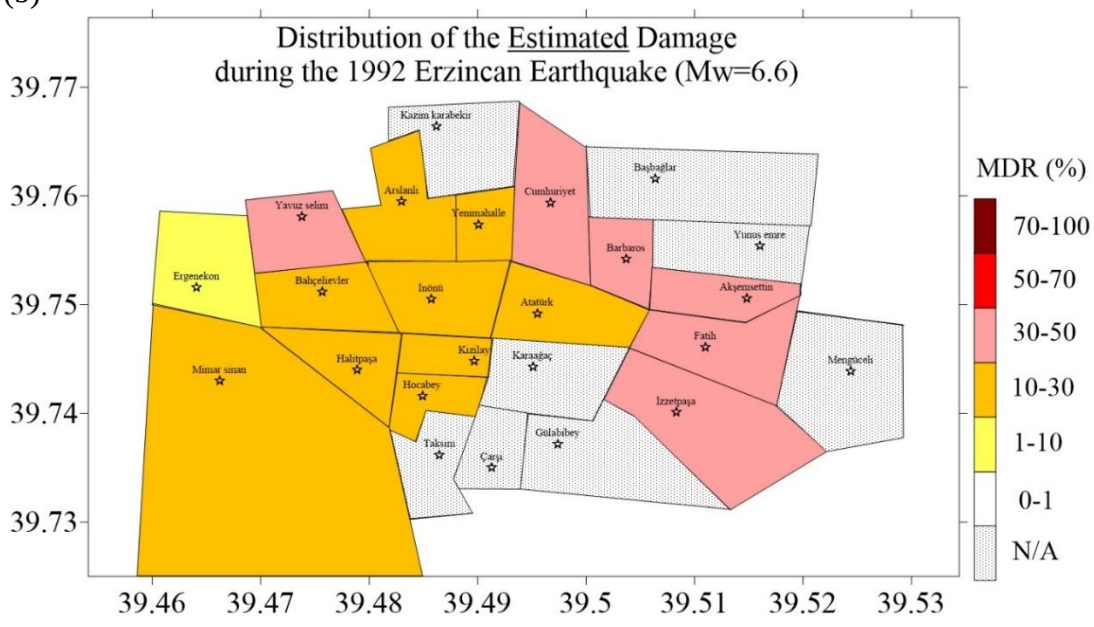

Figure 4.39 Spatial distribution of the (a) observed and (b) estimated MDRs in the Erzincan region for the 1992 Erzincan earthquake

4.6.2.2 Estimated Damage for Potential Earthquakes

The objective of this section is to anticipate the potential seismic damage for the scenario events of Mw=5.0, 5.5, 6.0, 6.5, 7.0, and 7.5. Tables 4.10 and 4.11 summarize the results of PGA and PGV for the scenario events at the selected residential areas, respectively. Figures 4.40-4.45 illustrate the spatial distribution of PGA and PGV for all scenarios in the dıstrıct centers. DPMs for all building stock and scenario events are constructed using these values as input ground motions. The estimated MDRs with DEA3 are listed in Table 4.12. Figures 4.40.c-4.45.c show the spatial distribution of damage in terms of MDRs for the scenario events. The results of Table 4.12 reveal that under the scenario events of Mw=5.0, 5.5, and 6.0 all of the residential areas exhibit none to light damage levels (0%<=MDR<=10%). The results for the scenario event of Mw=6.5 demonstrate that almost 80% of the residential areas are subjected to moderate damage (10%<=MDR<=50%) whereas the remaining 20% are expected to experience light damage (1%<=MDR<=10%). The results for the scenario event of Mw=7.0 reveal that six of the residential areas experience severe damage (50%<=MDR<=100%). However, the remaining buildings fall into the moderate damage state (10%<=MDR<=50%). Finally, the results corresponding to the scenario event with Mw=7.5 show that all of the residential areas are expected to suffer severe damage as anticipated. In summary, the Mw=6.5 scenario is a threshold event in terms of structural damage for the case study presented herein. This finding also explains the widespread damages observed during the 1992 event with Mw=6.6. Considering the anticipated damage levels in larger events, further investigations (detailed screening, more complex modeling, strengthening and etc.) are required in the study area.

Table 4.10 Estimated PGA values for all scenario earthquakes

District	Latitude (°)	Longitude (°)	PGA (g)					
			Mw=5.0	Mw=5.5	Mw=6.0	Mw=6.5	Mw=7.0	Mw=7.5
İnönü	39.7505	39.4857	0.03	0.1	0.15	0.49	1.06	3.05
İzzetpaşa	39.7401	39.5083	0.03	0.12	0.17	0.37	0.82	1.05
Akşemsettin	39.7506	39.5148	0.04	0.14	0.25	0.55	1.05	2.13
Arslanli	39.7595	39.483	0.03	0.08	0.15	0.4	1.03	1.98
Atatürk	39.7492	39.4955	0.05	0.1	0.25	0.45	0.98	2.52
Bahçelievler	39.7512	39.4757	0.03	0.08	0.11	0.34	1.06	1.45
Barbaros	39.7542	39.5037	0.05	0.13	0.31	0.54	0.9	2.02
Cumhuriyet	39.7594	39.4967	0.04	0.07	0.19	0.37	0.84	1.55
Ergenekon	39.7516	39.4641	0.02	0.06	0.15	0.38	0.96	1.07
Halitpaşa	39.744	39.4789	0.04	0.06	0.16	0.42	0.85	2.28
Hocabey	39.7416	39.4849	0.05	0.1	0.26	0.39	0.68	2.34
Kizilay	39.7448	39.4897	0.05	0.08	0.19	0.34	0.84	1.95
Mimar Sinan	39.743	39.4662	0.03	0.09	0.12	0.31	0.86	1.33
Yavuz Selim	39.7581	39.4738	0.03	0.09	0.12	0.26	0.94	1.2
Yenimahalle	39.7574	39.4901	0.04	0.09	0.22	0.41	0.87	1.67
Fatih	39.7461	39.511	0.03	0.08	0.23	0.39	1.21	1.53

Table 4.11 Estimated PGV values for all scenario earthquakes

District	Latitude (°)	Longitude (°)	PGV (cm/s)					
			Mw=5.0	Mw=5.5	Mw=6.0	Mw=6.5	Mw=7.0	Mw=7.5
İnönü	39.7505	39.4857	1.09	6.37	8.97	25.76	65.84	97.02
İzzetpaşa	39.7401	39.5083	1.37	7.58	13.97	30.99	59.43	110.4
Akşemsettin	39.7506	39.5148	1.61	4.67	14.57	28.15	55.42	127.6
Arslanli	39.7595	39.483	1.4	4.84	8.93	23.92	39.62	111.42
Atatürk	39.7492	39.4955	1.82	5.03	10.04	28.68	58.37	121.09
Bahçelievler	39.7512	39.4757	1.12	5.36	12.32	28.4	61.55	86.78
Barbaros	39.7542	39.5037	2.23	4.67	14.24	32.24	62.99	96.56
Cumhuriyet	39.7594	39.4967	1.11	3.35	9.32	35.47	42.84	55.48
Ergenekon	39.7516	39.4641	1.69	4.76	12.86	35.19	102.91	88.39
Halitpaşa	39.744	39.4789	1.37	3.16	8.19	17.05	50.78	111.29
Hocabey	39.7416	39.4849	1.8	2.85	10.66	21.31	42.33	119.35
Kizilay	39.7448	39.4897	2.08	5.61	14.07	34.77	52.91	109.44
Mimar Sinan	39.743	39.4662	2.7	4.55	7.21	26.07	53.53	88.19
Yavuz Selim	39.7581	39.4738	1.99	6.51	8.81	34.99	101.7	88.06
Yenimahalle	39.7574	39.4901	1.61	6.67	9.83	34.86	38.34	106.58
Fatih	39.7461	39.511	2.08	4.45	12.87	42.68	95.1	116.44

Table 4.12 Estimated MDRs for all scenario earthquakes (DEA3)

District	Latitude (°)	Longitude (°)	MDR (%)					
			Mw=5.0	Mw=5.5	Mw=6.0	Mw=6.5	Mw=7.0	Mw=7.5
İnönü	39.7505	39.4857	0.09	1.02	2.39	19.57	55.46	80.14
İzzetpaşa	39.7401	39.5083	0.04	1.08	2.75	14.79	52.14	67.35
Akşemsettin	39.7506	39.5148	0.09	1.51	5.6	28.91	61.19	82.03
Arslanli	39.7595	39.483	0.09	0.77	3.3	17.67	43	82.93
Atatürk	39.7492	39.4955	0.2	0.81	5.69	17.29	44.64	81.25
Bahçelievler	39.7512	39.4757	0.08	0.59	1.68	10.99	45.29	66.47
Barbaros	39.7542	39.5037	0.25	1.37	8.98	24.16	46	75.29
Cumhuriyet	39.7594	39.4967	0.16	0.48	3.27	13.02	41.13	62.94
Ergenekon	39.7516	39.4641	0.01	0.38	2.51	9.71	69.36	59.98
Halitpaşa	39.744	39.4789	0.14	0.4	2.61	19.23	48.65	83.75
Hocabey	39.7416	39.4849	0.22	0.78	7.03	15.58	37.28	83.9
Kizilay	39.7448	39.4897	0.16	0.38	2.21	8.89	41.74	82.38
Mimar Sinan	39.743	39.4662	0.07	0.36	0.86	5.57	28.17	60.31
Yavuz Selim	39.7581	39.4738	0.07	0.95	1.7	10.26	73.28	72.01
Yenimahalle	39.7574	39.4901	0.16	1	6.38	21.84	48.5	80.72
Fatih	39.7461	39.511	0.06	0.39	3.84	12.83	54.81	77.72

(a)

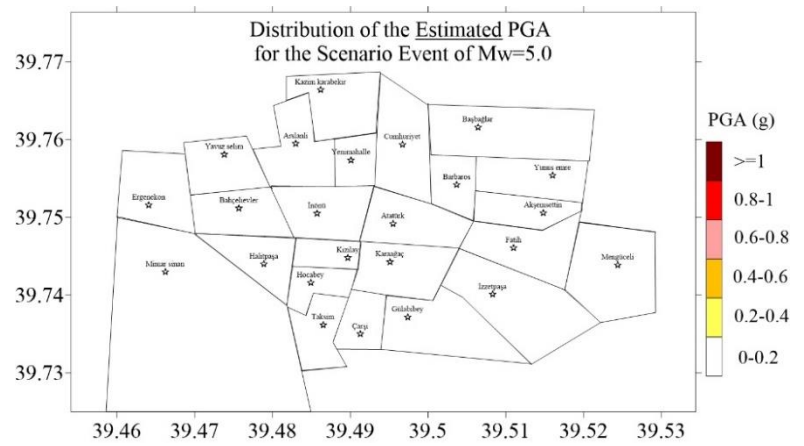

(b)

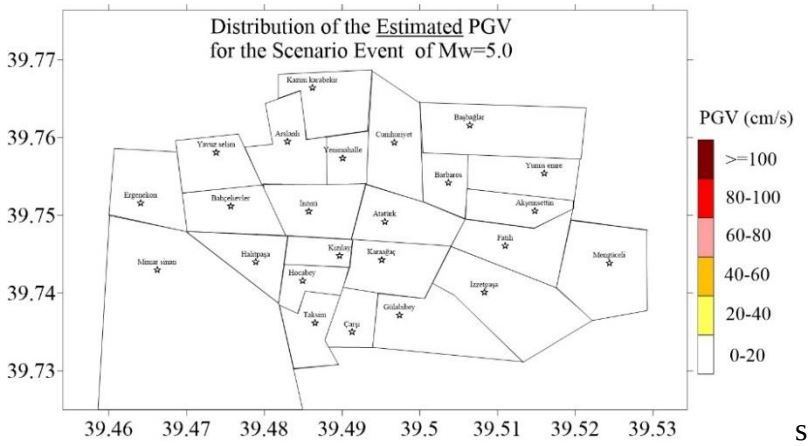

s

(c)

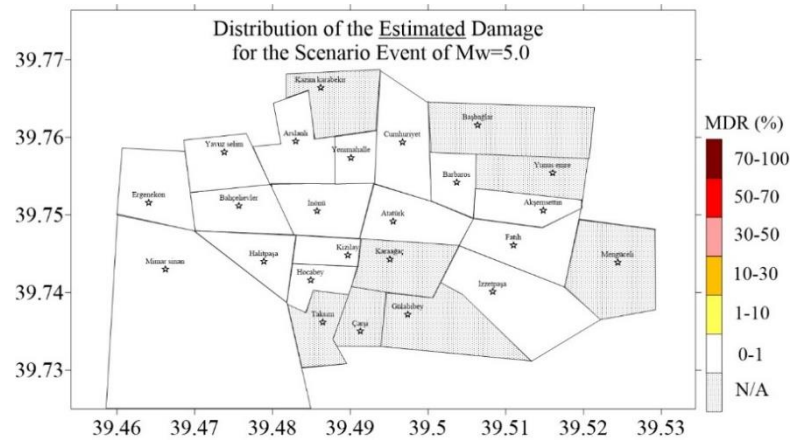

Figure 4.40 Spatial distribution of the estimated (a) PGA (b) PGV (c) MDR in the Erzincan region for scenario event of Mw=5.0

(a)

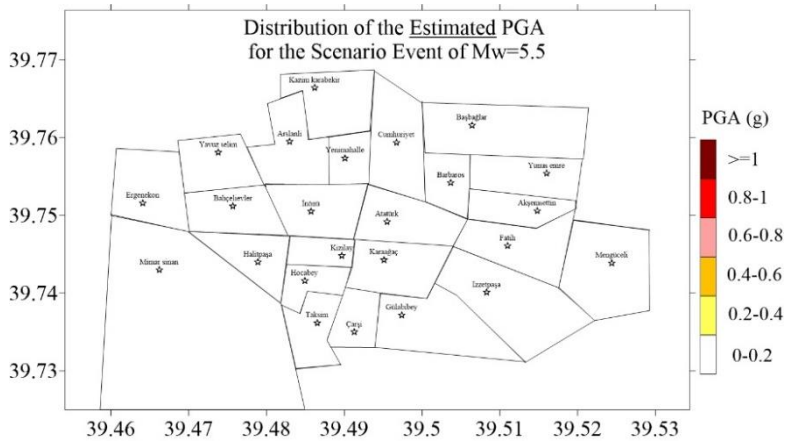

(b)

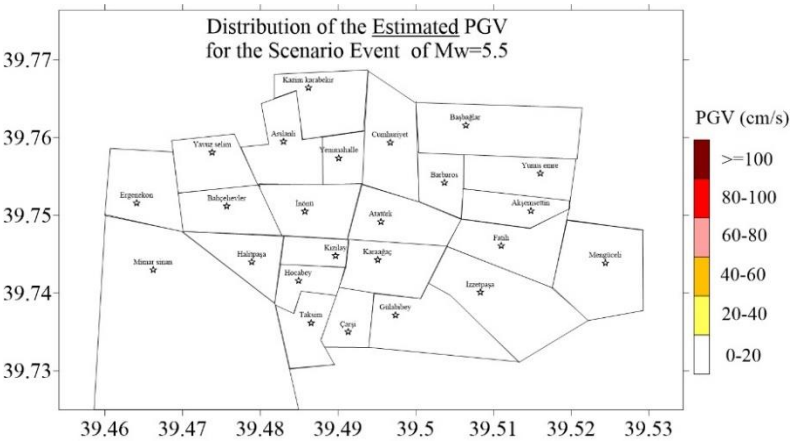

(c)

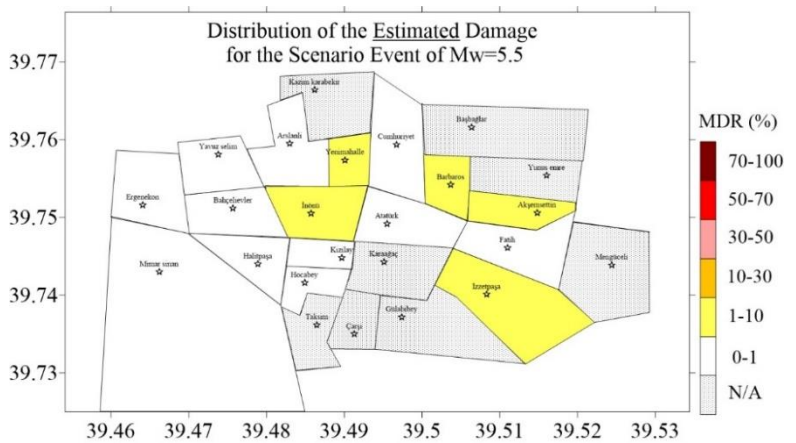

Figure 4.41 Spatial distribution of the estimated (a) PGA (b) PGV (c) MDR in the Erzincan region for scenario event of Mw=5.5

(a)

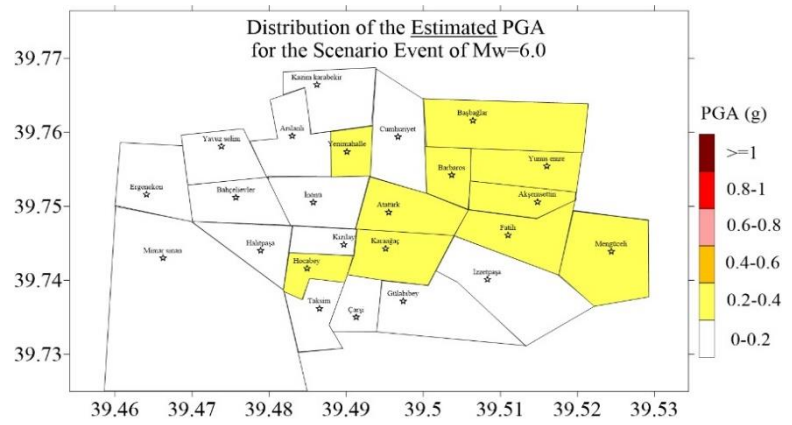

(b)

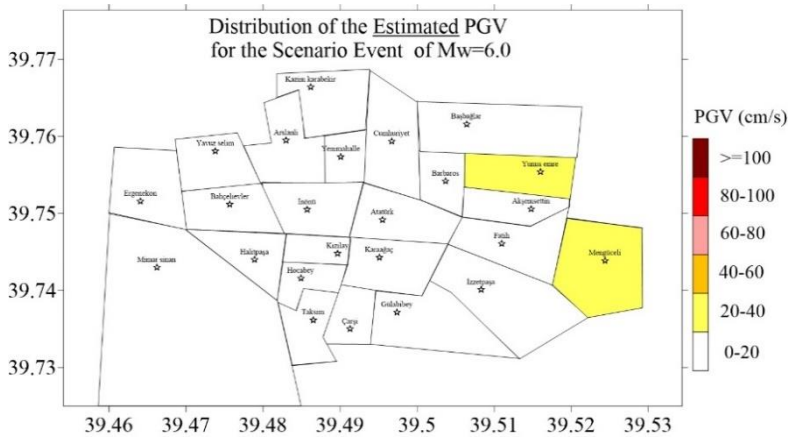

(c)

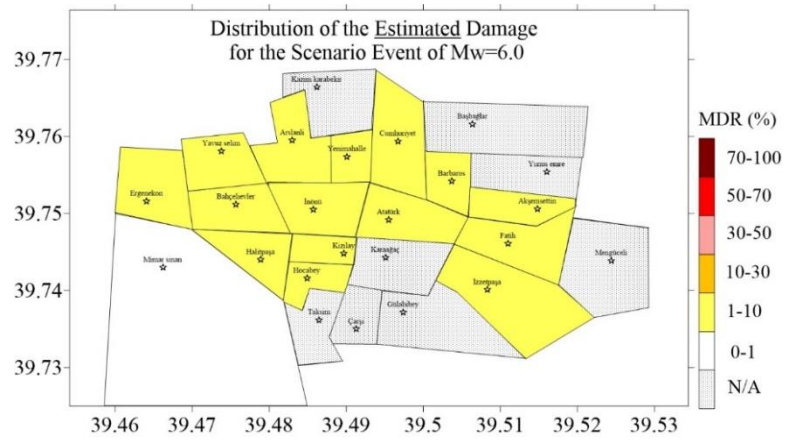

Figure 4.42 Spatial distribution of the estimated (a) PGA (b) PGV (c) MDR in the Erzincan region for scenario event of Mw=6.0

(a)

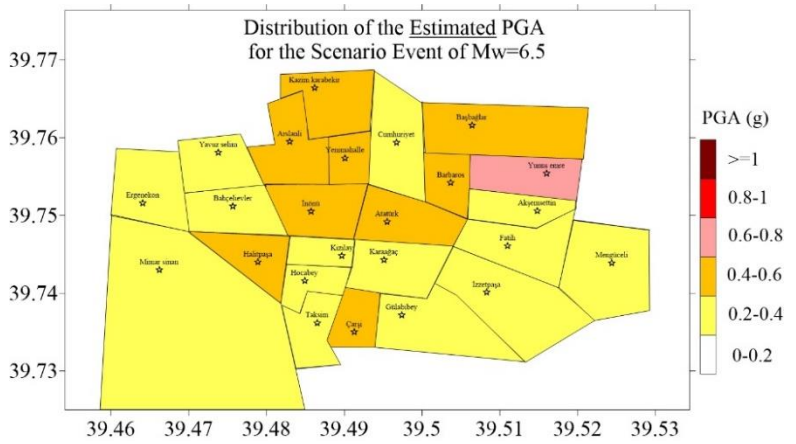

(b)

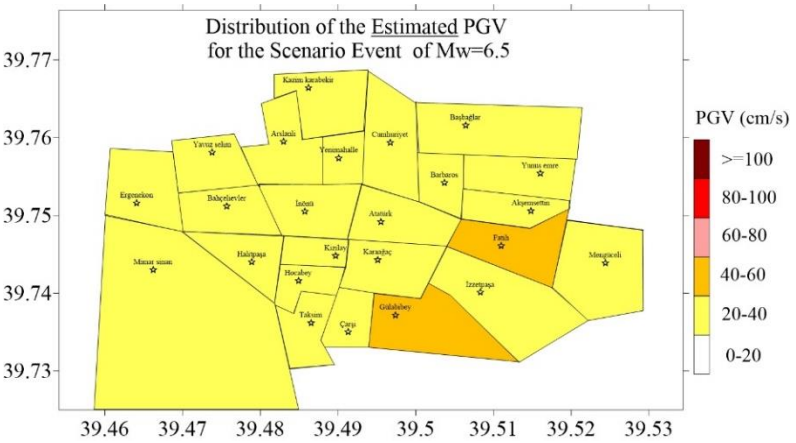

(c)

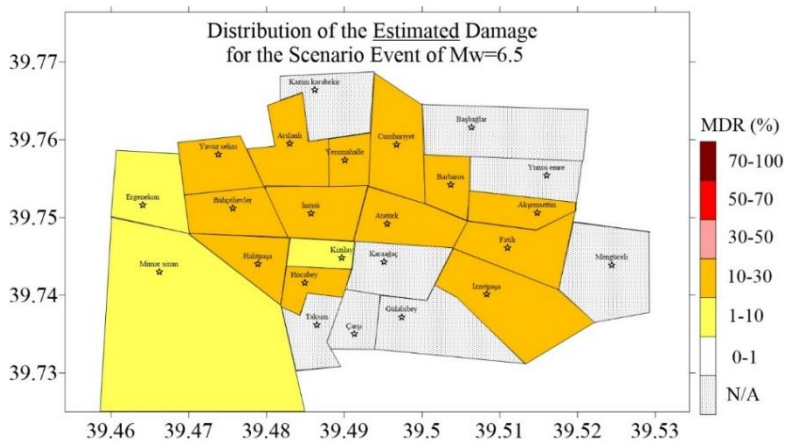

Figure 4.43 Spatial distribution of the estimated (a) PGA (b) PGV (c) MDR in the Erzincan region for scenario event of Mw=6.5

(a)

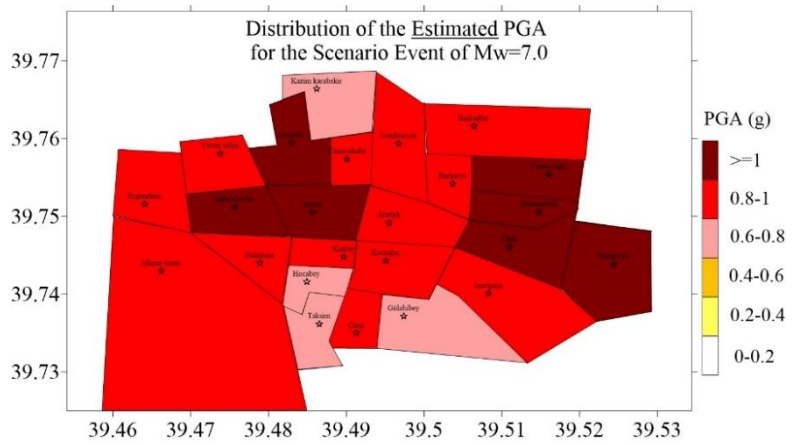

(b)

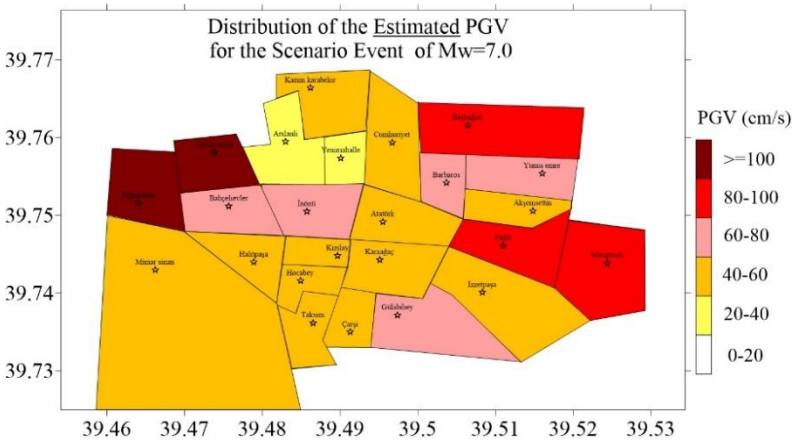

(c)

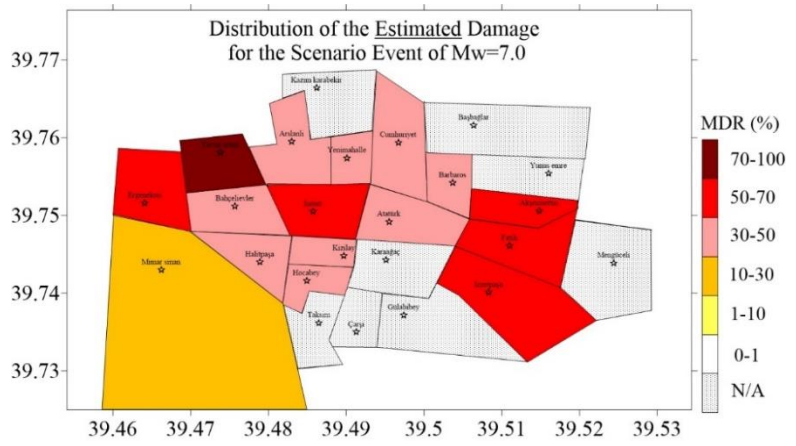

Figure 4.44 Spatial distribution of the estimated (a) PGA (b) PGV (c) MDR in the Erzincan region for scenario event of Mw=7.0

(a)

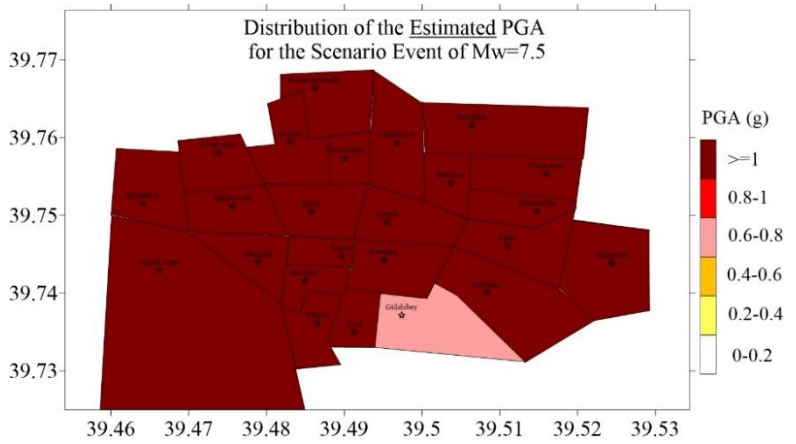

(b)

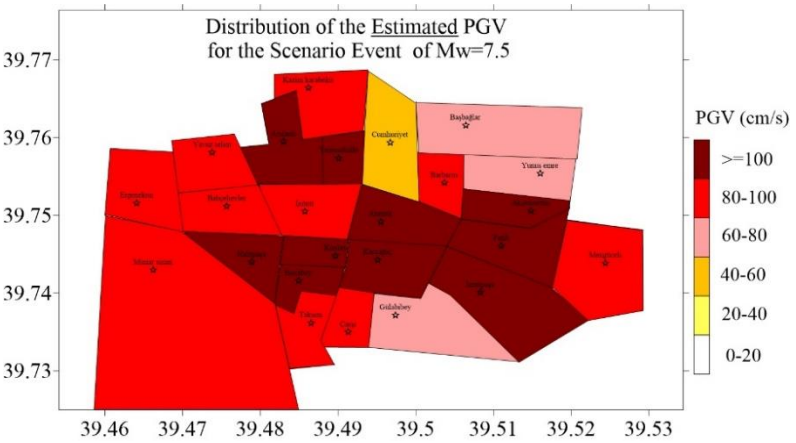

(c)

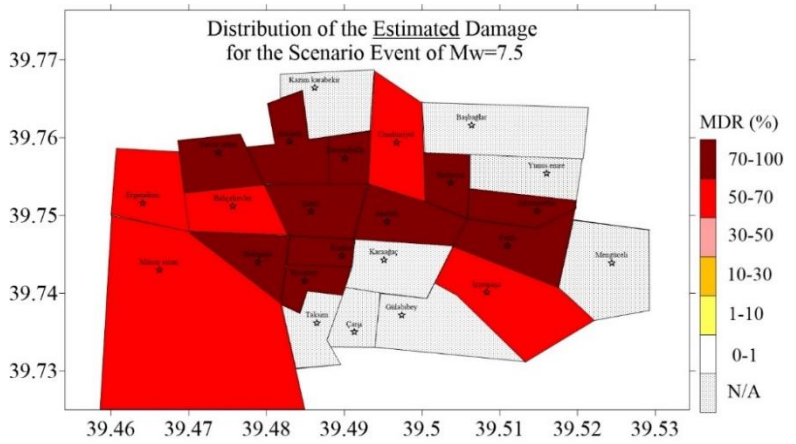

Figure 4.45 Spatial distribution of the estimated (a) PGA (b) PGV (c) MDR in the Erzincan region for scenario event of Mw=7.5

4.7 Uncertainties Involved in the Earthquake Loss Estimation

Every earthquake loss estimation study is based on a number of assumptions and simplifications leading to uncertainties in the measurements. In this study, similarly simplifications and assumptions are made to reduce the computational and data collection effort. This section briefly mentions the uncertainties involved in this study for seismic damage assessment. A quantification of such uncertainties would be a complex but valuable effort, yet it is out of scope herein.

Irrespective of the particular approach used to obtain seismic hazard, all hazard models are based on some assumptions and simplifications which introduce a major uncertainty to any earthquake loss estimation study. In this thesis, to account for the physical effects of fault process and wave propagation, the input ground motions are modeled through stochastic finite-fault methodology. The use of a ground motion simulation methodology is much more realistic than the other simplified techniques based on ground motion prediction equations. Yet, the stochastic finite-fault methodology still involves certain uncertainties related to input parameters and model simplifications such as dynamic rupture effects and lack of full wave propagation. These assumptions introduce inherent uncertainties and errors.

In this study among 123 stations, in only nine of them detailed shear wave velocity soil profiles are available. However, there is no information related to soil conditions at the other stations. Therefore, the Vs30 of the closest node is assigned to each grid point. These assumptions introduce uncertainty to the simulation process.

Next, in this thesis, the inventory database for existing building stock in Erzincan is compiled by a walk-down survey. This process naturally involves expert opinion in the field and brings in uncertainties to earthquake loss estimation. Classification of buildings into a number of specified typology classes also introduces some uncertainty to earthquake vulnerability estimation. The aim of any building classification in earthquake loss estimations is to place all buildings with comparable performance during ground shaking into a single representative group. However, this process not

only depends on the parameters influencing structural performance, but also the availability of detailed data (Coburn and Spence, 2002). In this thesis, buildings are categorized with respect to the construction materials, main load-bearing structural system, number of stories, and level of compliance with the code. Other parameters such as detailed height information or plan details are missing and this constitutes another source of uncertainty.

Another simplification corresponds to the categorization of the building damage into discrete damage states while the real seismic damage follows a continuous pattern which is a function of earthquake demand (Kircher *et al.*, 1997). This simplification is believed to be practical because representing damage states as continuous function of seismic demand or with a large number of damage states makes the quantification of damage levels practically impossible. Therefore, unlike the actual pattern of earthquake damage, in this study damage classes are considered with a finite number of damage states. Again, in this study, as a global measure of damage, MDR is used to express the spatial distribution of damage. Computation of MDR is based on CDRs which need detailed replacement information also introducing uncertainties for this study.

Another error is present within the verification process: The building data are gathered in 2013 by a walk-down survey. However, comparison of the estimated damage levels are accomplished against observed damage database gathered in 1992 after the earthquake. In addition, certain subjectivity is involved with assigning damage states for the damaged buildings in the field after the earthquake.

Given all the assumptions and subjectivities associated with the computations or observations, the proposed method involves certain inherent errors. Despite the verifications provided, this study and other loss estimations studies should always be used with care and awareness in practice.

4.8 Summary and Main Findings of Chapter 4

This section discusses the main results and findings of seismic damage assessment carried out for Erzincan using ground motion records simulated with the stochastic finite-fault methodology.

To account for regional seismicity and Turkish construction practices, seismic damage estimation of a test case in Erzincan, was performed considering both regional seismic hazard and local building data. A verification analysis was performed for the 1992 Erzincan earthquake of Mw=6.6. The effects of alternative intensity measure parameters (PGV and PGA) in loss estimations were examined. The first approach considered PGA (DEA1), the second one PGV (DEA2), and the third one used a combination of PGA as well as PGV (DEA3) for seismic loss estimation. Then, damage distribution during the past event of the 1992 Erzincan earthquake was compared with the predicted damage from these approaches. The final results in terms of the MDRs from alternative approaches resulted in negligible differences. However, the estimations from the last approach (DEA3) were still closer to the observed damage. This once again proves that damage to ductile buildings is associated with PGV while for non-ductile buildings PGA is the main damage parameter. Finally, results indicate that the proposed method effectively estimates distribution of seismic damage by considering the specific characteristics of the earthquake rupture through ground motion simulations and local building information.

After validation, damage prediction was performed to assess the distribution of seismic damage in the study area corresponding to different scenario events using DEA3. For this purpose, scenario earthquakes with six magnitude levels were assumed. The estimated damage levels in the city center for scenario earthquakes larger than Mw=6.5 revealed that Erzincan is under significant seismic threat due to its close distance from the fault system in the North as well as seismic vulnerability of the existing building stock.

Finally, earthquake loss estimation is a multidisciplinary research effort requiring various fields of expertise and as a consequence involving a large number of uncertainties. In spite of these uncertainties, based on the presented results, it is observed that stochastic finite-fault methodology is capable of modeling the seismic hazard of the respective area to assess an effective prediction of damage via simple SDOF structural models. Finally, the approach proposed herein can be implemented with care in the seismic risk assessment packages for disaster mitigation purposes for potential large events.

CHAPTER 5

APPLICATION OF SIMULATED RECORDS IN NONLINEAR TIME HISTORY ANALYSES OF MULTI- DEGREE-OF-FREEDOM STRUCTURES

5.1 Introduction

For purposes of seismic design and retrofitting of structures, it is essential to utilize reliable estimates of the seismic loads to which structures will be exposed during their lifetimes. Majority of the engineering structures are exposed to nonlinear behavior due to the changes in their physical properties during severe earthquakes. For the sake of realistic assessment of nonlinear responses, nonlinear time history analyses must be performed where full ground motion time histories are required as input. The stochastic simulations have become quite popular to produce physically-generated full time histories recently. Especially, in areas with sparse strong ground motion station networks, the practical application of the stochastic simulation methods makes their use even more common.

The key research question of interest in this Chapter is whether, on average, peak nonlinear responses of MDOF structures based on a set of simulated records are in agreement to those based on the corresponding set of observed records. The answer will help to decide whether simulated time histories can be employed to predict

inelastic responses of MDOF structures. To address this question, three case studies involving past large earthquakes are considered in this Chapter. For each case study and frame type studied, the maximum story displacement and drift ratio due to the simulated records are compared to those of the real records. Next, it is investigated whether the misfits in terms of seismological measures (such as Fourier amplitude spectrum, energy content and etc.) between the real and simulated records correspond to consistent differences in engineering demand parameters. For this purpose, novel goodness of fit criterion is defined for simulated records in terms of engineering demand parameters.

In this chapter, first, in Section 5.2 the selected frames and their physical properties are presented. In the following sections after that, simulations of observed records are performed and evaluated against the real records for each earthquake studied. Then, nonlinear structural responses to simulated records are compared with those to the real ground motions of three events. Section 5.3 presents the first case study, simulation of the 13 March 1992 Erzincan (eastern Turkey) earthquake (Mw=6.6), which is recorded at only three strong ground motion stations, using the stochastic finite-fault method. The second case study which is considered to be the 1999 Düzce earthquake (Turkey) (Mw=7.1) is presented in Section 5.4. Finally, Section 5.5 presents the third case study which is the 2009 L'Aquila (Italy) (Mw=6.3). Different than the previous case studies, simulated records of 6 April 2009 L'Aquila (Italy) earthquake (Mw=6.3) are simulated using two alternative simulation techniques: the Hybrid-Integral-Composite (HIC) method and the stochastic finite-fault method. Figure 5.1 presents the main steps of the algorithm used in this Chapter for all case studies.

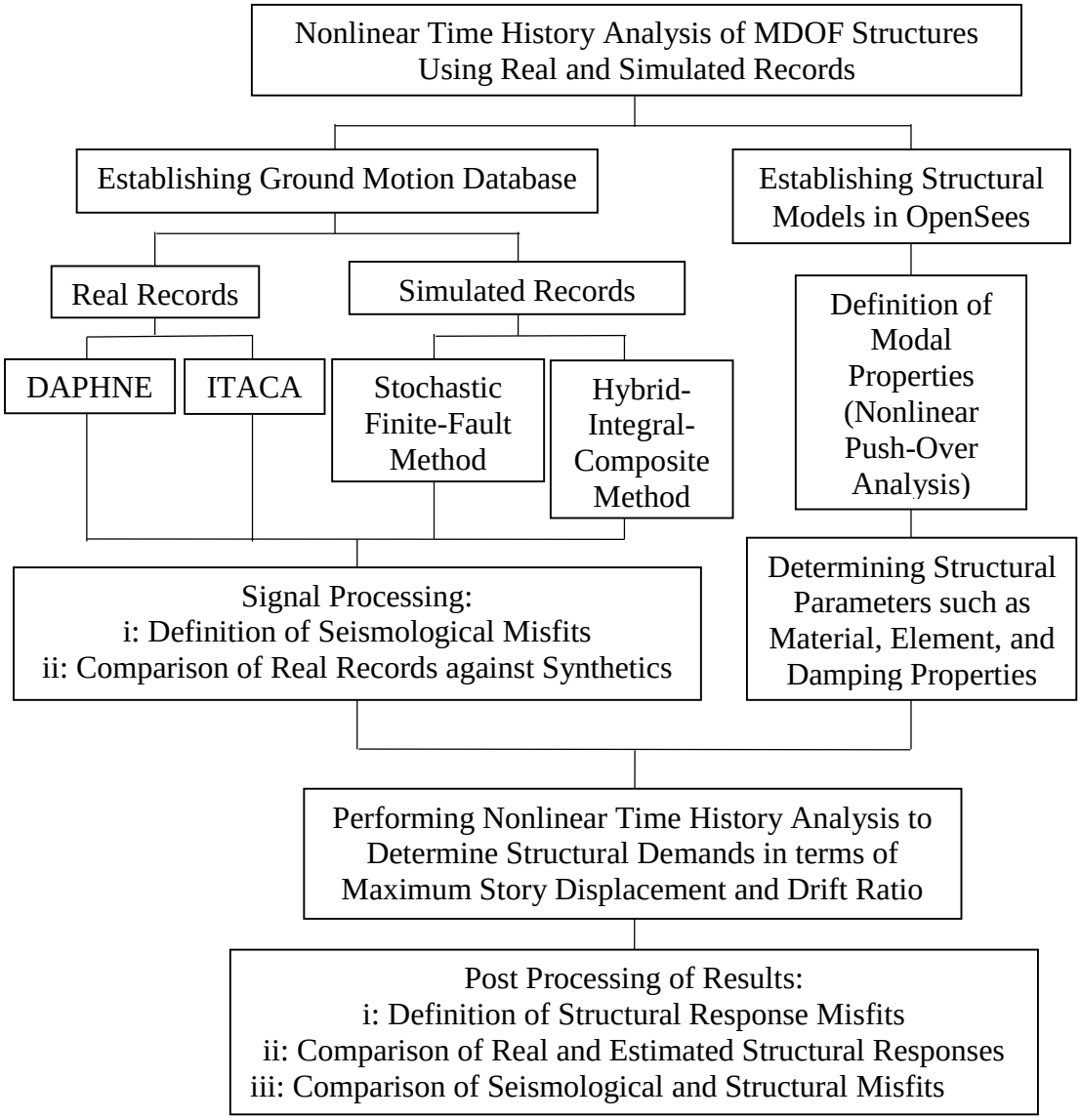

Figure 5.1 Main steps for NTHA of MDOF structures used in this study

5.2 Description of the Frame Models

In this Chapter, nine two-dimensional, regular and symmetric reinforced-concrete frames are selected to model building structures for NLTHA. This frame set is particularly selected to yield a range of fundamental periods and to represent typical RC buildings with varying number of stories and bays from worldwide. The first and second frames (F1-3S2B and F2-3S2B) are three-story-two-bay frames. The third frame (F3-3S3B) is a three-story-three-bay frame. The fourth and fifth frames (F4-4S3B and F5-4S3B) are four-story-three-bay frames. The sixth frame (F6-5S2B) is a five-story-two-bay frame whereas the seventh frame (F7-5S4B) is a five-story-four-bay frame. The eighth Frame (F8-7S3B) is a seven-story-three-bay frame and finally the ninth frame (F9-8S3B) is an eight-story-three-bay frame. Among these frames, F1-3S2B and F6-5S2B are selected from the existing structures located in Bursa city center (Turkey). F2-3S2B is the deficient form of the F1-3S2B with structural deficiencies such as minimum reinforcement ratio, smaller sectional sizes, and weak materials. F3-3S3B and F8-7S3B are designed to have sufficient strength and ductility capacities under severe earthquakes and to satisfy the requirements of the previous Turkish seismic design code (1997). F4-4S3B is designed according to the most active seismic zone (zone 1, where effective peak ground acceleration of the design spectrum is considered to be 0.4g) in the previous Turkish seismic design code (1997). Frames F5-4S3B and F7-5S4B are extracted from the Düzce damage database. F9-8S3B is designed using the 1982 Uniform Building Code in California (Kadaş, 2006; Yılmaz, 2007).

The geometric and sectional properties of the frames are provided in Appendix D while the dynamic properties of these frames are presented in Table 5.1.

Table 5.1 Total mass and fundamental period of the selected frames

Frame ID	Total Mass (t)	Fundamental Period T_1 (s)
F1-3S2B	226.50	0.4718
F2-3S2B	226.50	0.7177
F3-3S3B	153.68	0.5348
F4-4S3B	212.22	0.6925
F5-4S3B	75.30	0.4940
F6-5S2B	260.20	0.7807
F7-5S4B	166.02	0.5198
F8-7S3B	365.59	1.0521
F9-8S3B	1816.10	1.3064

To model structural elements of RC frames, nonlinear fiber-based beam-column elements are used. OpenSees has the ability of distributing plasticity throughout the element and the dynamic inelastic behavior of structural elements can be presented by a particular element type. Based on the results of a previous study by Taucer *et al.* (1991), the fiber-based beam-column element is proposed to be the most reliable and computationally efficient element type in order to model the biaxial bending and axial force that are induced to reinforced-concrete members by cycle loading. This beam-column finite element model has been widely used for 25 years to model hysteresis behavior of reinforced-concrete structural members under cyclic loading conditions.

Longitudinal steel and concrete fibers form the fiber-based beam-column element model. The force-deformation relationship of the section is attained by integration of the stress-strain relationship of the fibers. Since the nonlinear behavior of the element is derived entirely from the nonlinear stress-strain relation of the fibers, there is no need to define the nonlinear force-deformation relation of the element. This model assumes that the bending deformations are so small such that the plane sections remain plane under any deformation during loading history. In addition, the model neglects the effects of shearing and torsional deformations in the formulation of the element.

Since the total response is determined numerically by integration of the response at the control sections in the member, the total element response is very sensitive to the number of integration points. In this study, in order to estimate with confidence curvature, rotation ductility demands and plastic hinge lengths in a reinforced-concrete member, these points are selected with special care. Additionally, a single section is subdivided into an optimum number of subsections along its width and length in order to satisfy the maximum accuracy and minimum calculation time. The schematic representation of a sample fiber-based beam-column element including separate reinforcing steel along with both confined and unconfined concrete models is presented in Figure 5.2.

For all elements, Kent-Scott-park concrete model with no tensile strength (Kent and Park, 1971; Scott *et al.*, 1982) is used for modeling of both confined and unconfined concrete. This model named as Concrete01 uniaxial material in OpenSees platform, is used to construct a uniaxial Kent-Scott-Park concrete material type with degraded linear unloading/reloading stiffness based on the work of Karsan-Jirsa (1969) (Figure 5.3.a). The 28-day compressive and crushing strengths, concrete strains at maximum and crushing strengths are required as input parameters of this concrete model.

To model reinforcement of reinforced-concrete sections, a uniaxial bilinear steel model with kinematic hardening named as Steel01 uniaxial material in OpenSees platform is selected (Figure 5.3.b). For all frames, the reinforcing steel material is assumed to have the strain hardening ratio and initial elastic tangent equal to 0.005 and 200000 MPa, respectively (Kadaş, 2006). The yielding strength, however, varies with the section type. Material properties of concrete and reinforcing steel for the selected frames are listed in Appendix D.

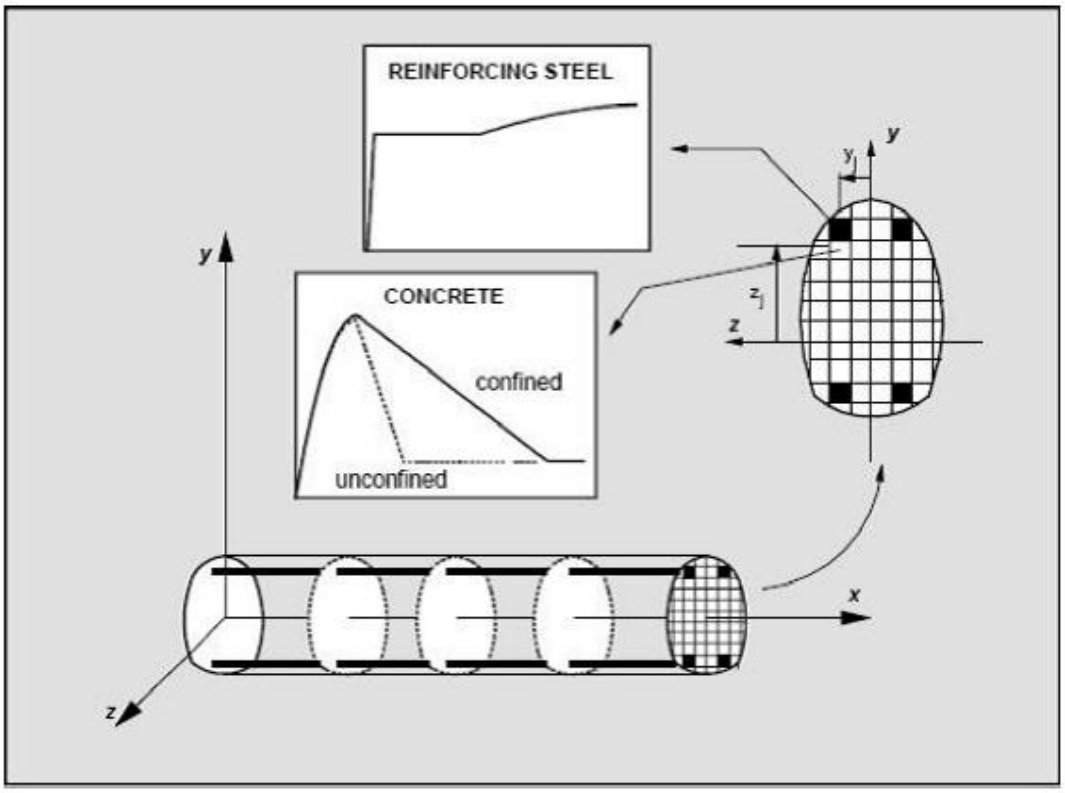

Figure 5.2 Graphical representation of a fiber element (Adopted from Taucer *et al.*, 1991)

(a)

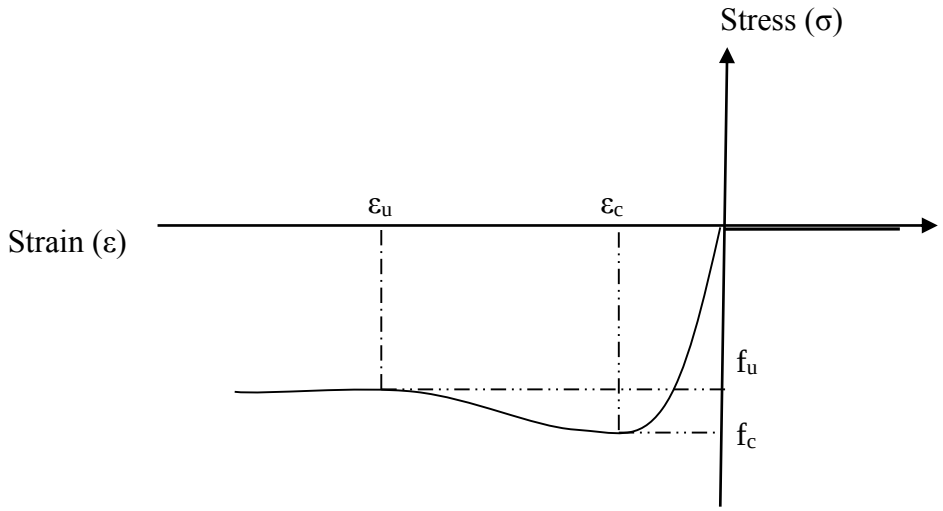

(b)

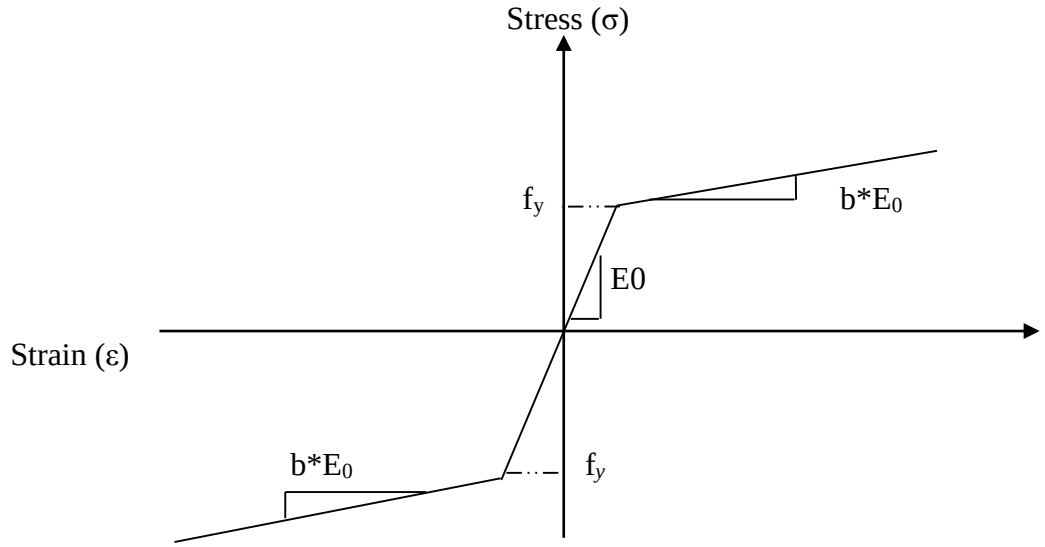

Figure 5.3 Material models for (a) steel and (b) concrete; (In this figure, f_y is the yield strength, E_0 is the initial elastic tangent, b is the strain-hardening ratio of the steel, f_c is the concrete compressive strength at 28 days, ε_c is the concrete strain at maximum strength, f_u is the concrete crushing strength, ε_u is the concrete strain at crushing strength

For all frames, the story masses, loads on beams, and modal properties are provided in Appendix D. Assuming 100% dead load and 25% live load contributions to the total mass, the eigenvalue analyses yield fundamental periods of the frames that range between 0.47 and 1.3 seconds (Table 5.1). Damping ratio of the first mode for all frames is assumed to be 5%.

Numerical modeling of the frames is carried out by the use of OPENSEES software that employs finite elements for spatial discretization where the equation of motion is as described previously in Chapter 3 in details. Two-dimensional modeling is preferred due to the symmetry of the selected buildings. To compare the nonlinear dynamic response of the frames, maximum displacement of each story is computed and stored for all case studies and each record employed.

5.3 First Case Study: Ground Motion Simulation of the 1992 Erzincan (Mw=6.6) Earthquake

5.3.1 General

As described in detail in Chapter 4, Erzincan city center experienced large events in the last century in 1939 and 1992. The reasons for considering Erzincan earthquake as one of the case studies in this Chapter are the following: first the eastern segments of NAF are much less investigated than the western segments, and second, there exists relatively sparse ground motion network in the eastern part of NAF. As mentioned before, the major objective of this chapter is to investigate the validity of synthetic records generated from stochastic finite-fault methodology in prediction of the nonlinear responses of typical reinforced-concrete buildings using detailed MDOF models. Therefore, Erzincan 1992 earthquake is selected as the first case study. The 1992 Erzincan earthquake caused more than 500 deaths along with an economic loss of 5-10 trillion Turkish Liras or approximately $13.5 million (Akinci *et al.*, 2001).

In Section 5.3.2, real acceleration time histories of Erzincan earthquake in each station including their properties are presented. In Section 5.3.3, synthetic records of Erzincan earthquake at the selected stations along with the input parameters used in simulation

process are summarized. Comparison of the simulated time histories versus real ground motion records are discussed in Section 5.3.4. Then, misfits in terms of seismological measures in between the observed and simulated records are calculated. Finally, in Section 5.3.5, results of nonlinear time history analyses with the selected frames to both real and simulated ground motion records are presented in detail.

5.3.2 Real ground motion data of the 1992 Erzincan earthquake

Erzincan is one of the most hazardous cities located in the Eastern part of Turkey within a tectonically complicated area, at the conjunction of three strike-slip faults. A pull apart basin is generated in the area with a moderate size (50*15 km^2) due to the interactions in between Ovacik and North Anatolian Faults. Alluvial deposits have considerable thickness at the center of the basin compared to the borders near the mountains. As a result, seismic risk to Erzincan as well as other cities located on the proximity of basin increases due to basin effects which magnifies ground motion amplitudes.

Until recently, Erzincan was a region with very limited number of stations to record ground motions. Unfortunately, there were only three strong ground motion stations that recorded the mainshock for the 1992 Erzincan earthquake. The map of the meizoseismal region with the epicenter, fault plane and the locations of the three stations are illustrated in Figure 5.4. The properties of the existing stations containing their names, codes, hypocentral coordinates, site classification according to National Earthquake Hazards Reduction Program (NEHRP), epicentral distances (R_{epi}: The distance from a site to the epicenter), two horizontal (North-South, NS and East-West, EW) PGA values along with PGVs are all given in Table 5.2. The raw time histories of the records of the three mentioned stations are derived from strong ground motion database of Turkey (http://daphne.deprem.gov.tr:89/2K/daphne_v4.php). All records are baseline corrected and filtered in the frequency range of 0.1-10 Hz with 4^{th} order Butterworth filter type.

Table 5.2 Information on the strong motion stations that recorded the 1992 Erzincan earthquake

Station	Code	Latitude (°)	Longitude (°)	Site Class (NEHRP)	R_{epi} (km)	PGA-EW (cm/s^2)	PGA-NS (cm/s^2)	PGV-EW (cm/s)	PGV-NS (cm/s)
Erzincan -Merkez	ERC	39.752	39.487	D	12.83	430.66	509.20	56.80	79.84
Refahiye	REF	39.899	38.768	C	76.45	75.26	66.78	3.67	3.93
Tercan	TER	39.777	40.391	D	65.62	25.56	37.90	4.30	2.86

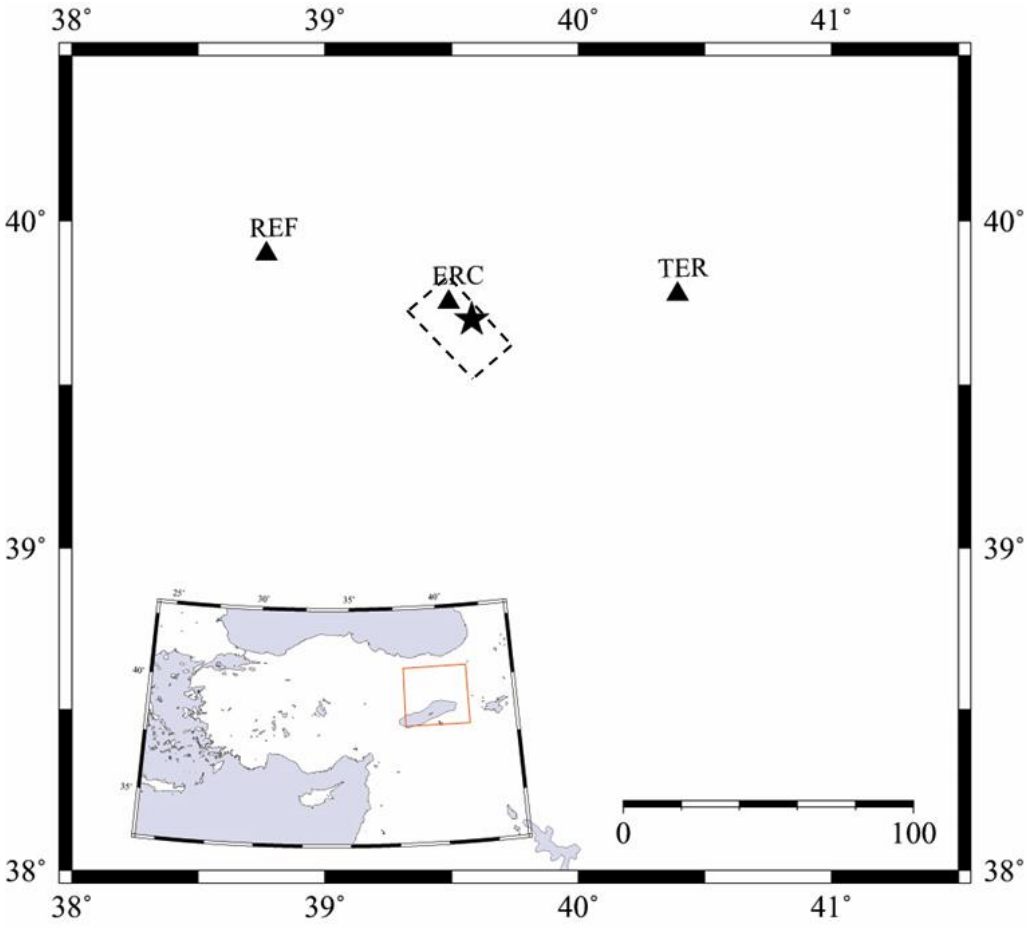

Figure 5.4 Map showing the fault plane and epicenter of the 1992 Erzincan earthquake with the locations of the stations

5.3.3 Simulated ground motion data for the 1992 Erzincan (Mw=6.6) earthquake

For simulation of the Erzincan earthquake, the validated source, path, and site parameters of Askan *et al.* (2013) are employed as inputs of EXSIM program. In that study, the verified models of the previous studies are used for source and path models. However, site effects are derived based on the existing records by the authors of the mentioned study.

5.3.3.1 Source model

Askan *et al.* (2013) recommends that among various models in the literature for source mechanism, model proposed by Bernard *et al.* (1997) results in the minimum error in terms of FAS of the real versus simulated records at observation points, especially in lower frequency content of the ground motions which is mostly affected by source parameters. The assumed source parameters, consisting of hypocenter location, hypocenter depth, depth to the top of the fault plane, fault orientation (strike and dip angles), fault plane dimensions, crustal shear wave velocity, rupture velocity, crustal density, stress drop, and finally pulsing area percentage are all stated in Table 5.3. Additionally, uniform slip distribution is employed over the fault plane through the observations by Legrand and Delouis (1999). Following Askan *et al.* (2013), in this thesis for simulation of the Erzincan earthquake, the input parameter for stress drop and pulsing area percentage is equal to 80 bars and 50%, respectively. Because these values are the optimal estimates which give the minimum overall misfit in between time histories and FAS of the real versus simulated records.

Table 5.3 Source parameters of the 1992 Erzincan earthquake

Parameter	**Value**
Moment Magnitude	6.6
Epicenter Location	39.716ºN, 39.629ºE
Hypocenter Depth	9 km
Depth to the Top of the Fault Plane	2 km
Fault Orientation	Strike=125 º; Dip=90 º
Fault Dimensions	25 km x 9 km
Sub-fault Dimensions	5 km x 3 km
Crustal Shear Wave Velocity (β)	3500 m/s
Rupture Velocity	0.8β
Crustal Density	2800 kg/m^3
Stress Drop	80 bars
Pulsing Area Percentage	50

5.3.3.2 Path model

The radiation of the seismic waves from source to the bedrock layers at a site is influenced by the path effects. Here, path model can be represented as a function which includes the contribution of three components; frequency-dependent intrinsic attenuation (expressed with the quality factor), geometric spreading, and additional duration effects due to scattering of seismic waves. For the quality factor, the model proposed by Grosser *et al.* (1998) and given as $Q = 122f^{0.68}$ is selected due to its accurate modeling of the spectral amplitudes. The geometrical spreading model proposed by Akıncı *et al.* (2001) for Erzincan region is adopted. The following piecewise functional form shows the mentioned model:

$$\begin{aligned} &R^{-1.1}, && R \leq 25\ Km \\ &R^{-0.5}, && R > 25\ Km \end{aligned} \tag{5.1}$$

For the duration effects, Herrmann (1985) gives a model as a linear function of source duration and hypocentral distance as follows:

$$T = T_0 + 0.05R \tag{5.2}$$

where T_0 is the source duration, and R is the hypocentral distance. In this thesis, to consider the effects of ascending in duration of ground motion records in Erzincan, this model is used.

5.3.3.3 Site model

Site effects can be modeled as combination of two different effects on the ground motion records: Local site amplification and high frequency decay as a result of kappa factor. Due to the lack of high quality real records at stations REF, and TER, site amplification spectrum was estimated by performing theoretical 1D site response analysis at each station for consistency instead of empirical horizontal to vertical spectra ration (HVSR) method. To do site response analysis at each station, the bedrock record was selected to be a weak motion recorded at ERC station with PGA of 0.001g during an earthquake with Mw=3.4. The site amplification factors calculated at the three stations (Figure 3 in Askan *et al.*, 2013) are used in this chapter.

In Askan *et al.* (2013), it was observed that the records of three stations have almost the same decay in high frequency portion of FAS. Therefore, a regional kappa model by considering the records of all stations was calculated. In stochastic finite-fault methodology, the zero-distance kappa value (κ_0) is used in order to eliminate the regional path attenuation effects which are taken into account through the frequency-dependent quality factor. The value for κ_0 was computed to be 0.066 based on the analyses of existing data in the region of interest (Figure 4 in Askan *et al.*, 2013).

5.3.4 Comparison of simulated and real ground motion data for the 1992 Erzincan (Mw=6.6) earthquake

After the simulations, there is a total of 1 simulated and 2 real horizontal components at every station. However, at ERC, the observed records are subjected to forward directivity effects resulting in the high amplitude and short duration pulses. To evaluate the effects of forward directivity in nonlinear responses of MDOF structures, at this station two types of synthetic records are generated: Simulated record without considering the forward directivity effects and simulated record considering the

forward directivity effects with an analytical pulse. In the original stochastic finite-fault method, the directivity effects are modeled insufficiently, yet in EXSIM platform there is an analytical solution of directivity pulses which can be superimposed onto the generated synthetic time history. It is possible to use this analytical pulse option in the validation of an observed earthquake with known information on the characteristics of the observed pulse. In this study, the parameters mentioned by Azari *et al.* (2014) are employed to simulate the pulse existing in the parallel component of the real record in addition to the generated simulated record at this station. Based on the technique introduced by Mavroeidis and Papageorgiou (2003), for generation of the pulse in the record, an analytical approach with definition of four parameters consisting of pulse amplitude (A), phase angle (ν), oscillatory character (γ), and time shift to specify the epoch of the envelope's peak (t_o) is examined. The mentioned four parameters have the values of 80, 180, 2.3, and 21.875, respectively. Then, the simulated record is combined with the generated pulse to reach the final modeled ground motion.

It should be noted that the simulated and real records are not scaled or modified by any means other than baseline corrections and filtering between 0.1 and 10 Hz with 4^{th} order Butterworth filter type. Figures 5.5-5.7 display the acceleration time histories, the corresponding Fourier amplitude spectra and elastic response spectra with 5% damping (PSA) for both real and simulated records at each station.

(a)

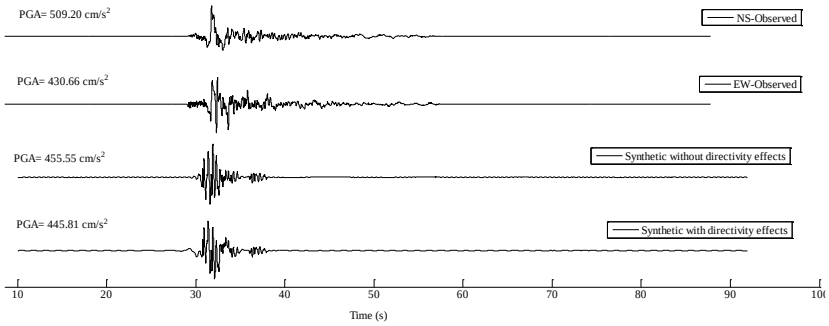

(b)

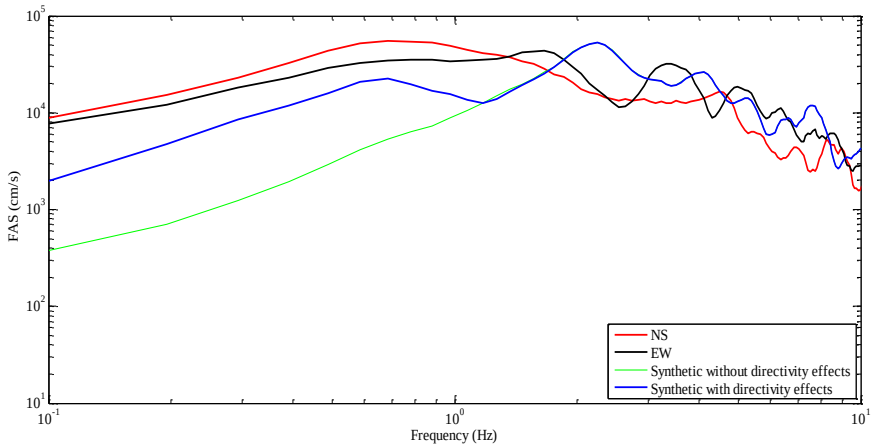

(c)

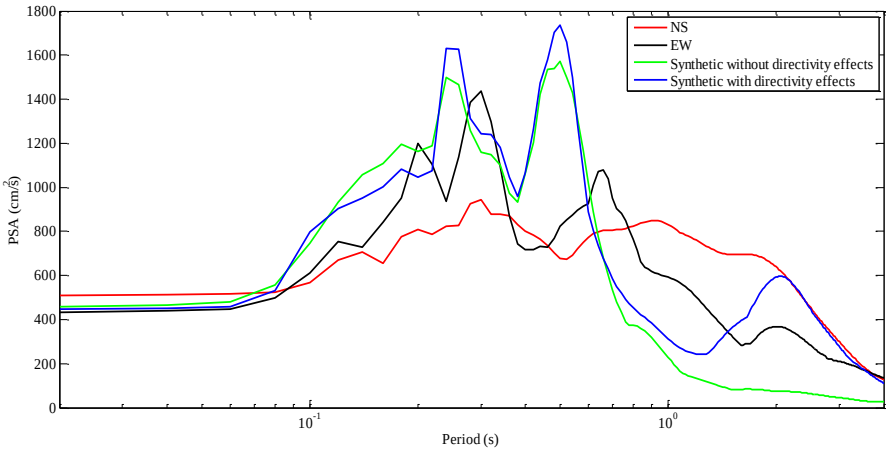

Figure 5.5 Station ERC; (a) Observed and simulated accelerograms (b) Fourier Amplitude Spectra (c) Response Spectra with 5% damping obtained for observed (NS and EW) and simulated horizontal component (Synthetic with and without directivity effects)

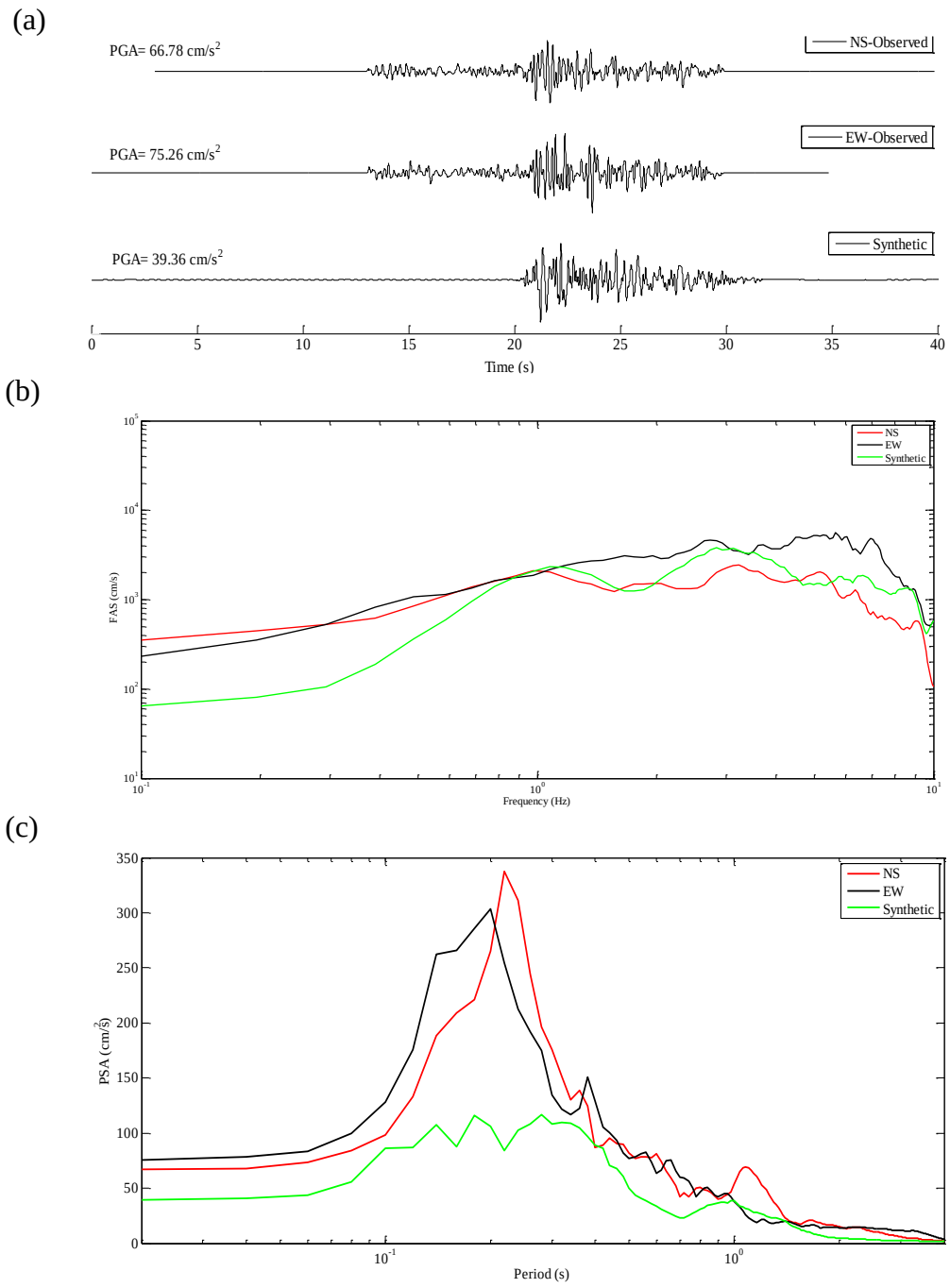

Figure 5.6 Station REF; (a) Observed and simulated accelerograms (b) Fourier Amplitude Spectra (c) Response Spectra with 5% damping obtained for observed (NS and EW) and simulated horizontal component (Synthetic)

(a)

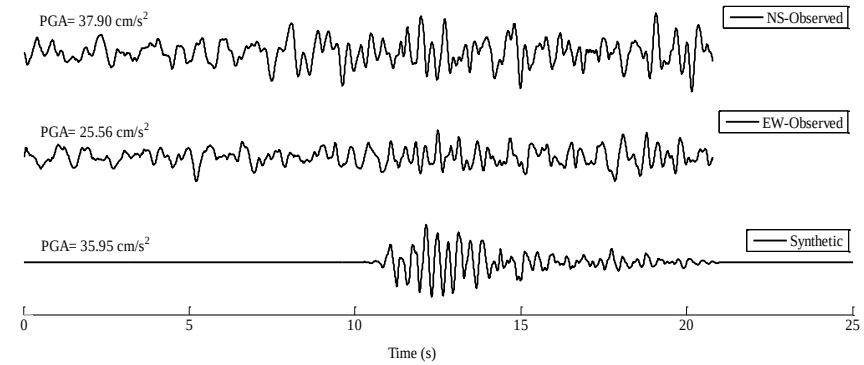

(b)

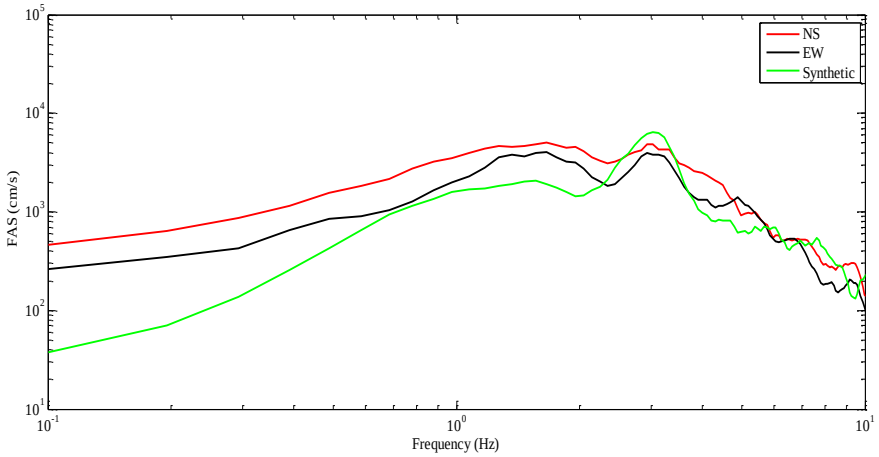

(c)

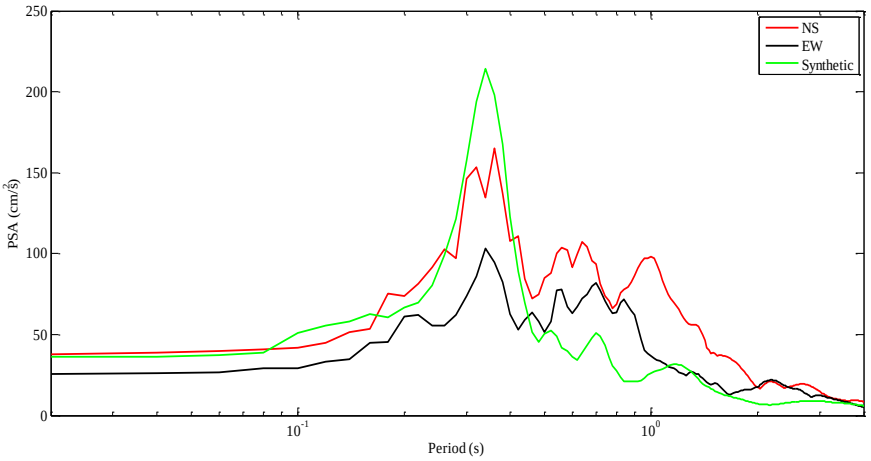

Figure 5.7 Station TER; (a) Observed and simulated accelerograms (b) Fourier Amplitude Spectra (c) Response Spectra with 5% damping obtained for observed (NS and EW) and simulated horizontal component (Synthetic)

Comparison of the results presented in Figure 5.5 for station ERC demonstrates that there is a close match between the real and synthetic Fourier amplitude spectra for higher frequencies (or lower periods of RS) regardless of the directivity effects. Due to existence of forward directivity effects at station ERC, the real records include larger amplitudes with shorter durations. Therefore, as it is expected, at the lower frequencies of FAS which mainly are influenced by source model, the results corresponding to two types of simulated records are different. The first type of simulated records which ignores directivity effects, underestimates the lower frequencies of FAS (or higher periods of RS). In contrast, for the second type when the pulse is simulated using the analytical model, a specific improvement is observed in the match of spectral amplitudes corresponding to lower frequencies. Figure 5.6 presents that, at station REF, NS component of FAS matches closely with the synthetic spectra for frequencies higher than 1 Hz. At the same station FAS of the EW component is higher than both NS and simulated spectral amplitudes for the same frequencies. When the synthetic RS at station REF is considered, for periods less than 1 s underestimation of the observed responses is observed. Finally, the results corresponding to station TER as presented in Figure 5.7 reveals that there is a good agreement in between spectral amplitudes of the real and simulated records in both EW and NS directions for frequencies higher than 1 Hz. However, in both of these stations (REF and TER) amplitudes of response spectra are slightly underestimated with simulated records at frequencies less than 1 Hz.

In this thesis, in order to quantify the misfit between observed and simulated ground motions, different types of error functions are utilized. In total, seven different types of misfits are defined. The first two types of misfits are frequency/period-dependent. These misfits are quantified (considering the fundamental periods of each frame) between the simulated and real records in terms of Fast Fourier amplitude spectra and elastic Response Spectra (RS) with 5% damping. To obtain the frequency/period-dependent misfits, first, discrete errors as a function of frequency are computed by dividing simulated FAS/RS to observed FAS/RS at each frequency. Then, these discrete values are averaged over a particular frequency/period band defined for each

frame to obtain the final misfits. For each frame, a period-band is considered separately with respect to the fundamental period of that frame as follows: The lower value of the period-band is selected with respect to the highest modal frequency of the considered frame (20 percent of the first fundamental period), and the upper period band is selected to consider the nonlinearity effects resulting in an increase of the period of each frame after dynamic analysis (120 percent of the first fundamental period). From this point onwards, the frequency/period-dependent misfits are named as Spectral Seismological (SS) misfits. These SS misfits in frequency/period domain for both FAS and RS are defined as follows:

$$Misfit_{FAS} = \frac{1}{n_f}\sum_{f=1}^{n_f}\left|log\frac{FAS_{syn}(f)}{FAS_{real}(f)}\right| \tag{5.3}$$

$$Misfit_{RS} = \frac{1}{n_T}\sum_{T=1}^{n_T}\left|log\frac{RS_{syn}(T)}{RS_{real}(T)}\right| \tag{5.4}$$

where n_f and n_T is the number of discrete frequencies and periods in the selected period-band (for each frame) used in the FAS and RS computations, respectively. $FAS_{syn}(f)$ and $FAS_{real}(f)$ corresponds to the synthetic and observed Fourier amplitude at frequency f, respecetively. $RS_{syn}(T)$ and $RS_{real}(T)$ is the synthetic and observed response spectral amplitude in period T, respectively.

The other five types of misfits used in this study compute the difference between the simulated and real records in terms of other major seismological parameters, representing intensity level, duration, and energy content of ground motion records. For this purpose, following parameters are selected: *PGA*, Significant Duration (t_{eff}), Arias Intensity (I_a), Cumulative Absolute Velocity (*CAV)*, and Housner Intensity (*HI).* From this point onwards, the misfits for these parameters are named as Non-Spectral Seismological (NSS) misfits.

First, PGA which represents a significant proportion of relatively high frequencies, is considered to define a single intensity of each ground motion record.

Then, t_{eff} is considered to take into account the duration content of a record. It is defined as the time interval between the 5% and 95% of the accumulated Arias intensity. I_a is calculated as follows:

$$I_a = \frac{\pi}{2g} \int_0^{T_d} a(t)^2 \, dt \tag{5.5}$$

where $a(t)$ is ground motion acceleration at time t and T_d is the total duration of the record.

Next, *CAV* (EPRI, 1988) and *HI* (Housner, 1952) are calculated for each record as follows:

$$CAV = \int_0^{T_d} |a(t)| dt \tag{5.6}$$

$$HI = \int_{0.1}^{2.5} PSV(\xi = 0.05, T) \, dT \tag{5.7}$$

where $|a(t)|$ is the absolute value of the acceleration time series at time *t*, T_d is the total duration of the record, *PSV* is the pseudo-velocity spectrum, and ξ is the viscous damping ratio.

Finally, the NSS misfits in terms of *PGA*, t_{eff}, I_a, *CAV*, or *HI* values are defined as follows:

$$Misfit_R = \left| \frac{R_{syn}}{R_{real}} \right| - 1 \tag{5.8}$$

where R_{syn} and R_{real} is the synthetic and real responses in terms of *PGA*, t_{eff}, I_a, *CAV*, or *HI* values, respectively. It must be noted that the geometric mean of the corresponding parameters computed from the two horizontal components is used in the misfit computations. Tables 5.4-5.6 list all misfits obtained at the stations.

Table 5.4 SS misfits in terms of fast Fourier amplitude spectra ($Misfit_{FAS}$) for real and simulated data at the stations for the 1992 Erzincan earthquake

Frame ID	Station			
	ERC-without directivity effects	ERC-with directivity effects	REF	TER
F1-3S2B	0.6235	0.4121	0.5164	0.5907
F2-3S2B	0.8967	0.3391	0.5111	0.7120
F3-3S3B	0.7083	0.3603	0.5024	0.6421
F4-4S3B	0.8360	0.3292	0.4984	0.7038
F5-4S3B	0.5947	0.4295	0.4864	0.5652
F6-5S2B	0.9439	0.3516	0.5438	0.7392
F7-5S4B	0.6506	0.3793	0.5078	0.6138
F8-7S3B	1.2179	0.3951	0.6674	0.7782
F9-8S3B	1.3880	0.4703	0.7463	0.7329

Table 5.5 SS misfits in terms of response spectra ($Misfit_{RS}$) for real and simulated data at the stations for the 1992 Erzincan earthquake

Frame ID	Station			
	ERC-without directivity effects	ERC-with directivity effects	REF	TER
F1-3S2B	0.3898	0.4088	0.5254	0.3566
F2-3S2B	0.4516	0.4167	0.5834	0.5397
F3-3S3B	0.3638	0.3763	0.5652	0.4252
F4-4S3B	0.4359	0.4081	0.5984	0.4984
F5-4S3B	0.3874	0.4024	0.5342	0.3745
F6-5S2B	0.4916	0.4422	0.5368	0.6118
F7-5S4B	0.3699	0.3809	0.5533	0.4096
F8-7S3B	0.7657	0.5817	0.4725	0.6146
F9-8S3B	0.9791	0.5672	0.3957	0.5832

Table 5.6 NSS misfits for real and simulated data at the stations for the 1992 Erzincan earthquake

Station	**Misfit** $_{PGA}$	**Misfit** $_{teff}$	**Misfit** $_{Ia}$	**Misfit** $_{CAV}$	**Misfit** $_{HI}$
ERC-without directivity effects	-0.0272	-0.7097	-0.1566	-0.4231	-0.6493
ERC-with directivity effects	-0.0480	-0.7128	0.1324	-0.2473	-0.0556
REF	-0.4448	-0.3606	-0.7151	-0.5344	-0.4338
TER	0.1551	-0.7013	-0.4406	-0.5476	-0.4455

Tables 5.4 and 5.5 demonstrate that at station ERC, by simulating the directivity effects with an analytical model, SS misfits in terms of FAS or RS become smaller than those for the simulated record without considering the directivity effects. This observation is particularly evident for frames with higher fundamental periods. The seismic responses of long-period engineering structures are influenced by directivity effects in ground motion records. Therefore, it is essential to model reliable directivity effects when the seismic responses of structures with higher fundamental periods are of concern. For the other two stations, the SS misfits are mostly close to each other regardless of the frame type. Although the frequency/period-dependent misfits reveal a close match in all three stations for both real and simulated records, the results for NSS misfits differ. The statistical values listed in Table 5.6 show that at stations ERC and TER, both real and simulated records have almost same PGA levels. However, simulated records have smaller significant duration, Arias intensity, cumulative absolute velocity, and Housner intensity compared to the real records. Finally, at station REF, all estimated parameters in terms of duration, energy, and intensity values corresponding to the simulated record are less than those of the observed record.

As it is mentioned before, Erzincan is influenced by alluvial basin effects; therefore, long amplitude surface waves with longer duration are inherent in real records. However, stochastic method focuses on simulation of shear wave portion of ground motions. Thus, the duration of simulated records is mostly shorter when compared to

real ones. In order to have a better estimation of duration content of real records, regional duration models including the complexity of the wave propagation effects must be used in stochastic models.

Next, the nonlinear responses of the selected frame buildings are assessed due to the both real and simulated ground motion datasets.

5.3.5 Comparison of dynamic responses of the buildings to observed and simulated records for the 1992 Erzincan earthquake

The fundamental purpose of this part is to examine whether the nonlinear responses of MDOF building structures to simulated records are consistent with the "real" responses (which are defined as the responses from the corresponding real records). Another essential question of interest is whether the measured seismological misfits are consistent with the nonlinear response misfits. To investigate this, a novel goodness of fit criterion for synthetic ground motion records in terms of Nonlinear Response (NR) under real and simulated motions is defined. The NR misfit is defined as follows:

$$Misfit_{NR} = \frac{1}{n_s}\sum_{s=1}^{n_s}\left|log\frac{NR_{syn}(s)}{NR_{real}(s)}\right| \quad (5.9)$$

where n_s is the total number of stories in the frames. $NR_{syn}(s)$ and $NR_{real}(s)$ is the nonlinear responses of each frame at story level s subjected to synthetic and real records, respectively.

Initially, to investigate the differences in seismic responses of reinforced-concrete frame structures under real and simulated records, maximum displacements and drift ratios are calculated at each story level for all nine buildings. The results are displayed in Figures 5.8-5.16. In addition, geometric means of the real top story displacements in EW and NS directions along with the ratio of the top story displacements computed from simulated records with respect to the corresponding real ones are listed in Table 5.7. The pushover analyses of the frames and comparison of the capacity curves with

the results of NLTHA is presented in Appendix E.1. Next, Table 5.8 presents the nonlinear response misfits calculated using Equation 5.9 for all frames.

(a)

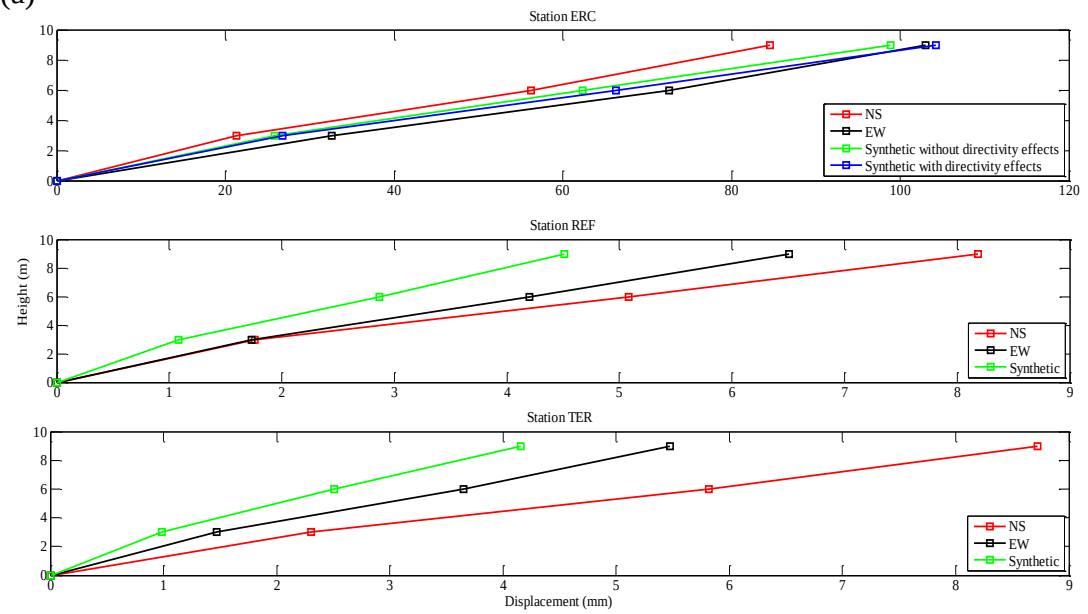

(b)

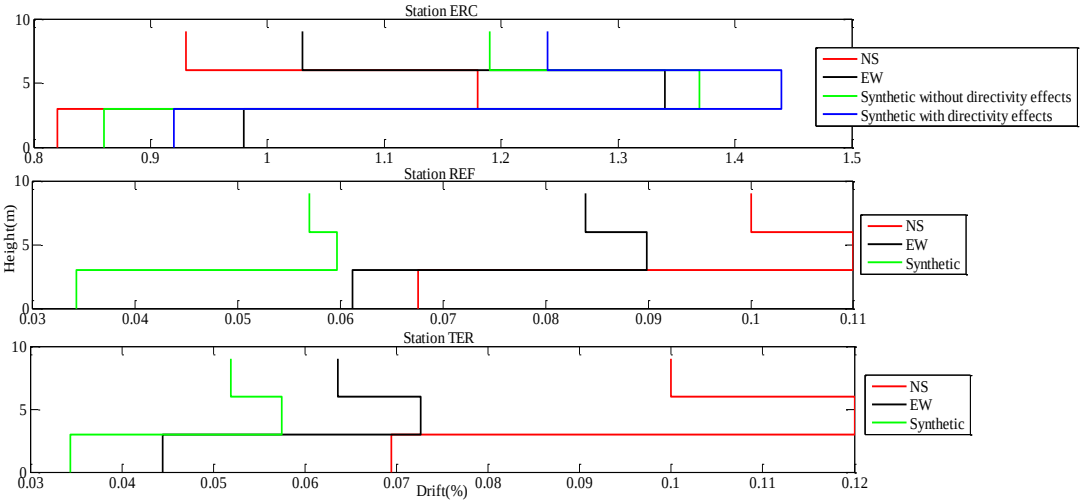

Figure 5.8 Distribution of (a) maximum story displacements and (b) maximum drift ratios due to the real and simulated records of Erzincan Earthquake – F1-3S2B

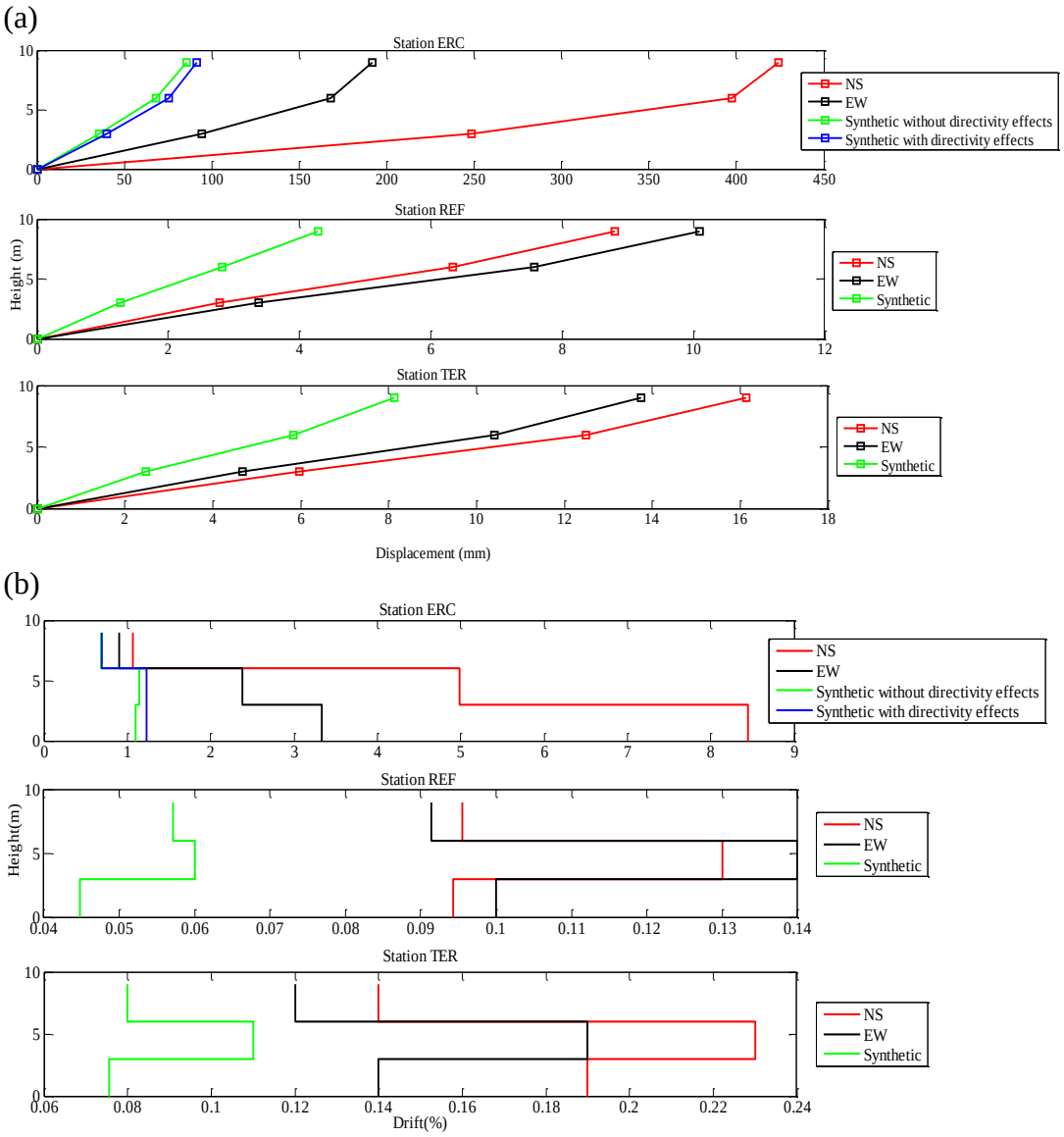

Figure 5.9 Distribution of (a) maximum story displacements and (b) maximum drift ratios due to the real and simulated records of Erzincan Earthquake – F2-3S2B

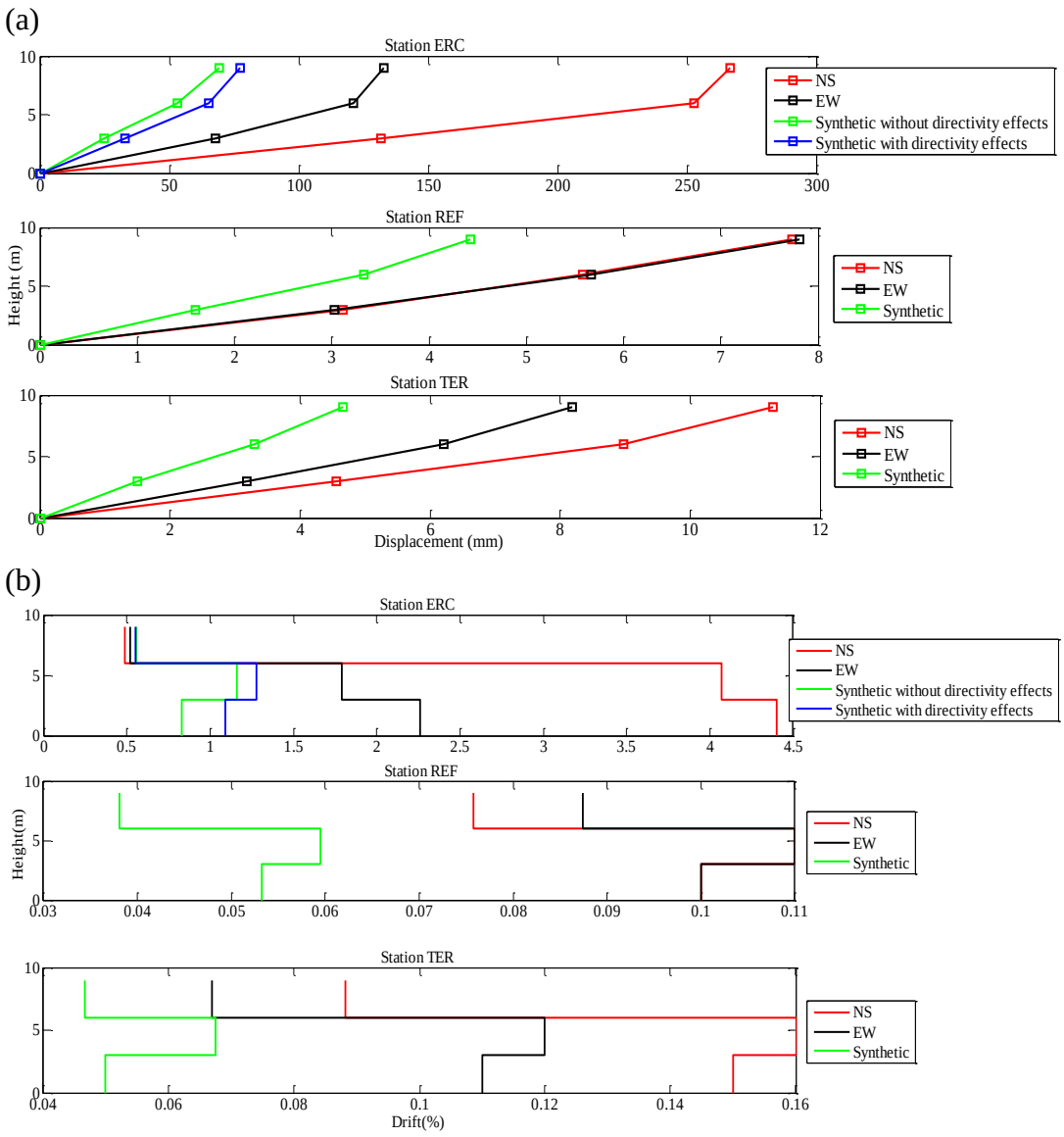

Figure 5.10 Distribution of (a) maximum story displacements and (b) maximum drift ratios due to the real and simulated records of Erzincan Earthquake – F3-3S3B

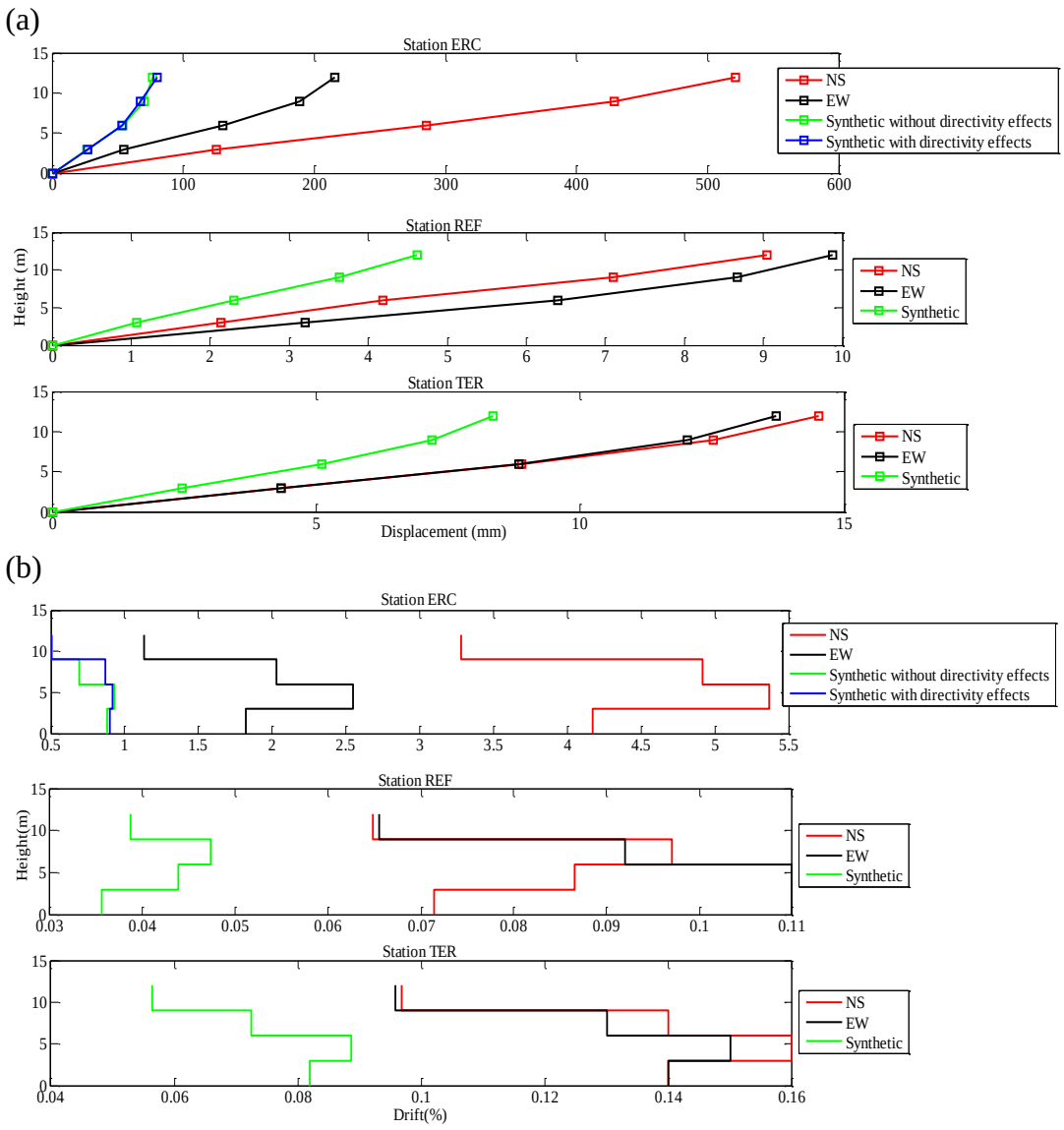

Figure 5.11 Distribution of (a) maximum story displacements and (b) maximum drift ratios due to the real and simulated records of Erzincan Earthquake – F4-4S3B

(a)

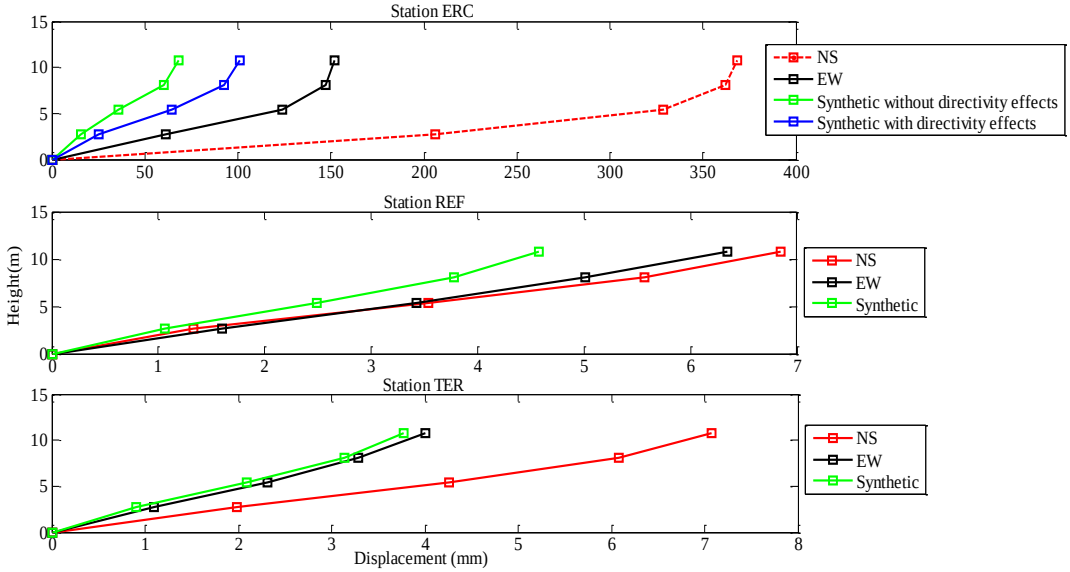

(b)

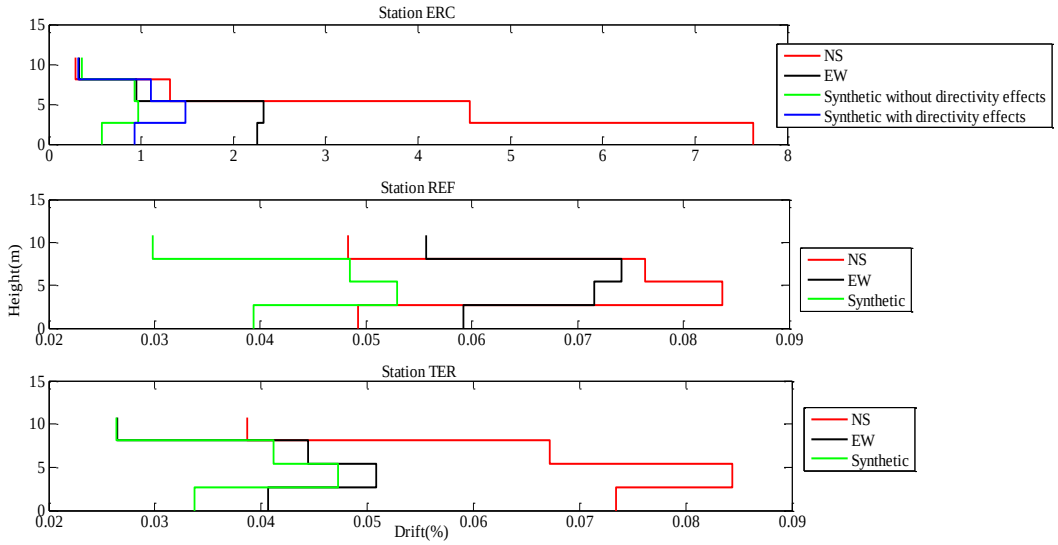

Figure 5.12 Distribution of (a) maximum story displacements and (b) maximum drift ratios due to the real and simulated records of Erzincan Earthquake – F5-4S3B

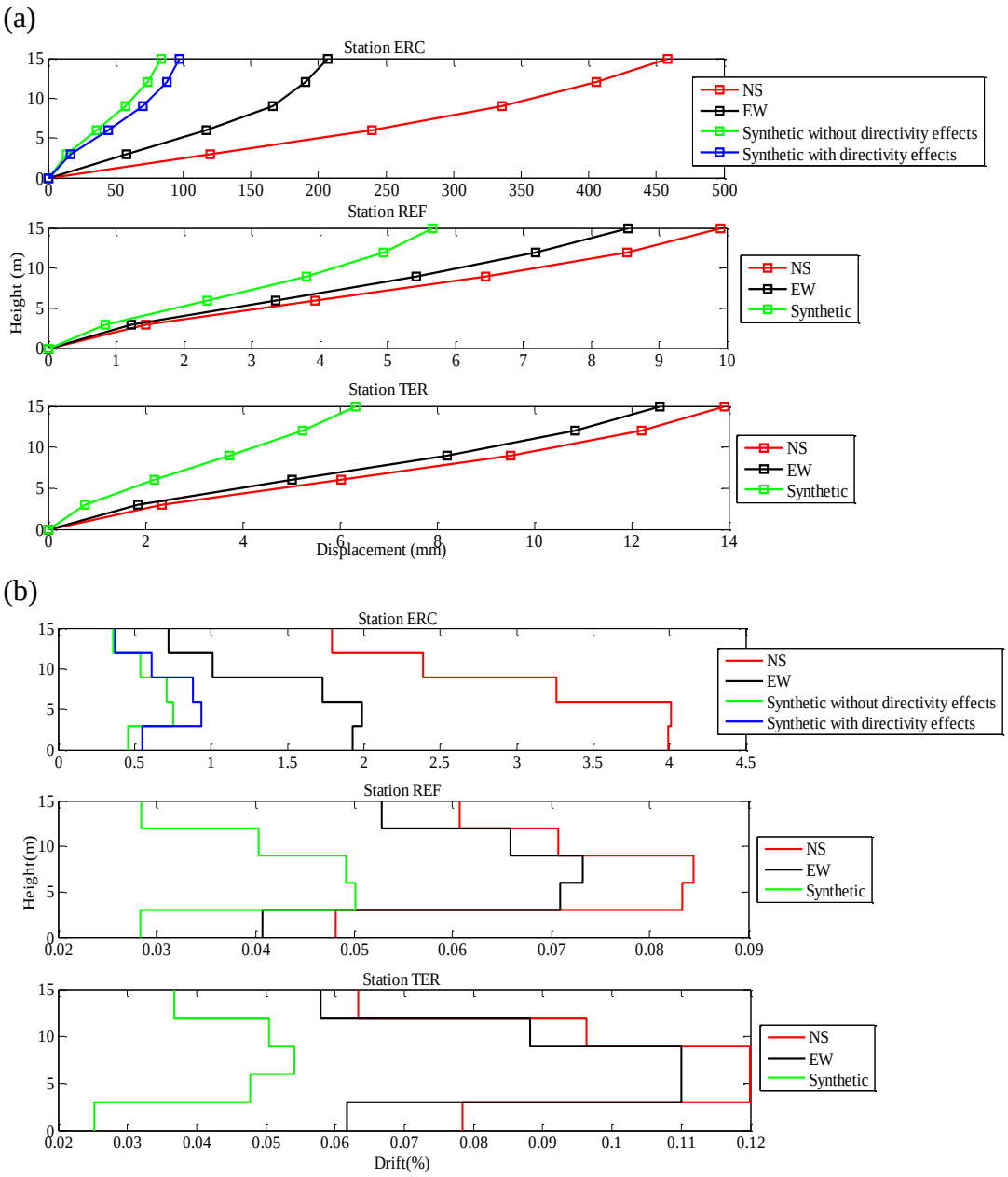

Figure 5.13 Distribution of (a) maximum story displacements and (b) maximum drift ratios due to the real and simulated records of Erzincan Earthquake – F6-5S2B

(a)

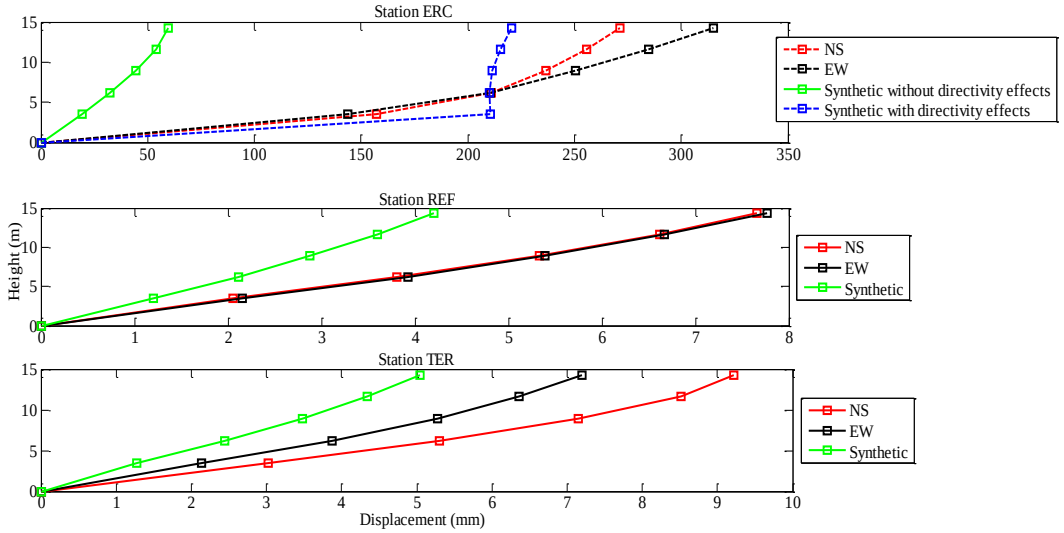

(b)

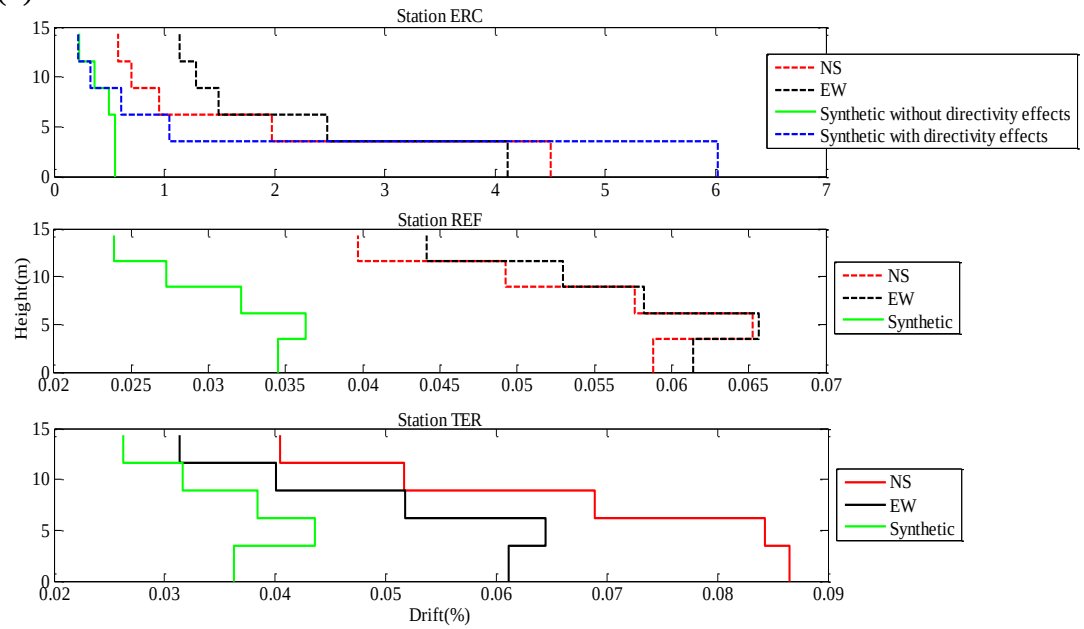

Figure 5.14 Distribution of (a) maximum story displacements and (b) maximum drift ratios due to the real and simulated records of Erzincan Earthquake – F7-5S4B

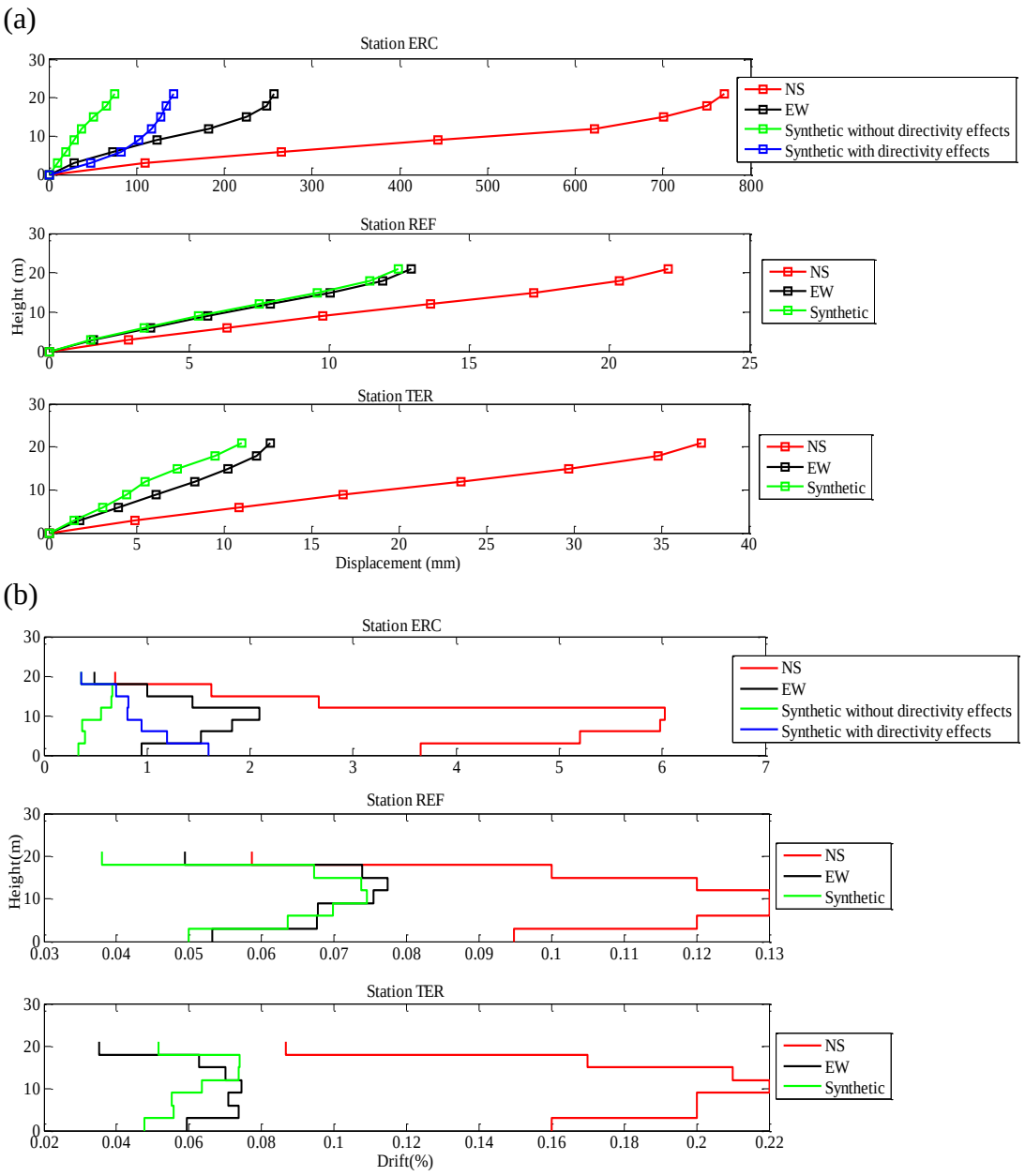

Figure 5.15 Distribution of (a) maximum story displacements and (b) maximum drift ratios due to the real and simulated records of Erzincan Earthquake – F8-7S3B

(a)

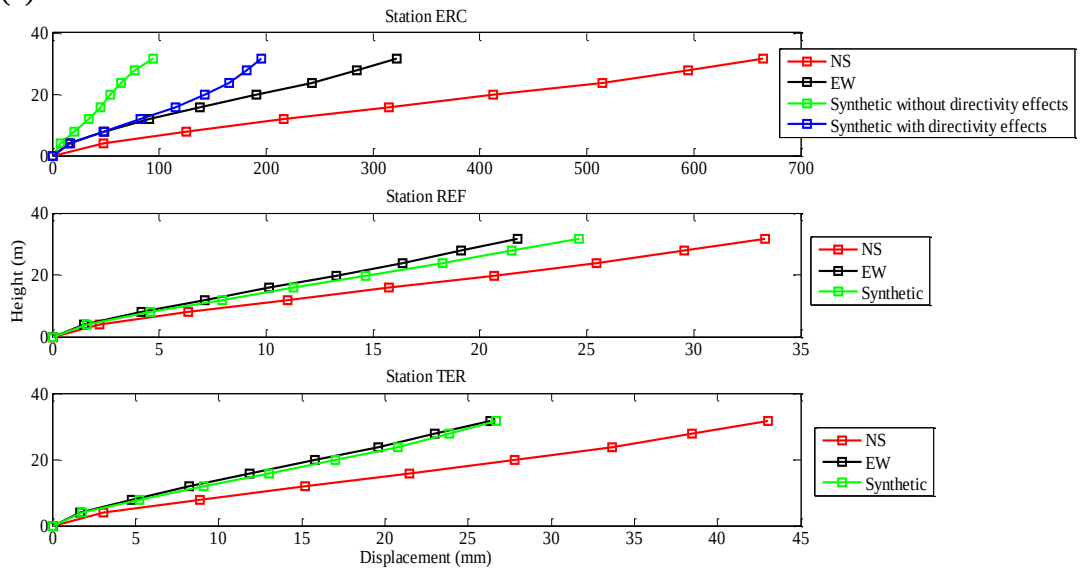

(b)

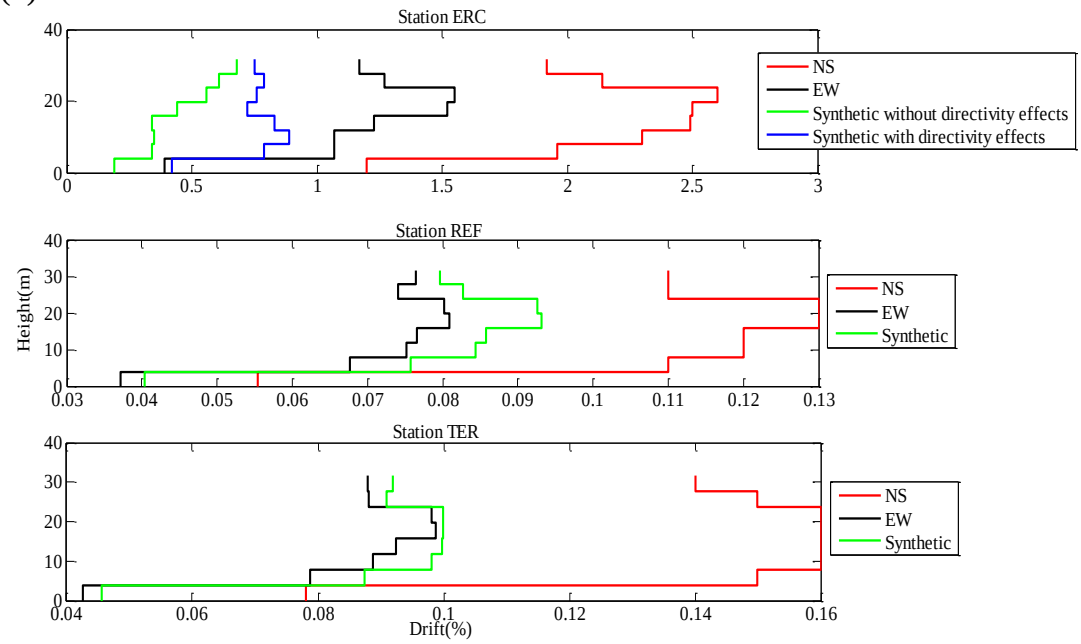

Figure 5.16 Distribution of (a) maximum story displacements and (b) maximum drift ratios due to the real and simulated records of Erzincan Earthquake – F9-8S3B

Table 5.7 Top story displacements of observed and simulated data at the stations for the 1992 Erzincan earthquake

Frame ID	Top Story Displacement	Station			
		ERC-without directivity effects	ERC-with directivity effects	REF	TER
F1-3S2B	Real (mm)	93.3493	93.3493	7.2968	6.9101
	Synthetic /Real	1.0589	1.1164	0.6179	0.6010
F2-3S2B	Real (mm)	285.3930	285.3930	9.4249	14.8970
	Synthetic /Real	0.2999	0.3211	0.4550	0.5457
F3-3S3B	Real (mm)	188.1380	188.1380	7.7724	9.6067
	Synthetic /Real	0.3675	0.4120	0.5691	0.4845
F4-4S3B	Real (mm)	335.4037	335.4037	9.4499	14.1120
	Synthetic /Real	0.2286	0.2381	0.4892	0.5920
F5-4S3B	Real (mm)	236.7419	236.7419	6.5924	5.3204
	Synthetic /Real	0.2868	0.4259	0.6943	0.7088
F6-5S2B	Real (mm)	308.0666	308.0666	9.1998	13.2298
	Synthetic /Real	0.2709	0.3163	0.6155	0.4778
F7-5S4B	Real (mm)	292.2516	292.2516	7.7127	8.1494
	Synthetic /Real	0.2036	0.7541	0.5454	0.6189
F8-7S3B	Real (mm)	444.4866	444.4866	16.8984	21.7336
	Synthetic /Real	0.1692	0.3198	0.7382	0.5068
F9-8S3B	Real (mm)	462.8248	462.8248	26.9403	33.6495
	Synthetic /Real	0.2038	0.4223	0.9139	0.7933

Table 5.8 Misfits in terms of nonlinear responses ($Misfit_{NR}$) to real and simulated data at the stations for the 1992 Erzincan earthquake

Frame ID	Station			
	ERC-without directivity effects	**ERC-with directivity effects**	**REF**	**TER**
F1-3S2B	0.0633	0.0612	0.2052	0.2313
F2-3S2B	0.5468	0.5025	0.3690	0.2916
F3-3S3B	0.4882	0.3962	0.2520	0.3502
F4-4S3B	0.5453	0.5429	0.3410	0.2365
F5-4S3B	0.6491	0.4272	0.1470	0.1145
F6-5S2B	0.6193	0.5369	0.1939	0.3739
F7-5S4B	0.7675	0.0841	0.2605	0.2421
F8-7S3B	0.8078	0.3466	0.0768	0.2605
F9-8S3B	0.6346	0.2236	0.0807	0.0799

Results expressed in Figures 5.8-5.16 and Tables 5.4-5.8 corresponding to all frames are summarized as follows:

- F1-3S2B has a fundamental period of 0.47 s. The results at station ERC reveals that both real and simulated structural responses are in nonlinear ranges. Regardless of the nonlinearity and existence of analytical directivity effects, a good match in terms of estimated structural responses and drift ratios is obtained for this station. However, when the results of stations REF and TER are considered, underestimation of the real structural responses by a factor of 1.5 is observed at these two stations (Figure 5.8).

- The fundamental period of frame F2-3S2B, which is the deficient form of F1-3S2B, is 0.71 s. For this frame at all stations, real responses are underestimated; however, the level of underestimation is different for them. At station ERC, stochastic finite-fault method underestimates the maximum top story displacement by a factor of about 3, while for stations REF and TER

the factor of underestimation of real nonlinear responses is approximately 2 (Figure 5.9 and Table 5.7). This conclusion can also be verified by a comparison of NR misfits (Table 5.8).

- Frame F3-3S3B is designed according to the previous Turkish seismic design code (1997) and has a fundamental period of 0.53 s. For this frame, similar to the frame F2-3S2B, at all stations underestimation of the real dynamic responses is observed. The levels of underestimation of maximum top story displacement for this frame are 2.5 for station ERC and 2 for stations REF and TER (Figure 5.10 and Table 5.7). It is noted that, at station ERC, the simulated record with considering directivity effects results in closer responses to the real ones in contrast to the simulated record without considering directivity effects. The longer fundamental period is believed to cause this observation. For this frame all nonlinear response misfits are in agreement with the observations.

- F4-4S3B which is designed according to the zone 1 of previous Turkish seismic design code (1997) has a fundamental period of 0.69 s. The results of nonlinear time history analyses for this frame demonstrate underestimation of the real dynamic responses with the simulated data (Figure 5.11). When the results in Table 5.7 are compared, it becomes clear that the level of underestimation of maximum top story displacements is around 5 for ERC station whereas for stations REF and TER the value is approximately 2.

- Figure 5.12 demonstrates a clear failure of the frame F5-4S3B which is extracted from the Düzce damage database, when subjected to NS component of real time history at station ERC with PGA of 0.5g. The (real) maximum top story displacement is underestimated by a factor of 2.5 and 3 by simulated records with and without modeling directivity effects, respectively. At stations REF and TER, the real responses are similarly underestimated and the factor of underestimation is smaller around 1.5.

- F6-5S2B is one of the existing structures located in the city of Bursa in Turkey with a fundamental period of 0.78 s. The real nonlinear responses of this frame are underestimated with simulated records at all stations. At station ERC, the value of top story displacement slightly becomes closer to the real one as the simulated record takes into account the directivity effects with analytical modeling of long duration velocity pulse. Simulated records of stations REF and TER have almost same levels of error with clear underestimation of the nonlinear responses with a factor of approximately 2 (Figure 5.13 and Table 5.7).

- F7-5S4B is a deficient frame extracted from the Düzce damage database. The results of nonlinear responses in terms of maximum story displacement and drift ratio for this frame as illustrated in Figure 5.14 demonstrate failure of the structure with real records at station ERC. This observation is simulated with the synthetic record that takes into account the directivity effects. However, at this station, simulated record in which directivity effects are not modeled is insufficient to estimate the real response where the level of underestimation is approximately 5. At the other stations, REF and TER, the real responses are underestimated by a factor of almost 2.

- When the NLTHA results of frame F8-7S3B are considered in Figure 5.15, it can be seen that for this frame modeling directivity effects improve the estimation of real dynamic responses at station ERC. Yet, at this station the real responses are still underestimated by a factor of 3. At stations REF and TER, the estimated dynamic responses are quite similar to real ones in EW direction, while slight underestimation persists for the NS component.

- F9-8S3B is a tall building designed using the 1982 Uniform Building Code in California with a fundamental period of 1.30. For this frame, the constructive effects of modeling directivity effects is obvious at station ERC where the level of underestimation of maximum top story displacement is improved

from 5 to 2.5 (Figure 5.16). For stations REF and TER, the estimated nonlinear responses in terms of either maximum story displacement or drift ratio are quite similar to those of real ones, though some differences still persist particularly for the NS component.

When seismological misfits are compared against nonlinear response misfits for Erzincan earthquake that occurred on a deep alluvial basin, the following observations are derived:

For station ERC, the highest agreement is observed to be between the frequency/period-dependent SS misfits and the NR misfits. For most of the frames, RS misfit is a better indicator of the structural response than the FAS misfit. However, modeling directivity effects at this station improves the accuracy of SS misfits particularly in terms FAS. For this station with pronounced forward directivity effects located on soft soil, among all NSS misfits, the one representing significant duration of the record is the most dominant indicator of the nonlinear response misfits. On the other hand, misfits in terms of I_a and *PGA* are the least dominant indicators of nonlinear behavior (lowest consistency with NR misfits), other than the frames with very short fundamental periods. It is observed that modeling directivity effects decreases the NSS misfits in terms of both *CAV* and *HI*. This observation is in agreement with NR misfits of structures especially with increasing fundamental periods.

For station REF, both the frequency/period-dependent RS and FAS misfits are consistent with NR misfits. For this station, all NSS misfits are consistent with the nonlinear responses. However, the t_{eff}, *HI*, and *PGA* misfits are more accurate indicators than *CAV* and I_a.

For station TER, both of the frequency/period-dependent SS misfits are in agreement with NR misfits where for most of the frames, RS misfit is a better indicator than FAS misfit. For this station, all NSS misfits are in agreement with nonlinear response

misfits except PGA. However, the misfits in terms of I_a and *HI* are more accurate indicators of the nonlinear response than *CAV* and t_{eff}.

Further details about the comparison of seismological misfits with nonlinear response misfits for Erzincan earthquake are presented in Appendix F.1.

5.4 Second Case Study: Ground Motion Simulation of the 1999 Düzce (Mw=7.1) Earthquake

5.4.1 General

The western segments of the NAFZ are considered critical due to the existence of most densely-populated areas of Turkey surrounded by major industrial facilities. Düzce is located in the western part of NAF, on an alluvial pull-apart basin. Düzce earthquake, occurred on 12 November 1999 with Mw=7.1, led to destructive damages of the city along with almost 900 mortalities and 3000 injuries (Akyuz, 2002). This earthquake is the second largest earthquake which caused 45 km surface rupture associated with horizontal and vertical displacements of 3 and 5 m, respectively (Sahin and Tari, 2000). In this thesis, the 1999 Düzce earthquake is selected as the second case study to investigate the ability of simulated records in predicting the nonlinear MDOF responses

Section 5.4.2 presents the observed ground motion records of the 1999 Düzce earthquake at the selected stations with their properties. Section 5.4.3 summarizes the input parameters used for the simulation of the 1999 Düzce earthquake and the simulated time histories. Section 5.4.4 discusses the differences in between the simulated time histories versus real ground motion records by using the seismological misfits as defined previously. In Section 5.4.5, the nonlinear time history analyses results for the selected frames to both real and simulated ground motion records are presented and discussed in detail.

5.4.2 Real ground motion data of the 1999 Düzce (Mw=7.1) earthquake

There were a total of 32 strong ground motion stations that recorded the mainshock of this earthquake. Among these in this thesis, 5 of them with epicentral distances less than 125 km are selected. Figure 5.17 demonstrates the epicenter, fault plane, and the locations of these selected stations for the 1999 Düzce earthquake. Table 5.9 gives information on the selected strong ground motion stations containing their names, codes, hypocentral coordinates, site class (NEHRP), epicentral distances, and horizontal PGA values in both directions along with the PGVs. The raw time histories of the selected five stations are derived from strong ground motion database of Turkey (http://daphne.deprem.gov.tr:89/2K/daphne_v4.php). All ground motion records are baseline corrected and filtered in the frequency range of 0.1-10 Hz with 4th order Butterworth filter type.

Table 5.9 Information on the strong motion stations that recorded the 1999 Düzce earthquake

Station	**Code**	**Latitude (°)**	**Longitude (°)**	**Site Class (NEHRP)**	**R_{epi} (km)**	**PGA-EW (cm/s^2)**	**PGA-NS (cm/s^2)**	**PGV-EW (cm/s)**	**PGV-NS (cm/s)**
Düzce	DZC	40.8436	31.1488	D	9.314	520.41	328.03	86.54	54.53
Göynük	GYN	40.3965	30.7830	D	55.163	22.17	25.79	5.84	4.49
İznik	IZN	40.4416	29.7168	D	123.67	20.06	21.25	1.97	2.27
İzmit	IZT	40.7665	29.9172	C	100.7	16.41	18.73	2.27	1.73
Yarımca Petkim	YPT	40.7639	29.7620	D	116.85	16.15	23.47	4.08	8.38

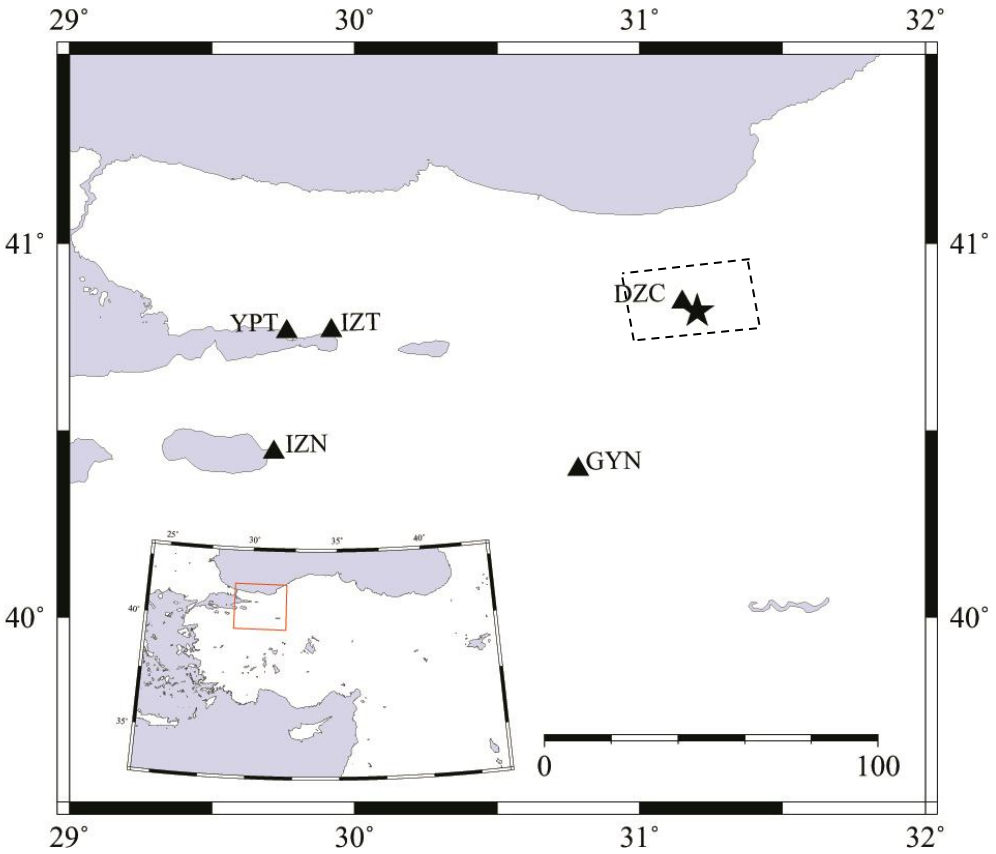

Figure 5.17 Map showing the fault plane and epicenter of the 1999 Düzce earthquake with the locations of the stations

5.4.3 Simulated ground motion data for the 1999 Düzce (Mw=7.1) earthquake

The main purpose of this section is to simulate the records of Düzce earthquake by using the regional parameters verified by Ugurhan and Askan (2010) with a minor modification on the soil amplification factors. Next, the source, path, and site models are discussed in detail.

5.4.3.1 Source model

To define the source model, parameters corresponding to the geometry of the fault plane including the hypocenter location, depth of the fault, geometry, slip distribution,

sub-fault size, strike and dip angles should be determined. The data provided by Earthquake Research Department of Turkey (ERD) states the coordinates of the epicenter as 40.82º N, 31.20º E. The focal depth of the event is considered to be 12.5 km (Milkereit *et al.*, 1999). The fault plane is assumed to have a length of 65 km and a width of 25 km (Umutlu *et al.*, 2004) where the sub-fault sizes are assumed to be 5 km in each direction. Strike and dip angles of the fault plane are specified as 64º and 264º. Ugurhan and Askan (2010) validated that among different slip distribution models, a bilateral fault rupture model introduced by Umutlu *et al.* (2004) gives the much more accurate ground motion records with smaller FAS misfits in between real and synthetic data at the observation points. Estimated stress drop value for simulation of Düzce earthquake is equal to 100 bars. The assumed source parameters are listed in Table 5.10.

Table 5.10 Source parameters of the 1999 Düzce earthquake

Parameter	**Value**
Moment Magnitude	7.1
Epicenter Location	40.82º N, 31.20º E
Hypocenter Depth	12.5 km
Depth to the top of the Fault Plane	2 km
Fault Orientation	Strike=264 º; Dip=64 º
Fault Dimensions	65 km x25 km
Sub-fault Dimensions	5 km x 5 km
Crustal Shear Wave Velocity (β)	3700 m/s
Rupture Velocity	0.8β
Crustal Density	2800 kg/m^3
Stress Drop	100 bars
Pulsing Area Percentage	30

5.4.3.2 Path model

For this case study, geometrical spreading model of Ansel *et al.* (2009) is assumed. The considered model is a piecewise function of distance defined as follows:

$$\begin{cases} R^{-1} & R \leq 30\ Km \\ R^{-0.4} & 30 < R \leq 60\ Km \\ R^{-0.6} & 60 < R \leq 90\ Km \\ R^{-0.8} & 90 < R \leq 100\ Km \\ R^{-0.5} & R > 100\ Km \end{cases} \quad (5.10)$$

To account for the inelastic attenuation, among different frequency-dependent quality factor equations, the quality factor of $Q = 88f^{0.9}$ recommended by Boore (1984) is selected. The test results in Ugurhan and Askan (2010) indicated that this quality factor results in more accurate spectral amplitudes at higher frequencies. Finally, for duration effects, the global model mentioned by Herrmann (1985) as previously given in Equation 5.2 is employed.

5.4.3.3 Site model

To simulate a reliable ground motion record for a single station, site effects should be determined as accurate as possible. It should be noted that, the largest amount of uncertainty is due to the parameters specified for the site model especially in areas with sparse geotechnical data. Site effects include both amplification function as a result of seismic impedance effect due to the change of soil velocity profile in depth and the attenuation function due to kappa factor. As defined in Chapter 2 in detail, there are various models for determining the site amplification factors like quarter wavelength technique (Boore and Joyner ,1997), Standard Spectral Ratio (SSR) method (Borcherdt, 1970), and Horizontal to Vertical (H/V) ratio methodology (Nakamura, 1989). For stations of this case study, two types of site amplification factors are implemented: The values proposed by Ugurhan and Askan (2010) using

H/V method and the generic soil amplifications of Boore and Joyner (1997). Then, for each ground motion station, the observed ground motion records are compared against the two simulated records using alternative site amplification factors. Comparisons are made in terms of PGA, PGV, and FAS values. It is observed that for stations DZC, GYN, IZT, and YPT, the site amplification factors proposed by Ugurhan and Askan (2010) result in the best fit of the simulated records to the observed ground motions. The site amplification factors which are used in the mentioned four stations are the ones shown in Figure 2 of Ugurhan and Askan (2010). However, at station IZN, generic soil amplification factors proposed by Boore and Joyner (1997) corresponding to site class D provide better fit to the observed records.

When the kappa factor is considered, the estimated vertical kappa, κ_0 (equal to 0.047) for Düzce region by Ugurhan and Askan (2010) is employed.

5.4.4 Comparison of simulated and real ground motion data for the 1999 Düzce (Mw=7.1) earthquake

As a result of simulation at every station, there is a total of 1 simulated and 2 real horizontal components of time histories. Therefore, the total number of time histories to be used for nonlinear time history analysis of each frame is 15 (at 5 stations). The simulated time histories are also baseline corrected and filtered between 0.1 and 10 Hz with 4th order Butterworth filter type. To visually check the accuracy of the generated ground motions, all time histories together with the FAS and elastic RS with 5% damping are plotted. Figures 5.18-5.22, display the results at all stations where PSA corresponds to the 5% damped pseudo acceleration. Figure 5.18.a presents that, at station DZC, the estimated PGA from stochastic finite-fault methodology is almost equal to the NS component of the observed record, while, it is approximately 2/3 times of the EW component. Comparison of the results of Figures 5.18.b and 5.18.c demonstrate that there is a good match of the real and synthetic spectra (both FAS and RS) for lower frequency or higher period ranges ($f < 1\ Hz\ or\ T > 1\ s$). However, when higher frequencies (lower periods) are of concern, the FAS/RS amplitudes corresponding to the EW component are slightly higher than both NS and synthetic

spectral amplitudes. At stations GYN, IZN, and IZT simulated records slightly overestimate the real spectral amplitudes as well as the PGA values for all frequency ranges (Figures 5.19-5.21). Finally, at station YPT, there is a good agreement in between PGA values of the observed NS component and the simulated record while the PGA of EW component is overestimated by a factor of almost 1.5 (Figure 5.22.a). In addition, at this station, synthetic spectral amplitudes in terms of FAS and RS closely match with the real amplitudes at frequencies larger than approximately 1 Hz. However, the observed spectral amplitudes are slightly underestimated at frequencies less than 1 Hz (Figures 5.22.b and 5.22.c).

(a)

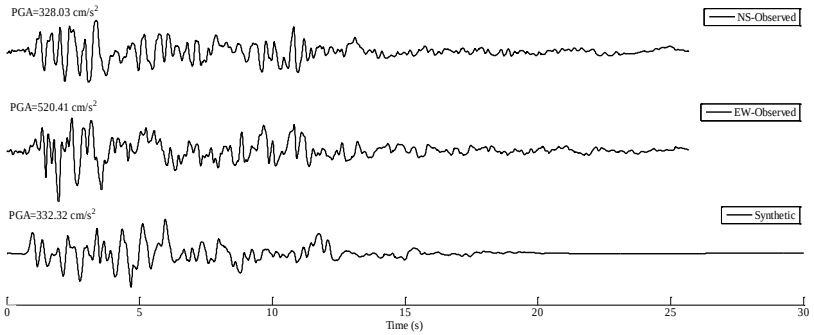

(b)

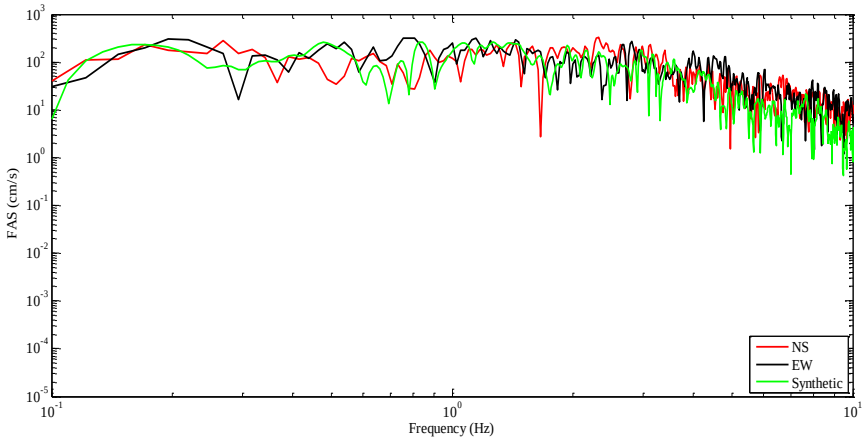

(c)

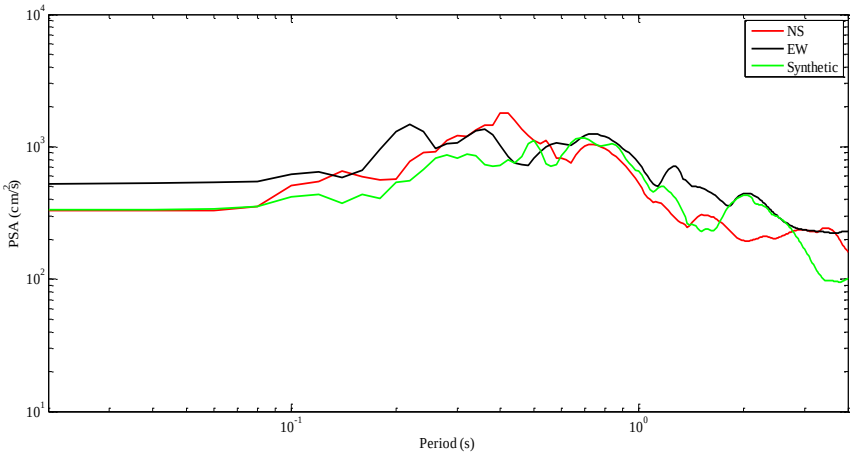

Figure 5.18 Station DZC; (a) Observed and simulated accelerograms (b) Fourier amplitude spectra (c) Response spectra with 5% damping obtained for observed (NS and EW) and simulated horizontal component (Synthetic)

(a)

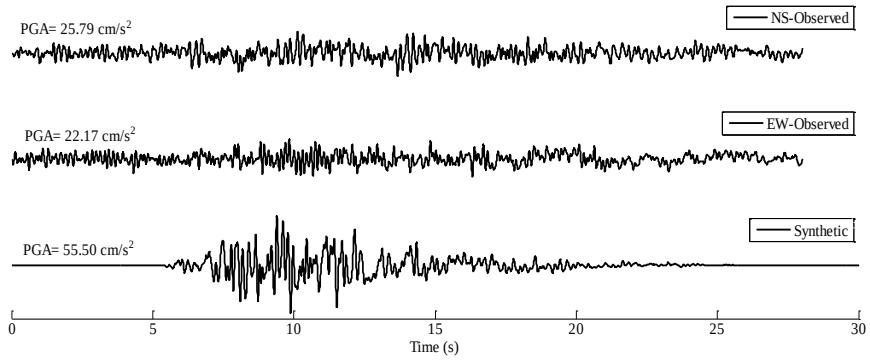

(b)

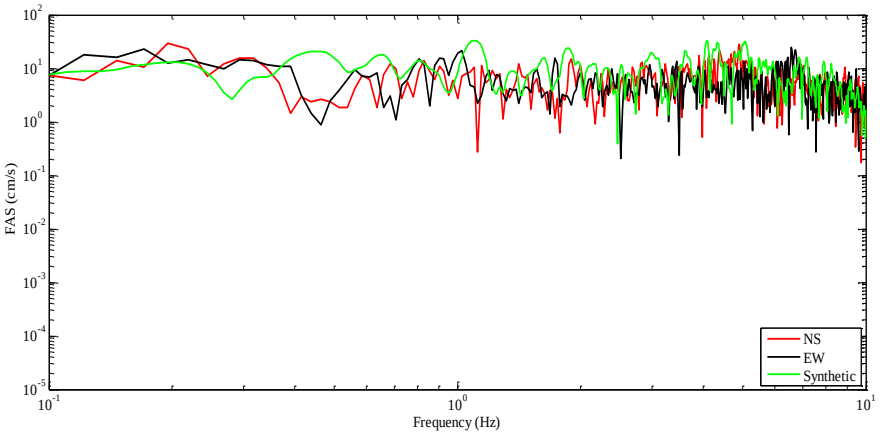

(c)

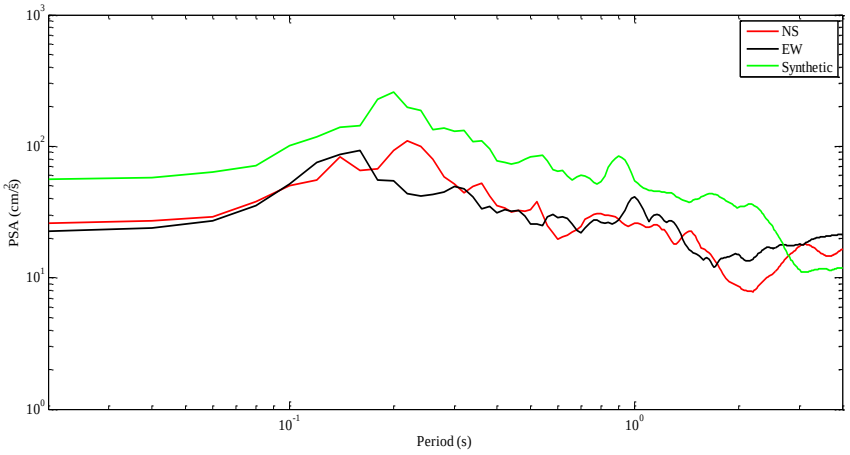

Figure 5.19 Station GYN; (a) Observed and simulated accelerograms (b) Fourier amplitude spectra (c) Response spectra with 5% damping obtained for observed (NS and EW) and simulated horizontal component (Synthetic)

(a)

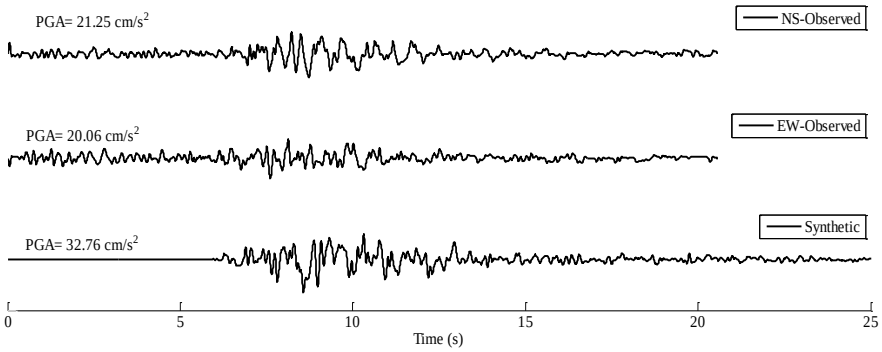

(b)

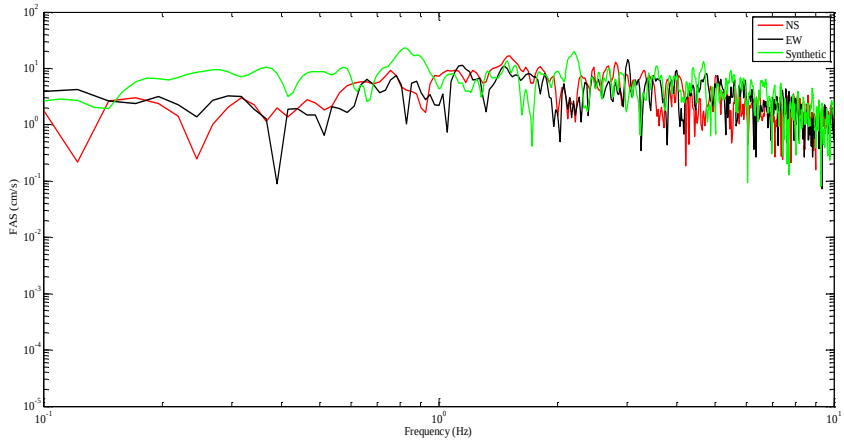

(c)

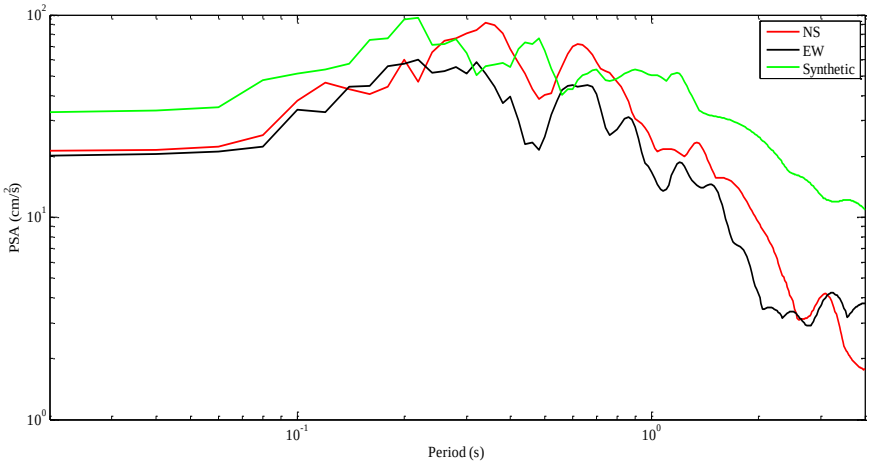

Figure 5.20 Station IZN; (a) Observed and simulated accelerograms (b) Fourier amplitude spectra (c) Response spectra with 5% damping obtained for observed (NS and EW) and simulated horizontal component (Synthetic)

(a)

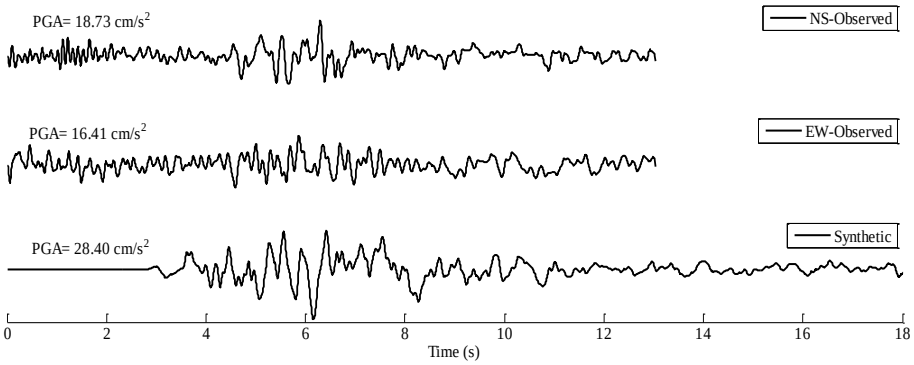

(b)

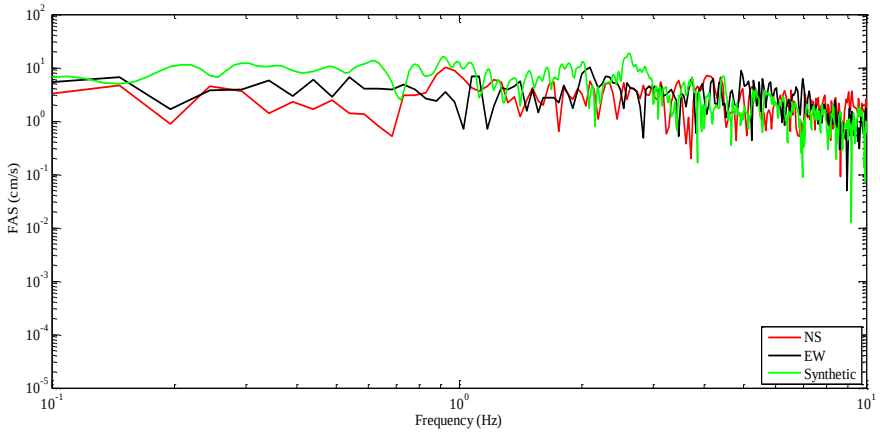

(c)

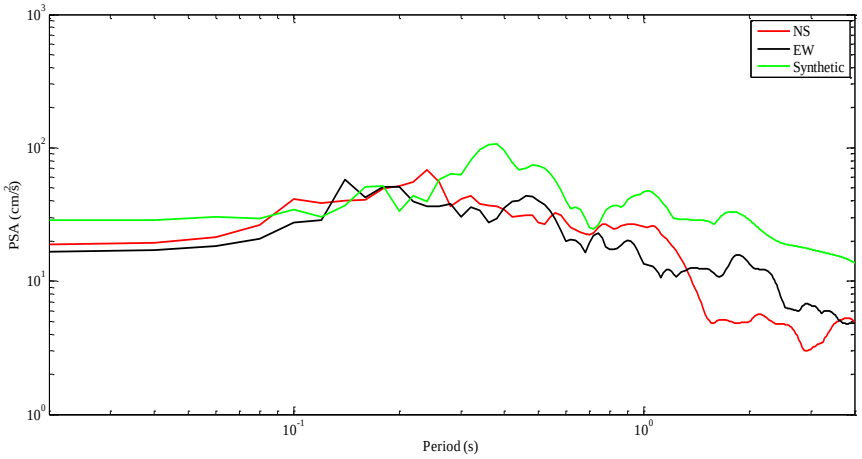

Figure 5.21 Station IZT; (a) Observed and simulated accelerograms (b) Fourier mplitude spectra (c) Response spectra with 5% damping obtained for observed (NS and EW) and simulated horizontal component (Synthetic)

(a)

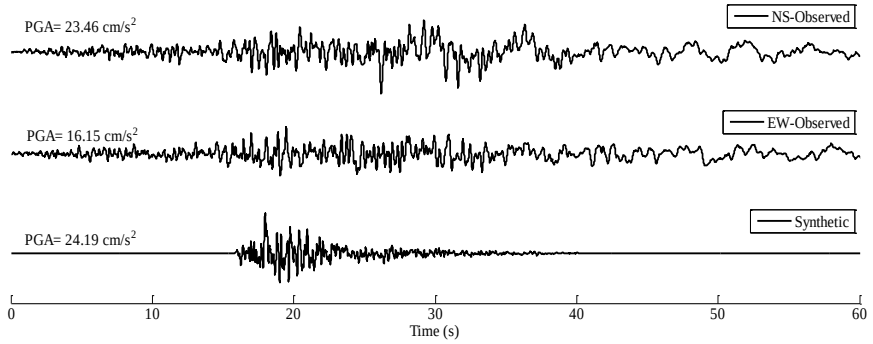

(b)

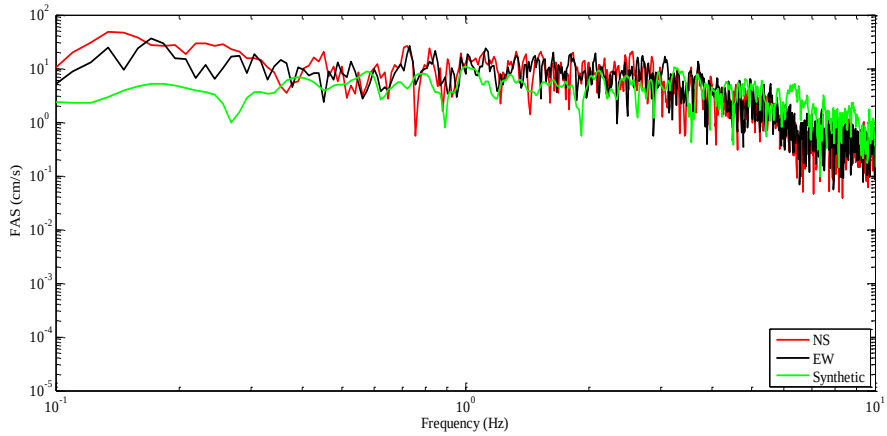

(c)

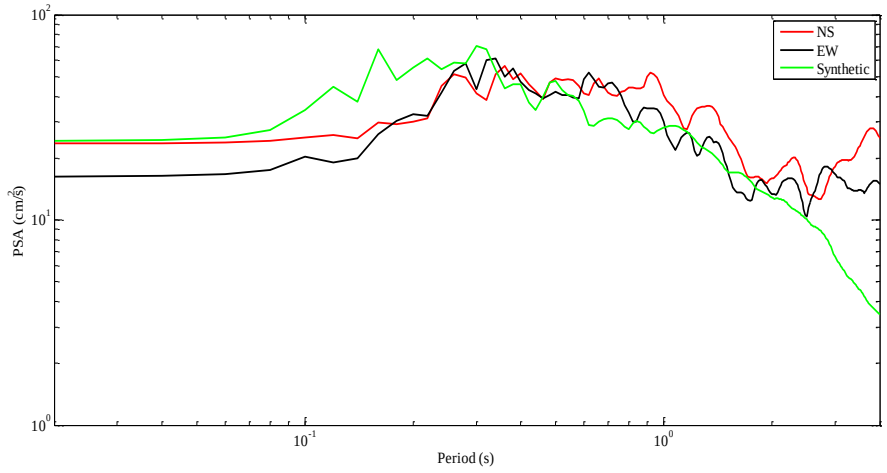

Figure 5.22 Station YPT; (a) Observed and simulated accelerograms (b) Fourier amplitude spectra (c) Response spectra with 5% damping obtained for observed (NS and EW) and simulated horizontal component (Synthetic)

For this case study, error between the observed and simulated ground motions is quantified using all of the seismological misfits as previously presented in Section 5.3.4. The results of SS misfits in terms of FAS and RS are listed in Tables 5.11 and 5.12, respectively. Next, Table 5.13 lists the computed misfits in terms of non-spectral seismological parameters including PGA,t_{eff}, I_a, CAV, and HI.

Table 5.11 SS misfits in terms of fast Fourier amplitude spectra (Misfit$_{FAS}$) for real and simulated data at the stations for the 1999 Düzce earthquake

Frame ID	**Station**				
	DZC	**GYN**	**IZN**	**IZT**	**YPT**
F1-3S2B	0.8987	0.5960	0.5045	0.5411	0.8153
F2-3S2B	0.6904	0.6277	0.5422	0.5745	0.7151
F3-3S3B	0.7635	0.5904	0.5238	0.5618	0.7481
F4-4S3B	0.6992	0.6293	0.5447	0.5735	0.7265
F5-4S3B	0.8200	0.5742	0.5087	0.5543	0.7659
F6-5S2B	0.6338	0.6504	0.5384	0.5639	0.6899
F7-5S4B	0.7864	0.5825	0.5224	0.5603	0.7440
F8-7S3B	0.4655	0.6153	0.5667	0.6264	0.5829
F9-8S3B	0.4592	0.5805	0.5321	0.6266	0.6058

Table 5.12 SS misfits in terms of response spectra ($Misfit_{RS}$) for real and simulated data at the stations for the 1999 Düzce earthquake

Frame ID	Station				
	DZC	GYN	IZN	IZT	YPT
F1-3S2B	0.3891	0.9154	0.4182	0.5798	0.2909
F2-3S2B	0.2862	0.9047	0.3584	0.5330	0.2814
F3-3S3B	0.3447	0.9110	0.4118	0.5505	0.2758
F4-4S3B	0.2958	0.9014	0.3571	0.5337	0.2855
F5-4S3B	0.3824	0.9237	0.4038	0.5808	0.2755
F6-5S2B	0.2720	0.9253	0.3708	0.5394	0.2788
F7-5S4B	0.3635	0.9297	0.3947	0.5734	0.2824
F8-7S3B	0.2407	0.8157	0.5503	0.6442	0.2348
F9-8S3B	0.2583	0.7891	0.5646	0.6983	0.2341

Table 5.13 NSS misfits for real and simulated data at the stations for the 1999 Düzce earthquake

Station	Misfit $_{PGA}$	Misfit $_{Teff}$	Misfit $_{Ia}$	Misfit $_{CAV}$	Misfit $_{HI}$
DZC	-0.1957	-0.0245	-0.2660	-0.2163	0.0012
GYN	1.3209	-0.6330	1.2166	0.0239	1.4634
IZN	0.5864	-0.3370	0.8312	0.2215	1.2109
IZT	0.6198	-0.0848	1.3761	0.6311	1.4942
YPT	0.2428	-0.7867	-0.6626	-0.7204	0.5185

Through the comparison of misfits presented in Tables 5.11 and 5.12, it is observed that at station DZC as fundamental period of the frames decreases, misfits in terms of either FAS or RS monotonically increases. This observation can be attributed to the underestimation of the observed response spectra with simulated record at higher frequencies in this station. A slight overestimation of the response spectra by simulated cords was previously observed at stations GYN, IZN, and IZT. At these stations, RS

and FAS misfits are almost at the same range regardless of the frame. Finally, at station YPT a good match was obtained between the real and simulated response spectral amplitudes particularly at frequencies higher than 1 Hz. At YPT, the spectral misfits are about in the same range for all frames.

The results of Table 5.13 indicate that almost for all of the stations except DZC, the simulated PGA values are higher than the observed PGAs. However, when durations of the records are compared, it is observed that for the near and intermediate field stations duration content of the simulated records is consistent with the observed ones. Yet, for some far-field stations (GYN, IZN, and YPT) the simulated durations are smaller than the real durations. The reason behind this is the existence of surface waves in the real records with larger wavelengths and longer durations mostly produced by basin effects, which are not modeled by stochastic finite-fault simulation technique.

It should be noted that during 1999 Düzce earthquake, the recording devices of ground motions were not placed in the free field. Consequently, the structural responses may have influenced the frequency and amplitude content of the recorded motions. Such effects certainly cannot be included in the ground motion simulations.

Next, it is aimed to assess the nonlinear response of the selected frame buildings due to real and simulated ground motion database of the 1999 Düzce event.

5.4.5 Comparison of dynamic responses of the buildings to observed and simulated records for the 1999 Düzce (Mw=7.1) earthquake

To assess the accuracy of the simulated motions in predicting the structural behavior, Figures 5.23-5.31 present the maximum displacements and drift ratios calculated at each story level for all nine structures. Table 5.14 demonstrates the geometric means of the real top story displacements in both EW and NS directions along with the ratio of the simulated top story displacements to the real ones. The pushover analyses of the frames and comparison of the capacity curves with the results of NLTHA is presented in Appendix E.2. Finally, misfits in terms of nonlinear responses are listed in Table 5.15.

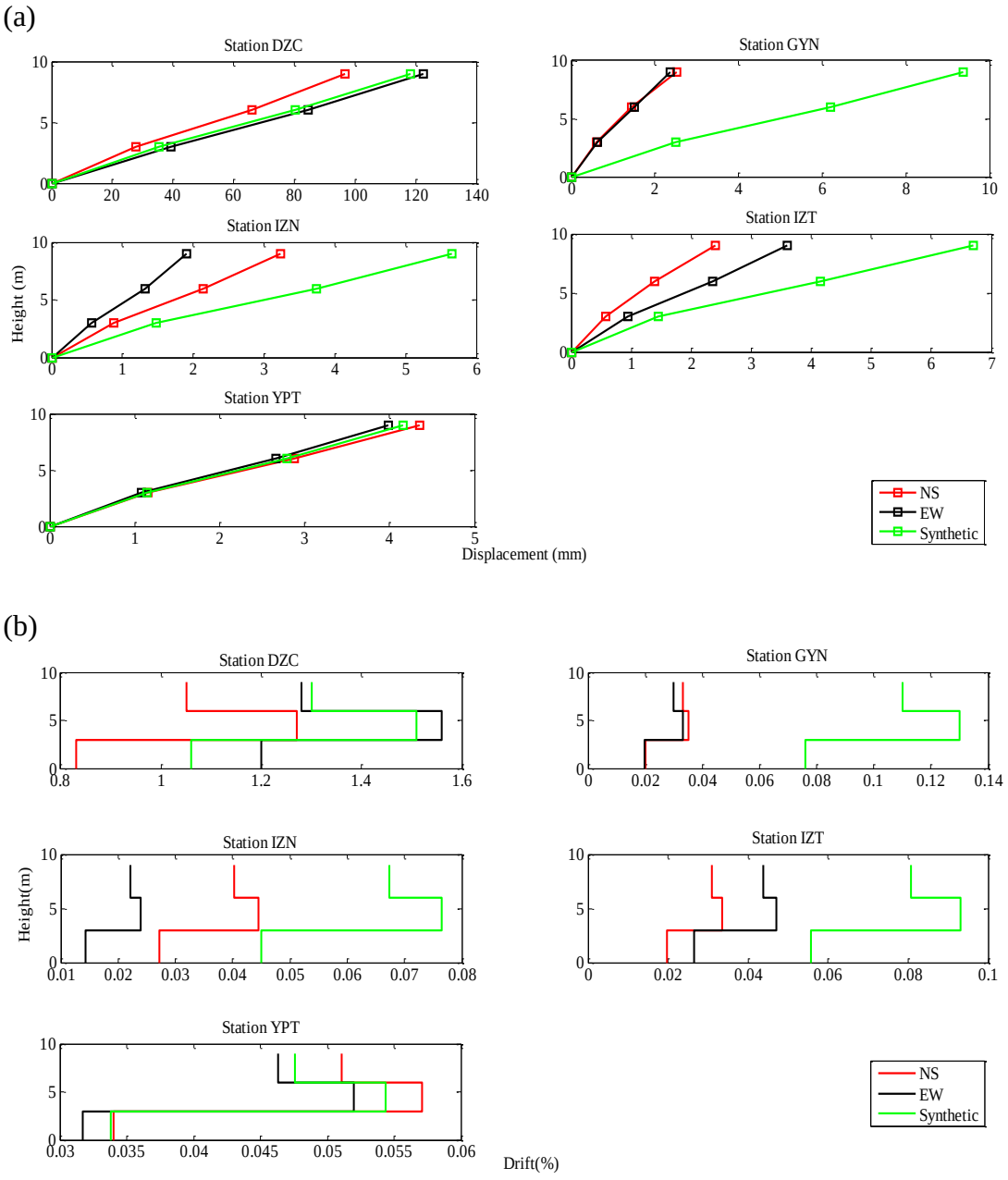

Figure 5.23 Distribution of (a): maximum story displacements and (b): maximum drift ratios due to the real and simulated records of Düzce Earthquake – F1-3S2B

(a)

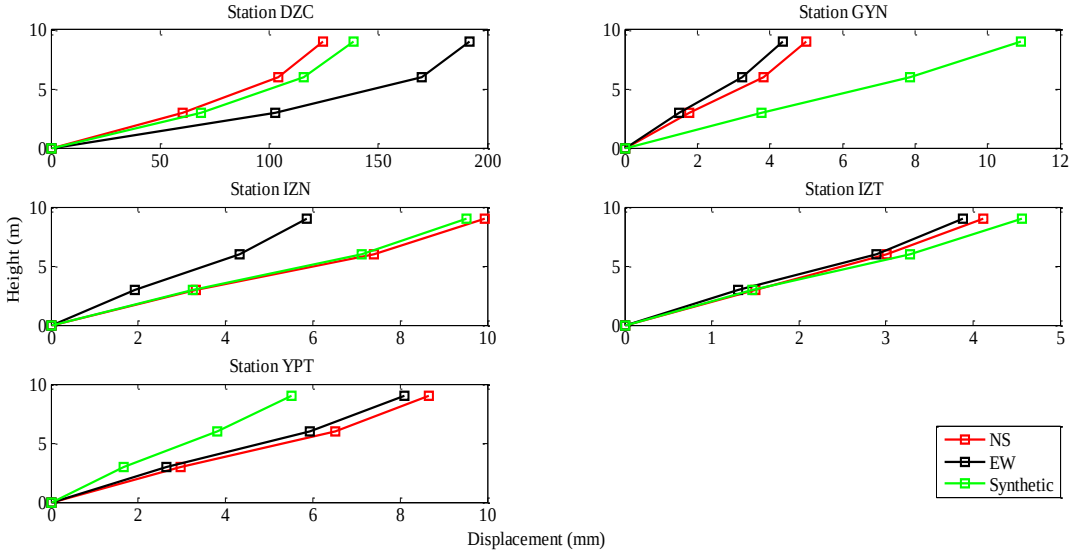

(b)

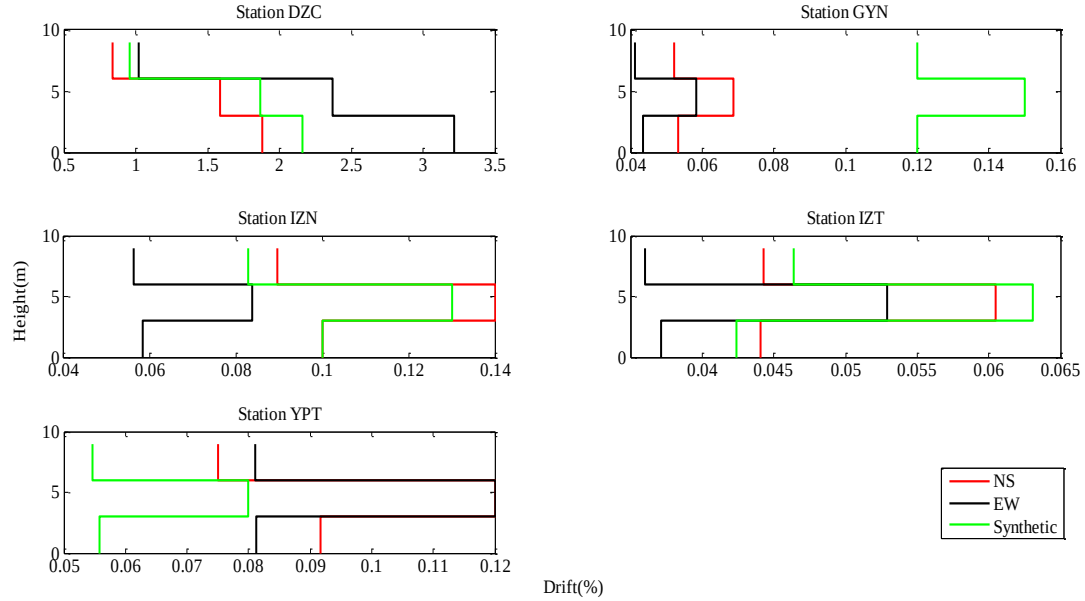

Figure 5.24 Distribution of (a): maximum story displacements and (b): maximum drift ratios due to the real and simulated records of Düzce Earthquake – F2-3S2B

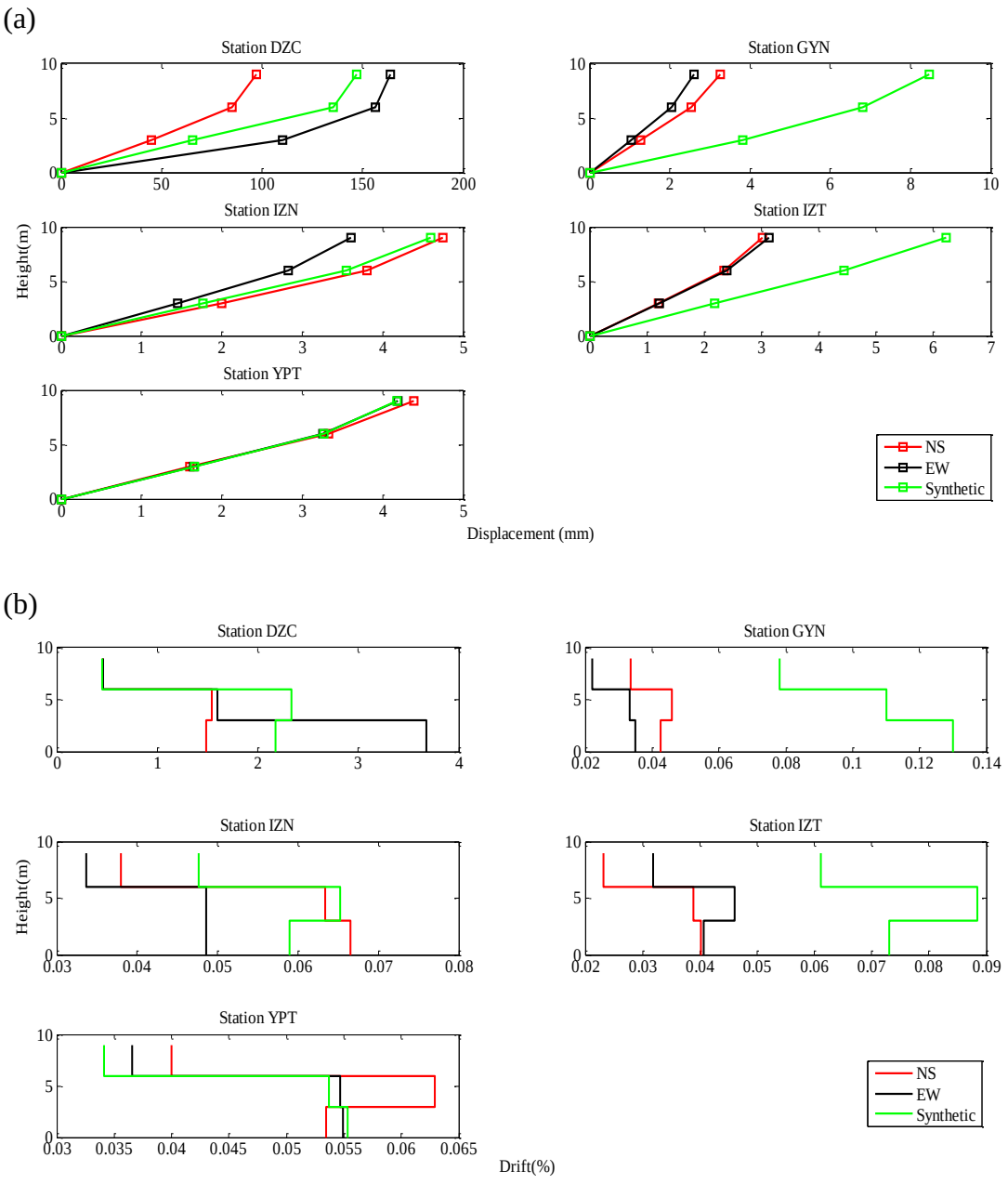

Figure 5.25 Distribution of (a): maximum story displacements and (b): maximum drift ratios due to the real and simulated records of Düzce Earthquake – F3-3S3B

(a)

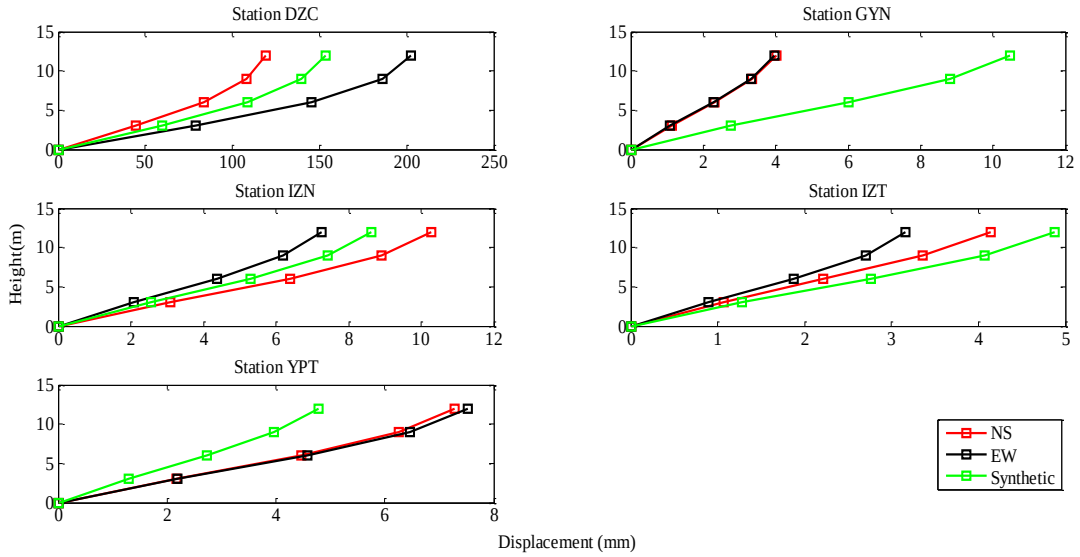

(b)

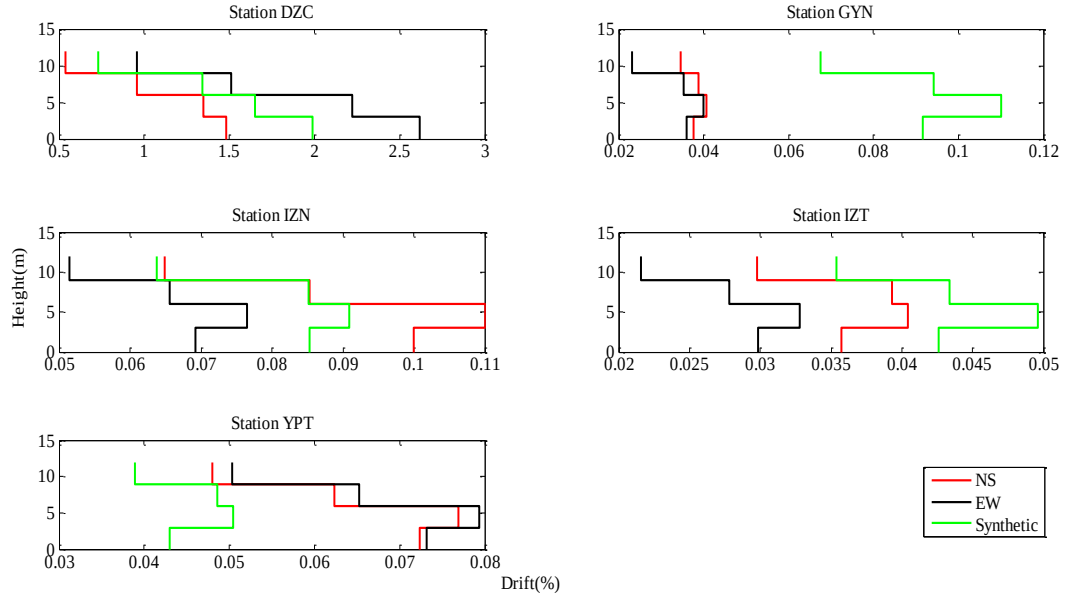

Figure 5.26 Distribution of (a): maximum story displacements and (b): maximum drift ratios due to the real and simulated records of Düzce Earthquake – F4-4S3B

(a)

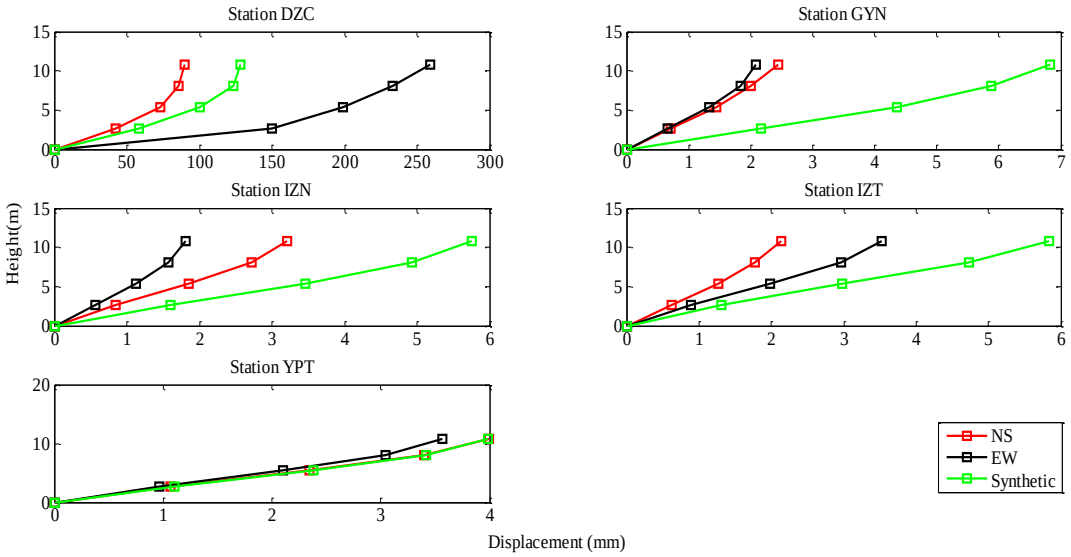

(b)

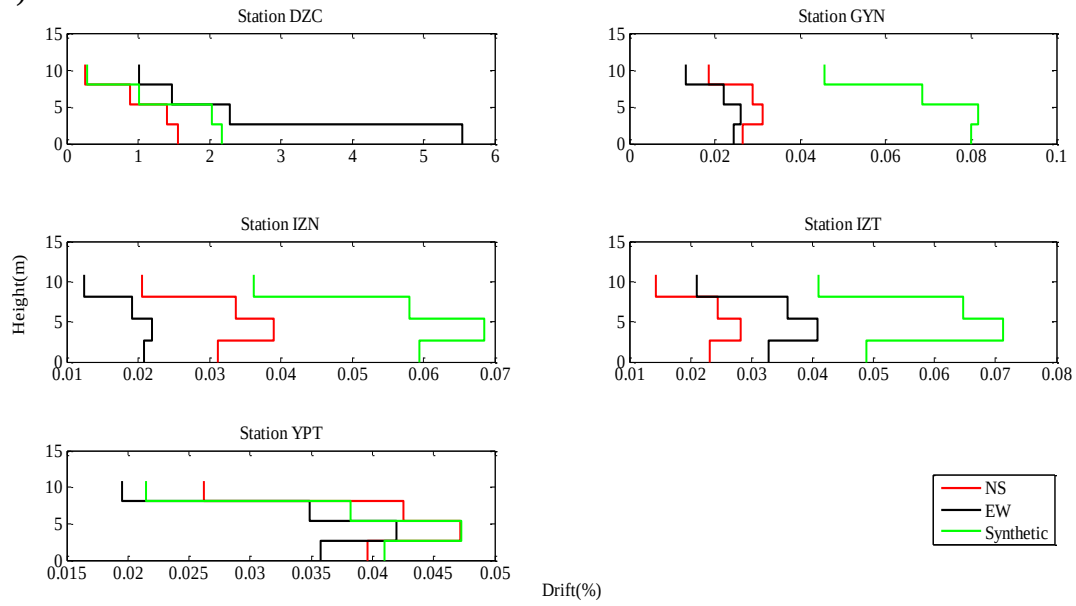

Figure 5.27 Distribution of (a): maximum story displacements and (b): maximum drift ratios due to the real and simulated records of Düzce Earthquake – F5-4S3B

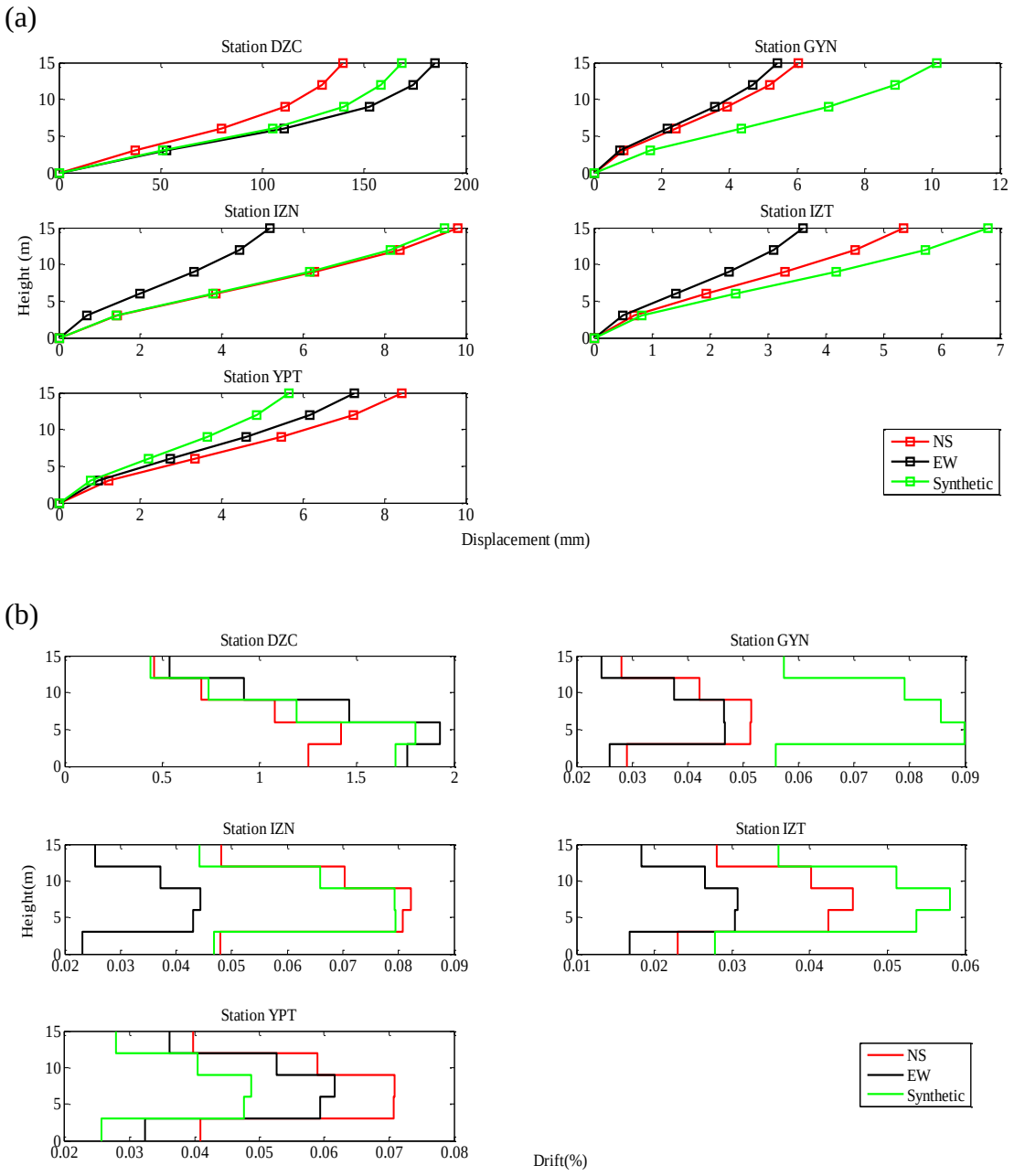

Figure 5.28 Distribution of (a): maximum story displacements and (b): maximum drift ratios due to the real and simulated records of Düzce Earthquake – F6-5S2B

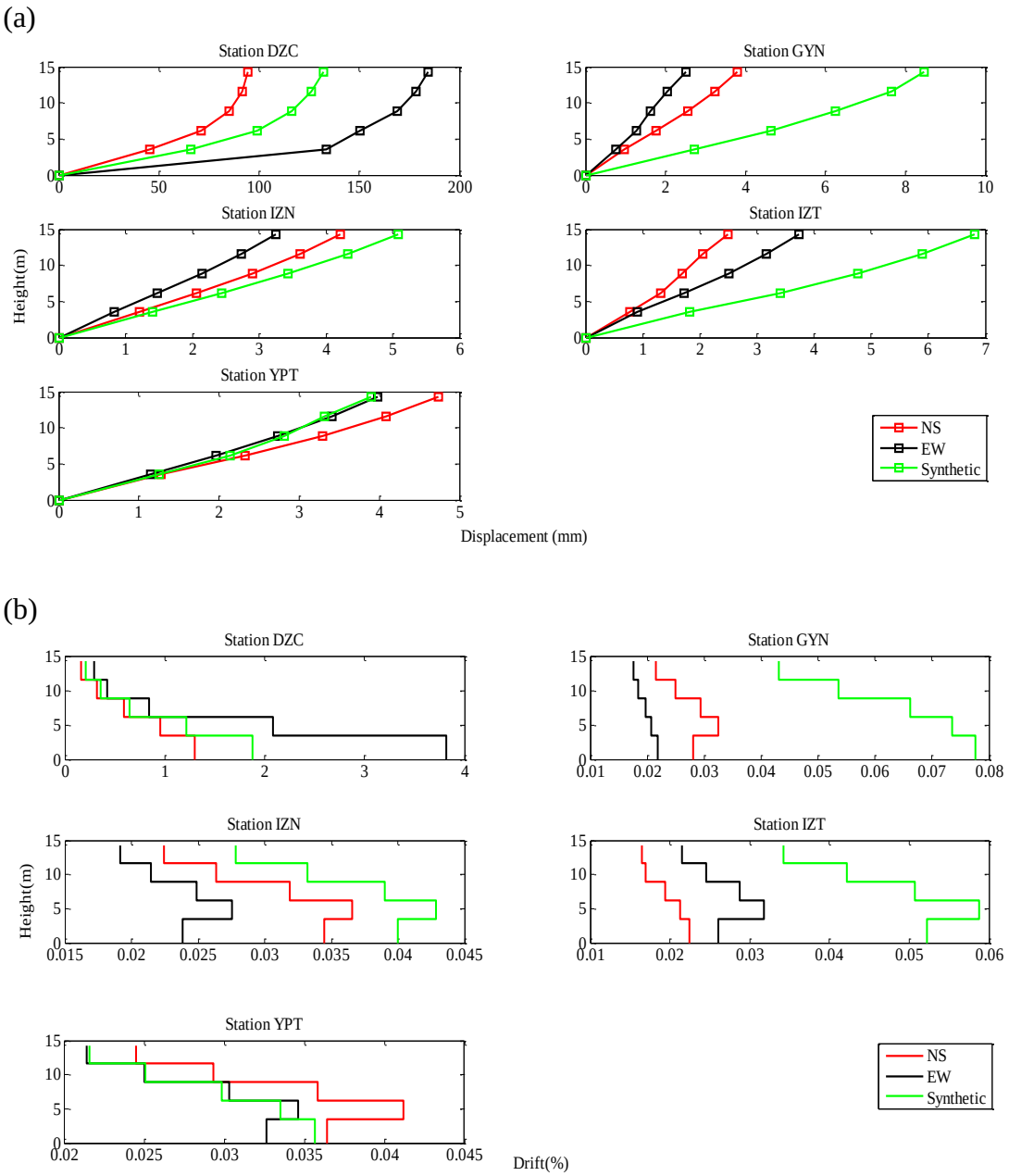

Figure 5.29 Distribution of (a): maximum story displacements and (b): maximum drift ratios due to the real and simulated records of Düzce Earthquake – F7-5S4B

(a)

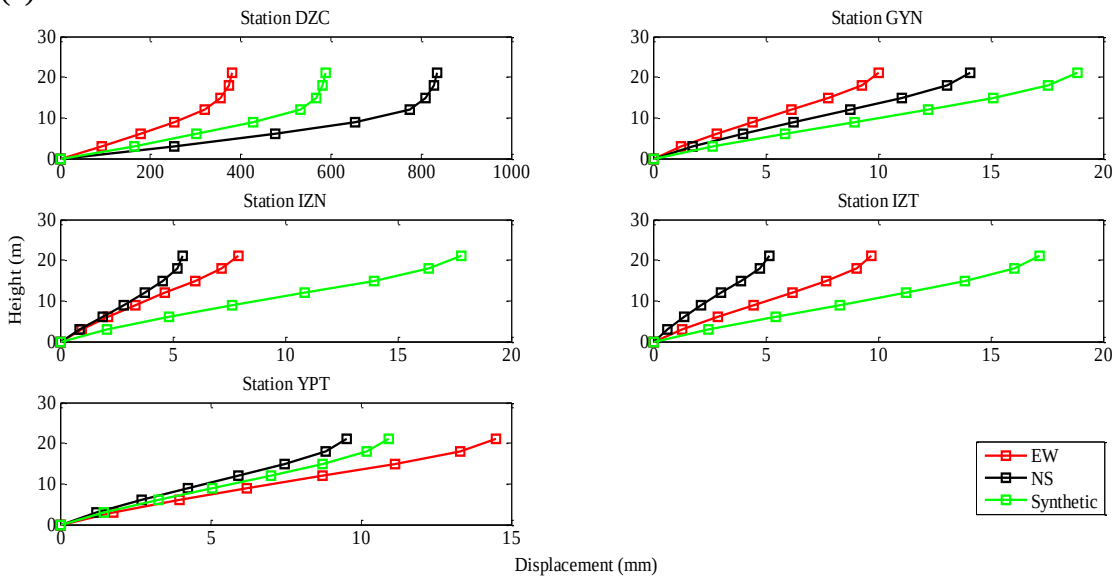

(b)

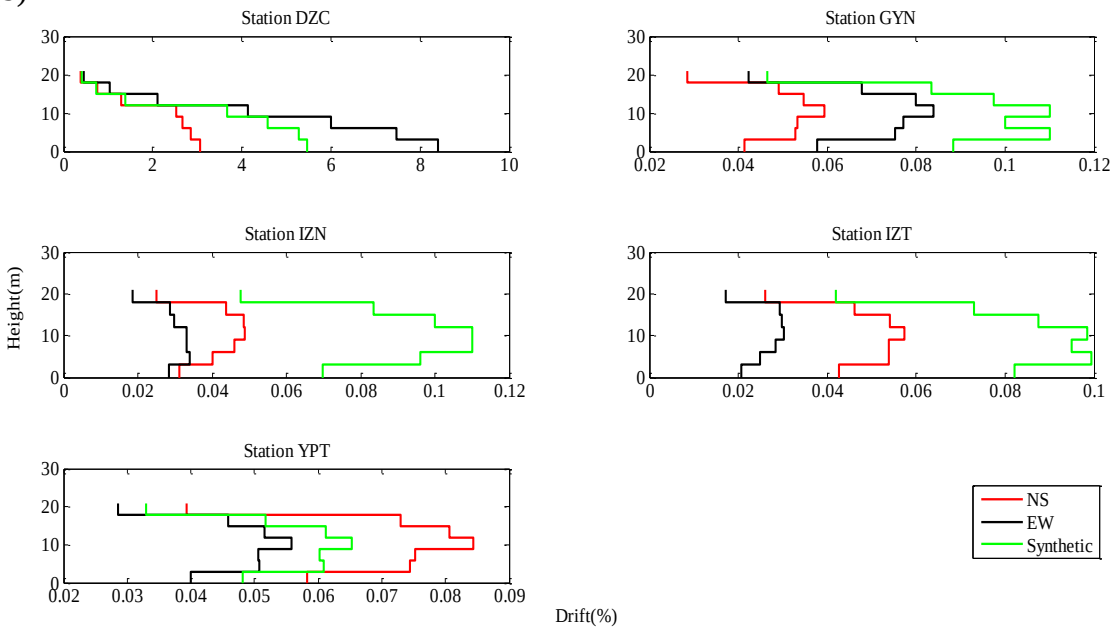

Figure 5.30 Distribution of (a): maximum story displacements and (b): maximum drift ratios due to the real and simulated records of Düzce Earthquake – F8-7S3B

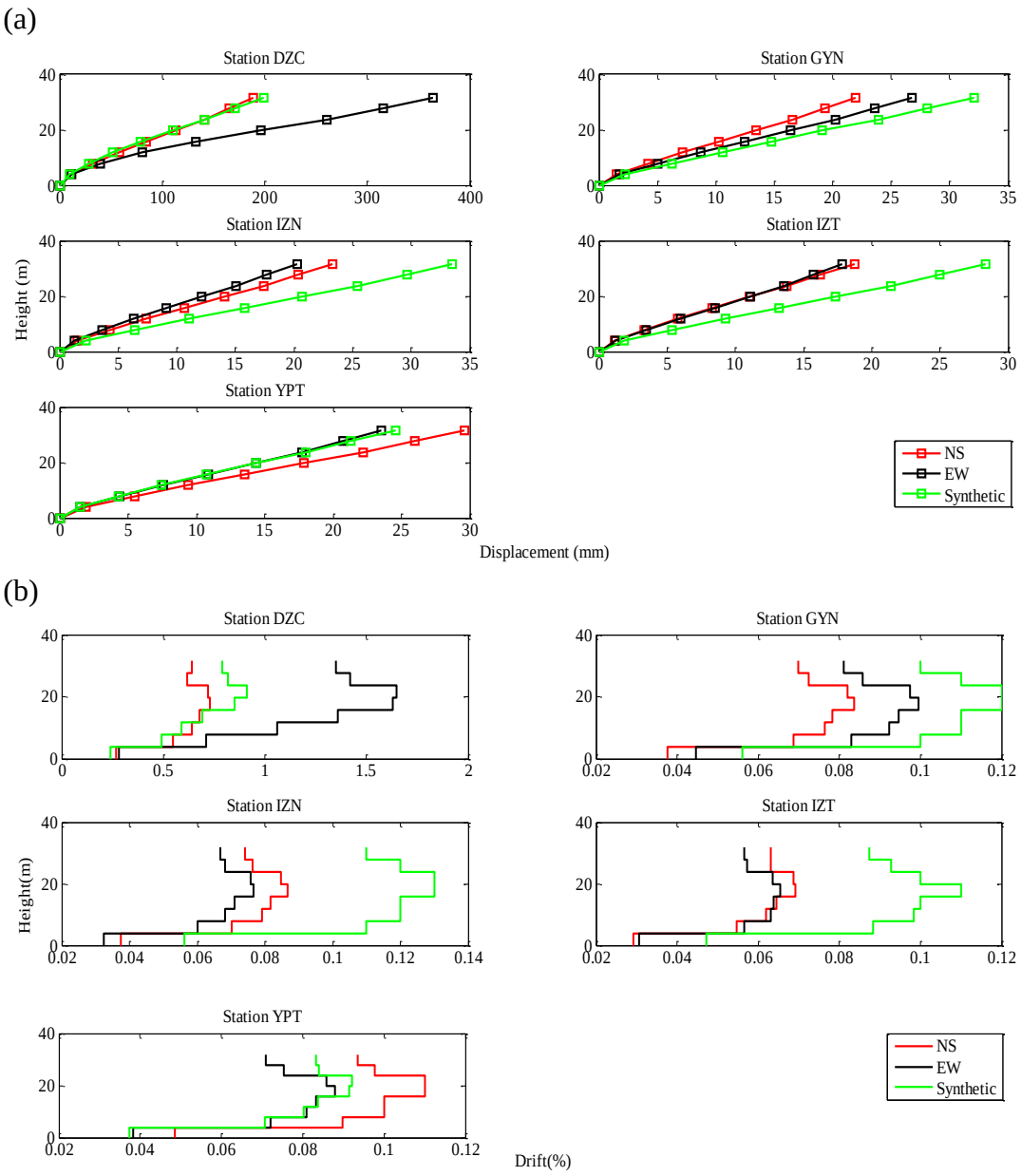

Figure 5.31 Distribution of (a): maximum story displacements and (b): maximum drift ratios due to the real and simulated records of Düzce Earthquake – F9-8S3B

Table 5.14 Top story displacements of observed and simulated data at the stations for the 1999 Düzce earthquake

Frame ID	Top Story Displacement	Station				
		DZC	GYN	IZN	IZT	YPT
F1-3S2B	Real (mm)	108.7733	2.4395	2.4800	2.9443	4.1638
	Synthetic /Real	1.0868	3.8405	2.2789	2.2755	0.9983
F2-3S2B	Real (mm)	154.7119	4.6696	7.6369	4.0036	8.3841
	Synthetic /Real	0.8950	2.3382	1.2454	1.1392	0.6570
F3-3S3B	Real (mm)	126.3496	2.9137	4.1395	3.0760	4.2833
	Synthetic /Real	1.1637	2.9099	1.1096	2.0218	0.9761
F4-4S3B	Real (mm)	155.1622	3.9962	8.6460	3.6219	7.4045
	Synthetic /Real	0.9900	2.6232	0.9991	1.3460	0.6452
F5-4S3B	Real (mm)	152.2708	2.2616	2.4103	2.7429	3.7784
	Synthetic /Real	0.8446	3.0203	2.3890	2.1278	1.0553
F6-5S2B	Real (mm)	160.5637	5.7227	7.1243	4.3898	7.8122
	Synthetic /Real	1.0482	1.7715	1.4230	1.5463	0.7249
F7-5S4B	Real (mm)	131.7978	3.0930	3.6972	3.0489	4.3450
	Synthetic /Real	1.0021	2.7401	1.3739	2.2355	0.8971
F8-7S3B	Real (mm)	564.5692	11.8811	6.5486	7.0597	11.7391
	Synthetic /Real	1.0424	1.5863	2.7133	2.4305	0.9314
F9-8S3B	Real (mm)	262.2008	24.2472	21.7067	18.3138	26.3956
	Synthetic /Real	0.7606	1.3244	1.5437	1.5469	0.9304

Table 5.15 Misfits in terms of nonlinear responses (Misfit$_{NR}$) to real and simulated data at the stations for the 1999 Düzce earthquake

Frame ID	Station				
	DZC	GYN	IZN	IZT	YPT
F1-3S2B	0.0506	0.6054	0.3258	0.3223	0.0166
F2-3S2B	0.0895	0.3587	0.0571	0.0420	0.2059
F3-3S3B	0.1426	0.4837	0.0560	0.2780	0.0051
F4-4S3B	0.1192	0.4142	0.0807	0.1184	0.2104
F5-4S3B	0.2184	0.4890	0.3594	0.2740	0.0188
F6-5S2B	0.0567	0.2704	0.0541	0.1569	0.1353
F7-5S4B	0.1658	0.4705	0.1238	0.3465	0.0353
F8-7S3B	0.1920	0.2115	0.4040	0.3855	0.0843
F9-8S3B	0.0773	0.1147	0.1984	0.1962	0.0296

Results expressed in Figures 5.23-5.31 and Tables 5.11-5.15 corresponding to all frames are summarized as follows:

- Nonlinear time history analyses of frame F1-3S2B reveal that at stations DZC and YPT a good match is obtained in between the real and estimated dynamic responses in terms of either maximum story displacement or drift ratio (Figure 5.23 and Table 5.14). The simulated motions provide conservative displacement values compared to real ones where the factor of overestimation is approximately 4 at station GYN, and 2 at stations IZN and IZT. The nonlinear response misfits presented in Table 5.15 demonstrates that the calculated error at stations DZC and YPT is almost zero. However this misfit is larger for the other stations.

- The estimated nonlinear responses for frame F2-3S2B, as a deficient frame, are satisfactory at most of the stations. Both predicted and real nonlinear responses are at the same range at stations DZC, IZN, and IZT despite negligible differences. Overestimation of the real responses is observed at station GYN by a factor of approximately 2 (Figure 5.24). On the other hand, estimated nonlinear responses are smaller than the observed ones at station YPT.

- For frame F3-3S3B, Figure 5.25 reveals that the predicted nonlinear responses are in the same ranges with the real ones at stations DZC, IZN, and YPT. However, real responses are overestimated at stations GYN and IZT by factors of 3 and 2, respectively.

- The predicted structural responses for frame F4-4S3B are satisfactory at stations DZC, IZN, and IZT. Simulated motion overestimates the real responses by a factor of 2.5 at station GYN whereas it underestimates the real responses by a factor of approximately 1.5 at station YPT (Figure 5.26).

- Results presented in Figure 5.27 for frame F5-5S3B demonstrate a good fit for real responses at stations DZC and YPT; however, at the other stations (GYN, IZN, and IZT), the observed maximum story displacements as well as the drift ratios are overestimated by simulated records. The real structural responses are overestimated by a factor of 3 at station GYN and 2 at stations IZN and IZT.

- For frame F6-5S2B, the real and simulated records at stations DZC and YPT result in approximately similar dynamic responses. For this frame, at stations GYN and IZT, the real responses are overestimated by a factor of 1.5. Simulated record at station IZN yields practically the same dynamic response with the real responses corresponding to the NS component of real record (Figure 5.28).

- Frame F7-5S4B has approximately same structural behavior to that of frame F6-5S2B under simulated ground motion records at all stations. For this frame, the real and simulated records at stations DZC, IZN, and YPT result in similar dynamic responses, despite some slight differences. However, the results corresponding to stations GYN and IZT reveal that real structural responses are overestimated by a factor of 2.5 with simulated records (Figure 5.29).

- For F8-7S3B, the estimated structural responses are close to the real ones at stations DZC and YPT (Figure 5.30). At other stations, the observed maximum top story displacement is overestimated by a factor of 1.5 at station GYN, and 2.5 at stations IZN and IZT.

- Finally, the simulated nonlinear responses are reasonable when compared to real responses at all stations for frame F9-8S3B (Figure 5.31). However, dynamic responses at stations GYN, IZN, and IZT are still slightly overestimated.

When seismological misfits are compared against nonlinear response misfits for Düzce earthquake that occurred on a shallower alluvial basin compared to Erzincan, the following observations are derived:

For station DZC, both of the frequency/period-dependent misfits are close indicators of NR misfits. Among NSS misfits, I_a, *PGA*, and *CAV* are in closet agreement with NR misfits (having the same order in terms of average misfits with maximum of 20% difference) while t_{eff} and *HI* misfits are not.

For stations GYN and IZN, both RS and FAS misfits are in agreement with NR misfits. When NSS misfits are considered, it is observed that *CAV* has the least agreement with NR misfits (97% difference).

For station IZT, all seismological misfits are in agreement with NR misfits (with maximum of 14% difference in average) except t_{eff}.

Finally at station YPT, misfit in terms of *PGA* has the largest agreement with NR misfits (in average 14% difference). For this station, similarly, both frequency/period-dependent misfits are close indicators of NR misfits while the RS misfit has larger accuracy than FAS.

Further details about the comparison of seismological misfits with nonlinear response misfits for Düzce earthquake are presented in Appendix F.2.

5.5 Third Case Study: Ground Motion Simulation of the 2009 L'Aquila (Mw=6.3) Earthquake

5.5.1 General

L'Aquila earthquake (Mw=6.3), occurred on April 6, 2009 at 1:32 GMT in the Abruzzo region of central Italy, very close to the L'Aquila town with approximately 70,000 inhabitants. This event occurred on a NW–SE trending normal fault with strike, dip, and rake angles of 133°, 54°, -102°. The 20 km long rupture was in the central Apennines, a mountain which is created as result of subduction of the Adria micro-

plate underneath the Apennines from east to west (Cirella *et al.*, 2009; Gallovič and Zahradník, 2012). The epicenter was located in 95 km NE of Rome, about 5 km SW of L`Aquila and 10 km west of Paganica where the main surface rupture was mapped.

Despite its intermediate size, 6 April 2009 L'Aquila earthquake led to extreme structural damage and loss of life with approximately 300 casualties and 1,500 injured people in the near-fault area. In this event, around 17,000 people were moved out to emergency shelters and the total cost of damage to buildings is estimated to be 2–3 billion Euros (Salamon, 2010). It is considered as the third largest earthquake occurred in Italy after the 1980, Mw= 6.9, Irpinia and the 1976, M= 6.4, Friuli earthquakes.

Unlike two previous case studies, in the review of the literature, a detailed source model is found for the L'Aquila earthquake by Ameri *et al.* (2009) which made it possible to model both lower and higher frequencies of ground motion records by implementing a hybrid approach. Thus, the 2009 L'Aquila earthquake was simulated using two alternative simulation techniques: Stochastic finite-fault methodology by Ugurhan *et al.* (2012) and Hybrid-Integral-Composite method (HIC) by Ameri *et al.* (2012). In this section, the simulation results from these two previous studies are readily used.

Description of the earthquake along with the real strong ground motion dataset is presented in Section 5.5.2. Section 5.5.3 includes simulated ground motion dataset that was generated for this event using two alternative ground motion simulation methods. Also, in this section, the hybrid-integral-composite method is described in detail. Comparison of the real and simulated results in terms of time histories and seismological misfits are all presented in Section 5.5.4. Finally, nonlinear time history analyses of the structures with the corresponding observations are given in Section 5.5.5.

5.5.2 Real ground motion data of the 2009 L'Aquila (Mw=6.3) earthquake

L'Aquila earthquake is identified as an event with evident forward and backward directivity effects. The records measured at stations that are located in the forward direction of the rupture propagation have higher peak ground accelerations with shorter durations. On the other hand, the stations oriented in the opposite directions have smaller peak amplitudes with longer durations.

Overall, there exist 264 aftershock and mainshock records at 56 strong ground motion stations. However, within 50 km of epicenter of earthquake, the mainshock was recorded at 14 strong motion stations. The large variability of ground motion amplitudes around the fault plane may be attributed to a combination of source and wave propagation effects (Ameri *et al.*, 2012). Most of the near-fault stations are located on sites with class A according to EC8 soil classification; however, some stations are located on softer soils where local site effects are pronounced.

In this study, for use in nonlinear time history analyses of the selected MDOF buildings, records of only 7 stations from the near-fault area are employed. Four out of these stations are located on site class A. The raw real records are taken from Italian strong ground motion database (ITACA, http://itaca.mi.ingv.it/ItacaNet). Figure 5.32 displays the map of the meizoseismal region with the epicenter, fault plane, and locations of the selected stations. Table 5.16 lists further information regarding the locations and site classes of these stations.

Table 5.16 Information on the strong motion stations that recorded the 2009 L'Aquila earthquake

Station	Code	Latitude (°)	Longitude (°)	Site Class (EC8)	R_{epi} (km)	PGA-EW (cm/s^2)	PGA-NS (cm/s^2)	PGV-EW (cm/s)	PGV-NS (cm/s)
V. Aterno-F. Aterno	AQA	42.376	13.339	B	4.2	350.46	347.59	29.86	24.07
Celano	CLN	42.085	13.5207	A	31.79	73.49	76.57	4.61	6.56
Fiamignano	FMG	42.268	13.1172	A	23.17	20.12	24.53	2.52	1.67
Gran Sasso	GSA	42.421	13.5194	B	14.15	131.88	139.02	9.63	7.41
Leonessa	LSS	42.558	12.9689	A	40.62	9.21	7.61	0.71	0.72
Montereale	MTR	42.524	13.2448	A	22.13	42.17	51.65	3.25	3.09
Sulmona	SUL	42.09	13.9343	C	54.29	27.04	24.53	2.69	2.82

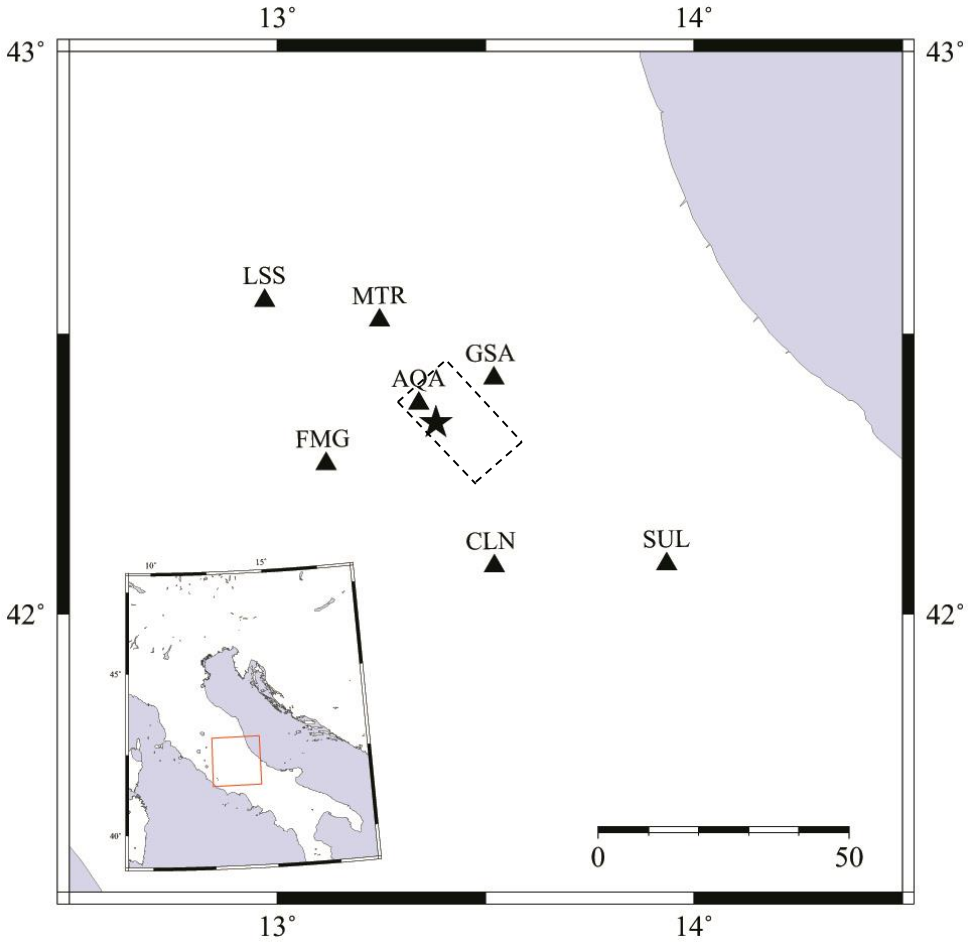

Figure 5.32 Map showing the fault plane and epicenter of 2009 L'Aquila earthquake with the locations of the selected stations

5.5.3 Simulated ground motion data for the 2009 L'Aquila (Mw=6.3) earthquake

The first objective of this case study is to compare the horizontal real records observed at the selected seven stations with the corresponding simulated records obtained from two alternative simulation approaches introduced in two recent papers (Ugurhan *et al.*, 2012 and Ameri *et al.*, 2012). The two different simulation techniques used by these authors are stochastic finite-fault method (Motazedian and Atkinson, 2005) and hybrid-integral-composite method (Gallovič and Brokešová, 2007), respectively. Next, the techniques used for simulating the L'Aquila earthquake along with the source, path, and site models are summarized briefly.

5.5.3.1 Simulated records from the stochastic finite-fault method

Ugurhan *et al.* (2012) used the stochastic finite-fault method based on a dynamic corner frequency approach (Motazedian and Atkinson, 2005) to simulate the 2009 L'Aquila earthquake. The authors used this method to test four different sets of models for alternative source, path, and site parameters to simulate the 2009 L'Aquila mainshock. They performed sensitivity analyses for source and path effects by employing two finite-fault source models that take into account the source complexity of the event along with two alternative path models derived from regional weak and strong ground motion databases. To pick the most physical and reliable input parameters set, they minimized the misfit in terms of the Fourier amplitude spectra at 21 near-field stations. Attenuation of the synthetics with distance was also compared with the ground motion prediction equations. The simulated ground motions were further validated against the spatial distribution of shaking intensity obtained from the "Did You Feel It?" project (http://earthquake.usgs.gov/data/dyfi/) and site survey results. The source, path, and site parameters used for simulation of the L'Aquila earthquake are described in detail below.

5.5.3.1.1 Source model

The coordinates of 2009 L'Aquila earthquake's epicenter was reported as 42.423º N, 13.395º E by the Institute of Geophysics and Volcanology (INGV) in Italy. The focal

depth was reported as 9 km by the same institution. Following the fault definitions stated in Cirella *et al.* (2009), the fault plane was modeled with 28 km length and 17.5 km width along with sub-fault dimensions of 1 km x 1 km. The top of the rupture plane is 0.5 km from the Earth's surface. The strike and dip angles of the fault plane are 133º and 54º, respectively. Ugurhan *et al.* (2012) validated that, among different slip distribution models existing in the literature, the model by Cirella *et al.* (2009) minimizes the error in between the real and simulated records in the lower frequency domain. The stress drop for simulation of the 2009 L'Aquila earthquake is assumed as 150 bars. The applied source parameters are presented in Table 5.17.

Table 5.17 Source parameters of the 2009 L'Aquila earthquake

Parameter	**Value**
Moment Magnitude	6.3
Epicenter Location	42.423ºN, 13.395ºE
Hypocenter Depth	9 km
Depth to the top of the Fault Plane	0.5 km
Fault Orientation	Strike=133º; Dip=54º
Fault Dimensions	28 km x 17.5 km
Sub-fault Dimensions	1 km x 1 km
Crustal Shear Wave Velocity (β)	3500 m/s
Rupture Velocity	0.8β
Crustal Density	2800 kg/m^3
Stress Drop	150 bars
Pulsing Area Percentage	50

5.5.3.1.2 Path model

For this case study, among various models in the literature for frequency-dependent and geometrical attenuation, the ones proposed by Malagnini *et al.* (2008) are used. These parameters are obtained through regression analyses of a set of weak motion records from Central Italy where frequency-dependent attenuation is specified as $Q =$

$140f^{0.25}$. For geometrical spreading, the following piecewise function of hypocentral distance is utilized:

$$\begin{cases} R^{-1.1}, & R < 10\ Km \\ R^{-07}, & 10 \leq R < 30\ Km \\ R^{-0.5}, & R \geq 30\ Km \end{cases} \quad (5.11)$$

Duration model of Malagnini *et al.* (2008) is assessed based on random vibration theory (e.g.: Cartwright and Longuet-Higgins, 1956) and is a pricewise linear function of the hypocentral distance as follows:

$$\begin{cases} 0.1607R, & 0 < R \leq 40 \\ 0.10673R, & 40 < R \leq 80 \\ 0.005R, & R \geq 80 \end{cases} \quad (5.12)$$

5.5.3.1.3 Site model

For this case study at all stations, the generic site amplification factors proposed by Boore and Joyner (1997) obtained based on quarter wavelength theory were utilized. According to EC8 soil classification, AQA and GSA are located on class B sites which correspond to soil class C according to NEHRP classification. Therefore, for these stations, NEHRP class C soil amplification factors as listed in Table 5 of Boore and Joyner (1997) were utilized. Stations CLN, FMG, LSS, and MTR are identified as soil class A according to EC8 where generic rock amplification factors proposed by Boore and Joyner (1997) were implemented. Station SUL is located on soil class C according to EC8 classification and generic soil amplification factors were considered. The spectral decay at high frequencies was modeled by assuming a uniform κ=0.035 at all stations (Malagnini *et al.*, 2008).

From this point onward, in this thesis the simulated ground motions obtained from this technique are named as Synthetic-SFF records. It should be noted that there is only one Synthetic-SFF record per station as the stochastic method provides a single horizontal component at each simulation site.

5.5.3.2 Simulated records from the hybrid-integral-composite method

To regenerate the observed records of the 2009 L'Aquila earthquake, Ameri *et al.* (2012) used a broadband hybrid-integral-composite technique. Introduced by Gallovič and Brokešová (2007), HIC method relies on the representation theorem with a k-squared slip distribution over the fault plane in the low-frequency band. For the high frequencies, the method uses a composite application of Brune's source time functions with proper seismic moment and corner frequency defined by the sub-fault sizes. The amplitudes from the integral and composite approaches are combined in a cross-over frequency band which is selected carefully depending on the upper limit of the frequencies where directivity effects are to be modeled. In this method, full waveform Green's functions for both calculations are calculated by the discrete wave-number technique (Bouchon, 1981) for a general 1D layered model; and if available, 1D local soil models at the stations.

Ameri *et al.* (2012) simulated the near-fault records of the L'Aquila earthquake over the entire frequency band of engineering concern (0.1 - 10 Hz) using HIC method where source parameters were constrained in the low-frequency range by a detailed source inversion (Gallovič and Zahradník, 2012). The authors compared the observed and simulated records in time and frequency domains and adopted the Olsen and Mayhew (2010) goodness-of-fit criteria to quantify the quality of their modeling. The further details and main parameters used in simulation can be found in Table 3 of Ameri *et al.* (2012).

From this point onward, in this thesis the simulated ground motions obtained from this technique are named as Synthetic-HIC records. There will be two horizontal Synthetic-HIC components at each site as the method can effectively simulate EW and NS components of the ground motion.

5.5.4 Comparison of simulated and real ground motion data for the 2009 L'Aquila (Mw=6.3) earthquake

Obtained from Synthetic-SFF and Synthetic-HIC record sets, at every station there is a total of 3 simulated and 2 real horizontal components which sum up to 35 records at 7 stations used as input ground motions to dynamic analyses of the selected frames. Similar to the previous two case studies, the simulated and real records are not scaled or modified by any means other than baseline correction and filtering between 0.1 and 10 Hz with 4^{th} order Butterworth filter type. Figures 5.33-5.39 display the real and simulated acceleration time histories, the corresponding Fourier amplitude spectra, and elastic response spectra with 5% damping at each station.

It is noted that the two alternative simulation methods are performed in two independent studies thus identical source or path models were not employed. Hence, it might not seem valid to compare these simulations with each other. However, these models use different but consistent model parameters. In addition, they are compared against the real records and not directly with each other.

(a)

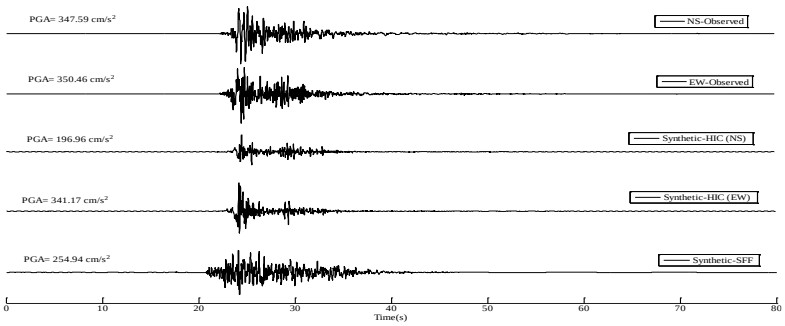

(b)

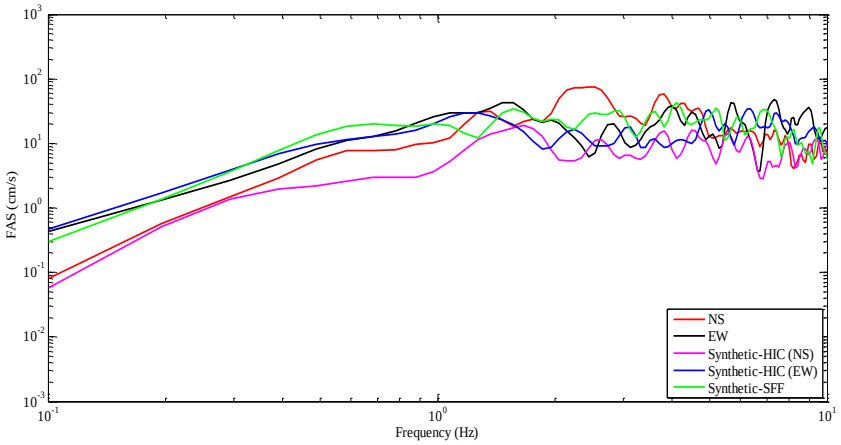

(c)

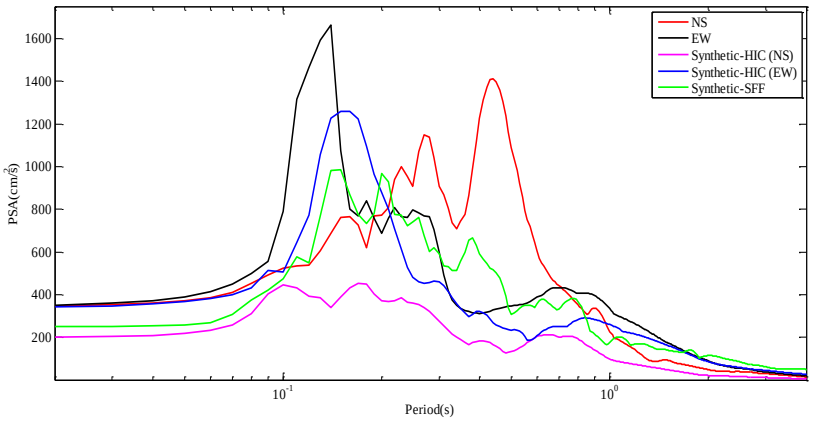

Figure 5.33 Station AQA; (a) Observed and simulated accelerograms (b) Fourier amplitude spectra (c) Response spectra with 5% damping obtained for observed (NS and EW) and simulated horizontal components (Synthetic-SFF and Synthetic-HIC)

(a)

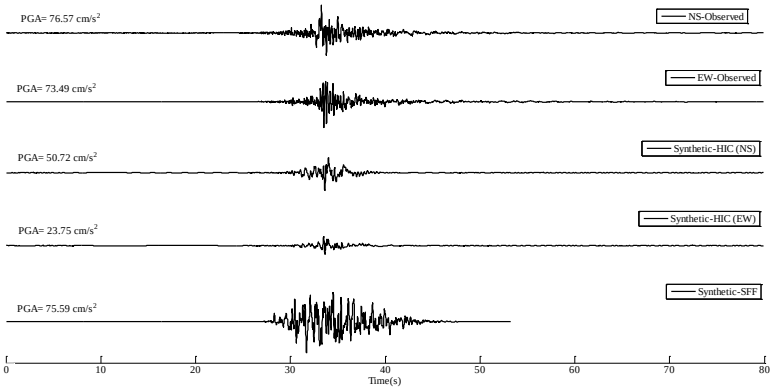

(b)

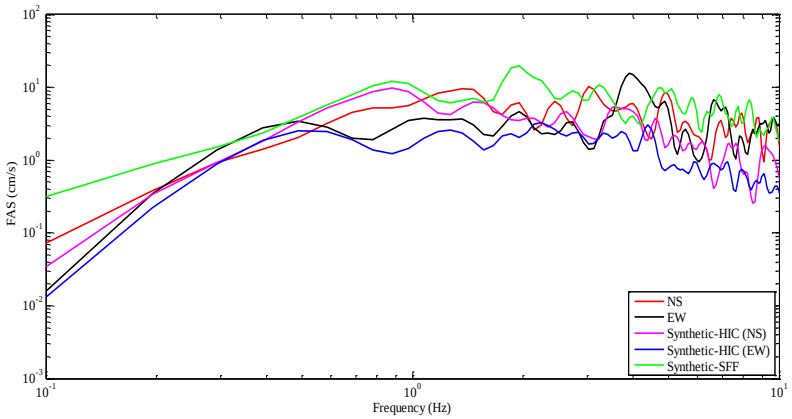

(c)

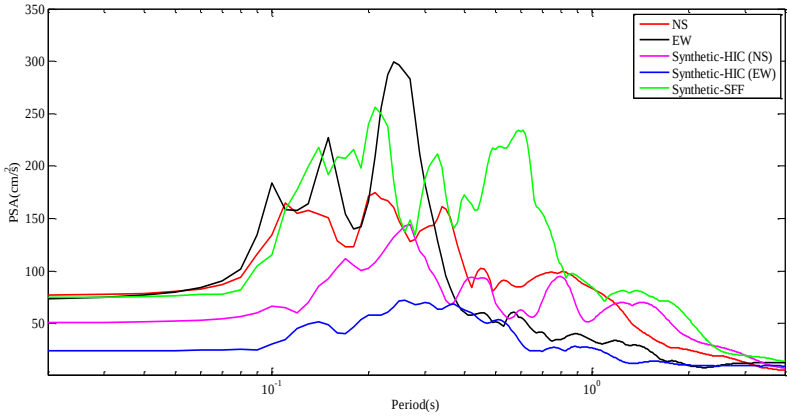

Figure 5.34 Station CLN; (a) Observed and simulated accelerograms (b) Fourier amplitude spectra (c) Response spectra with 5% damping obtained for observed (NS and EW) and simulated horizontal components (Synthetic-SFF and Synthetic-HIC)

(a)

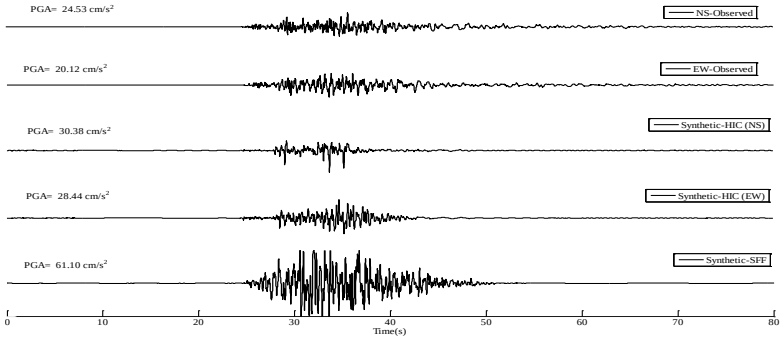

(b)

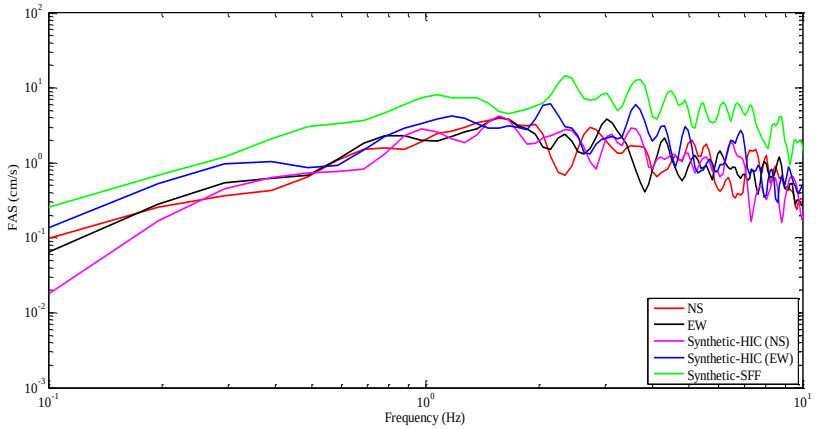

(c)

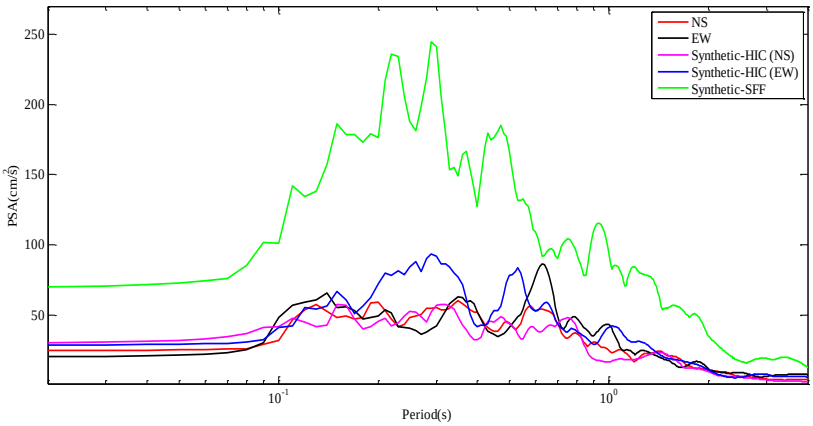

Figure 5.35 Station FMG; (a) Observed and simulated accelerograms (b) Fourier amplitude spectra (c) Response spectra with 5% damping obtained for observed (NS and EW) and simulated horizontal components (Synthetic-SFF and Synthetic-HIC)

(a)

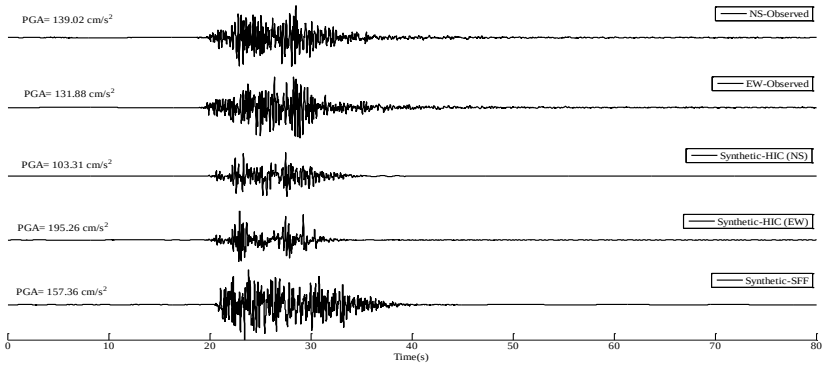

(b)

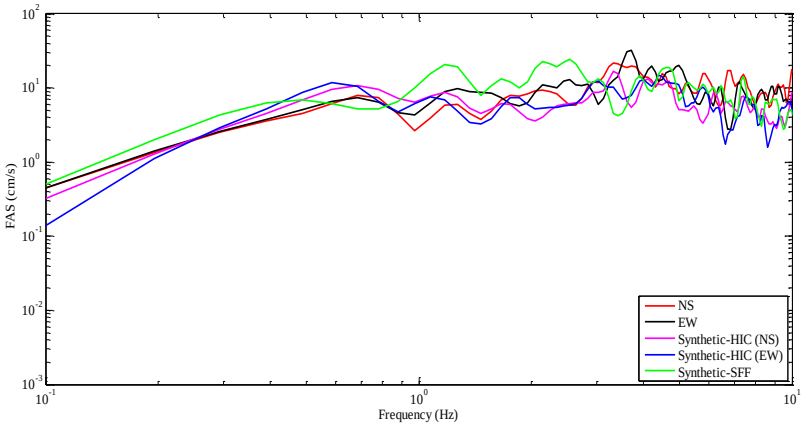

(c)

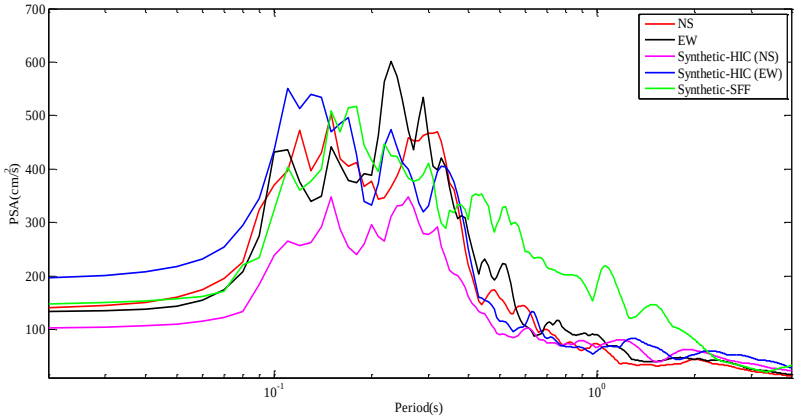

Figure 5.36 Station GSA; (a) Observed and simulated accelerograms (b) Fourier amplitude spectra (c) Response spectra with 5% damping obtained for observed (NS and EW) and simulated horizontal components (Synthetic-SFF and Synthetic-HIC)

(a)

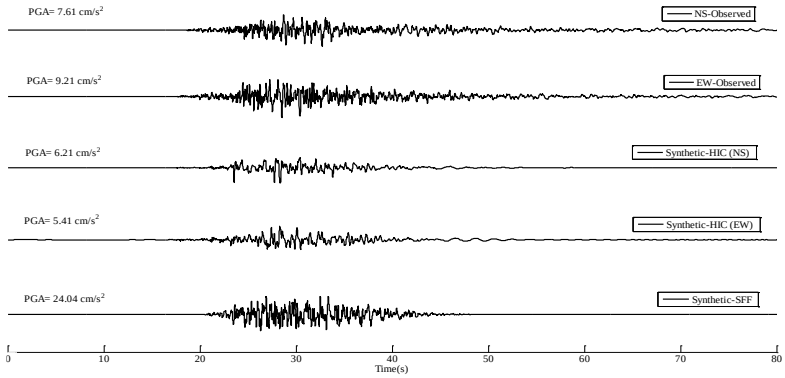

(b)

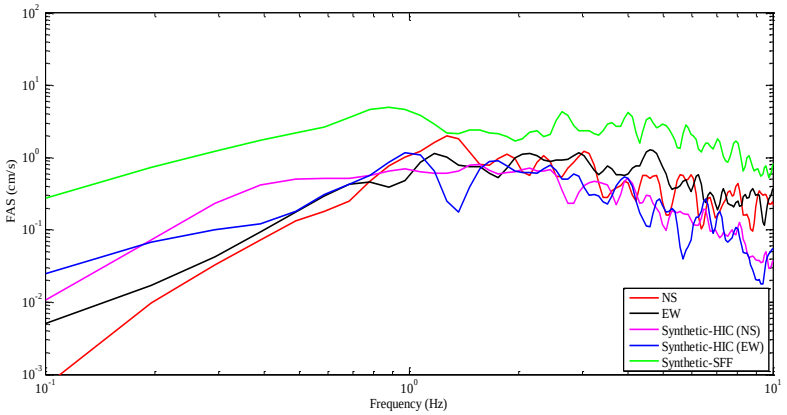

(c)

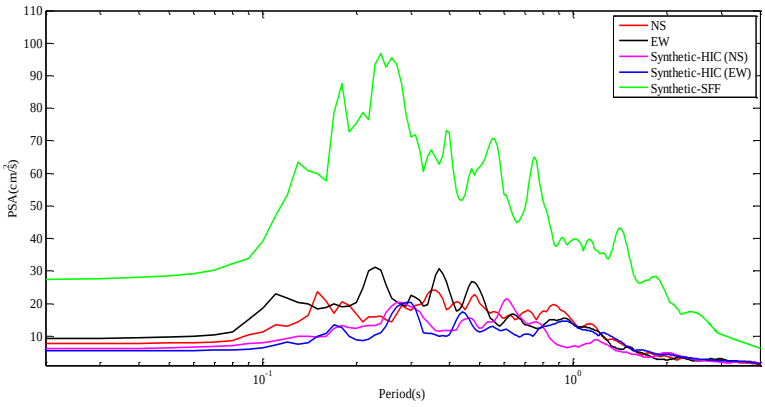

Figure 5.37 Station LSS; (a) Observed and simulated accelerograms (b) Fourier amplitude spectra (c) Response spectra with 5% damping obtained for observed (NS and EW) and simulated horizontal components (Synthetic-SFF and Synthetic-HIC)

(a)

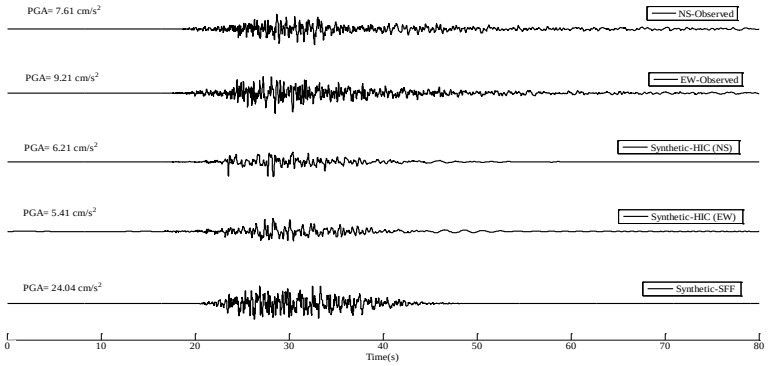

(b)

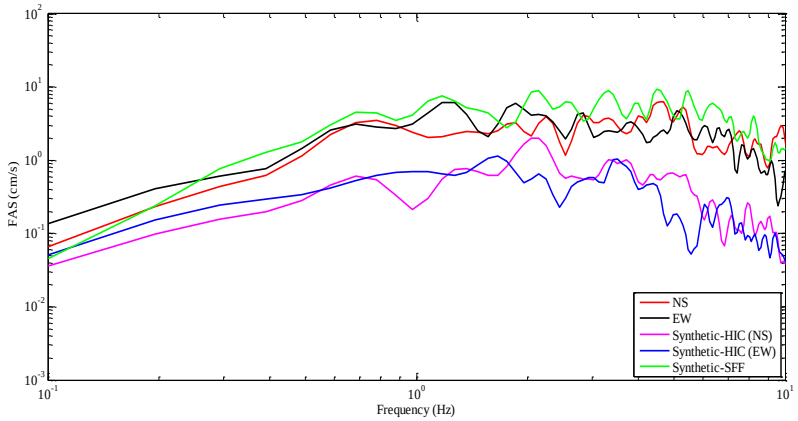

(c)

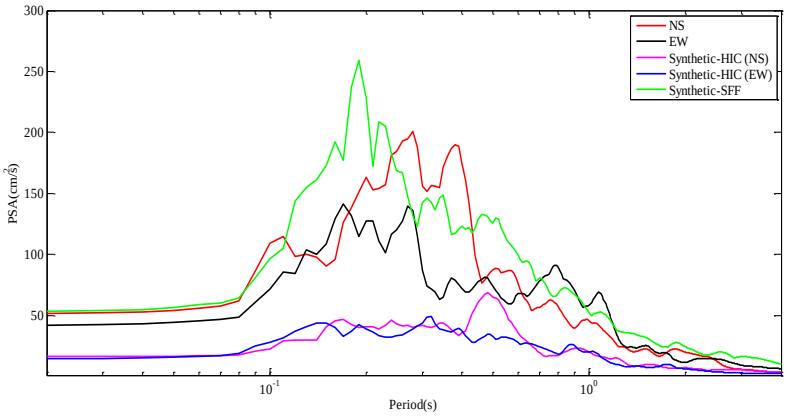

Figure 5.38 Station MTR; (a) Observed and simulated accelerograms (b) Fourier amplitude spectra (c) Response spectra with 5% damping obtained for observed (NS and EW) and simulated horizontal components (Synthetic-SFF and Synthetic-HIC)

(a)

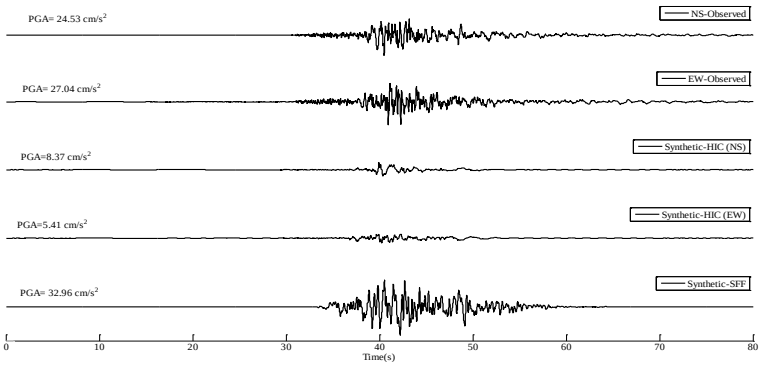

(b)

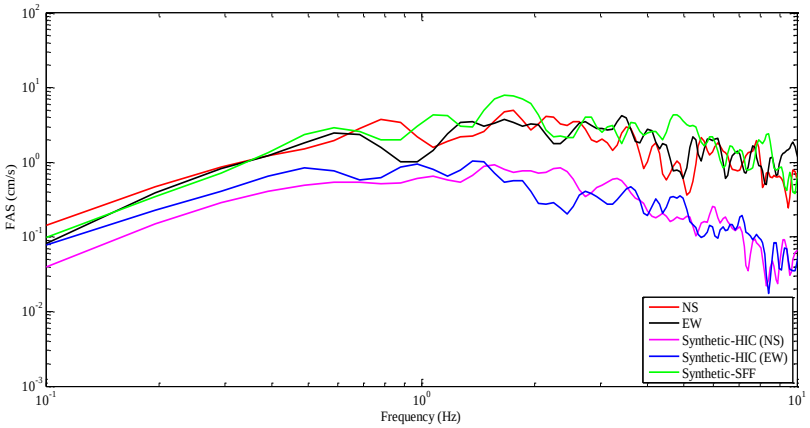

(c)

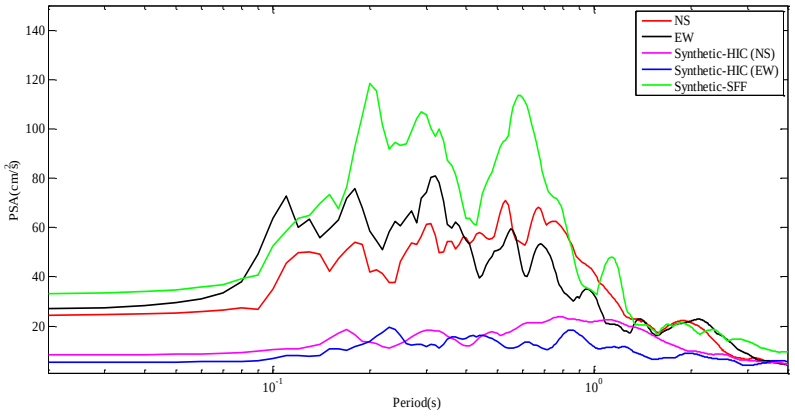

Figure 5.39 Station SUL; (a) Observed and simulated accelerograms (b) Fourier amplitude spectra (c) Response spectra with 5% damping obtained for observed (NS and EW) and simulated horizontal components (Synthetic-SFF and Synthetic-HIC)

The results presented in Figure 5.33 demonstrate a remarkable fit between EW component of real and simulated records from Synthetic-HIC method in terms of PGA, Fourier amplitude spectra, and response spectra for station AQA. However, NS component of real records is underestimated by the Synthetic-HIC method. For this station, Synthetic-SFF technique closely reproduces the major features of the observed records in both directions. Figure 5.34 reveals that, at station CLN, high-frequency content of the observed record is well estimated by Synthetic-SFF method whereas the low-frequency content is effectively reproduced by Synthetic-HIC technique. In addition, the observed PGA is well simulated by Synthetic-SFF technique. At station FMG, the observed FAS, RS, and PGA values are in close agreement with the simulated ones from the Synthetic-HIC method. However, these values are overestimated by the simulated time series using the Synthetic-SFF technique (Figure 5.35). At station GSA, Figure 5.36 demonstrates a good match between the real and simulated records from two alternative techniques for all frequencies. The results corresponding to station LSS as presented in Figure 5.37 shows a good agreement in FAS and RS amplitudes of the real and simulated records from Synthetic-HIC method for all frequencies. However, there exist a minor overestimation and underestimation of the lower and higher frequencies, respectively. As a result, the PGA values are slightly underestimated by Synthetic-HIC method. On the other hand, at this station, Synthetic-SFF technique overestimates the PGA, FAS, and RS amplitudes overall. When the results at stations MTR and SUL are considered, it becomes clear that among these two methods, the Synthetic-SFF technique predicts the real amplitudes more accurately as compared to the Synthetic-HIC technique (Figures 5.38 and 5.39).

Before presenting nonlinear time history analyses of the MDOF structures, in this section, it is aimed to quantify the differences between the real and simulated records at the selected stations. For this purpose, results corresponding to all seismological misfits are listed in Tables 5.18-5.20.

Table 5.18 SS misfits in terms of fast Fourier amplitude spectra ($Misfit_{FAS}$) for real and simulated data at the stations for the 2009 L'Aquila earthquake

Frame ID	Method	Station						
		AQA	CLN	FMG	GSA	LSS	MTR	SUL
F1-3S2B	Synthetic-HIC	0.8658	1.1674	0.7627	0.7626	1.2673	2.1634	2.1624
	Synthetic-SFF	0.7040	0.8732	1.5523	0.8484	1.3853	0.8448	0.7913
F2-3S2B	Synthetic-HIC	0.9570	0.9125	0.7353	0.6978	0.9721	1.8451	1.7999
	Synthetic-SFF	0.6814	0.9834	1.5702	0.8038	1.4570	0.9232	0.6868
F3-3S3B	Synthetic-HIC	0.8999	1.0390	0.8025	0.7471	1.1005	2.0473	2.0709
	Synthetic-SFF	0.7005	0.9440	1.5442	0.8060	1.4367	0.8356	0.7640
F4-4S3B	Synthetic-HIC	0.9786	0.9110	0.7706	0.7065	0.9621	1.8754	1.8345
	Synthetic-SFF	0.6675	0.9806	1.5906	0.7826	1.4898	0.9148	0.6977
F5-4S3B	Synthetic-HIC	0.8556	1.2311	0.7624	0.8013	1.3474	2.3009	2.1933
	Synthetic-SFF	0.6981	0.8743	1.5254	0.8643	1.3511	0.8430	0.7923
F6-5S2B	Synthetic-HIC	0.9368	0.8528	0.7184	0.7000	0.9559	1.7680	1.7970
	Synthetic-SFF	0.6356	1.0125	1.4790	0.7800	1.3901	0.9140	0.7018
F7-5S4B	Synthetic-HIC	0.8935	1.0727	0.7938	0.7412	1.1496	2.1007	2.1108
	Synthetic-SFF	0.6952	0.9174	1.5812	0.8013	1.4550	0.8403	0.7805
F8-7S3B	Synthetic-HIC	0.9256	0.8069	0.6534	0.6613	0.8250	1.5054	1.6127
	Synthetic-SFF	0.6149	0.9536	1.4315	0.8762	1.3231	0.9176	0.6929
F9-8S3B	Synthetic-HIC	0.8456	0.6697	0.6398	0.6249	0.7291	1.3616	1.6027
	Synthetic-SFF	0.6616	1.0241	1.2805	0.8628	1.3078	0.9295	0.6341

Table 5.19 SS misfits in terms of response spectra (Misfit$_{RS}$) for real and simulated data at the stations for the 2009 L'Aquila earthquake

Frame ID	Method	Station						
		AQA	CLN	FMG	GSA	LSS	MTR	SUL
F1-3S2B	Synthetic-HIC	0.6101	0.5053	0.2535	0.3285	0.4583	0.9797	1.3848
	Synthetic-SFF	0.3956	0.5367	1.2538	0.3082	1.2032	0.3866	0.4182
F2-3S2B	Synthetic-HIC	0.6488	0.3915	0.2444	0.2870	0.3586	1.0101	1.2330
	Synthetic-SFF	0.3083	0.6616	1.0442	0.5257	1.2203	0.3457	0.4506
F3-3S3B	Synthetic-HIC	0.6605	0.4891	0.2657	0.3158	0.4224	0.9502	1.3448
	Synthetic-SFF	0.3750	0.6367	1.1442	0.3766	1.2184	0.3858	0.4750
F4-4S3B	Synthetic-HIC	0.6559	0.3980	0.2492	0.2913	0.3524	1.0106	1.2561
	Synthetic-SFF	0.3078	0.6759	1.0528	0.5093	1.2337	0.3480	0.4591
F5-4S3B	Synthetic-HIC	0.6338	0.4997	0.2555	0.3239	0.4387	0.9646	1.3756
	Synthetic-SFF	0.3903	0.5744	1.2190	0.3358	1.2186	0.3842	0.4387
F6-5S2B	Synthetic-HIC	0.6409	0.3839	0.2558	0.2848	0.3700	0.9928	1.1816
	Synthetic-SFF	0.3300	0.6360	1.0560	0.5643	1.1868	0.3391	0.4292
F7-5S4B	Synthetic-HIC	0.6561	0.4868	0.2619	0.3159	0.4272	0.9548	1.3534
	Synthetic-SFF	0.3822	0.6178	1.1761	0.3598	1.2235	0.3854	0.4660
F8-7S3B	Synthetic-HIC	0.5786	0.3509	0.2531	0.2953	0.3299	0.9884	0.9715
	Synthetic-SFF	0.3567	0.5577	1.0894	0.7394	1.1501	0.2914	0.4037
F9-8S3B	Synthetic-HIC	0.5044	0.3881	0.2107	0.3475	0.3006	0.9694	0.8504
	Synthetic-SFF	0.3682	0.6282	1.0789	0.8876	1.2543	0.3091	0.3152

Table 5.20 NSS misfits for real and simulated data at the stations for the 2009 L'Aquila earthquake

Station		AQA	CLN	FMG	GSA	LSS	MTR	SUL
$Misfit_{PGA}$	Synthetic-HIC	-0.2573	-0.5374	0.3232	0.0489	-0.3078	-0.6721	-0.7386
	Synthetic-SFF	-0.2696	0.0077	1.7503	0.1621	1.8716	0.1713	0.2798
$Misfit_{Teff}$	Synthetic-HIC	-0.0577	-0.2495	-0.6145	-0.1931	-0.4749	-0.2404	-0.3172
	Synthetic-SFF	0.5649	0.0016	-0.5155	0.3182	-0.4919	-0.0306	-0.5177
$Misfit_{Ia}$	Synthetic-HIC	-0.7489	-0.7751	-0.3091	-0.5194	-0.6243	-0.8984	-0.9143
	Synthetic-SFF	-0.1425	1.6278	7.049	0.6148	10.5016	1.076	0.8447
$Misfit_{CAV}$	Synthetic-HIC	-0.6064	-0.6281	-0.5109	-0.4882	-0.5377	-0.7635	-0.7824
	Synthetic-SFF	0.0072	0.388	0.8524	0.2127	1.4918	0.1761	-0.1231
$Misfit_{HI}$	Synthetic-HIC	-0.4258	-0.1018	-0.0514	0.1477	-0.0997	-0.6249	-0.5462
	Synthetic-SFF	-0.0031	1.2335	1.9966	1.0248	3.2999	0.2918	0.1776

Tables 5.18 and 5.19 demonstrate that the frequency/period-dependent misfits from Synthetic-HIC method at stations SUL and MTR are larger than the ones corresponding to the other stations. According to Ameri *et al.* (2012), these two stations are characterized by dominant site effects resulting in locally generated surface waves that cannot be modeled with the Synthetic-HIC methodology. For this case study, all frequency/period-dependent misfits from Synthetic-HIC methodology have decreasing trend with the increase of structural fundamental period at all stations. This is mainly because synthetic-HIC method models the lower frequencies that correspond to higher fundamental periods more effectively. In contrast, misfits from Synthetic-SFF technique are almost at the same ranges for all buildings and all stations except stations FMG and LSS.

Table 5.20 demonstrates that Synthetic-SFF method closely estimates most of the real non-spectral seismological parameters at all stations except FMG and LSS. The simulated records from Synthetic-SFF have smaller significant duration and larger *PGA*, I_a, *CAV*, and *HI* at these stations with backward directivity effects. This may be due to inherent weakness of the stochastic finite-fault method in modeling directivity effects resulting in smaller amplitudes along with longer durations. However, when the Synthetic-HIC method is considered, at most of the stations the simulated records exhibit non-spectral seismological ground motion parameters slightly smaller than the real ones. However, in some stations such as station GSA, a close match for the real and simulated values is obtained.

Next, it is aimed to assess the nonlinear response of the selected frame buildings due to the both real and simulated ground motion database.

5.5.5 Comparison of dynamic responses of the buildings to observed and simulated records for the 2009 L'Aquila (Mw=6.3) earthquake

The maximum displacements along with the drift ratios determined at each story level for all nine buildings under the real and simulated ground motions of the L'Aquila event are displayed in Figures 5.40-5.48. Table 5.21 lists the geometric means of the maximum real top story displacements in EW and NS directions as well as the ratios of the maximum top story displacements computed from alternative simulation methods to the corresponding real ones. The pushover analyses of the frames and comparison of the capacity curves with the results of NLTHA is presented in Appendix E.3. Finally, Table 5.22 presents the nonlinear response misfits computed using Equation 5.9.

(a)

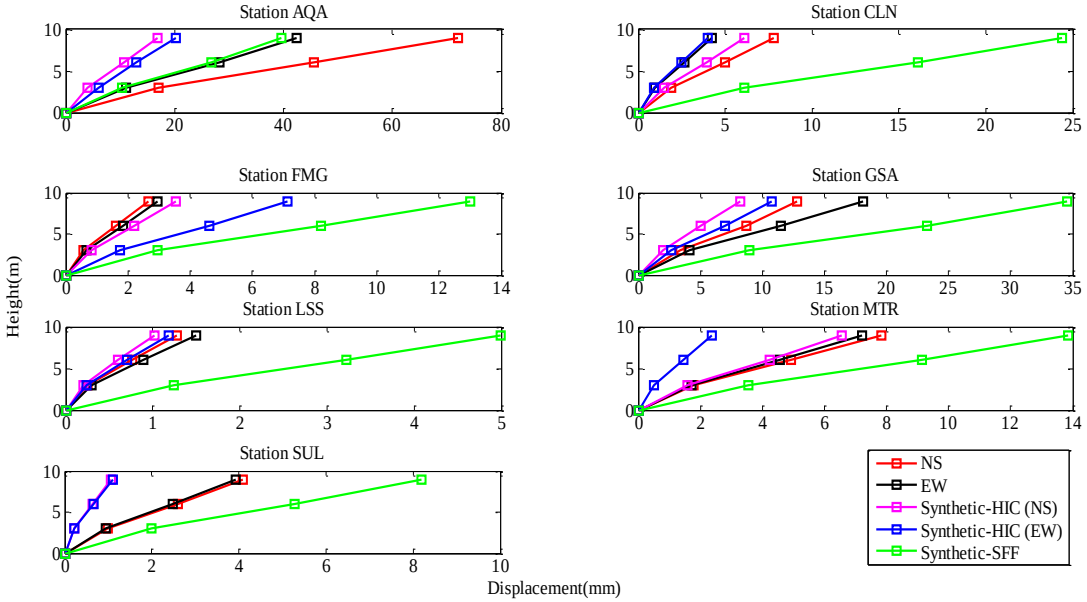

(b)

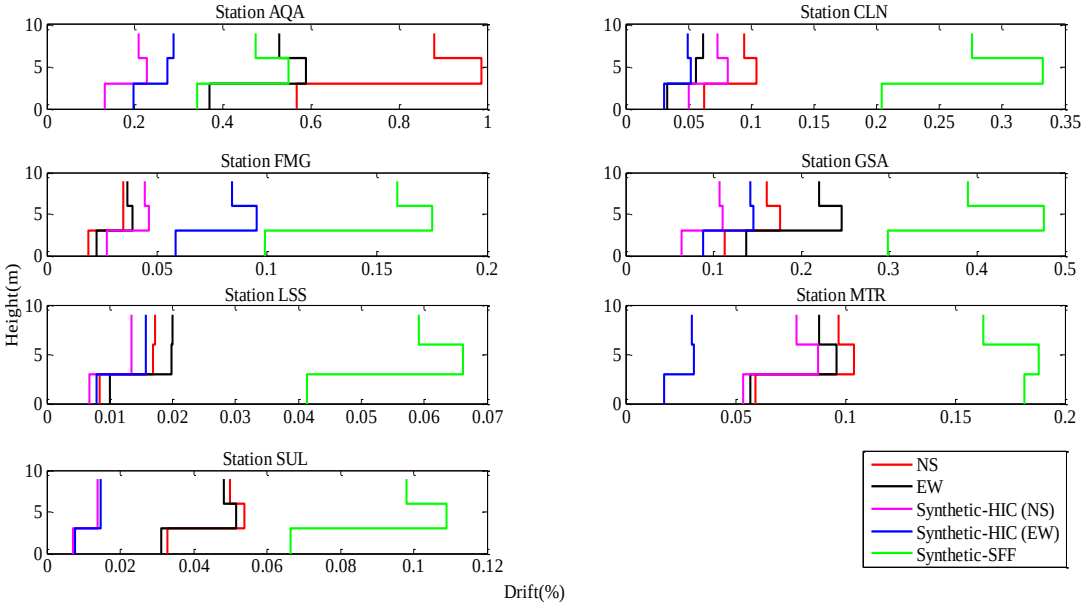

Figure 5.40 Distribution of (a): maximum story displacements and (b): maximum drift ratios due to the real and simulated records of L'Aquila Earthquake – F1-3S2B

(a)

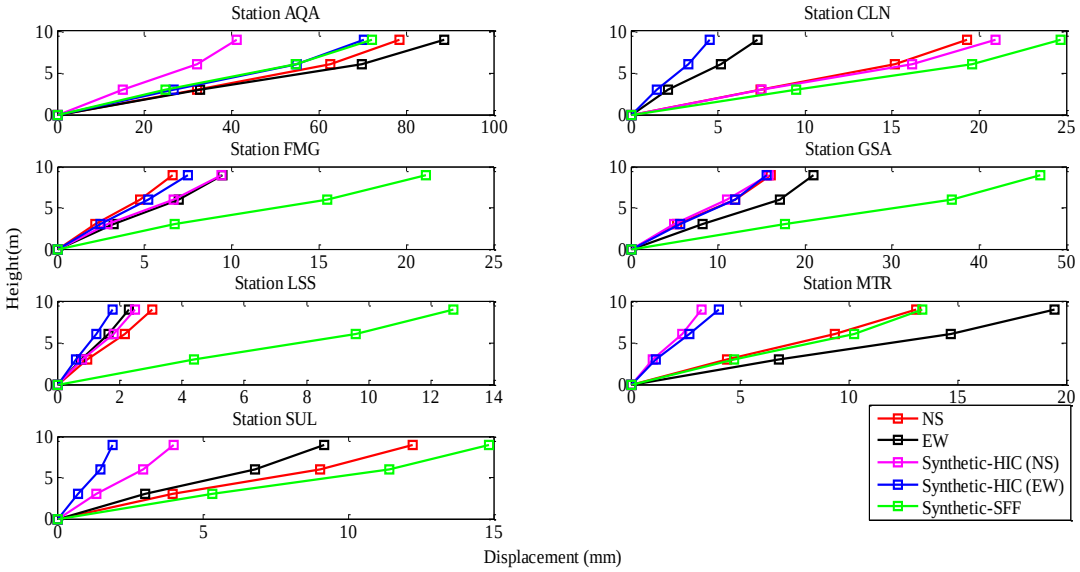

(b)

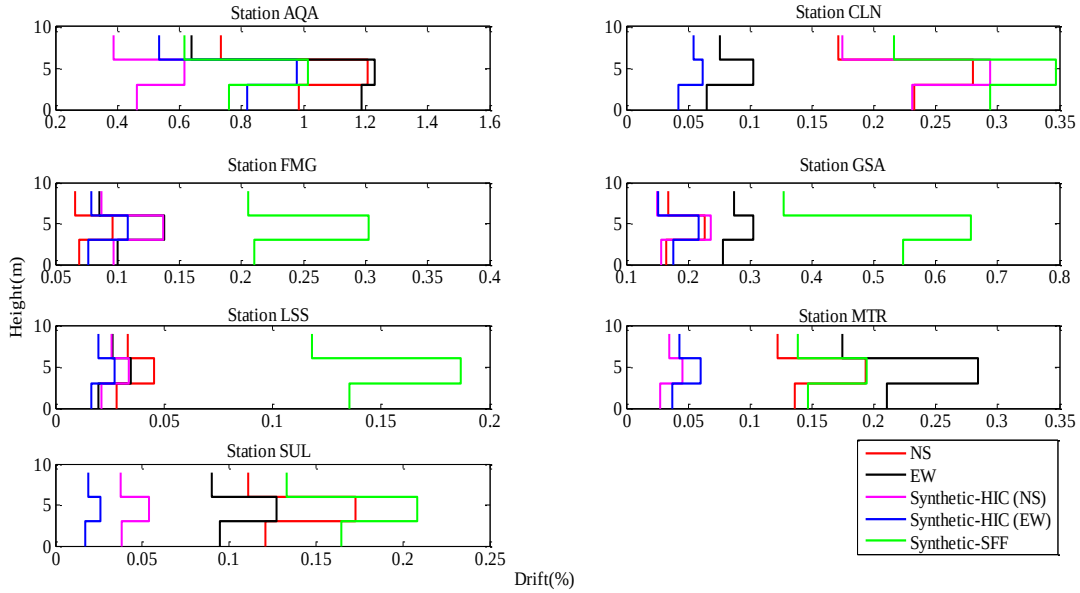

Figure 5.41 Distribution of (a): maximum story displacements and (b): maximum drift ratios due to the real and simulated records of L'Aquila Earthquake – F2-3S2B

(a)

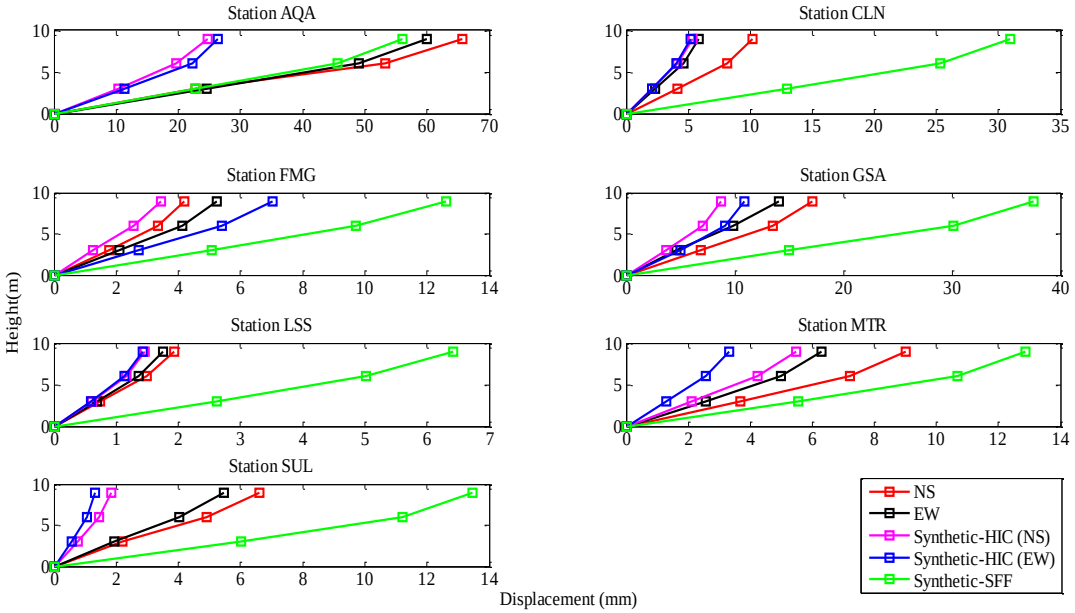

(b)

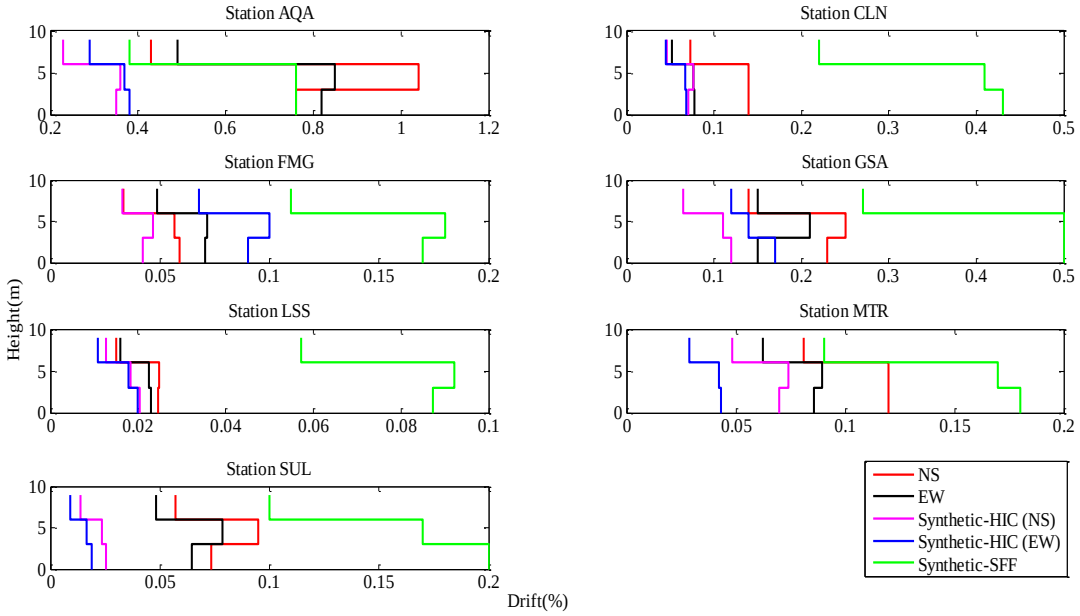

Figure 5.42 Distribution of (a): maximum story displacements and (b): maximum drift ratios due to the real and simulated records of L'Aquila Earthquake – F3-3S3B

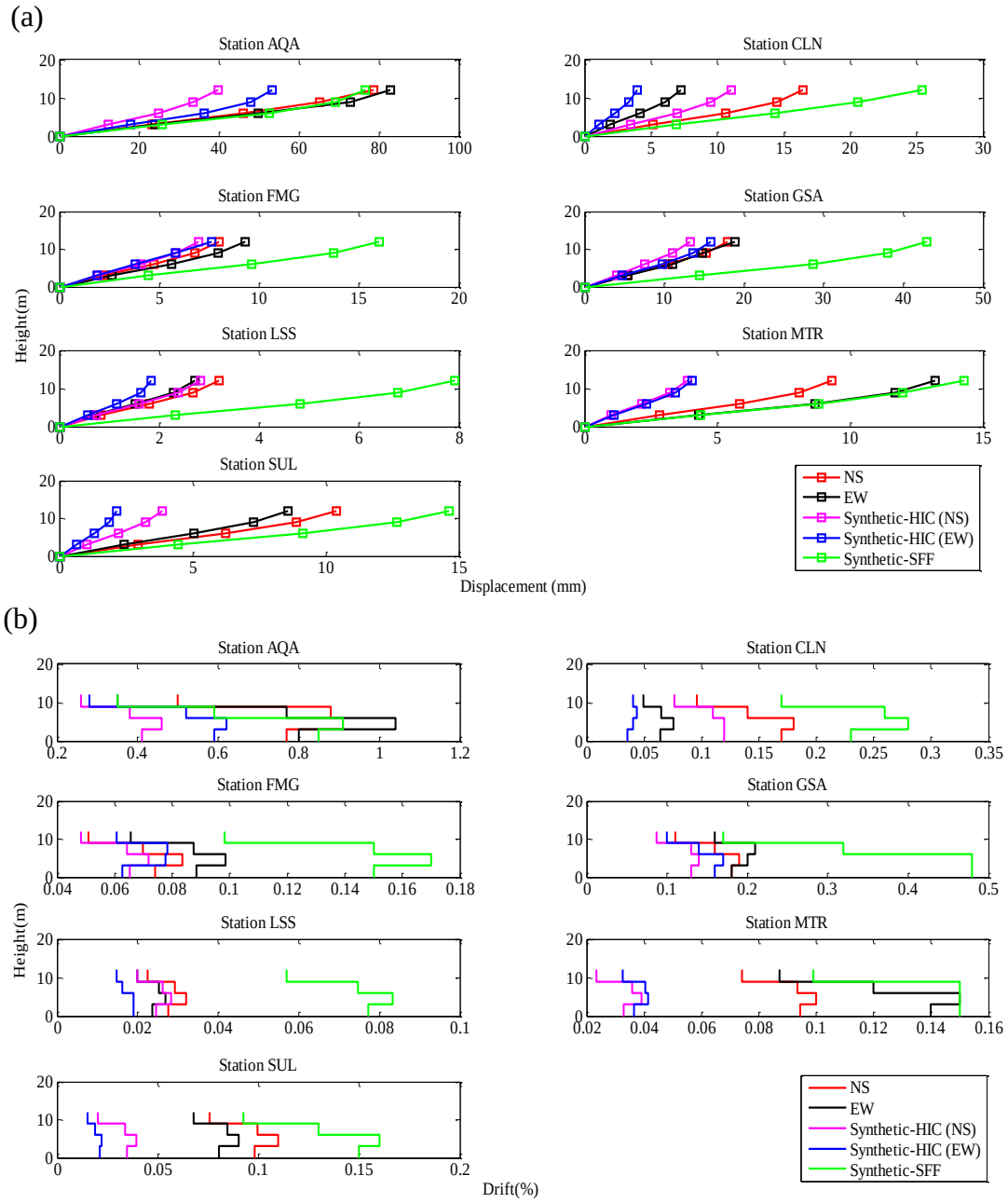

Figure 5.43 Distribution of (a): maximum story displacements and (b): maximum drift ratios due to the real and simulated records of L'Aquila Earthquake – F4-4S3B

(a)

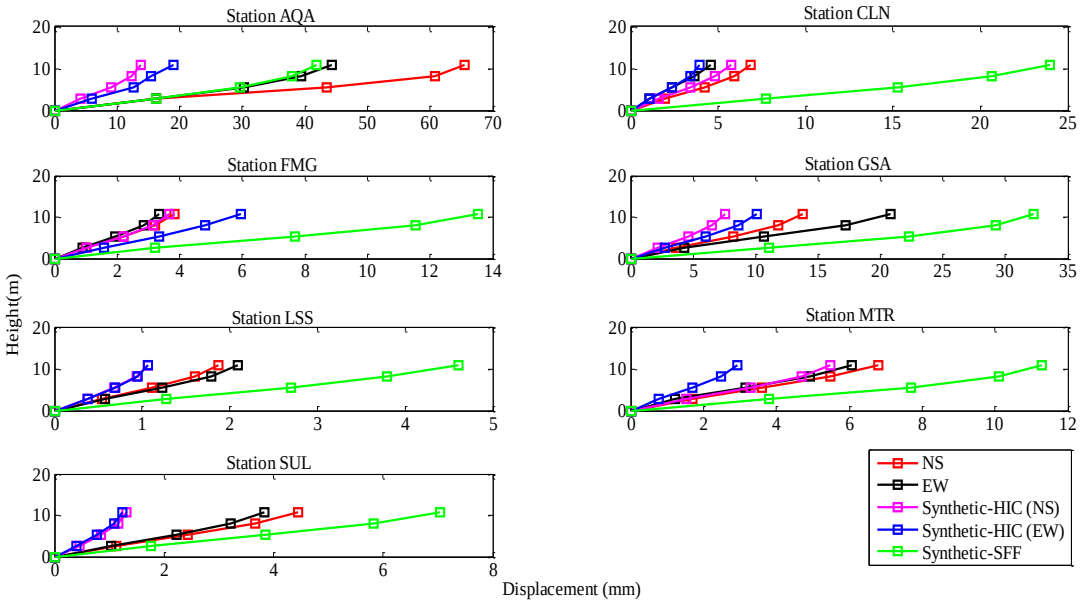

(b)

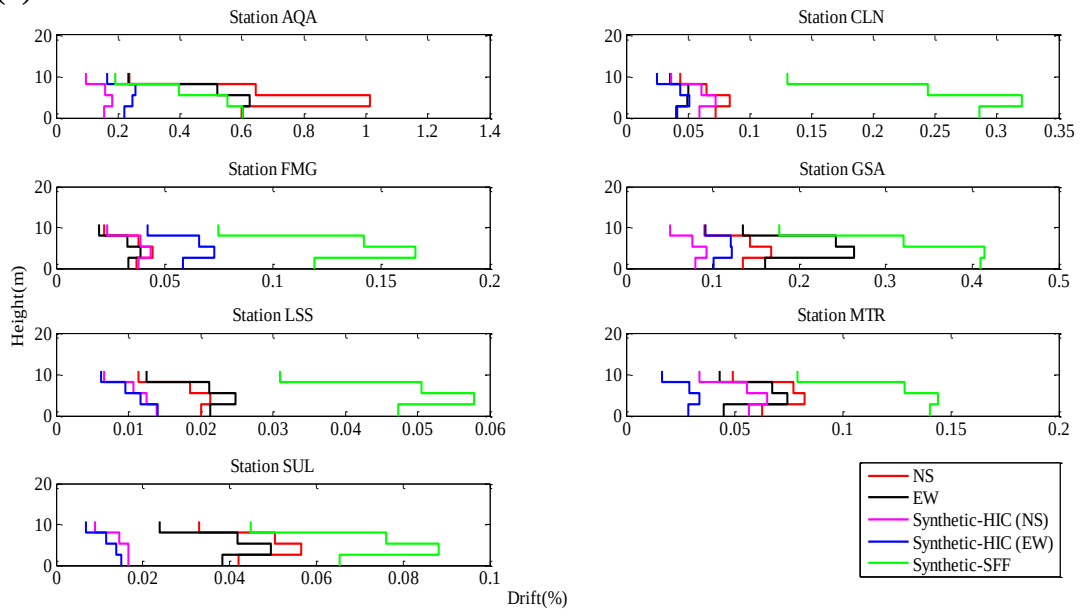

Figure 5.44 Distribution of (a): maximum story displacements and (b): maximum drift ratios due to the real and simulated records of L'Aquila Earthquake – F5-4S3B

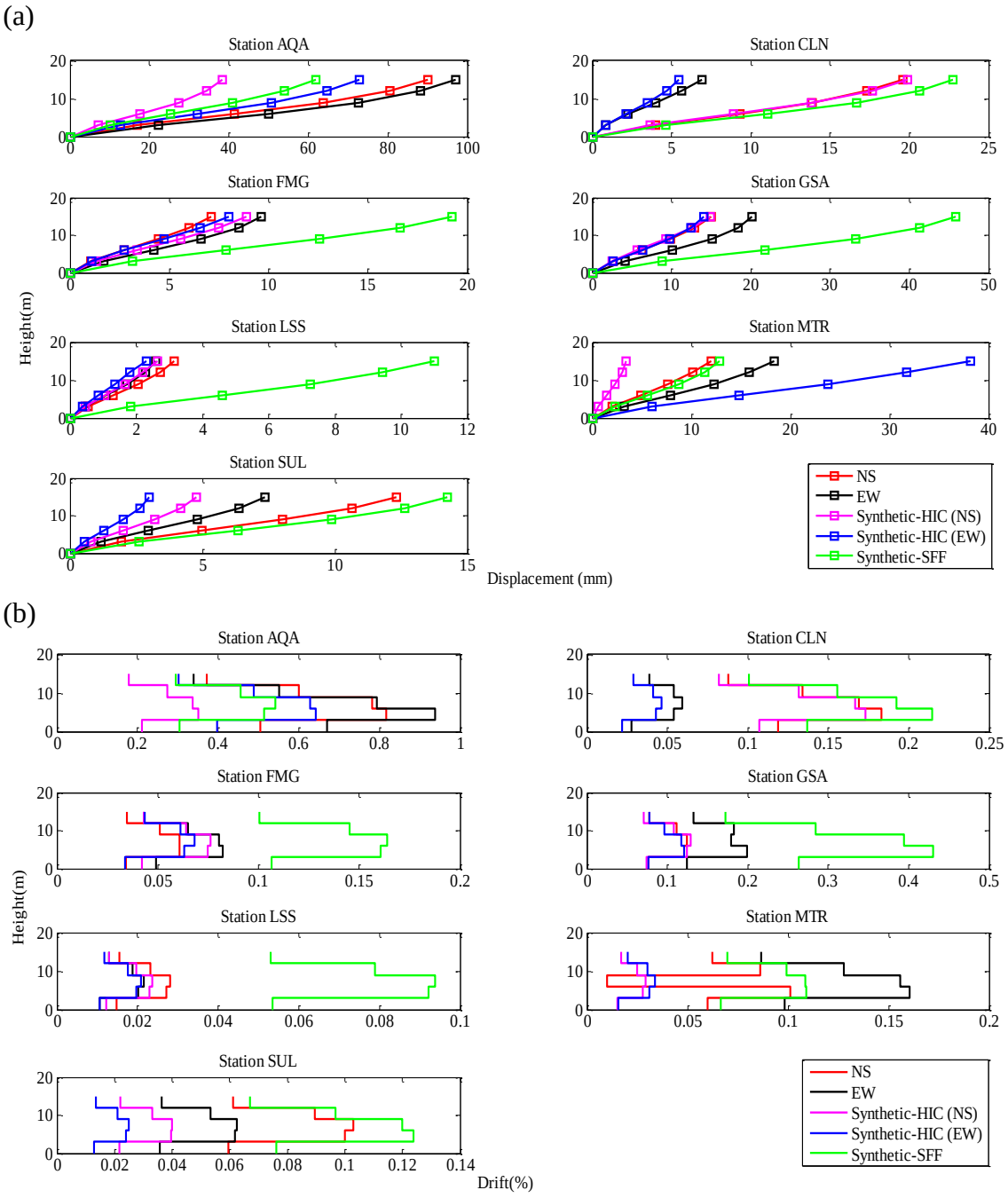

Figure 5.45 Distribution of (a): maximum story displacements and (b): maximum drift ratios due to the real and simulated records of L'Aquila Earthquake – F6-5S2B

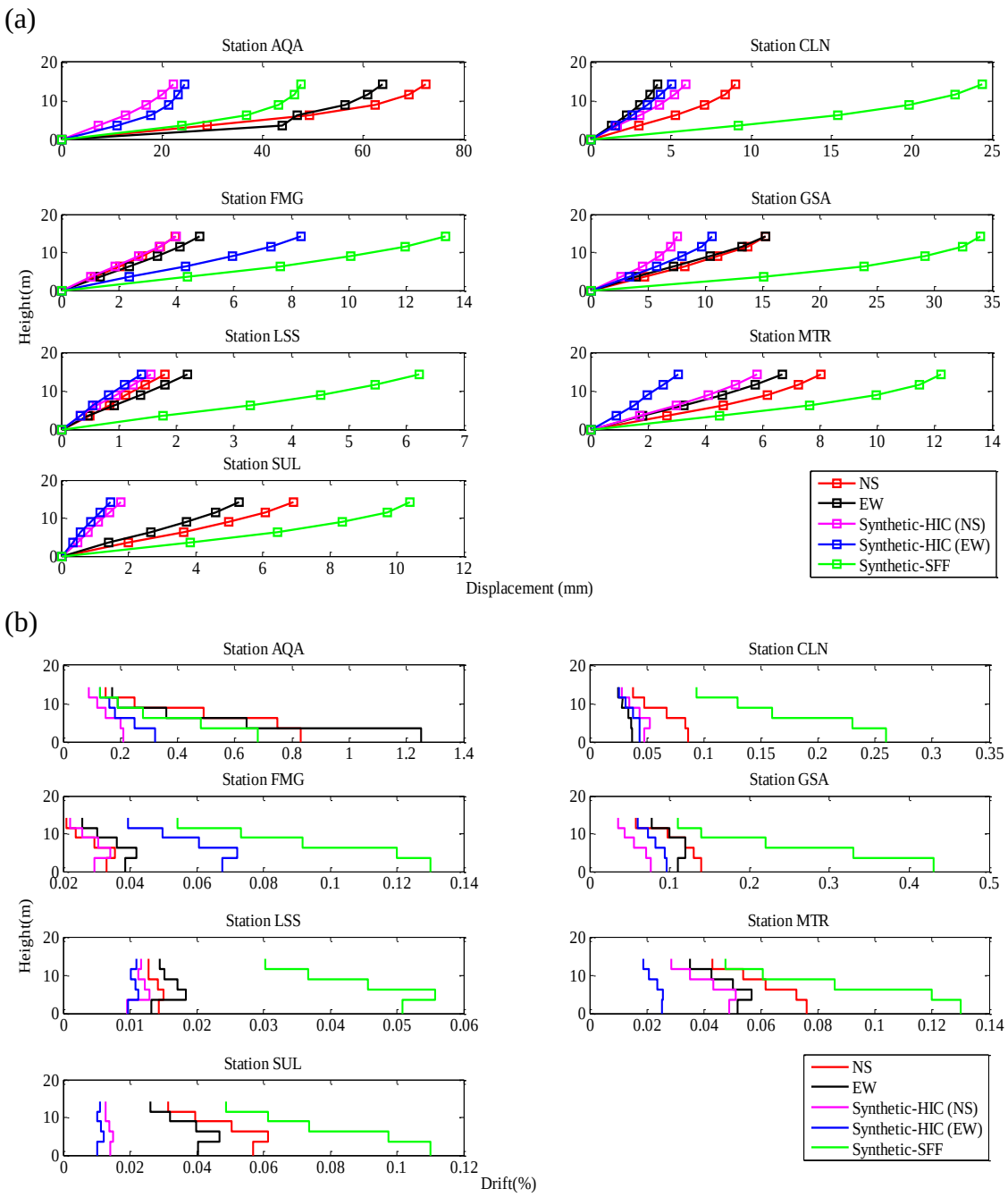

Figure 5.46 Distribution of (a): maximum story displacements and (b): maximum drift ratios due to the real and simulated records of L'Aquila Earthquake – F7-5S4B

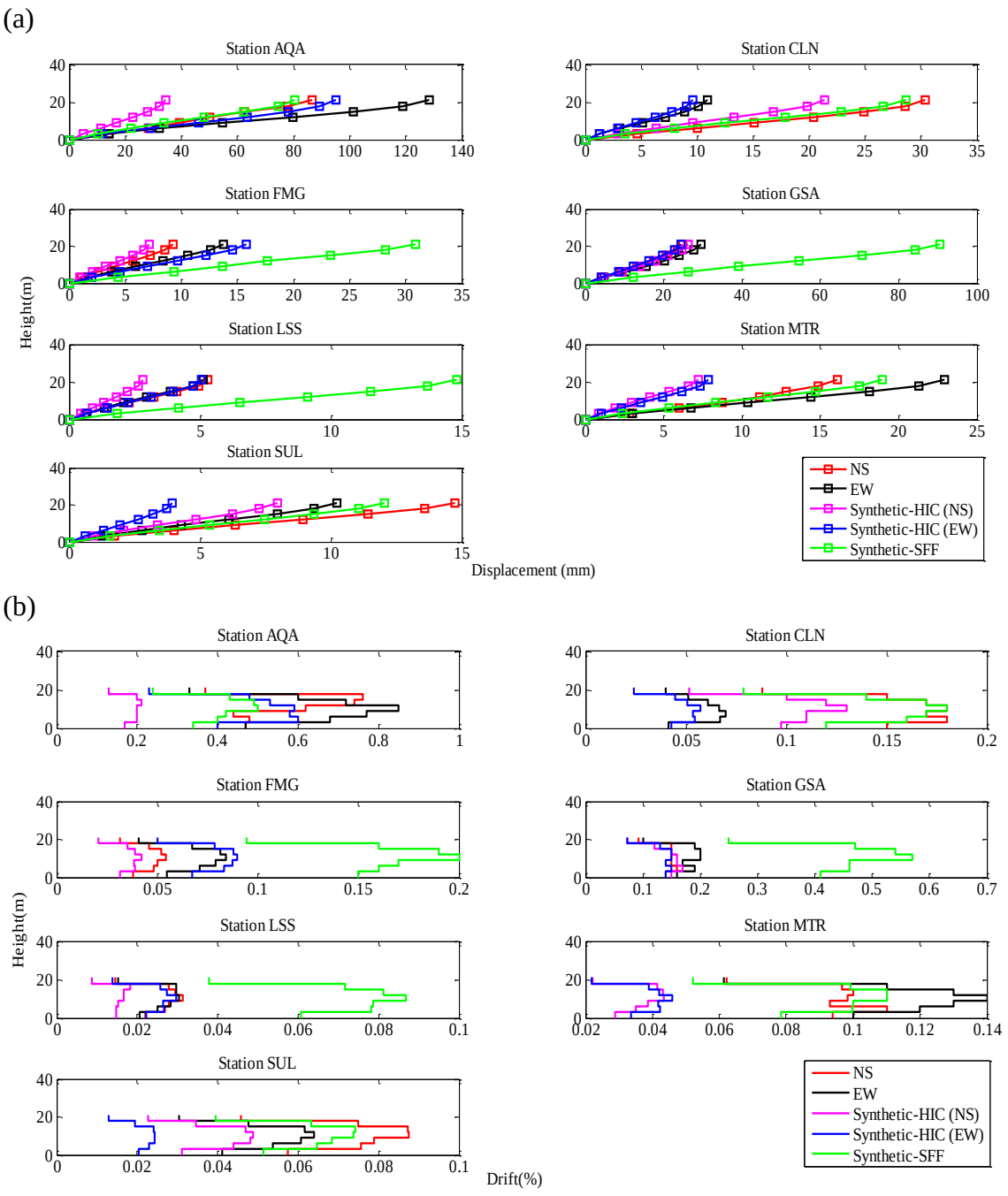

Figure 5.47 Distribution of (a): maximum story displacements and (b): maximum drift ratios due to the real and simulated records of L'Aquila Earthquake – F8-7S3B

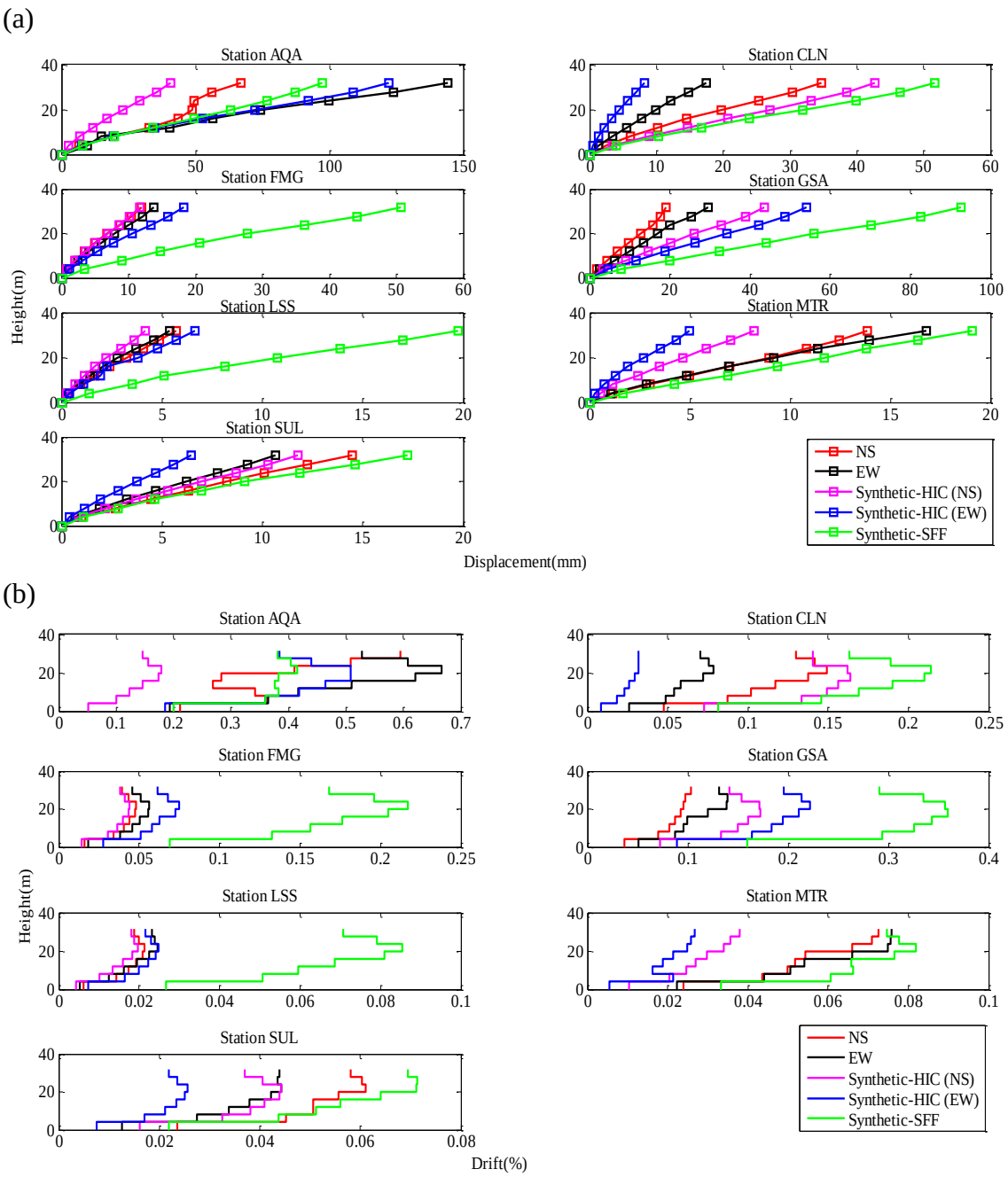

Figure 5.48 Distribution of (a): maximum story displacements and (b): maximum drift ratios due to the real and simulated records of L'Aquila Earthquake – F9-8S3B

Table 5.21 Top story displacements of observed and simulated data at the stations for the 2009 L'Aquila earthquake

Frame ID	Top Story Displacement	Station						
		AQA	CLN	FMG	GSA	LSS	MTR	SUL
F1-3S2B	Real (mm)	53.8982	6.3555	3.6783	15.7911	1.97	7.5813	4.9958
	Synthetic -HIC /Real	0.3603	0.8039	1.59	0.6246	0.5627	0.5972	0.2357
	Synthetic -SFF /Real	0.7162	3.644	3.7489	2.1809	2.7183	1.8518	1.687
F2-3S2B	Real (mm)	83.4356	11.8399	7.9211	18.3664	2.6454	15.9715	10.5884
	Synthetic -HIC /Real	0.6445	0.8217	1.0598	0.8525	0.7984	0.2278	0.2607
	Synthetic -SFF /Real	0.8636	2.0833	2.6653	2.5587	4.799	0.8396	1.4028
F3-3S3B	Real (mm)	62.7724	7.6964	4.687	15.5185	1.8424	7.5216	6.0073
	Synthetic -HIC /Real	0.4065	0.6833	1.0491	0.627	0.7796	0.5678	0.2589
	Synthetic -SFF /Real	0.8925	4.0244	2.6917	2.4164	3.487	1.71	2.2411
F4-4S3B	Real (mm)	80.7707	10.9077	8.619	18.3819	2.9464	11.0864	9.4415
	Synthetic -HIC /Real	0.5696	0.6076	0.8465	0.7879	0.7743	0.3565	0.3035
	Synthetic -SFF /Real	0.9489	2.3324	1.8576	2.3327	2.6876	1.2876	1.5489

Table 5.21 Continued

Frame ID	Top Story Displacement	Station						
		AQA	CLN	FMG	GSA	LSS	MTR	SUL
F5-4S3B	Real (mm)	53.8558	5.6018	3.5793	16.9164	1.978	6.4237	4.1286
	Synthetic -HIC /Real	0.3009	0.8533	1.3063	0.5163	0.5382	0.6241	0.3084
	Synthetic -SFF /Real	0.7784	4.2823	3.7794	1.9077	2.3296	1.7582	1.7071
F6-5S2B	Real (mm)	93.3877	11.7848	8.3229	17.0733	2.8434	15.0158	9.4576
	Synthetic -HIC /Real	0.5647	0.8747	1.0271	0.85	0.9064	0.2407	0.3892
	Synthetic -SFF /Real	0.6599	1.9194	2.2956	2.6733	3.9042	0.8564	1.4966
F7-5S4B	Real (mm)	68.0217	6.1436	4.361	15.2646	1.9893	7.3338	6.0573
	Synthetic -HIC /Real	0.3437	0.8946	1.3246	0.5872	0.741	0.5737	0.2664
	Synthetic -SFF /Real	0.7017	3.9698	3.0633	2.2249	3.1298	1.664	1.7162
F8-7S3B	Real (mm)	105.4814	18.1824	11.2801	27.1535	5.2118	19.1924	12.2769
	Synthetic -HIC /Real	0.5432	0.7891	0.941	0.9353	0.7218	0.3924	0.4546
	Synthetic -SFF /Real	0.7626	1.5767	2.7371	3.3357	2.8409	0.987	0.98
F9-8S3B	Real (mm)	97.0789	24.5896	12.8187	23.6624	5.5325	15.2584	12.4225
	Synthetic -HIC /Real	0.7268	0.7599	1.1384	2.0547	0.9504	0.4192	0.7022
	Synthetic -SFF /Real	1.0035	2.1033	3.9559	3.9163	3.5644	1.2518	1.3886

Table 5.22 Misfits in terms of nonlinear responses ($Misfit_{NR}$) to real and simulated data at the stations for the 2009 L'Aquila earthquake

Frame ID	Method	Station						
		AQA	CLN	FMG	GSA	LSS	MTR	SUL
F1-3S2B	Stochastic-HIC	0.4374	0.0592	0.1091	0.1968	0.2089	0.1633	0.5913
	Stochastic-SFF	0.0956	0.5351	0.5566	0.3530	0.4001	0.2921	0.2578
F2-3S2B	Stochastic-HIC	0.1717	0.0640	0.1270	0.0606	0.0940	0.6705	0.5622
	Stochastic-SFF	0.0854	0.2508	0.4119	0.4072	0.6969	0.0658	0.1542
F3-3S3B	Stochastic-HIC	0.3716	0.1237	0.1171	0.1304	0.0897	0.2569	0.5453
	Stochastic-SFF	0.0381	0.6022	0.4197	0.4037	0.5512	0.2338	0.4040
F4-4S3B	Stochastic-HIC	0.2127	0.2141	0.0904	0.0880	0.0830	0.4808	0.5110
	Stochastic-SFF	0.0309	0.2843	0.2666	0.4058	0.4519	0.0509	0.2012
F5-4S3B	Stochastic-HIC	0.5124	0.0451	0.0488	0.2584	0.2300	0.1290	0.4631
	Stochastic-SFF	0.0419	0.6621	0.5638	0.3469	0.3593	0.3258	0.2220
F6-5S2B	Stochastic-HIC	0.2490	0.0454	0.1036	0.0356	0.0256	0.6423	0.4166
	Stochastic-SFF	0.2526	0.2145	0.4094	0.4799	0.6709	0.0834	0.1810
F7-5S4B	Stochastic-HIC	0.5042	0.1240	0.0725	0.1768	0.1433	0.2408	0.6180
	Stochastic-SFF	0.1627	0.6762	0.5779	0.4908	0.6073	0.2933	0.3183
F8-7S3B	Stochastic-HIC	0.1908	0.0900	0.0829	0.0418	0.0738	0.4480	0.3147
	Stochastic-SFF	0.1033	0.1626	0.4406	0.4719	0.4627	0.0707	0.0796
F9-8S3B	Stochastic-HIC	0.1447	0.2247	0.0411	0.3044	0.1246	0.4056	0.1338
	Stochastic-SFF	0.1049	0.3185	0.5964	0.5854	0.5625	0.1270	0.0939

The results expressed in Figures 5.40-5.48 and Tables 5.18-5.22 corresponding to all frames can be summarized as follows:

- For F1-3S2B at station AQA, nonlinear dynamic responses are underestimated by both Synthetic-HIC and Synthetic-SFF records when compared to the real records; however, Synthetic-SFF yields closer estimated responses for this frame. This is mostly due to the bad fit of the simulated record from Synthetic-HIC method for the NS component at AQA (Ameri *et al.*, 2012). At station

CLN, dynamic responses to Synthetic-HIC records are closer to the real responses than those of Synthetic-SFF. On the other hand, nonlinear analyses with Synthetic-SFF records yield much more conservative (larger) responses when compared to the real story displacements. At station FMG, it is observed that both of the simulation techniques yield larger nonlinear responses than the real ones. Figure 5.40 and Table 5.21 reveal that Synthetic-SFF method overestimates the maximum top story displacement of this frame by a factor of almost 3.5, while the factor of overestimation is 1.5 for Synthetic-HIC method. At stations GSA, LSS and MTR, responses from Synthetic-HIC records are closer to the real responses; however, the maximum top story displacement is underestimated by a factor of 2. NR misfits for these three stations (GSA, LSS, and MTR) as shown in Table 5.22 indicate that simulated records from the Synthetic-HIC method perform better than those from the Synthetic-SFF method at these stations. However, Table 5.21 shows that the Synthetic-SFF method is more conservative and overestimates the real roof displacements by factors of about 2, 2.5, and 1.5 for stations GSA, LSS, and MTR, respectively. Finally, for station SUL, stochastic finite-fault method yields closer results to the real responses based on the NR misfits. One critical observation at this station is that Synthetic-HIC method underestimates the real maximum roof displacement by a factor of almost 5. This is mostly due to the fact that the higher frequencies of the record at this station are not well represented by Synthetic-HIC records (Figure 5.39). In addition, SUL is a EC8 class C station (Table 5.16) and the station is characterized by site effects which led to the bad fit of the Synthetic-HIC records due to not considering the particular site effects (Ameri *et al.*, 2012). For this frame, at most of the stations both RS and FAS misfits are in agreement with the NR misfits. However, through a comparison of the values in Tables 5.18 and 5.19, it is observed that for station GSA only FAS misfit whereas for station CLN only RS misfit governs the accuracy of the nonlinear response. Also, at station MTR, neither of the FAS nor RS misfits matches with the NR misfit while NR misfits in Table 5.22

clearly show smaller misfits from Synthetic-HIC method compared to the Synthetic-SFF method.

- For F2-3S2B, structural responses under simulated records of two simulation methods are similar to those of frame F1-3S2B at most of the stations. One exception is the result corresponding to Synthetic-SFF method at station MTR. For this frame, at station AQA, an underestimation of nonlinear responses is observed by both Synthetic-HIC and Synthetic-SFF records when compared to the real records.. At station CLN, Synthetic-HIC method results in closer responses to the real ones although the real responses are slightly underestimated for EW component. On the other hand, at this station, Synthetic-SFF method overestimates the maximum top story displacement by a factor of 2. At station FMG, it is observed that both of the simulation techniques overestimate nonlinear responses compared to the real ones except the EW component from Synthetic-HIC method. Synthetic-SFF records overestimate the maximum top story displacement by a factor of about 2.5, while the responses from Synthetic-HIC record are closer to the real responses. NR misfits for station GSA shown in Table 5.22 indicate that simulated records from Synthetic-HIC method perform better than those from Synthetic-SFF method at this station. Table 5.21 shows that Synthetic-SFF method is however more conservative than Synthetic-HIC method and the Synthetic-SFF records overestimate the real roof displacement by a factor of about 2.5 for this frame. At station LSS, responses from Synthetic-HIC records are closer to the real responses with a slight underestimation. On the other hand, stochastic finite-fault method overestimates the real maximum roof story displacement by a factor of almost 5. For MTR station, the nonlinear responses due to records from Synthetic-SFF method are much closer to the real responses than the simulated records obtained from Synthetic-HIC method (Figure 5.41); however, both simulated records underestimate the real responses. For this station, simulated ground motions obtained from Synthetic-HIC method were not considered good fits by the authors of the corresponding study (Ameri, *et*

al. 2012). Therefore, when a poor fit is obtained from a seismological point of view, a similar observation is made for nonlinear response of the frame. Finally, for station SUL, Synthetic-SFF technique provides closer results to the real responses whereas Synthetic-HIC method underestimates the maximum top story displacement or drift ratio by a factor of 4. For this frame, when the misfits in Tables 5.18, 5.19, and 5.22 are considered, it can be seen that for all stations both FAS and RS misfits are consistent with the NR misfits. However, RS misfit is more sensitive to the differences in nonlinear behavior for both simulation techniques.

- Nonlinear dynamic behavior of F3-3S3B is similar to frame F1-3S2B at all stations except for the results of NS component of Synthetic-HIC method at station FMG. Unlike F1-3S2B, at this station Synthetic-HIC method underestimates the nonlinear responses slightly (Figure 5.42). In addition, for this frame both FAS and RS misfits are consistent with the NR misfits for all stations except CLN where only RS misfit governs the accuracy of NR misfit.

- For frame F4-4S3B, results from the two simulated techniques are consistent with the results of frame F1-3S2B at all stations except for the results of Synthetic-HIC method at station FMG. At this station, the dynamic responses are slightly underestimated by Synthetic-HIC technique (Figure 5.43). Another exception is the following: unlike F1-3S2B, a comparison of the misfits presented in Tables 5.18, 5.19, and 5.22 shows the consistency of both FAS and also RS misfits with the NR misfits for this frame at all stations. For this frame, similar to F2-3S2B, in between FAS and RS misfits, RS misfit is more sensitive to the differences in nonlinear behavior as a result of Synthetic-HIC and Synthetic-SFF methods.

- For frame F5-4S3B, results from the alternative simulation methods are in agreement with the results of frame F1-3S2B at all stations (Figure 5.44). For this frame, at most of the stations both RS and FAS misfits are in agreement with the nonlinear response misfits. However, through a comparison of the

results of Tables 5.18 and 5.19 it is clear that for station CLN only RS misfit governs the accuracy of the nonlinear response. Also, at station MTR, neither of the FAS nor RS misfits matches with the NR misfit where NR misfits in Table 5.22 clearly show that Synthetic-HIC method predicts the real responses more accurate than Synthetic-SFF method.

- F6-5S2B has a similar response under simulated ground motion records from Synthetic-HIC and Synthetic-SFF methods to those of frame F2-3S2B at all stations (Figure 5.45).

- Results of nonlinear time history analyses under simulated records of two simulation methods for F7-5S4B are consistent with the results of F5-4S3B (Figure 5.46).

- The nonlinear dynamic results corresponding to frame F8-7S3B to alternative simulation techniques are similar to those of F2-3S2B with minor differences (Figure 5.47). For this frame, at station FMG, overestimation of real responses is observed with two alternative methods. However, unlike frame F2-3S2B, the NS component of simulated record from hybrid-integral-composite method underestimates the real responses. In addition, at station SUL, both simulation techniques yield closer results to the real responses when compared to those of frame F2-3S2B. This observation can also be verified by a comparison of NR misfits (Table 5.22).

- When frame F9-8S3B is considered it is seen that at station AQA the results are consistent with the findings from other frames. For this frame, at AQA Synthetic-HIC clearly underestimates the real response whereas Synthetic-SFF closely matches the real response. At stations CLN and FMG, the observations are similar to those from frames F2-3S2B, F3-3S3B, F5-4S3B, F6-5S2B, and F7-5S4B. The results at station FMG show that both of the simulation techniques yield larger nonlinear responses than the real records. The roof displacement from Synthetic-SFF record overestimates real roof displacement

by a factor of 4. At station GSA, both simulation methods result in an overestimation of the nonlinear response (Figure 5.48). However, from Table 5.22 it is noticeable that hybrid-integral-composite method performs better than stochastic finite-fault method. For the rest of stations, the story displacements from Synthetic-HIC records slightly underestimate the real responses while Synthetic-SFF records overestimate them. Table 5.22 illustrates that for station LSS, nonlinear response misfit from Synthetic-HIC is less than Synthetic-SFF method. In contrast, for stations MTR and SUL, Synthetic-SFF method performs better. Overall, due to the higher number of stories of the frame (or the longer fundamental period), response due to records from hybrid-integral-composite method (Synthetic-HIC) is closer to the real response. This is expected as Synthetic-HIC method matches closely with the low frequency content of the real record which corresponds to longer fundamental periods (Figures 5.33-5.39). For this frame, both the RS and FAS misfits are in agreement with the NR misfits.

For this case study when NSS misfits (for Synthetic-SFF records) are compared against NR misfits, overall it is observed that: For station AQA with stiffer soil condition and no basin effects, misfits in terms of I_a, *PGA*, and *HI* are better indicators of NR misfits while misfit in terms of t_{eff} is the least sensitive indicator of NR misfit. For station CLN, NSS misfits in terms of PGA and t_{eff} are not in agreement with NR misfits. Whereas misfit in terms of I_a results in the highest accuracy compared to nonlinear response misfits. For stations FMG, LSS, MTR, and SUL only t_{eff} is not in agreement with NR misfits. In contrast, at these stations I_a is the best indicator of NR misfits. At station GSA, all of the NSS misfits are in agreement with NR misfits. However, the accuracy of misfits in terms of *Ia* and *HI* are slightly larger.

Further details about the comparison of seismological misfits with nonlinear response misfits for L'Aquila earthquake are presented in Appendix F.3.

5.6 Uncertainties Involved in the Nonlinear Time History Analyses of MDOF Structures

Various sources of uncertainty can be encountered in each step of NTHA of MDOF structures using either real or simulated records. In this study these uncertainties are not quantified, but it is always possible to quantify such bias in future studies. This section summarizes the possible uncertainties involved in this chapter.

- The main source of uncertainty in structural response under seismic excitations is the variability associated with the ground motion records. The input ground motions can be either in the form of real or simulated time series where characteristics of the ground motion records have significant effects in assessment of structural responses. In this study, only 3 earthquakes with a finite number of ground motion records are investigated. These events and recording stations have certain physical properties. Thus, the results and conclusions are naturally dependent on such properties. In addition, the quality of the real records and the model assumptions in the simulated ones introduce uncertainty to the results and may therefore affect the conclusions.
- Another source of uncertainty comes from the numerical modeling of the real structures. It is difficult to realistically model an existing structure: the modeling assumptions on the building properties such as material models, damping ratios, definition of beam-column elements, strength and stiffness degradation properties all introduce uncertainty.
- Finally, solution techniques for equation of motion include certain numerical errors that cannot be eliminated. In this thesis, as long as a comparison process is performed for both real and simulated records using the same structural models, these mentioned uncertainties related to structural modeling may not affect the results.

5.7 Main Findings of Chapter 5

The main results and findings regarding the use of simulated ground motions in nonlinear time history analyses of MDOF structures can be summarized as follows:

- It is observed that stochastic finite-fault technique results in underestimation of recorded Fourier amplitudes for the case study with predominant basin effects (Erzincan). The station-wise mean ratio of simulated FAS over observed FAS at all frequencies varies between 0.25 and 1.5. Similarly, the mean ratio of simulated RS over observed RS lies between 0.4 and 1.2. The mean ratio for dynamic responses has a maximum underestimation value of 0.4. The discrepancies may be attributed to deep alluvial basin effects producing long-period surface waves which cannot be simulated by the stochastic finite-fault methodology. In case of basin effects, duration of the real records also increases due to the reflections and reflections as the seismic waves pass through an alluvial basin. However, the duration model applied herein is not able to simulate the duration of surface wave portion of the observed time histories in the Erzincan region. It is well known that the MDOF dynamic responses of structures are mostly affected by duration content of the records. In contrast, it is observed in Erzincan study that PGA has the least consistency with nonlinear responses except for frames with shorter periods. Finally, in this specific case with soil nonlinearity effects at the three stations, stochastic finite-fault method is not conservative in prediction of nonlinear responses of the MDOF frame structures in the selected period ranges.
- When the results corresponding to Düzce earthquake are considered, the mentioned mean ratio in terms of FAS oscillates around 1 and for some frequencies reaches to 1.5. Comparing the results of response spectrum as well as nonlinear response analyses shows the same trend for the mean ratio in terms of either RS or NR. Therefore, for this case study within a shallow alluvial basin, the stochastic finite-fault method is capable of simulating the main characteristics of the ground motion records expressed in terms of Fourier

amplitudes, response spectral amplitudes, energy content, duration, and intensity level. Among all parameters, for the Düzce event, PGA as well as Arias intensity are the most dominant indicators of the accuracy of the nonlinear responses. For this specific case, simulated records can be safely used for seismic design and assessment purposes of MDOF structures in the selected period ranges.

- For the third case study (L'Aquila earthquake), comparison of the results from two alternative simulation methods reveals that the mean ratio in terms of FAS ranges from 1 to 3 and 0.3 to 1 for stochastic finite-fault and hybrid-integral-composite techniques, respectively. The mean ratio in terms of both RS and NR changes from 1 to 2 and 0.5 to 1 for stochastic-finite-fault and hybrid-integral-composite methods, respectively. Therefore, in this case study, mostly simulated records of stochastic finite-fault methodology overestimate the real nonlinear responses whereas simulated records of hybrid-integral-composite method underestimate them. However, the accuracy of hybrid-integral-composite method increases at lower frequencies or for frames with higher fundamental periods. The other observation is that for this case study with stations located on stiffer soil compared to Erzincan and Düzce, duration of the record has the least predominant indicator of the dynamic responses. In contrast, Arias intensity has the largest agreement with nonlinear responses in most cases. Finally, stochastic finite-fault methodology for this case study could be conservatively used for seismic design and assessment purposes of MDOF structures in the studied period ranges. A similar recommendation cannot be made for the hybrid-integral-composite technique.
- When the overall results from 3 case studies are considered, it is observed that the match and mismatch between the real and simulated motions expressed in terms of frequency/period-dependent misfits (FAS and RS) are close indicators of the nonlinear response misfits. Among these two parameters, response spectral misfits between real and simulated data are better representatives of the corresponding dynamic structural responses for most of the cases. Thus, it

is important to simulate realistic amplitudes over the entire broadband frequency range of interest for earthquake engineering purposes in order to cover all types of buildings with a range of fundamental periods.

- When the other ground motion measures such as significant duration, peak ground acceleration, Housner intensity, cumulative absolute velocity, or Arias intensity is considered, it is observed that these parameters are not always sufficient by themselves to characterize the ground motions or the anticipated dynamic structural behavior.
- In this study, simulated records that seismologically satisfy a certain goodness of fit criterion yield nonlinear responses that are acceptable when compared to the observed responses (in terms of story displacements).
- If a record is seismologically acceptable in terms of both spectral measures such as Fourier amplitude spectra and response spectra along with non-spectral measures including energy content, duration, and intensity level, it can be practically employed in engineering purposes and vice versa.
- When dynamic responses of MDOF systems are of concern, the results of analyses under simulated ground motions depend on the characteristics of the earthquake and the building type. For the selected cases, stochastic finite-fault method can simulate the higher frequency portion of ground motions larger than 1 Hz. As a result, dynamic responses of most of the selected RC structures particularly the ones with lower period ranges (less than about 1 s) can be simulated with stochastic finite-fault methodology.
- Finally, if it is aimed to use a simulated record for seismic design and assessment purposes of MDOF structures, depending on the study area and frame properties the related misfits should be minimized in simulation process. Simulated motions can then be safely employed for earthquake engineering purposes.

CHAPTER 6

CONTRIBUTIONS, CONCLUSIONS, AND RECOMMENDATIONS

6.1 Main Contributions

The aim of this thesis was to investigate the efficiency of simulated motions for earthquake engineering purposes. The main simulation technique tested was the stochastic finite-fault methodology. Two main applications were presented: The first one was the use of simulated motions in SDOF building models for estimating spatial distribution of damage. The second application was the use of simulated time histories in detailed MDOF models for three different past earthquakes.

Following are the main contributions of this doctoral thesis to the existing literature:

- In this study, a novel framework is presented for estimation of spatial distribution of seismic damages using regional seismic characteristics and local building data. The use of simulations provided a large set of records that include the inherent variability in terms of source, path, and site effects.
- This study constitutes the first application of a city-level damage estimation using non-generic, regional fragility curves derived based on local building data collected during walk-down surveys.

- Different from previous studies in the literature, a wide range of building sub-classes are assessed and employed yielding a realistic spatial distribution of damage.
- This study is the first application of fragility derivation using a synthetic ground motion database obtained from multiple deterministic hazard scenarios.
- The proposed framework for seismic loss estimation can be employed practically for other regions of interest in our country or globally. Results can be employed for disaster mitigation and management purposes.
- The results of prediction exercises yield anticipated spatial distribution of ground motion levels and damage in Erzincan. These maps are novel products for this area which is not extensively studied long after the 1992 event.
- In this study, to assess the MDOF responses to simulated motions, three large earthquakes are studied in detail. The simulations of these events along with the scenarios conducted for the loss estimation applications constitute a large synthetic ground motion database that can be used in future studies.
- Similarly, a large building class database (both SDOF and MDOF models) is formed during this study. This information is open for use in future applications.
- Most of the previous studies that examine simulated motions involved only one detailed structure with records from a single earthquake. In this study, for the first time, simulated motions from three events are tested on a number of MDOF buildings. The three events had different source mechanisms and station densities which helped to study the variability in ground motions.
- In this study, novel definitions of period/frequency-dependent seismological misfits as well as nonlinear response misfits are made. These quantifications helped to assess the efficiency of simulated ground motions in comparison with real ones.

6.2 Conclusions

Following are the main conclusions derived in this thesis:

- The input parameters of the ground motion simulations in terms of source, path, and site models should be carefully selected as the reliability of the simulation results directly depends on the accuracy of the input parameters.
- Simulations performed with calibrated input parameters provide realistic spatial distribution of peak ground motion parameters by physically modeling the source, path, and site effects.
- Validations against the observed damage levels show that the simulated ground motions used as input to SDOF building models can effectively estimate the spatial distribution of damages from large events in urban areas. The reason can be explained by the case of SDOF models only the fundamental mode governs the response behavior. Therefore, the limited range of frequencies affect the dynamic response.
- The fundamental goal of this thesis is to investigate the capability of simulated ground motions on estimation of dynamic responses of both simple single-degree-of-freedom and detailed multiple-degree-of-freedom systems. This is accomplished through nonlinear time-history analyses using a wide data set of simulated time histories. For SDOF models, response is assessed in terms of a coarse parameter (damage) and for MDOF systems, response is defined in terms of maximum story displacement or inter story drift ratio.
- It is observed that the inherent regional variability included in the synthetic ground motion database has a large impact on the generated fragility curves. Locally-derived fragility curves involving both regional seismic properties and local building models yield damage rates that match closely with observations.
- The type of ground motion intensity used in derivation of fragility curves is observed to be important in capturing the seismic behavior. Use of PGA for rigid structures (masonry classes) and PGV for flexible ones (reinforced-

concrete classes), improved the accuracy of the results in terms of estimated damage levels.

- The prediction exercises in Erzincan for potential earthquakes with larger magnitudes of Mw=7.0 and 7.5 indicate that the urban area in the city is under significant seismic threat in terms of both anticipated hazard and risk levels.
- While the SDOF models with simulated motions yield accurate global damage levels, the detailed nonlinear MDOF responses to simulated time series are observed to be case-specific: For the simulation of 1992 Erzincan event with predominant basin effects calibrated with data at only three stations, in parallel to the discrepancies in the simulated motions as compared to real records, nonlinear responses from simulated records do not match the real responses. For the simulation of 1999 Düzce earthquake with less dominant basin effects calibrated with data at 9 stations, simulated records yield the most accurate nonlinear responses. For the simulation of 2009 L'Aquila event calibrated with respect to data at 14 stations located mostly on rock or stiff soil conditions, two simulation methods are considered. It is observed that the records obtained from the broadband method and the stochastic method systematically underestimated and overestimated the structural responses, respectively.
- On a broader level, it is observed that both the spectral misfits in terms of FAS and RS (around the fundamental period of the structure) and seismological misfits involving intensity level, energy content and duration effects of ground motion records are representative of the accuracy of the nonlinear responses. In other words, seismologically-acceptable records selected according to only certain parameters does not always yield structural responses close to the real ones.
- Finally, once the misfits between simulated and real records are negligible in terms of frequency content, intensity level, energy content, and duration, simulated motions from stochastic finite-fault method can be safely used in earthquake engineering, with either SDOF or MDOF models.

6.3 Fundamental Limitations of This Study and Related Future Work

In this study, several assumptions were made which introduced uncertainty to the results. These points need to be investigated further in future studies:

- Input parameters used in stochastic finite-fault methodology involve some assumptions regarding the fault plane, duration functions, and velocity models at sites. The accuracy of these input parameters can be increased by further investigations.
- It is observed that the stochastic finite-fault ground motion simulation methodology cannot simulate the low frequency content of ground motions realistically. To simulate broadband ground motions, hybrid methods that require complex source and wave velocity models are necessary. Thus, for future seismic response assessment of structures within a wide period range, it is essential to use broadband simulation techniques that combine the stochastic and deterministic methods.
- High-quality datasets are essential in terms of both ground motions and building inventories. Thus, continuous monitoring of seismic activities by dense station networks and damage data collection in the aftermath of large earthquakes are necessary in the future.
- For practicality in damage assessment methodology, detailed structural characteristics were not considered. Instead, all building stock was classified into 21 prototypes for which damage probability matrices were developed. For the future studies, more refined definitions can yield damage estimates with higher resolutions.
- This study only considered simple SDOF models and two-dimensional MDOF models with symmetric plans. For future studies, more investigations should be performed on the behavior of either three-dimensional or asymmetric structures.

- NLTHA is only applied for reinforced-concrete frames while the other building types such as tunnel-form or dual-form RC buildings are not investigated. Other structural types should also be studied in future works.
- Both the damage estimation and MDOF analyses are performed for selected case studies. Future applications are necessary for further validation of the proposed methods.

REFERENCES

Aagaard BT, Graves RW, Schwartz DP, Ponce DA, Graymer RW. Ground-motion modeling of Hayward fault scenario earthquakes, part i: Construction of the suite of scenarios. Bull Seismol Soc Am. 2010; 100(6):2927-2944. doi:10.1785/0120090324.

Akansel V, Ameri G, Askan A, Caner A, Erdil B, Kale Ö, Okuyucu, D. The 23 October 2011 M W 7.0 Van (Eastern Turkey) earthquake: Interpretations of recorded strong ground motions and post-earthquake conditions of nearby structures. Earthq Spectra. 2014; 30(2):657-682. doi:10.1193/012912EQS020M.

Aki K. Scaling law of seismic spectrum. J Geophys Res. 1967; 72(4):1217. doi:10.1029/JZ072i004p01217.

Aki K. Seismic displacements near a fault. J Geophys Res. 1968; 73(16):5359. doi:10.1029/JB073i016p05359.

Aki K. Space and time spectra of stationary stochastic waves, with special reference to microtremors. Bull Earthq Res Inst. 1957; 35:415-457. doi: 2261/11892.

Akinci A, Malagnini L, Herrmann RB, Pino NA, Scognamiglio L, Eyidogan H. High-frequency ground motion in the Erzincan region, Turkey: Inferences from small earthquakes. Bull Seismol Soc Am. 2001; 91(6):1446-1455. Doi: 10.1785/0120010125.

Akkar S, Aldemir A, Askan A, Bakır S, Canbay E, Demirel İO, Erberik MA, Gülerce Z, Gülkan P, Kalkan E, Prakash S. 8 March 2010 Elazig-Kovancilar (Turkey) earthquake: observations on ground motions and building damage. Seismol Res Lett. 2011; 82(1):42-58. doi:10.1785/gssrl.82.1.42.

Akkar S, Özen Ö. Effect of peak ground velocity on deformation demands for SDOF systems. Earthq Eng Struct Dyn. 2005; 34(13):1551-1571. doi:10.1002/eqe.492.

Akkar S, Sucuoğlu H, Yakut A. Displacement-Based Fragility Functions for Low- and Mid-rise Ordinary Concrete Buildings. Earthq Spectra. 2005; 21(4):901-927. doi:10.1193/1.2084232.

Akyuz HS. Surface Rupture and Slip Distribution of the 12 November 1999 Duzce earthquake (M 7.1), North Anatolian Fault, Bolu, Turkey. Bull Seismol Soc Am. 2002; 92(1):61-66. doi:10.1785/0120000840.

Ameri G, Gallovič F, Pacor F. Complexity of the Mw 6.3 2009 L'Aquila (central Italy) earthquake: 2. Broadband strong motion modeling. J Geophys Res. 2012; 117(B4):B04308. doi:10.1029/2011JB008729.

Ameri G, Massa M, Bindi D, Bindi D, D'Alema E, Gorini A, Luzi L, Marzorati S, Pacor F, Paolucci R, Puglia R, Smerzini C. The 6 April 2009 Mw 6.3 L'Aquila (Central Italy) earthquake: strong-motion observations. Seismol Res Lett. 2009; 80(6):951-966. doi:10.1785/gssrl.80.6.951.

American Society of Civil Engineers. Minimum design loads for buildings and other structures (ASCE/SEI 7-10); 2010.

Anderson J, Hough S. A model for the shape of the Fourier amplitude spectrum of acceleration at high frequencies. Bull Seismol Soc Am. 1984; 74(5): 1969-1993.

Anderson JG. Quantitative measure of the goodness-of-fit of synthetic seismograms. 13th World Conf Earthq Eng. 2004; (243): 775-784.

Ansal A, Akinci A, Cultrera G, Erdik M, Pessina V, Tönük G, Ameri G. Loss estimation in Istanbul based on deterministic earthquake scenarios of the Marmara Sea region (Turkey). Soil Dyn Earthq Eng. 2009; 29(4):699-709. doi:10.1016/j.soildyn.2008.07.006.

Aschheim M, Black E. Yield point spectra for seismic design and rehabilitation. Earthq Spectra. 2000; 16(2): 317-335. doi: 10.1193/1.1586115.

Askan A, Asten M, Erberik MA, Erkmen C, Karimzadeh S, Kilic N, Sisman FN, Yakut A. Seismic Damage Assessment of Erzincan, Turkish National Union of Geodesy and Geophysics project. Project no: TUJJB-UDP-01-12, Turkey, Ankara, 2015a.

Askan A, Karimzadeh S, Asten M, Kiliç N, Sisman FN, Erkmen C. Assessment of seismic hazard in the Erzincan (Turkey) region: construction of local velocity models and evaluation of potential ground motions. Turkish J Earth Sci. 2015b; 24(6):529-565.

Askan A, Karimzadeh S, Bilal M. Seismic intensity maps for North Anatolian Fault Zone (Turkey) based on recorded and simulated ground motion data, Book Chapter, Neotectonics and Earthquake Potential of the Eastern Mediterranean Region, AGU Books, 2016.

Askan A, Sisman F, Ugurhan B. Stochastic strong ground motion simulations in sparsely-monitored regions: A validation and sensitivity study on the 13 March 1992 Erzincan (Turkey) earthquake. Soil Dyn Earthq Eng. 2013; 55:170-181. doi:10.1016/j.soildyn.2013.09.014.

Askan A, Yucemen M. Probabilistic methods for the estimation of potential seismic damage: Application to reinforced concrete buildings in Turkey. Struct Saf. 2010; 32(4): 262-271.

Asten MW, Dhu T, Jones A, Jones T. Comparison of shear velocities measured from microtremor array studies and SCPT data acquired for earthquake site hazard classification in the northern suburbs of Perth W.A., Proceedings of a Conference of the Australian Earthquake Engineering Soc., 12 p., Melbourne, 2003.

ATC, Seismic evaluation and retrofit of concrete buildings, ATC-40, Applied Technology Council, Redwood City, 1996; 1.

Atkinson G, Assatourians K, Boore DM. A guide to differences between stochastic point-source and stochastic finite-fault simulations. Bull Seismol Soc Am. 2009; 99(6):3192-201. doi: 10.1785/0120090058.

Atkinson G, Boore DM. Earthquake ground-motion prediction equations for eastern North America. Bull Seismol Soc Am. 2006; 96(6): 2181-2205. doi: 10.1785/0120070023.

Atkinson G, Boore DM. Ground-motion relations for eastern North America. Bull Seismol Soc Am. 1995; 85(1):17-30.

Atkinson G, Goda K, Assatourians K. Comparison of nonlinear structural responses for accelerograms simulated from the stochastic finite-fault approach versus the hybrid broadband approach. Bull Seismol Soc Am. 2011; 101(6): 2967-2980. doi: 10.1785/0120100308.

Atkinson G, Goda K. Inelastic seismic demand of real versus simulated ground-motion records for Cascadia subduction earthquakes. Bull Seismol Soc Am. 2010; 100(1):102-115. doi:10.1785/0120090023.

Atkinson G, Macias M. Predicted ground motions for great interface earthquakes in the Cascadia subduction zone. Bull Seismol Soc Am. 2009; 99(3): 1552-1578. doi: 10.1785/0120080147.

Atkinson G, Mereu R. The shape of ground motion attenuation curves in southeastern Canada. Bull Seismol Soc Am. 1992; 82(5): 2014-2031.

Atkinson G, Silva W. Stochastic modeling of California ground motions. Bull Seismol Soc Am. 2000; 90(2):255-274. doi: 10.1785/0119990064.

Atkinson G. Attenuation of strong ground motion in Canada from a random vibrations approach. Bull Seismol Soc Am. 1984; 74.6: 2629-2653.

Atkinson G. Empirical attenuation of ground-motion spectral amplitudes in southeastern Canada and the northeastern United States. Bull Seismol Soc Am. 2004; 94.3: 1079-1095

Azari A, Askan A, Erberik MA. Site-Specific Uniform Hazard Spectrum Based on. In: Second European Conference on Earthquake Engineering and Seismology. Istanbul; 2014:9.

Baker J, Cornell C. Correlation of response spectral values for multicomponent ground motions. Bull Seismol Soc Am. 2006; 96(1): 215-227. doi: 10.1785/0120050060.

Bal I, Bommer J, Stafford P. The influence of geographical resolution of urban exposure data in an earthquake loss model for Istanbul. Earthq Spectra 2010; 26(3): 619-634. doi:10.1193/1.3459127.

Bao H, Bielak J, Ghattas O. Large-scale simulation of elastic wave propagation in heterogeneous media on parallel computers Comput Methods in Appl Mech Eng. 1998; 152(1-2): 85-102. doi: 10.1016/S0045-7825(97)00183-7.

Barbat A, Moya F, Canas J. Damage scenarios simulation for seismic risk assessment in urban zones. Earthq spectra. 1996; 12(3):371-394 .doi:10.1193/1.1585889.

Barka A. Tectonics of the Erzincan basin and its vicinity and 13 March 1992 Erzincan earthquake. Proc 2nd Natl Conf. 1993; 259-270.

Bazzurro P, Sjoberg B, Luco N. Post-elastic response of structures to synthetic ground motions. Report for Pacific Earthquake Engineering Research (PEER) Center Lifelines Program Project. 2004; 65-112.

Beresnev I, Atkinson G. Modeling finite-fault radiation from the ωn spectrum. Bull Seismol Soc Am. 1997; 87(1):67-84.

Beresnev I, Atkinson GM. FINSIM—a FORTRAN program for simulating stochastic acceleration time histories from finite-faults, Seism Res Lett. 1998(a); 69: 27–32.

Beresnev IA, Atkinson GM. Stochastic finite-fault modeling of ground motions from the 1994 Northridge, California, earthquake. I. Validation on rock sites. Bull Seismol Soc Am. 1998(b); 88(6):1392-401.

Bernard P, Gariel J, Dorbath L. Fault location and rupture kinematics of the magnitude 6.8, 1992 Erzincan earthquake, Turkey, from strong ground motion and regional records. Bull Seismol Soc Am. 1997; 87(5):1230-1243.

Biggs J. Introduction to structural dynamics. 1964; 276-314.

Boatwright J, Choy G. Acceleration source spectra anticipated for large earthquakes in northeastern North America. Bull Seismol Soc Am. 1992; 82:660-682.

Boore DM, Boatwright J. Average body-wave radiation coefficients. Bull Seismol Soc Am. 1984; 74(5):1615-1621.

Boore DM, Joyner W. Estimation of ground motion at deep-soil sites in eastern North America. Bull Seismol Soc Am. 1991; 81(6):2167-85.

Boore DM, Joyner W. Site amplifications for generic rock sites. Bull Seismol Soc Am. 1997; 87(2):327-341.

Boore DM. Comparing stochastic point-source and finite-source ground-motion simulations: SMSIM and EXSIM. Bull Seismol Soc Am. 2009. 99(6): 3202-3216. doi: 10.1785/0120090056.

Boore DM. Simulation of ground motion using the stochastic method. Pure Appl Geophys. 2003; 160(3):635-676. doi: 10.1007/PL00012553.

Boore DM. Stochastic simulation of high-frequency ground motions based on seismological models of the radiated spectra. Bull Seismol Soc Am. 1983. 73(6): 1865-1894.

Boore DM. Use of seismoscope records to determine ML and peak velocities. Bull Seismol Soc Am. 1984; 74(1):315-324.

Boore DM. SMSIM: Fortran programs for simulating ground motions from earthquakes. U.S. Geol. Surv. 1996; Open-file Rept. 96-80-A.

Borcherdt R. Effects of local geology on ground motion near San Francisco Bay. Bull Seismol Soc Am. 1970; 60(1):29-61.

Bouchon M. A simple method to calculate Green's functions for elastic layered media. Bull Seismol Soc Am. 1981; 71(4):959-971.

Brune J. Correction [to "Tectonic stress and the spectra, of seismic shear waves from earthquakes"]. J Geophys Res. 1971; 76(20):5002-5002. doi:10.1029/JB076i020p05002.

Brune J. Tectonic stress and the spectra of seismic shear waves from earthquakes. J Geophys Res. 1970; 75(26):4997. doi: 10.1029/JB075i026p04997.

Calvi GM, Pinho R, Magenes G, Bommer JJ, Restrepo-Vélez LF, Crowley H. Development of seismic vulnerability assessment methodologies over the past 30 years. ISET J Earthq Tech 2006; 43(3): 75-104.

Cartwright DE, Longuet-Higgins MS. The Statistical Distribution of the Maxima of a Random Function. Proceedings of the Royal Society A: Mathematical, Physical and Engineering Sciences. 1956; 237(1209):212-232. doi: 10.1098/rspa.1956.0173.

Castro R, Rovelli A, Cocco M. Stochastic simulation of strong-motion records from the 26 September 1997 (Mw 6), Umbria-Marche (Central Italy) earthquake. Bull Seismol Soc Am. 2001; 91(1), 27-39. doi:10.1785/0120000011.

Castro RR, Pacor F, Franceschina G, Bindi D, Zonno G, Luzi L. Stochastic strong-motion simulation of the Mw 6 Umbria–Marche earthquake of September 1997: Comparison of different approaches. Bull Seismol Soc Am. 2008; 98(2): 662-670.

Cen C. Eurocode 8: Design of structures for earthquake resistance—Part 1: General Rules. Seism Actions Rules Build. 2004.

Chen X, Zhang H. An efficient method for computing Green's functions for a layered half-space at large epicentral distances. Bull Seismol Soc Am. 2001; 91(4): 858-869.

Cirella A, Piatanesi A, Cocco M, Tinti E, Scognamiglio L, Michelini A, Lomax A, Boschi E. Rupture history of the 2009 L'Aquila (Italy) earthquake from non-linear joint inversion of strong motion and GPS data. Geophys Research Lett. 2009; 36(19). doi: 10.1029/2009GL039795.

Claprood M, Asten M. Use of SPAC, HVSR and strong motion analysis for site hazard study over the Tamar Valley in Launceston, Tasmania. Proc Conf. 2007.

Clough R, Johnston SB. Effect of stiffness degradation on earthquake ductility requirements, Proceedings, Second Japan National Conference on Earthquake Engineering. 1966: 227-232.

Coburn A, Spence R. Earthquake protection. Second edition, John Wiley & Sons Ltd. 2002; 420.

Cohen G, Joly P, Tordjman N. Construction and analysis of higher-order finite elements with mass lumping for the wave equation. Proc Second Int Conf on mathematical and numerical aspects of wave propagation. 1993.

Did You Feel It? http://earthquake.usgs.gov/data/dyfi/. Accessed March 14, 2016.

Dolce M, Kappos A, Zuccaro G, Coburn AW. State of the art Report of WG 3-seismic risk and vulnerability. In Proceedings of the 10th European Conference on Earthquake Engineering, Wien. 1994.

Durukal E. Critical evaluation of strong motion in Kocaeli and Düzce (Turkey) earthquakes. Soil Dyn Earthq Eng. 2002; 22(7): 589-609. doi: 22(7), 589-609.

Erberik M, Elnashai A. Fragility analysis of flat-slab structures. Eng Struct. 2004; 26(7): 937-948. doi: 10.1016/j.engstruct.2004.02.012.

Erberik M. Fragility-based assessment of typical mid-rise and low-rise RC buildings in Turkey. Eng Struct. 2008(b); 30(5): 1360-1374. doi: 10.1016/j.engstruct.2007.07.016.

Erberik M. Generation of fragility curves for Turkish masonry buildings considering in-plane failure modes. Earthq Eng Struct Dyn. 2008(a); 37(3): 387-405. doi: 10.1002/eqe.760.

Erdik M, Durukal E. A hybrid procedure for the assessment of design basis earthquake ground motions for near-fault conditions. Soil Dyn Earthq Eng. 2001; 21(5): 431-443. doi: 10.1016/S0267-7261(01)00025-2.

Erdik M, Yuzugullu O, Karakoc C, Yilmaz C, Akkas N. March 13, 1992 Erzincan (Turkey) earthquake. Earthq Eng Tenth World Conf. 1994:7045-7051.

EXSIM, A FORTAN program for simulating stochastic acceleration time histories from finite-faults with a dynamic corner frequency approach. http://www.daveboore.com/software_online.html, [last visited on December 2015].

Fajfar P, Fischinger M. N2-A method for non-linear seismic analysis of regular buildings. In Proceedings of the Ninth World Conference in Earthquake Engineering.1988; 5: 111-116.

FEMA F. 273: NEHRP Guidelines for the seismic rehabilitation of buildings. Fed Emerg Manag Agency. 1997.

Frankel A, Vidale J. A three-dimensional simulation of seismic waves in the Santa Clara Valley, California, from a Loma Prieta aftershock. Bull Seismol Soc Am. 1992; 82(5): 2045-2074

Frankel A. A constant stress-drop model for producing broadband synthetic seismograms: comparison with the next generation attenuation relations. Bull Seismol Soc Am. 2009; 99(2A):664-680. doi:10.1785/0120080079.

Frankel A. Three-dimensional simulations of ground motions in the San Bernardino Valley, California, for hypothetical earthquakes on the San Andreas fault. Bull Seismol Soc Am. 1993; 83(4): 1020-1041.

Galasso C, Zareian F. Elastic and post-elastic response of structures to hybrid broadband synthetic ground motions. Proc. of 9th International Conference on Urban Earthquake Engineering/4th Asia Conference on Earthquake Engineering. Marzo 6-8, 2012, Tokyo Institute of Technology, Tokyo, Japan. 2012.

Galasso C, Zareian F. Engineering validation of hybrid broadband ground motion simulation using historical events. Tenth U.S. National Conference on Earthquake Engineering. 2014.

Galasso C, Zhong P, Zareian F, Iervolino I, Graves RW. Validation of ground-motion simulations for historical events using MDoF systems. Earthq Eng Struct Dyn. 2013; 42(9): 1395-412.

Gallovič F, Brokešová J. Hybrid k-squared source model for strong ground motion simulations: Introduction. Phys Earth Planet Inter. 2007; 160(1): 34-50. doi: 10.1016/j.pepi.2006.09.002.

Gallovič F, Zahradník J. Complexity of the Mw 6.3 2009 L'Aquila (central Italy) earthquake: 1. Multiple finite-extent source inversion. J Geophys Res: Solid Earth. 2012; 117(B4). doi:10.1029/2011JB008729.

Gavali P, Shah M. Earthquake simulations of large scale structures using OpenSees software on grid and high performance computing in India. The 14th World Conference on Earthquake Engineering, Beijing, China, 2008.

Ghofrani H, Atkinson GM, Goda K, Assatourians K. Stochastic finite-fault simulations of the 2011 Tohoku, Japan, earthquake. Bull Seismol Soc Am. 2013; 103(2B):1307-1320. doi:10.1785/0120120228.

Girgin SC, Lu Y, Panagiotou M. Nonlinear cyclic truss model for shear-critical reinforced concrete columns. In: 2nd Turkish Conference on Earthquake Engineering and Seismology TDMSK 2013; 2013:1-10.

Goda K, Kurahashi S, Ghofrani H, Atkinson GM, Irikura K. Nonlinear response potential of real versus simulated ground motions for the 11 March 2011 Tohoku-oki earthquake. Earthq Spectra. 2015; 31(3):1711-34.

Graves R, Pitarka A. Broadband ground-motion simulation using a hybrid approach. Bull Seismol Soc Am. 2010. 100(5A), 2095-2123.

Grosser HE, Baumbach MI, Berckhemer HA, Baier BO, Karahan A, Schelle HO, Krüger FR, Paulat AR, Michel GE, Demirtas RA, Gencoglu SI. The Erzincan earthquake (Ms= 6.8) of March 13, 1992 and its aftershock sequence. Pure Appl geophys. 1998; 152(3):465-505.

Gurpinar A, Abali M, Yucemen M, Yesilcay Y. Feasibility of obligatory earthquake insurance in Earthquake Engineering Research Center, Civil Engineering Department, Middle East Technical University, Turkey, Report 78-05, 1978.

Halldorsson B. Near-fault and far-field strong ground-motion simulation for earthquake engineering applications using the specific barrier model. J Struct Eng. 2010; 137.3 (2010): 433-444. doi: 10.1061/(ASCE)ST.1943-541X.0000097.

Hanks T, Boore DM. Moment-magnitude relations in theory and practice. J Geophys Res: Solid Earth. 1984; 89(B7): 6229. doi: 10.1029/JB089iB07p06229.

Hanks T. b values and ω− γ seismic source models: Implications for tectonic stress variations along active crustal fault zones and the estimation of high-frequency strong. J Geophys Res Solid Earth. 1979; 84(B5): 2235-2242. doi: 10.1029/JB084iB05p02235.

Hanks T. F_max. Bull Seismol Soc Am. 1982; 72(6): 1867-1879.

Hanks TC, Kanamori H. A moment magnitude scale. J Geophys Res: Solid Earth. 1979; 84(B5):2348-2350. doi:10.1029/JB084iB05p02348.

Hanks TC, McGuire RK. The character of high-frequency strong ground motion. Bull Seismol Soc Am. 1981; 71(6):2071-2095.

Hartzell S, Harmsen S. Calculation of broadband time histories of ground motion: Comparison of methods and validation using strong-ground motion from the 1994 Northridge earthquake. Bull Seismol Soc Am. 1999; 89(6):1484-1504.

Hartzell S. Earthquake aftershocks as Green's functions. Geophys Res Lett. 1978; 5:1-4. doi: 10.1029/GL005i001p00001.

Haskell N. Crustal reflection of plane SH waves. J Geophys Res. 1960; 65(12): 4147-4150. doi:10.1029/JZ065i012p04147.

Haskell N. Total energy and energy spectral density of elastic wave radiation from propagating faults. Part II. A statistical source model. Bull Seismol Soc Am. 1966; 54(6):1811-1841.

Haskell N. Total energy and energy spectral density of elastic wave radiation from propagating faults. Bull Seismol Soc Am. 1964.

Heaton T, Hartzell S. Source characteristics of hypothetical subduction earthquakes in the northwestern United States. Bull Seismol Soc Am. 1986; 76(3): 675-708.

Heaton TH, Hall JF, Wald DJ, Halling MW. Response of high-rise and base-isolated buildings to a hypothetical mw 7.0 blind thrust earthquake. Science. 1995; 267(5195):206-211. doi:10.1126/science.267.5195.206.

Herrmann R. An extension of random vibration theory estimates of strong ground motion to large distances. Bull Seismol Soc Am. 1985; 75(5): 1447-1453.

Hirasawa T, Stauder W. On the seismic body waves from a finite moving source. Bull Seismol Soc Am. 1965; 55(2): 237-262.

Hisada Y. An efficient method for computing Green's functions for a layered half-space with sources and receivers at close depths. Bull Seismol Soc Am. 1994; 84(5): 1456-1472.

Hisada Y. Broadband strong motion simulation in layered half-space using stochastic Green's function technique. J Seismol. 2008; 12(2): 265-279.

Hough S, Dreger D. Source parameters of the 23 April 1992 M 6.1 Joshua Tree, California, earthquake and its aftershocks: Empirical Green's function analysis of GEOS and TERRAscope. Bull Seismol Soc Am. 1995; 85(6): 1576-1590.

Housner G. Characteristics of strong-motion earthquakes. Bull Seismol Soc Am. 1947; 37(1): 19-31.

Housner G. Properties of strong ground motion earthquakes. Bull Seismol Soc Am. 1955; 45(3): 197-218.

Housner GW. Intensity of ground motion during strong earthquakes. California Inst of Tech Pasadena Earthquake Engineering Research Lab, 1952.

Huang H, Teng T. An evaluation on H/V ratio vs. spectral ratio for site-response estimation using the 1994 Northridge earthquake sequences. Pure Appl Geophys. 1999; 156(4): 631-649. doi: 10.1007/s000240050316.

Ibarra L, Krawinkler H. Global collapse of frame structures under seismic excitations. Pacific Earthquake Engineering Research Center, 2005.

Ibarra LF, Medina RA, Krawinkler H. Hysteretic models that incorporate strength and stiffness deterioration. Earthq Eng Struc Dyn. 2005; 34(12):1489-511. doi: 10.1002/eqe.495.

Iervolino I, Cornell C. Record selection for nonlinear seismic analysis of structures. Earthq Spectra. 2005; 21(3): 685-713. doi: 10.1193/1.1990199.

International Conference on Building Officials (ICBO), Uniform Building Code, Whittier, CA, 1982.

Irikura K. Prediction of strong acceleration motion using empirical Green's function. Proc 7th Japan Earthq Eng Symp. 1986; 151:156.

Irikura K. Semi-Empirical Estimation During Large of Strong Earthquakes Ground Motions. Disaster Prev Res Institute, Kyoto Univ. 1983; 33: 63-104.

ITACA, Italian Accelerometric Archive. http://itaca.mi.ingv.it/ItacaNet, [last visited on November 2013].

Joyner W, Boore DM. On Simulating Large Earthquakes by Green's–Function Addition of Smaller Earthquakes. Earthq source Mech. 1986; 269-274. doi: 10.1029/GM037p0269.

Joyner W, Fumal T. Predictive mapping of earthquake ground motion. Evaluating Earthquake Hazards in the Los Angeles Region. An Earth Science Perspective, 1985; 1360: 203-220.

Kadaş K. Influence of idealized pushover curves on seismic response, MS Thesis, Department of Civil Eng, METU University, Ankara city, 2006.

Kamae K, Irikura K, Pitarka A. A technique for simulating strong ground motion using hybrid Green's function. Bull Seismol Soc Am. 1998; 88(2): 357-367.

Kappos A, Pitilakis K, Morfidis K, Hatzinikolaou N. Vulnerability and risk study of Volos (Greece) metropolitan area. In Proc. 2002.

Kappos A, Stylianidis K, Pitilakis K. Development of seismic risk scenarios based on a hybrid method of vulnerability assessment. Nat Hazards. 1998; 17(2): 177-192.

Karimzadeh S, Askan A, Erberik MA, Yakut A. Seismic damage assessment using synthetic ground motions: a case study for erzincan, 3rd Turkish conference on Earthquake Engineering and Seismology, Izmir, Turkey, 2015.

Karsan I, JirsaJ. Behavior of concrete under compressive loadings. J Struct Div. 1969; 95(12): 2543-2564.

Kawase H. Time-domain response of a semi-circular canyon for incident SV, P, and Rayleigh waves calculated by the discrete wavenumber boundary element method. Bull Seismol Soc Am. 1988; 78(4): 1415-1437.

Kennett BLN. Seismic wave propagation in a stratified half-space, Cambridge University Press, Cambridge. 1983.

Kent D, Park R. Flexural members with confined concrete. J Struct Div. 1971; 97(7): 1969-1990.

Kircher C, Nassar AA, Kustu O, Holmes WT. Development of building damage functions for earthquake loss estimation. Earthq spectra. 1997; 13(4): 663-682. doi: 10.1193/1.1585974.

Kircil M, Polat Z. Fragility analysis of mid-rise R/C frame buildings. Eng Struct. 2006; 28(9): 1335-1345. doi:10.1016/j.engstruct.2006.01.004.

Komatitsch D, Liu Q, Tromp J, Süss P, Stidham C, Shaw JH. Simulations of ground motion in the Los Angeles basin based upon the spectral-element method. Bull Seismol Soc Am. 2004; 94(1): 187-206. doi: 10.1785/0120030077.

Komatitsch D, Tromp J. Introduction to the spectral element method for three-dimensional seismic wave propagation. Geophys J Int. 1999; 139(3): 806-822. doi: 10.1046/j.1365-246x.1999.00967.x.

Komatitsch D, Vilotte J. The spectral element method: an efficient tool to simulate the seismic response of 2D and 3D geological structures. Bull Seismol Soc Am. 1998: 88(2); 368-392.

Komatitsch D. Spectral and spectral-element methods for the 2D and 3D elastodynamics equations in heterogeneous media. Paris, Fr Inst Phys du Globe. 1997.

Krishnan S, Ji C, Komatitsch D, Tromp J. Case studies of damage to tall steel moment-frame buildings in southern California during large San Andreas earthquakes. Bull Seismol Soc Am. 2006a; 96(4A): 1523-1537. doi: 10.1785/0120050145.

Krishnan S, Ji C, Komatitsch D, Tromp J. Performance of two 18-story steel moment-frame buildings in southern California during two large simulated San Andreas earthquakes. Earthq Spectra. 2006b; 22(4): 1035-1061. doi:10.1193/1.2360698.

Kwon OS, Elnashai A. The effect of material and ground motion uncertainty on the seismic vulnerability curves of RC structure. Eng Struct. 2006; 28(2): 289-303. doi:10.1016/j.engstruct.2005.07.010.

Lam N, Wilson J, Hutchinson G. Generation of synthetic earthquake accelerograms using seismological modelling: a review. J Earthq Eng. 2000; 4(03): 321-354.

Lang DH, Molina-Palacios S, Lindholm CD. Towards near-real-time damage estimation using a CSM-based tool for seismic risk assessment. J Earthq Eng. 2008; 12(S2): 199-210. doi:10.1080/13632460802014055.

Legrand D, Delouis B. Determination of the fault plane using a single near-field seismic station with a finite-dimension source model. Geophys J Int. 1999; 138(3): 801-808.

Lermo J, Chávez-García F. Are microtremors useful in site response evaluation? Bull Seismol Soc Am. 1994; 84(5): 1350-1364.

Li X, Bielak J, Ghattas O. Three-dimensional earthquake site response on a CM-2. Proc Tenth World Conf on Earthq Eng. 1992. (pp. 959-964).

Lignos D, Krawinkler H. Deterioration modeling of steel components in support of collapse prediction of steel moment frames under earthquake loading. J Struct Eng. 2010; 137(11): 1291-1302. doi:10.1061/(ASCE)ST.1943-541X.0000376.

Lignos D, Krawinkler H. Development and utilization of structural component databases for performance-based earthquake engineering. J Struct Eng. 2012; 139(8): 1382-1394. doi: 10.1061/(ASCE)ST.1943-541X.0000646.

Louie J. Faster, better: shear-wave velocity to 100 meters depth from refraction microtremor arrays. Bull Seismol Soc Am. 2001; 91(2): 347-364.

Luco JE, Wong HL, De Barros FCP. Three-dimensional response of a cylindrical canyon in a layered half-space. Earthq Eng Struct D. 1990; 19(6): 799-817. doi:10.1002/eqe.4290190603.

Mai P, Imperatori W, Olsen K. Hybrid broadband ground-motion simulations: Combining long-period deterministic synthetics with high-frequency multiple S-to-S backscattering. Bull Seismol Soc Am. 2010; 100(5A): 2124-2142.

Malagnini L, Scognamiglio L, Mercuri A, Akinci A, Mayeda K. Strong evidence for non-similar earthquake source scaling in central Italy. Geophys Res Lett. 2008; 35(17). doi:10.1029/2008GL034310.

Mavroeidis G, Papageorgiou A. A mathematical representation of near-fault ground motions. Bull Seismol Soc Am. 2003; 93(3): 1099-1131.

Mazılıgüney L, Yakut A, Kadaş K, Kalem İ. Fragility analysis of reinforced concrete school buildings using alternative intensity measure-based ground motion sets. 2nd Turkish Conference on Earthquake Engineering and Seismology – TDMSK -2013.

McGuire R, Hanks T. RMS accelerations and spectral amplitudes of strong ground motion during the San Fernando, California earthquake. Bull Seismol Soc Am. 1980; 70(5): 1907-1919.

Milkereit C, Zünbül S, Karakisa S, Iravul Y, Zschau J, Baumbach M, Grosser H, Günther E, Umutlu N, Kuru T, Erkul E. Preliminary aftershock analysis of the Mw= 7.4 Izmit and Mw= 7.1 Düzce earthquake in western Turkey. The. 1999; 179-187.

Moczo P, Kristek J, Vavryčuk V, Archuleta RJ, Halada L. 3D heterogeneous staggered-grid finite-difference modeling of seismic motion with volume harmonic and arithmetic averaging of elastic moduli and densities. Bull Seismol Soc Am. 2002; 92(8): 3042-3066.

Mohammadioun B, Serva L. Stress drop, slip type, earthquake magnitude, and seismic hazard. Bull Seismol Soc Am. 2001; 91(4): 694-707.

Motazedian D, Atkinson G. Stochastic finite-fault modeling based on a dynamic corner frequency. Bull Seismol Soc Am. 2005; 95(3): 995-1010.

Motazedian D, Moinfar A. Hybrid stochastic finite fault modeling of 2003, M6. 5, Bam earthquake (Iran). J Seismol. 2006; 10(1): 91-103.

Nakamura Y. A method for dynamic characteristics estimation of subsurface using microtremor on the ground surface. Q. Rep. Railw. Tech. Res. Inst. 1989; 30(1).

NEHRP guidelines for the seismic rehabilitation of buildings. 1997.

Olsen K, Archuleta R, Matarese J. Three-dimensional simulation of a magnitude 7.75 earthquake on the San Andreas fault. Science. 1995; 270(5242): 1628.

Olsen K, Archuleta R. Three-dimensional simulation of earthquakes on the Los Angeles fault system. Bull Seismol Soc Am. 1996; 86(3): 575-596.

Olsen K, Mayhew J. Goodness-of-fit criteria for broadband synthetic seismograms, with application to the 2008 Mw 5.4 Chino Hills, California, earthquake. Seismol Res Lett. 2010; 81(5): 715-723.

Olsson A, Sandberg G, Dahlblom O. On Latin hypercube sampling for structural reliability analysis. Struct Saf. 2003; 25(1):47-68.

OpenSees 2.4.5. Computer Software, University of California, Berkeley, CA. Retrieved from http://opensees.berkeley.edu, [last visited on December 2014]

Otani S. Hysteresis Models for Earthquake Response Analysis. Annual Research Publications, Aoyama Laboratory, Department of Architecture, Faculty of Engineering, University of Tokyo. 1993.

Pacor F, Cultrera G, Mendez A, Cocco M. Finite fault modeling of strong ground motions using a hybrid deterministic–stochastic approach. Bull Seismol Soc Am. 2005; 95(1): 225-240.

Papageorgiou A, Aki K. A specific barrier model for the quantitative description of inhomogeneous faulting and the prediction of strong ground motion. I. Description of the model. Bull Seismol Soc Am. 1983; 73(3): 693-722.

Park C, Miller R, Xia J. Multichannel analysis of surface waves. Geophys. 1999; 64(3): 800-808. doi: 10.1190/1.1444590.

Park Y, Reinhorn A, Kunnath S. IDARC: Inelastic damage analysis of reinforced concrete frame-shear-wall structures. 1987.

Pedersen H. Three-dimensional scattering by two-dimensional topographies. Bull Seismol Soc Am. 1994; 84(4): 1169-1183.

Pitarka A, Irikura K, Iwata T, Sekiguchi H. Three-dimensional simulation of the near-fault ground motion for the 1995 Hyogo-ken Nanbu (Kobe), Japan, earthquake. Bull Seismol Soc Am. 1998; 88(2): 428-440.

Pitarka A, Somerville P, Fukushima Y, Uetake T, Irikura K. Simulation of near-fault strong-ground motion using hybrid Green's functions. Bull Seismol Soc Am. 2000; 90(3): 566-586.

Porter KA, Kiremidjian AS. Assembly-based vulnerability of buildings and its uses in seismic performance evaluation and risk-management decision making. Report 139. Report of the John A. Blume Earthquake Engineering Research Center, Stanford, CA, United States. 2001; 196.

Priolo E, Carcione J, Seriani G. Numerical simulation of interface waves by high-order spectral modeling techniques. J Acoust Soc Am. 1994; 95(2): 681-693. doi: 10.1121/1.408428.

Qi X, Moehle J. Displacement design approach for reinforced concrete structures subjected to earthquakes. Earthquake Engineering Research Center, College of Engineering/University of California. 1991; 91(2).

Raghukanth S, Somala S. Modeling of strong-motion data in northeastern India: Q, stress drop, and site amplification. Bull Seismol Soc Am. 2009; 99(2A): 705-725.

Reitherman RK. Conversion of Damage Probability Matrices into Fragility Curves. Panel Earthq Loss Estim Natl Res Counc. 1986.

Rial J, Saltzman N, Ling H. Earthquake-induced resonance in sedimentary basins. Am Sci. 1992; 80(6), 566-578.

Romero S, Rix G. Regional variations in near surface shear wave velocity in the greater Memphis area. Eng Geol. 2001; 62(1), 137-158. doi:10.1016/S0013-7952(01)00059-X.

Rosenblad B, Li J. Comparative study of refraction microtremor (ReMi) and active source methods for developing low-frequency surface wave dispersion curves. J Environ Eng Geophys (JEEG). 2009; 14(3): 101-113.

Roufaiel M, Meyer C. Analytical modeling of hysteretic behavior of R/C frames. J Struct Eng. 1987; 113(3): 429-444. doi: 10.1061/(ASCE)0733-9445(1987).

Roumelioti Z, Kiratzi A, Theodulidis N. Stochastic strong ground-motion simulation of the 7 September 1999 Athens (Greece) earthquake. Bull Seismol Soc Am. 2004; 94(3): 1036-1052.

Sahin M, Tari E. The August 17 Kocaeli and the November 12 Duzce earthquakes in Turkey. Earth Planets Sp. 2000; 52(10): 753-757. doi:10.1186/BF03352277.

Saiidi M, Sozen M. Simple nonlinear seismic analysis of R/C structures. J Struct Div. 1981; 107(5), 937-953.

Salami MR, Goda K. Seismic loss estimation of residential wood-frame buildings in southwestern British Columbia: Considering mainshock-aftershock sequences. J Perform Constr Facil. 2013; 28(6): A4014002. doi:10.1061/(ASCE)CF.1943-5509.0000514.

Salamon A. The Mw6. 3, 2009, L'aquila Earthquake, Central Italy: Report of the GSI Team Visit to the Affected Area. Ministry of National Infrastructures-Geological survey of Israel. 2010.

Sanchez-Sesma F. Site effects on strong ground motion. Soil Dyn Earthq Eng. 1987; 6(2): 124-132. doi:10.1016/0267-7261(87)90022-4.

Sandi H. Seismic vulnerability and seismic intensity. Eur Conf Earthq Eng. 1982; 7: 431-438.

Schmidt R. Multiple emitter location and signal parameter estimation. Antennas Propagation, IEEE Trans. 1986; 34(3): 276-280. doi:10.1109/TAP.1986.1143830.

Scott B, Park R, Priestley M. Stress-strain behavior of concrete confined by overlapping hoops at low and high strain rates. J Proc. 1982; 79(1): 13-27.

Şengezer BS. The Damage Distribution during March 13, 1992 Erzincan Earthquake, proceedings, 2nd National Earthquake Engineering Conference. 1993; 404-415.

Shoja-Taheri J, Ghofrani H. Stochastic finite-fault modeling of strong ground motions from the 26 December 2003 Bam, Iran, earthquake. Bull Seismol Soc Am. 2007; 97(6): 1950-1959.

Silva W, Darragh R. Engineering Characterization of Earthquake Strong Ground Motion Recorded at Rock Sites. Electr Power Res Institute, Palo Alto, Calif. 1995.

Sivaselvan M, Reinhorn A. Hysteretic models for cyclic behavior of deteriorating inelastic structures. Tech Rep MCEER. 1999; 99.

Sørensen MB, Lang DH. Incorporating simulated ground motion in seismic risk assessment: Application to the lower Indian Himalayas. Earthq Spectra. 2015; 31(1): 71-95. doi:10.1193/010412EQS001M.

Stojadinovic B, Thewalt C. Energy balanced hysteresis models. In eleventh world conference on earthquake engineering, Earthquake engineering research at Berkeley, College of engineering, University of California at Berkeley. 1996; 1734.

Stokoe K, Wright S, Bay JA, Roesset JM. Characterization of geotechnical sites by SASW method, ISSMFE Technical Committee #10 for XIII ICSMFE, Geophysical characterization of sites. A. A. Balkema Publishers/Rotterdam & Brookfield, Netherlands. 1994; 15-25.

Strong Ground Motion Database of Turkey, DAPHNE, http://daphne.deprem.gov.tr:89/2K/daphne_v4.php, [last visited on September 2013].

Su Z, Ye L. Identification of damage using Lamb waves: from fundamentals to applications. Springer Science & Business Media 2009.

Sucuoğlu H, Anderson J, Zeng Y. Predicting intensity and damage distribution during the 1995 Dinar, Turkey, earthquake with generated strong motion accelerograms Bull Seismol Soc Am. 2003; 93(3): 1267-1279.

Sucuoğlu H, Erberik A. Energy-based hysteresis and damage models for deteriorating systems. Earthq Eng Struct D. 2004; 33(1): 69-88. doi:10.1002/eqe.338.

Sucuoğlu H, Tokyay M. 13 Mart 1992 Erzincan earthquake engineering report, civil engineering department, Ankara. 1992; 102.

Suzuki T, Adachi Y, Tanaka M. Application of microtremor measurements to the estimation of earthquake ground motions in Kushiro city during the Kushiro-Oki earthquake of 15 january 1993. Earthq Eng Struct D. 1995; 24(4): 595-613. doi:10.1002/eqe.4290240409.

Takeda T, Sozen M, Nielsen N. Reinforced concrete response to simulated earthquakes. J Struct Div. 1970; 96(12): 2557-2573.

Taucer FF, Spacone E, Filippou FC. A Fiber Beam-Column Element for Seismic Response Analysis of Reinforced Concrete Structures. Ucb/Eerc. 1991; 91(17).

Thomson W. Spectral aspect of earthquakes. Bull Seismol Soc Am. 1959; 49(1): 91-98.

Toro G, McGuire R. An investigation into earthquake ground motion characteristics in eastern North America. Bull Seismol Soc Am. 1987; 77(2): 468-489.

Toshinawa T, Ohmachi T. Love-wave propagation in a three-dimensional sedimentary basin. Bull Seismol Soc Am. 1992; 82(4): 1661-1677.

TÜİK, http://www.tuik.gov.tr/Web2013/iletisim/iletisim.html, [last visited on September 2013].

Turkish Ministry of Public Works and Settlement. Specification for structures to be built in disaster Areas, Ankara. 1997.

Turkish Ministry of Public Works and Settlement. Specification for structures to be built in disaster Areas, Ankara. 2007.

Ucar T, Duzgun M. Derivation of Analytical Fragility Curves for RC Buildings Based on Nonlinear Pushover Analysis. Tek DERGI. 2013; 24(3): 6421-6446.

Ugurhan B, Askan A, Erberik MA. A Methodology for Seismic Loss Estimation in Urban Regions Based on Ground-Motion Simulations. Bull Seismol Soc Am. 2011; 101(2):710-725. doi:10.1785/0120100159.

Ugurhan B, Askan A, Akinci A, Malagnini L. Strong-ground-motion simulation of the 6 April 2009 L'Aquila, Italy, earthquake. Bull Seismol Soc Am. 2012; 102(4): 1429-1445. doi: 10.1785/0120110060.

Ugurhan B, Askan A. Stochastic strong ground motion simulation of the 12 November 1999 Düzce (Turkey) earthquake using a dynamic corner frequency approach. Bull Seismol Soc Am. 2010; 100(4): 1498-1512. doi:10.1785/0120090358.

Umutlu N, Koketsu K, Milkereit C. The rupture process during the 1999 Düzce, Turkey, earthquake from joint inversion of teleseismic and strong-motion data. Tectonophysics. 2004; 391(1): 315-324. doi:10.1016/j.tecto.2004.07.019.

Wasti ST, Ozcebe G, eds. Seismic Assessment and Rehabilitation of Existing Buildings. Dordrecht: Springer Science & Business Media. 2003; 29. doi:10.1007/978-94-010-0021-5.

Wells D, Coppersmith K. New empirical relationships among magnitude, rupture length, rupture width, rupture area, and surface displacement. Bull Seismol Soc Am.1994; 84(4): 974-1002.

Whitman RV, Reed JW, Hong ST. Earthquake damage probability matrices. In Proceedings of the Fifth World conference on earthquake engineering. 1973; 2: 2531-2540.

Yalcinkaya E. Stochastic finite-fault modeling of ground motions from the June 27, 1998 Adana-Ceyhan earthquake. Earth Planets Sp. 2005; 57(2): 107-115.

Yılmaz H. Correlation of deformation demands with ground motion intensity, MS Thesis, Department of Civil Eng., METU University, Ankara city; 2007.

Yomogida K, Etgen J. 3-D wave propagation in the Los Angeles basin for the Whittier-Narrows earthquake. Bull Seismol Soc Am. 1993; 83(5): 1325-1344.

Zeng Y, Anderson J, Yu G. A composite source model for computing realistic synthetic strong ground motions. Geophys Res Lett. 1994; 21(8): 725-728. doi:10.1029/94GL00367.

Zhao Z, Xu J, Kubota R, Liu L. Strong ground motion simulation for seismic hazard assessment in an urban area. J Geophys Eng. 2007; 4(3): 308-316. doi:10.1088/1742-2132/4/3/S10.

APPENDIX A

DESCRIPTION OF THE SELECTED ESDOF MODELS

Table A.1 ESDOF parameters for all 20 buildings of sub-class RF1A

RF1A							
Building No.	**T(s)**	**η**	**μ**	**α_s (%)**	**α_c (%)**	**λ**	**γ**
1	0.07	0.54	14.23	4	-20	0.2	800
2	0.14	0.52	13.66	4	-20	0.2	800
3	0.16	0.49	12.76	4	-20	0.2	800
4	0.23	0.47	12.12	4	-20	0.2	800
5	0.25	0.47	11.51	4	-20	0.2	800
6	0.28	0.45	10.71	4	-20	0.2	800
7	0.31	0.44	10.53	4	-20	0.2	800
8	0.32	0.43	9.79	4	-20	0.2	800
9	0.34	0.41	9.72	4	-20	0.2	800
10	0.37	0.40	9.24	4	-20	0.2	800
11	0.39	0.39	8.98	4	-20	0.2	800
12	0.42	0.38	8.52	4	-20	0.2	800
13	0.43	0.37	8.07	4	-20	0.2	800
14	0.47	0.36	7.78	4	-20	0.2	800
15	0.48	0.35	7.31	4	-20	0.2	800
16	0.53	0.34	6.41	4	-20	0.2	800
17	0.55	0.32	5.97	4	-20	0.2	800
18	0.60	0.31	5.52	4	-20	0.2	800
19	0.67	0.28	4.40	4	-20	0.2	800
20	0.72	0.22	2.88	4	-20	0.2	800

Table A.2 ESDOF parameters for all 20 buildings of sub-class RF1B

RF1B							
Building No.	**T(s)**	**η**	**μ**	**α_s (%)**	**α_c (%)**	**λ**	**γ**
1	0.07	0.54	14.23	4	-25	0.2	400
2	0.14	0.52	13.66	4	-25	0.2	400
3	0.16	0.49	12.76	4	-25	0.2	400
4	0.23	0.47	12.12	4	-25	0.2	400
5	0.25	0.47	11.51	4	-25	0.2	400
6	0.28	0.45	10.71	4	-25	0.2	400
7	0.31	0.44	10.53	4	-25	0.2	400
8	0.32	0.43	9.79	4	-25	0.2	400
9	0.34	0.41	9.72	4	-25	0.2	400
10	0.37	0.40	9.24	4	-25	0.2	400
11	0.39	0.39	8.98	4	-25	0.2	400
12	0.42	0.38	8.52	4	-25	0.2	400
13	0.43	0.37	8.07	4	-25	0.2	400
14	0.47	0.36	7.78	4	-25	0.2	400
15	0.48	0.35	7.31	4	-25	0.2	400
16	0.53	0.34	6.41	4	-25	0.2	400
17	0.55	0.32	5.97	4	-25	0.2	400
18	0.60	0.31	5.52	4	-25	0.2	400
19	0.67	0.28	4.40	4	-25	0.2	400
20	0.72	0.22	2.88	4	-25	0.2	400

Table A.3 ESDOF parameters for all 20 buildings of sub-class RF1C

RF1C							
Building No.	**T(s)**	**η**	**μ**	**α_s (%)**	**α_c (%)**	**λ**	**γ**
1	0.07	0.54	14.23	4	-30	0.2	200
2	0.14	0.52	13.66	4	-30	0.2	200
3	0.16	0.49	12.76	4	-30	0.2	200
4	0.23	0.47	12.12	4	-30	0.2	200
5	0.25	0.47	11.51	4	-30	0.2	200
6	0.28	0.45	10.71	4	-30	0.2	200
7	0.31	0.44	10.53	4	-30	0.2	200
8	0.32	0.43	9.79	4	-30	0.2	200
9	0.34	0.41	9.72	4	-30	0.2	200
10	0.37	0.40	9.24	4	-30	0.2	200
11	0.39	0.39	8.98	4	-30	0.2	200
12	0.42	0.38	8.52	4	-30	0.2	200
13	0.43	0.37	8.07	4	-30	0.2	200
14	0.47	0.36	7.78	4	-30	0.2	200
15	0.48	0.35	7.31	4	-30	0.2	200
16	0.53	0.34	6.41	4	-30	0.2	200
17	0.55	0.32	5.97	4	-30	0.2	200
18	0.60	0.31	5.52	4	-30	0.2	200
19	0.67	0.28	4.40	4	-30	0.2	200
20	0.72	0.22	2.88	4	-30	0.2	200

Table A.4 ESDOF parameters for all 20 buildings of sub-class RF2A

RF2A							
Building No.	**T(s)**	**η**	**μ**	**α_s (%)**	**α_c (%)**	**λ**	**γ**
1	0.13	0.55	13.29	4	-20	0.2	800
2	0.35	0.48	10.52	4	-20	0.2	800
3	0.39	0.46	9.54	4	-20	0.2	800
4	0.44	0.43	9.38	4	-20	0.2	800
5	0.50	0.41	8.66	4	-20	0.2	800
6	0.56	0.40	8.61	4	-20	0.2	800
7	0.59	0.38	8.17	4	-20	0.2	800
8	0.61	0.38	7.90	4	-20	0.2	800
9	0.66	0.36	7.58	4	-20	0.2	800
10	0.70	0.35	7.36	4	-20	0.2	800
11	0.72	0.33	6.97	4	-20	0.2	800
12	0.74	0.31	6.66	4	-20	0.2	800
13	0.80	0.31	6.45	4	-20	0.2	800
14	0.82	0.29	6.00	4	-20	0.2	800
15	0.88	0.27	5.75	4	-20	0.2	800
16	0.90	0.26	5.33	4	-20	0.2	800
17	0.96	0.25	4.82	4	-20	0.2	800
18	1.04	0.20	4.43	4	-20	0.2	800
19	1.14	0.19	3.78	4	-20	0.2	800
20	1.19	0.12	3.12	4	-20	0.2	800

Table A.5 ESDOF parameters for all 20 buildings of sub-class RF2B

RF2B							
Building No.	**T(s)**	**η**	**μ**	**α_s (%)**	**α_c (%)**	**λ**	**γ**
1	0.13	0.55	13.29	4	-25	0.2	400
2	0.35	0.48	10.52	4	-25	0.2	400
3	0.39	0.46	9.54	4	-25	0.2	400
4	0.44	0.43	9.38	4	-25	0.2	400
5	0.50	0.41	8.66	4	-25	0.2	400
6	0.56	0.40	8.61	4	-25	0.2	400
7	0.59	0.38	8.17	4	-25	0.2	400
8	0.61	0.38	7.90	4	-25	0.2	400
9	0.66	0.36	7.58	4	-25	0.2	400
10	0.70	0.35	7.36	4	-25	0.2	400
11	0.72	0.33	6.97	4	-25	0.2	400
12	0.74	0.31	6.66	4	-25	0.2	400
13	0.80	0.31	6.45	4	-25	0.2	400
14	0.82	0.29	6.00	4	-25	0.2	400
15	0.88	0.27	5.75	4	-25	0.2	400
16	0.90	0.26	5.33	4	-25	0.2	400
17	0.96	0.25	4.82	4	-25	0.2	400
18	1.04	0.20	4.43	4	-25	0.2	400
19	1.14	0.19	3.78	4	-25	0.2	400
20	1.19	0.12	3.12	4	-25	0.2	400

Table A.6 ESDOF parameters for all 20 buildings of sub-class RF2C

RF2C							
Building No.	**T(s)**	**η**	**μ**	**α_s (%)**	**α_c (%)**	**λ**	**γ**
1	0.13	0.31	8.91	4	-30	0.2	200
2	0.35	0.27	7.11	4	-30	0.2	200
3	0.39	0.24	6.56	4	-30	0.2	200
4	0.44	0.23	6.43	4	-30	0.2	200
5	0.50	0.22	6.19	4	-30	0.2	200
6	0.56	0.20	5.83	4	-30	0.2	200
7	0.59	0.20	5.78	4	-30	0.2	200
8	0.61	0.19	5.46	4	-30	0.2	200
9	0.66	0.18	5.36	4	-30	0.2	200
10	0.70	0.18	5.26	4	-30	0.2	200
11	0.72	0.17	5.01	4	-30	0.2	200
12	0.74	0.16	4.79	4	-30	0.2	200
13	0.80	0.15	4.62	4	-30	0.2	200
14	0.82	0.14	4.44	4	-30	0.2	200
15	0.88	0.14	4.35	4	-30	0.2	200
16	0.90	0.12	3.95	4	-30	0.2	200
17	0.96	0.11	3.92	4	-30	0.2	200
18	1.04	0.10	3.41	4	-30	0.2	200
19	1.14	0.09	2.97	4	-30	0.2	200
20	1.19	0.07	2.22	4	-30	0.2	200

Table A.7 ESDOF parameters for all 20 buildings of sub-class RW1A

RW1A							
Building No.	**T(s)**	**η**	**μ**	**α_s (%)**	**α_c (%)**	**λ**	**γ**
1	0.01	6.40	7.52	8	-20	0.2	1200
2	0.02	4.12	6.37	8	-20	0.2	1200
3	0.02	3.30	5.27	8	-20	0.2	1200
4	0.03	3.15	4.65	8	-20	0.2	1200
5	0.03	2.88	4.22	8	-20	0.2	1200
6	0.03	2.55	4.01	8	-20	0.2	1200
7	0.04	2.35	3.64	8	-20	0.2	1200
8	0.04	2.16	3.31	8	-20	0.2	1200
9	0.04	2.03	3.18	8	-20	0.2	1200
10	0.05	1.96	3.01	8	-20	0.2	1200
11	0.05	1.81	2.73	8	-20	0.2	1200
12	0.05	1.73	2.55	8	-20	0.2	1200
13	0.06	1.63	2.25	8	-20	0.2	1200
14	0.06	1.48	2.15	8	-20	0.2	1200
15	0.07	1.37	1.93	8	-20	0.2	1200
16	0.07	1.29	1.79	8	-20	0.2	1200
17	0.08	1.18	1.70	8	-20	0.2	1200
18	0.09	0.96	1.47	8	-20	0.2	1200
19	0.12	0.80	1.18	8	-20	0.2	1200
20	0.17	0.74	0.50	8	-20	0.2	1200

Table A.8 ESDOF parameters for all 20 buildings of sub-class RF2A

RW2A							
Building No.	**T(s)**	**η**	**μ**	**α_s (%)**	**α_c (%)**	**λ**	**γ**
1	0.05	3.72	6.76	8	-20	0.2	1200
2	0.06	2.59	5.43	8	-20	0.2	1200
3	0.07	2.20	4.87	8	-20	0.2	1200
4	0.09	2.04	4.29	8	-20	0.2	1200
5	0.09	1.81	3.88	8	-20	0.2	1200
6	0.10	1.71	3.59	8	-20	0.2	1200
7	0.11	1.59	3.31	8	-20	0.2	1200
8	0.12	1.45	3.10	8	-20	0.2	1200
9	0.13	1.37	2.78	8	-20	0.2	1200
10	0.14	1.27	2.58	8	-20	0.2	1200
11	0.15	1.19	2.39	8	-20	0.2	1200
12	0.16	1.16	2.38	8	-20	0.2	1200
13	0.17	1.07	2.14	8	-20	0.2	1200
14	0.19	0.98	2.00	8	-20	0.2	1200
15	0.20	0.89	1.75	8	-20	0.2	1200
16	0.23	0.87	1.65	8	-20	0.2	1200
17	0.25	0.80	1.47	8	-20	0.2	1200
18	0.28	0.69	1.27	8	-20	0.2	1200
19	0.34	0.61	1.11	8	-20	0.2	1200
20	0.36	0.46	0.54	8	-20	0.2	1200

Table A.9 ESDOF parameters for all 20 buildings of sub-class RH1A

RH1A							
Building No.	**T(s)**	**η**	**μ**	**α_s (%)**	**α_c (%)**	**λ**	**γ**
1	0.02	3.25	12.87	4	-20	0.2	1000
2	0.03	2.11	10.81	4	-20	0.2	1000
3	0.04	1.60	9.94	4	-20	0.2	1000
4	0.04	1.54	8.62	4	-20	0.2	1000
5	0.04	1.36	7.88	4	-20	0.2	1000
6	0.05	1.25	7.00	4	-20	0.2	1000
7	0.05	1.17	6.70	4	-20	0.2	1000
8	0.06	1.09	5.99	4	-20	0.2	1000
9	0.06	0.98	5.69	4	-20	0.2	1000
10	0.07	0.93	5.25	4	-20	0.2	1000
11	0.08	0.85	5.06	4	-20	0.2	1000
12	0.09	0.77	4.61	4	-20	0.2	1000
13	0.09	0.76	4.43	4	-20	0.2	1000
14	0.10	0.69	4.13	4	-20	0.2	1000
15	0.11	0.62	3.70	4	-20	0.2	1000
16	0.12	0.58	3.52	4	-20	0.2	1000
17	0.14	0.54	3.18	4	-20	0.2	1000
18	0.15	0.45	2.80	4	-20	0.2	1000
19	0.21	0.35	2.23	4	-20	0.2	1000
20	0.34	0.30	0.91	4	-20	0.2	1000

Table A.10 ESDOF parameters for all 20 buildings of sub-class RH1B

RH1B							
Building No.	**T(s)**	**η**	**μ**	**α_s (%)**	**α_c (%)**	**λ**	**γ**
1	0.02	1.95	10.75	4	-25	0.2	500
2	0.03	1.51	9.14	4	-25	0.2	500
3	0.04	1.41	8.49	4	-25	0.2	500
4	0.04	1.21	7.46	4	-25	0.2	500
5	0.04	1.12	6.37	4	-25	0.2	500
6	0.05	1.00	5.95	4	-25	0.2	500
7	0.05	0.98	5.32	4	-25	0.2	500
8	0.06	0.88	5.10	4	-25	0.2	500
9	0.06	0.80	4.72	4	-25	0.2	500
10	0.07	0.78	4.31	4	-25	0.2	500
11	0.08	0.73	4.24	4	-25	0.2	500
12	0.09	0.64	3.76	4	-25	0.2	500
13	0.09	0.63	3.51	4	-25	0.2	500
14	0.10	0.58	3.36	4	-25	0.2	500
15	0.11	0.52	3.04	4	-25	0.2	500
16	0.12	0.47	2.91	4	-25	0.2	500
17	0.14	0.43	2.45	4	-25	0.2	500
18	0.15	0.39	2.36	4	-25	0.2	500
19	0.21	0.30	1.92	4	-25	0.2	500
20	0.34	0.28	1.10	4	-25	0.2	500

Table A.11 ESDOF parameters for all 20 buildings of sub-class RH2A

RH2A							
Building No.	**T(s)**	**η**	**μ**	**α_s (%)**	**α_c (%)**	**λ**	**γ**
1	0.09	1.46	11.45	11.45	-20	0.2	1000
2	0.16	1.30	9.49	9.49	-20	0.2	1000
3	0.18	1.10	8.58	8.58	-20	0.2	1000
4	0.23	0.97	7.72	7.72	-20	0.2	1000
5	0.24	0.82	7.26	7.26	-20	0.2	1000
6	0.27	0.79	6.32	6.32	-20	0.2	1000
7	0.31	0.72	5.94	5.94	-20	0.2	1000
8	0.32	0.65	5.41	5.41	-20	0.2	1000
9	0.36	0.62	5.37	5.37	-20	0.2	1000
10	0.38	0.58	5.01	5.01	-20	0.2	1000
11	0.43	0.55	4.49	4.49	-20	0.2	1000
12	0.44	0.52	4.12	4.12	-20	0.2	1000
13	0.50	0.47	3.86	3.86	-20	0.2	1000
14	0.52	0.44	3.82	3.82	-20	0.2	1000
15	0.60	0.41	3.51	3.51	-20	0.2	1000
16	0.63	0.39	3.09	3.09	-20	0.2	1000
17	0.75	0.34	2.97	2.97	-20	0.2	1000
18	0.82	0.30	2.44	2.44	-20	0.2	1000
19	0.90	0.28	2.35	2.35	-20	0.2	1000
20	1.20	0.23	1.73	1.73	-20	0.2	1000

Table A.12 ESDOF parameters for all 20 buildings of sub-class RH2B

RH2B							
Building No.	**T(s)**	**η**	**μ**	**α_s (%)**	**α_c (%)**	**λ**	**γ**
1	0.09	1.16	9.68	11.45	-25	0.2	500
2	0.16	1.01	8.00	9.49	-25	0.2	500
3	0.18	0.88	7.06	8.58	-25	0.2	500
4	0.23	0.77	6.46	7.72	-25	0.2	500
5	0.24	0.69	5.84	7.26	-25	0.2	500
6	0.27	0.64	5.16	6.32	-25	0.2	500
7	0.31	0.59	4.93	5.94	-25	0.2	500
8	0.32	0.53	4.49	5.41	-25	0.2	500
9	0.36	0.51	4.35	5.37	-25	0.2	500
10	0.38	0.48	3.98	5.01	-25	0.2	500
11	0.43	0.43	3.72	4.49	-25	0.2	500
12	0.44	0.42	3.44	4.12	-25	0.2	500
13	0.50	0.39	3.27	3.86	-25	0.2	500
14	0.52	0.37	3.04	3.82	-25	0.2	500
15	0.60	0.34	2.76	3.51	-25	0.2	500
16	0.63	0.30	2.57	3.09	-25	0.2	500
17	0.75	0.28	2.39	2.97	-25	0.2	500
18	0.82	0.24	2.10	2.44	-25	0.2	500
19	0.90	0.21	1.67	2.35	-25	0.2	500
20	1.20	0.19	1.37	1.73	-25	0.2	500

Table A.13 ESDOF parameters for all 20 buildings of sub-class MU1A

MU1A							
Building No.	**T(s)**	**η**	**μ**	**α_s (%)**	**α_c (%)**	**λ**	**γ**
1	0.01	2.38	9.48	0	-0.92	0.2	600
2	0.03	1.64	7.05	0	-2.43	0.2	600
3	0.03	1.36	5.55	0	-2.99	0.2	600
4	0.03	1.31	5.39	0	-3.58	0.2	600
5	0.04	1.21	4.90	0	-3.80	0.2	600
6	0.04	1.09	4.44	0	-4.35	0.2	600
7	0.04	1.02	4.24	0	-4.10	0.2	600
8	0.05	0.95	4.06	0	-5.06	0.2	600
9	0.05	0.90	3.75	0	-5.36	0.2	600
10	0.05	0.88	3.62	0	-6.34	0.2	600
11	0.06	0.82	3.45	0	-6.62	0.2	600
12	0.06	0.79	3.24	0	-6.72	0.2	600
13	0.07	0.75	2.95	0	-8.03	0.2	600
14	0.07	0.69	2.81	0	-8.73	0.2	600
15	0.08	0.65	2.58	0	-10.21	0.2	600
16	0.08	0.61	2.42	0	-10.86	0.2	600
17	0.09	0.57	2.36	0	-13.29	0.2	600
18	0.10	0.48	2.14	0	-11.81	0.2	600
19	0.13	0.41	1.88	0	-19.97	0.2	600
20	0.16	0.38	1.63	0	-29.02	0.2	600

Table A.14 ESDOF parameters for all 20 buildings of sub-class MU1B

MU1B							
Building No.	**T(s)**	**η**	**μ**	**α_s (%)**	**α_c (%)**	**λ**	**γ**
1	0.01	2.00	7.18	0	-0.94	0.2	300
2	0.03	1.27	6.05	0	-2.28	0.2	300
3	0.03	1.07	5.56	0	-2.92	0.2	300
4	0.03	0.96	5.03	0	-3.18	0.2	300
5	0.04	0.90	4.65	0	-3.45	0.2	300
6	0.04	0.83	4.37	0	-4.05	0.2	300
7	0.04	0.79	4.11	0	-3.90	0.2	300
8	0.05	0.72	3.91	0	-4.69	0.2	300
9	0.05	0.67	3.59	0	-4.83	0.2	300
10	0.05	0.64	3.38	0	-5.57	0.2	300
11	0.06	0.61	3.19	0	-5.89	0.2	300
12	0.06	0.58	3.18	0	-6.04	0.2	300
13	0.07	0.56	2.93	0	-7.29	0.2	300
14	0.07	0.49	2.77	0	-7.55	0.2	300
15	0.08	0.47	2.50	0	-8.94	0.2	300
16	0.08	0.44	2.39	0	-9.23	0.2	300
17	0.09	0.41	2.17	0	-11.14	0.2	300
18	0.10	0.36	1.94	0	-10.48	0.2	300
19	0.13	0.34	1.75	0	-20.00	0.2	300
20	0.16	0.29	1.00	0	-22.31	0.2	300

Table A.15 ESDOF parameters for all 20 buildings of sub-class MU1C

MU1C							
Building No.	**T(s)**	**η**	**μ**	**α_s (%)**	**α_c (%)**	**λ**	**γ**
1	0.01	0.84	6.78	0	-0.51	0.2	150
2	0.03	0.67	5.99	0	-1.51	0.2	150
3	0.03	0.59	5.20	0	-2.02	0.2	150
4	0.03	0.55	4.74	0	-2.29	0.2	150
5	0.04	0.51	4.41	0	-2.47	0.2	150
6	0.04	0.49	4.24	0	-3.05	0.2	150
7	0.04	0.45	3.94	0	-2.81	0.2	150
8	0.05	0.43	3.67	0	-3.50	0.2	150
9	0.05	0.40	3.56	0	-3.64	0.2	150
10	0.05	0.38	3.42	0	-4.23	0.2	150
11	0.06	0.36	3.18	0	-4.38	0.2	150
12	0.06	0.34	3.03	0	-4.45	0.2	150
13	0.07	0.33	2.75	0	-5.38	0.2	150
14	0.07	0.31	2.66	0	-5.96	0.2	150
15	0.08	0.27	2.45	0	-6.50	0.2	150
16	0.08	0.27	2.32	0	-7.35	0.2	150
17	0.09	0.25	2.23	0	-8.70	0.2	150
18	0.10	0.22	2.01	0	-8.50	0.2	150
19	0.13	0.18	1.70	0	-12.76	0.2	150
20	0.16	0.15	0.90	0	-14.17	0.2	150

Table A.16 ESDOF parameters for all 20 buildings of sub-class MU2A

MU2A							
Building No.	**T(s)**	**η**	**μ**	**α_s (%)**	**α_c (%)**	**λ**	**γ**
1	0.05	1.54	6.61	0	-3.93	0.2	600
2	0.05	1.29	5.85	0	-4.85	0.2	600
3	0.06	1.17	5.03	0	-4.68	0.2	600
4	0.06	1.06	4.19	0	-5.42	0.2	600
5	0.07	1.00	3.76	0	-7.06	0.2	600
6	0.08	0.88	3.63	0	-6.80	0.2	600
7	0.09	0.83	3.24	0	-7.44	0.2	600
8	0.09	0.76	3.11	0	-7.97	0.2	600
9	0.10	0.75	2.94	0	-10.03	0.2	600
10	0.11	0.71	2.70	0	-10.44	0.2	600
11	0.11	0.64	2.64	0	-10.50	0.2	600
12	0.12	0.59	2.45	0	-11.01	0.2	600
13	0.13	0.55	2.30	0	-11.44	0.2	600
14	0.14	0.55	2.06	0	-14.29	0.2	600
15	0.16	0.51	1.96	0	-16.49	0.2	600
16	0.16	0.45	1.83	0	-14.88	0.2	600
17	0.19	0.43	1.75	0	-22.71	0.2	600
18	0.22	0.36	1.45	0	-23.15	0.2	600
19	0.26	0.35	1.31	0	-34.14	0.2	600
20	0.29	0.26	0.97	0	-28.20	0.2	600

Table A.17 ESDOF parameters for all 20 buildings of sub-class MU2B

MU2B							
Building No.	**T(s)**	**η**	**μ**	**α_s (%)**	**α_c (%)**	**λ**	**γ**
1	0.05	0.98	6.00	0	-2.89	0.2	300
2	0.05	0.79	5.29	0	-3.33	0.2	300
3	0.06	0.73	4.55	0	-3.36	0.2	300
4	0.06	0.68	4.19	0	-4.11	0.2	300
5	0.07	0.59	3.69	0	-4.79	0.2	300
6	0.08	0.57	3.53	0	-5.19	0.2	300
7	0.09	0.51	3.15	0	-5.29	0.2	300
8	0.09	0.50	2.91	0	-6.08	0.2	300
9	0.10	0.45	2.77	0	-6.67	0.2	300
10	0.11	0.44	2.68	0	-7.43	0.2	300
11	0.11	0.40	2.39	0	-7.38	0.2	300
12	0.12	0.38	2.34	0	-8.22	0.2	300
13	0.13	0.35	2.14	0	-8.34	0.2	300
14	0.14	0.34	2.05	0	-10.14	0.2	300
15	0.16	0.30	1.88	0	-11.02	0.2	300
16	0.16	0.28	1.80	0	-10.59	0.2	300
17	0.19	0.27	1.53	0	-15.17	0.2	300
18	0.22	0.22	1.50	0	-16.40	0.2	300
19	0.26	0.20	1.34	0	-21.21	0.2	300
20	0.29	0.13	1.11	0	-16.00	0.2	300

Table A.18 ESDOF parameters for all 20 buildings of sub-class MU2C

MU2C							
Building No.	**T(s)**	**η**	**μ**	**α_s (%)**	**α_c (%)**	**λ**	**γ**
1	0.05	0.52	5.71	0	-1.90	0.2	150
2	0.05	0.43	5.41	0	-2.29	0.2	150
3	0.06	0.38	4.56	0	-2.21	0.2	150
4	0.06	0.35	3.83	0	-2.58	0.2	150
5	0.07	0.32	3.70	0	-3.30	0.2	150
6	0.08	0.30	3.31	0	-3.42	0.2	150
7	0.09	0.28	3.01	0	-3.68	0.2	150
8	0.09	0.25	2.97	0	-3.77	0.2	150
9	0.10	0.24	2.75	0	-4.38	0.2	150
10	0.11	0.23	2.59	0	-4.75	0.2	150
11	0.11	0.21	2.48	0	-4.83	0.2	150
12	0.12	0.20	2.24	0	-5.20	0.2	150
13	0.13	0.19	2.19	0	-5.67	0.2	150
14	0.14	0.17	2.00	0	-6.40	0.2	150
15	0.16	0.17	1.79	0	-7.42	0.2	150
16	0.16	0.15	1.69	0	-7.12	0.2	150
17	0.19	0.13	1.57	0	-9.17	0.2	150
18	0.22	0.12	1.32	0	-10.20	0.2	150
19	0.26	0.11	1.22	0	-13.28	0.2	150
20	0.29	0.09	0.78	0	-14.55	0.2	150

Table A.19 ESDOF parameters for all 20 buildings of sub-class MU3A

MU3A							
Building No.	**T(s)**	**η**	**μ**	**α_s (%)**	**α_c (%)**	**λ**	**γ**
1	0.06	1.29	6.90	0	-3.37	0.2	600
2	0.07	0.87	4.27	0	-3.48	0.2	600
3	0.09	0.75	3.97	0	-4.64	0.2	600
4	0.10	0.72	3.38	0	-5.35	0.2	600
5	0.11	0.64	3.06	0	-5.82	0.2	600
6	0.12	0.59	2.92	0	-6.16	0.2	600
7	0.13	0.53	2.73	0	-7.32	0.2	600
8	0.14	0.49	2.50	0	-7.31	0.2	600
9	0.15	0.47	2.30	0	-8.64	0.2	600
10	0.16	0.42	2.17	0	-8.27	0.2	600
11	0.17	0.41	2.01	0	-9.80	0.2	600
12	0.19	0.38	1.96	0	-10.78	0.2	600
13	0.20	0.34	1.75	0	-10.46	0.2	600
14	0.22	0.32	1.60	0	-11.80	0.2	600
15	0.23	0.29	1.56	0	-11.89	0.2	600
16	0.26	0.28	1.45	0	-14.99	0.2	600
17	0.28	0.24	1.23	0	-14.97	0.2	600
18	0.29	0.23	1.05	0	-14.66	0.2	600
19	0.35	0.17	1.04	0	-16.42	0.2	600
20	0.41	0.16	0.66	0	-19.87	0.2	600

Table A.20 ESDOF parameters for all 20 buildings of sub-class MU3B

MU3B							
Building No.	**T(s)**	**η**	**μ**	**α_s (%)**	**α_c (%)**	**λ**	**γ**
1	0.06	0.65	5.73	0	-1.86	0.2	300
2	0.07	0.62	4.78	0	-3.08	0.2	300
3	0.09	0.51	3.63	0	-3.79	0.2	300
4	0.10	0.46	3.31	0	-4.08	0.2	300
5	0.11	0.41	3.17	0	-4.49	0.2	300
6	0.12	0.36	2.85	0	-4.41	0.2	300
7	0.13	0.34	2.62	0	-5.58	0.2	300
8	0.14	0.31	2.46	0	-5.42	0.2	300
9	0.15	0.28	2.24	0	-6.11	0.2	300
10	0.16	0.27	2.12	0	-6.43	0.2	300
11	0.17	0.25	1.98	0	-7.14	0.2	300
12	0.19	0.23	1.85	0	-7.85	0.2	300
13	0.20	0.22	1.66	0	-8.19	0.2	300
14	0.22	0.21	1.60	0	-9.03	0.2	300
15	0.23	0.19	1.52	0	-9.49	0.2	300
16	0.26	0.17	1.37	0	-10.68	0.2	300
17	0.28	0.16	1.18	0	-12.08	0.2	300
18	0.29	0.13	1.13	0	-10.35	0.2	300
19	0.35	0.12	0.94	0	-13.47	0.2	300
20	0.41	0.10	0.68	0	-15.37	0.2	300

Table A.21 ESDOF parameters for all 20 buildings of sub-class MU3C

MU3C							
Building No.	**T(s)**	**η**	**μ**	**α_s (%)**	**α_c (%)**	**λ**	**γ**
1	0.06	0.37	4.84	0	-1.34	0.2	150
2	0.07	0.31	4.03	0	-1.91	0.2	150
3	0.09	0.25	3.52	0	-2.36	0.2	150
4	0.10	0.21	3.34	0	-2.40	0.2	150
5	0.11	0.21	2.89	0	-2.84	0.2	150
6	0.12	0.18	2.80	0	-2.84	0.2	150
7	0.13	0.17	2.46	0	-3.52	0.2	150
8	0.14	0.16	2.36	0	-3.47	0.2	150
9	0.15	0.15	2.12	0	-4.13	0.2	150
10	0.16	0.14	2.00	0	-4.29	0.2	150
11	0.17	0.13	1.89	0	-4.66	0.2	150
12	0.19	0.12	1.72	0	-5.13	0.2	150
13	0.20	0.11	1.63	0	-5.28	0.2	150
14	0.22	0.11	1.52	0	-5.78	0.2	150
15	0.23	0.10	1.43	0	-6.34	0.2	150
16	0.26	0.09	1.29	0	-7.00	0.2	150
17	0.28	0.08	1.17	0	-7.46	0.2	150
18	0.29	0.07	1.06	0	-6.94	0.2	150
19	0.35	0.06	0.92	0	-8.80	0.2	150
20	0.41	0.05	0.66	0	-9.29	0.2	150

APPENDIX B

SENSITIVITY ANALYSIS FOR DERIVATION OF FRAGILITY CURVES

To investigate the influence of ground motion variability and fragility curve generation methodology on the final fragility curves, in this study sensitivity analysis is conducted.

B.1 Sensitivity of Fragility Curves to Ground Motion Records

In this study, to examine sensitivity of the generated fragility curves with respect to variability in seismic demand, fragility curves for masonry sub-classes are obtained based on an alternative set of records where variability in seismic demand is not taken into account. For this purpose, instead of using 10 records for each intensity level mentioned in Section 4.5.1, only one record is randomly selected. As a result, the alternative group of records includes a total of 20 samples. Distribution of seismic parameters including PGV, significant duration, Housner intensity, and Arias intensity regarding to this group of ground motions are illustrated in Figure B.1. Comparison of Figures 4.19 and B.1 demonstrates the efficiency of the previously used approach where even records of a specified level of seismic intensity are taken from different earthquakes with varying levels of magnitude and distance, and site conditions.

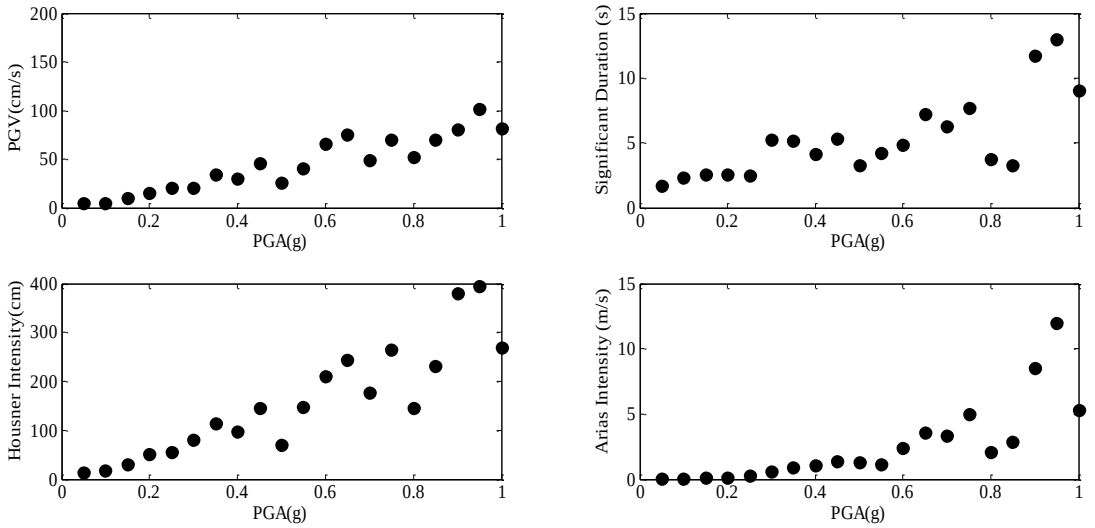

Figure B.1 Distribution of the ground motion parameters corresponding to records selected with respect to PGA without considering ground motion variability

Keeping all of the parameters same as the ones described in Sections 4.5.2, 4.5.3, and 4.5.4 for building samples, limit state values, and fragility curve generation methodology, the new sets of fragility curves are generated using the alternative set of ground motion records. For this purpose, in order to derive fragility curve of a single sub-class, since there exist 20 buildings, and the number of records in a specified intensity level (PGA) is 1, the number of response data points for an intensity level counts as 20. Since there are totally 20 intensity groups, the number of SDOF analyses required to obtain the response statistics becomes 400. The new set of fragility curves are presented in Figure B.2.

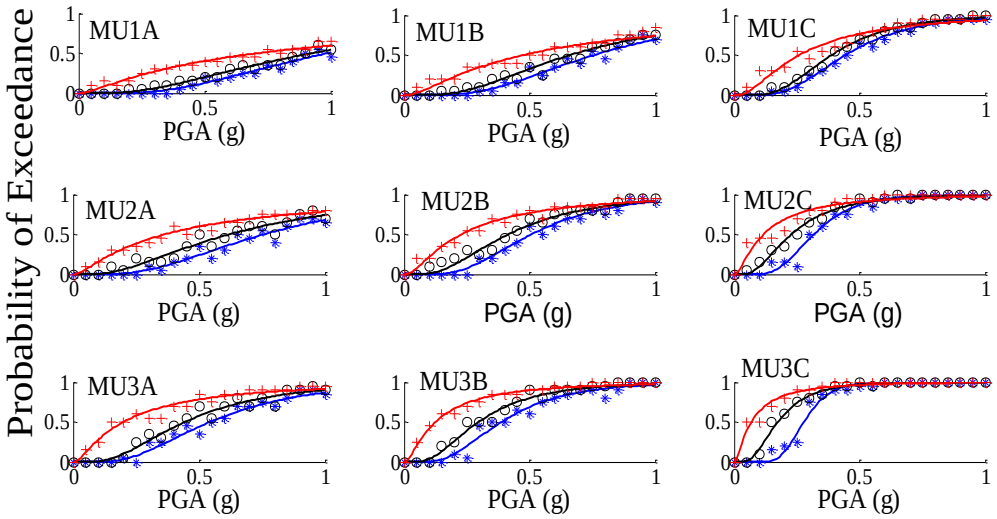

Figure B.2 Fragility curves developed for all masonry subclasses corresponding to records selected with respect to PGA without considering ground motion variability

Comparison of Figure 4.28.a and Figure B.2 presents that the ground motion set in which for a certain intensity level a total of 10 random records were selected resulted in smaller deviation of the scattered data from the smooth curves. To investigate the quality of alternative ground motion sets, error in terms of Square Root of the Sum of the Squares (SRSS) for the deviations of the scatted data from the smooth curves are calculated. Results are listed in Table B.1. For all masonry subclasses it is observed that SRSS errors are smaller for the previous set of records in which variability was considered in seismic demand compared to the new set of records without considering variability in seismic demand. In other words, the calculated errors propose the effectiveness of considering variability in ground motion records even for a certain intensity level.

Table B.1 SRSS errors for all masonry subclasses as well as the mean values of the errors using alternative ground motion sets

SRSS Error										
Ground Motion Set	**MU1A**	**MU1B**	**MU1C**	**MU2A**	**MU2B**	**MU2C**	**MU3A**	**MU3B**	**MU3C**	**Mean**
Figure 4.19	0.55	0.75	0.69	0.82	0.83	0.8	0.9	0.74	0.58	0.73
Figure B.1	0.37	0.47	0.57	0.35	0.51	0.45	0.43	0.48	0.34	0.43

B.2 Sensitivity of Fragility Curves to Methodology

In this study, for generation of fragility curves, an alternative approach is applied. Figure B.3 is the schematic representation of the alternative procedure for generation of fragility curve. The only difference in between the two approaches is the procedure applied for calculation of the conditional probability of exceedance of a certain limit state (Figures 4.24.b and B.3.b). In the new approach, instead of using Equation 4.3, a normal distribution is assumed for scattered data of each vertical strip. The assumption of normal distribution is logical, because the probability of having negative values for displacement is almost equal to zero. The conditional probability of attainment or exceedance of the i^{th} limit state (LS_i) at the j^{th} ground motion intensity level for the new approach is calculated by the following formula:

$$P[D \geq LS_i | GMI_j] = a_A \tag{B.1}$$

where a_A is the area above the i^{th} limit state (Figure B.3.b).

Keeping all of the parameters same as the ones described in Sections 4.5.1, 4.5.2, and 4.5.3 for ground motion set, building samples, and limit state values, the new sets of fragility curves are generated using normal distribution assumption for calculation of the conditional probability of exceedance. The new set of fragility curves are presented in Figure B.4. SRSS errors are calculated for two pairs and the results are listed in Table B.2.

When fragility curves are compared with respect to two alternative methodologies, it is observed that for all building sub-classes the SRSS errors for the previous methodology in which probability of exceedance is calculated by using Equation 4.3 are less than the ones for the methodology with assumption of normal distribution function using Equation B.1. Thus, the effectiveness of the previously applied methodology is demonstrated.

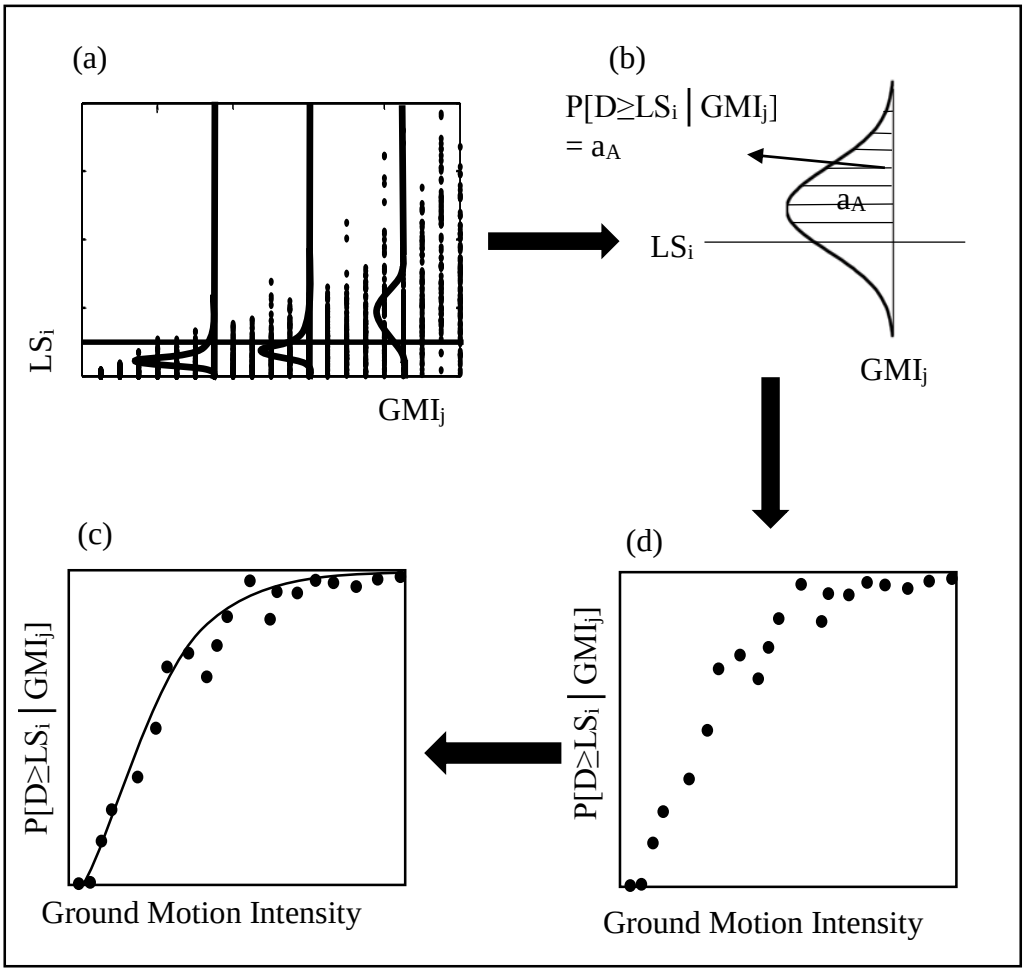

Figure B.3 Schematic representation of the alternative fragility curve generation procedure

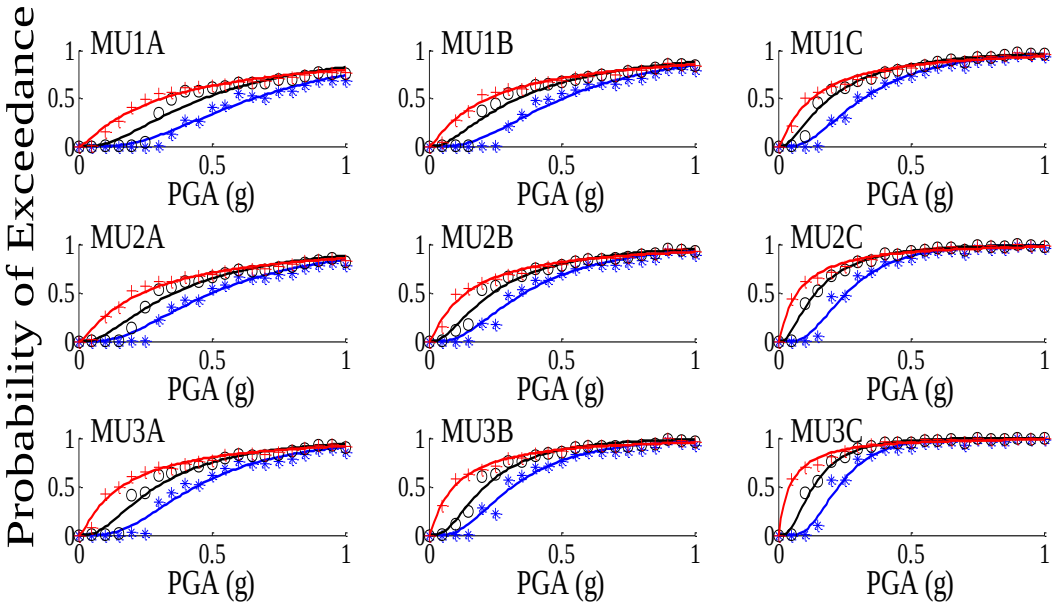

Figure B.4 Fragility curves developed for all masonry sub-classes with respect to PGA using new approach

Table B.2 SRSS errors for all masonry subclasses as well as the mean values of the errors using alternative fragility curve generation methodologies

SRSS Error										
Fragility Curve Generation Method	**MU1A**	**MU1B**	**MU1C**	**MU2A**	**MU2B**	**MU2C**	**MU3A**	**MU3B**	**MU3C**	**Mean**
Figure 4.24	0.9	0.76	0.57	0.76	0.65	0.51	0.77	0.64	0.54	0.67
Figure B.3	0.37	0.47	0.57	0.35	0.51	0.45	0.43	0.48	0.34	0.43

APPENDIX C

COMPARISON OF DIFFERENT DAMAGE ESTIMATION APPROACHES

The estimated damage levels are further examined in terms of their trends with respect to the scenario event with different levels of magnitude. For each scenario event, mean damage ratios are averaged in the sixteen residential districts and the three damage estimation approaches. A comparison of the results is presented in Figure C.1. This figure shows that the three trends have roughly similar shape, with significant damage increase after scenario event with Mw=6.5. To explain more, the damage increases slightly from magnitude levels of 5.0 to 6.0, much faster from 6.0 to 6.5, and more dramatically from 6.5 to 7.5. It is clear from this figure that for all three approaches, regardless of the selected seismic intensity parameter, the average MDRs are similar for scenario events with Mw=5.0 through Mw=6.5. However, the influence of the intensity parameter becomes more pronounced with increasing event magnitude; the maximum difference in between two alternative methodologies (first and second ones) being approximately 10% in magnitudes 7.0 and 7.5. DEA1 results in larger losses for the study area compared to DEA2 whereas the results of DEA3 are in between. Based on the results of the verification

process and the type of buildings in the Erzincan region which were both reinforced-concrete and masonry, in this thesis, for spatial damage assessment of potential scenario events, DEA3 is applied.

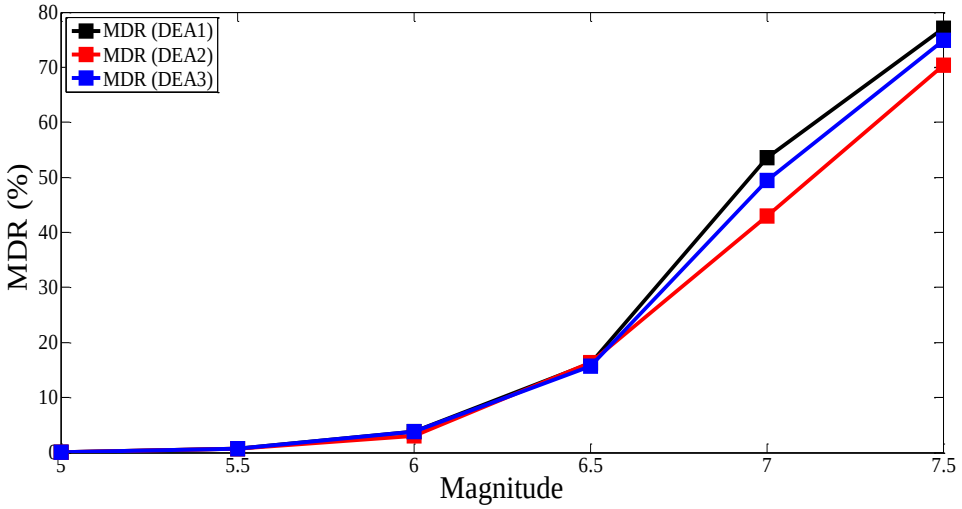

Figure C.1 Comparison of the average MDRs for Erzincan presented for three approaches: DEA1, DEA2, and DEA3

APPENDIX D

DESCRIPTION OF SELECTED FRAMES

Table D.1 Sectional properties of frame F1-3S2B

Structural Member	Section	Width (mm)	Depth (mm)	Clear Cover (mm)	Total Reinforcing Rebar Area (mm^2)	
Beams	B1	250	500	50	1342(top)	3148 (bottom)
	B2	250	500	50	1342 (top)	2503 (bottom)
Columns	C1	700	700	50	7742.4	

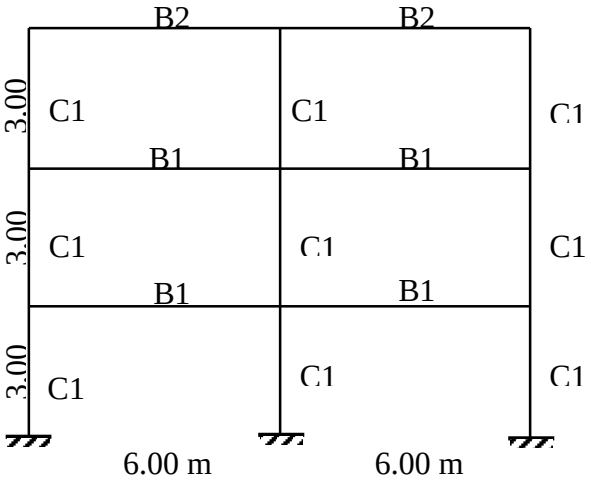

Figure D.1 Frame F1-3S2B

Table D.2 Sectional properties of frame F2-3S2B

Structural Member	Section	Width (mm)	Depth (mm)	Clear Cover (mm)	Total Reinforcing Rebar Area (mm^2)	
Beams	B1	250	500	50	1073.6 (top)	2518.4 (bottom)
	B2	250	500	50	1073.6 (top)	2002.4 (bottom)
Columns	C1	500	500	50	2942.12	

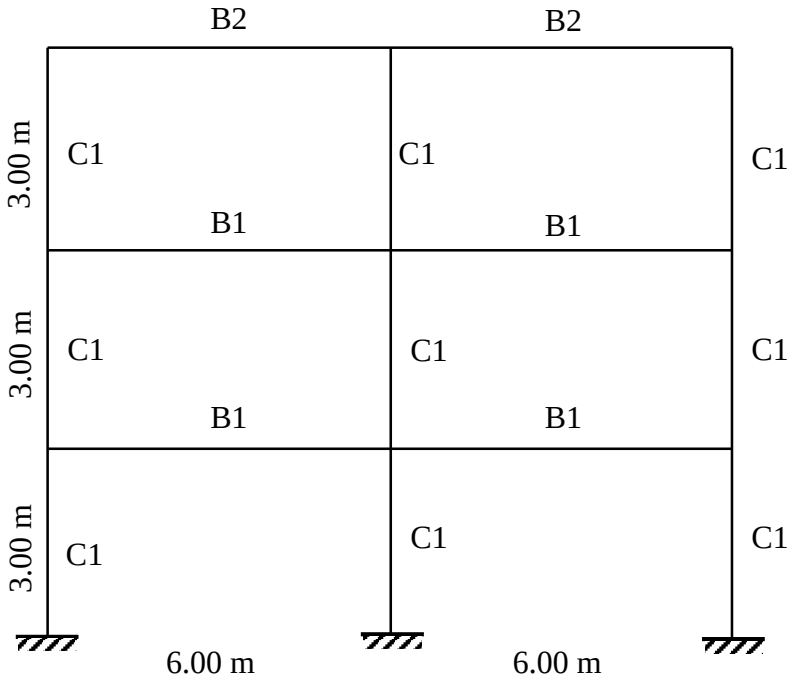

Figure D.2 Frame F2-3S2B

Table D.3 Sectional properties of frame F3-3S3B

Structural Member	Section	Width (mm)	Depth (mm)	Clear Cover (mm)	Total Reinforcing Rebar Area (mm^2)	
Beams	B1	300	500	50	1458 (top)	845 (bottom)
	B2	300	500	50	1368 (top)	845 (bottom)
	B3	300	500	50	1274 (top)	822.5 (bottom)
	B4	300	500	50	1219 (top)	787 (bottom)
	B5	300	500	50	871 (top)	509.5 (bottom)
	B6	300	500	50	845 (top)	548 (bottom)
Columns	C1	400	400	50	2948	
	C2	400	400	50	1916	
	C3	400	400	50	1600	
	C4	400	400	50	2303	

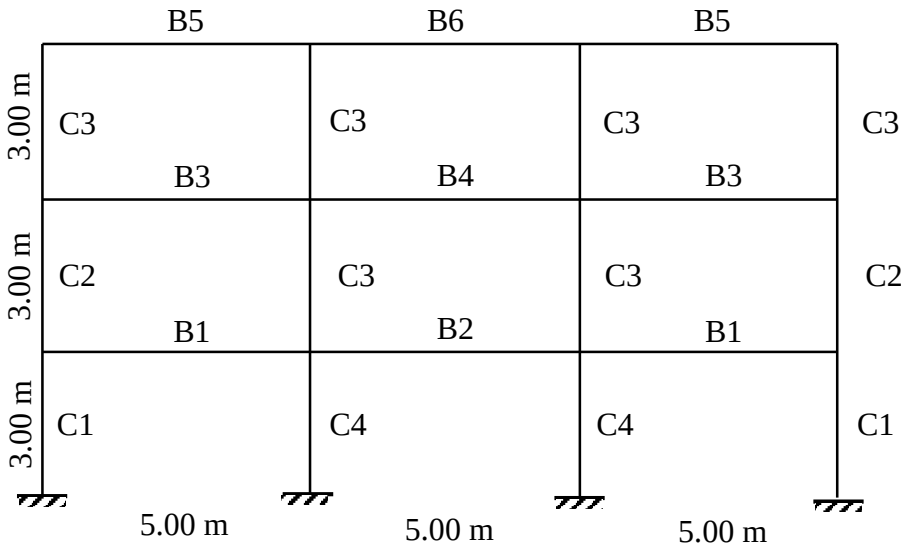

Figure D.3 Frame F3-3S3B

Table D.4 Sectional properties of frame F4-4S3B

Structural Member	Section	Width (mm)	Depth (mm)	Clear Cover (mm)	Total Reinforcing Rebar Area (mm^2)	
Beams	B1	250	550	50	803 (top)	432 (bottom)
	B2	250	550	50	761 (top)	432 (bottom)
	B3	250	550	50	797 (top)	432 (bottom)
	B4	250	550	50	648.5 (top)	416 (bottom)
	B5	250	550	50	632 (top)	406 (bottom)
	B6	250	550	50	642 (top)	416 (bottom)
	B7	250	550	50	445 (top)	287 (bottom)
	B8	250	550	50	445 (top)	290 (bottom)
	B9	250	550	50	445 (top)	284 (bottom)
Columns	C1	500	500	50	2500	

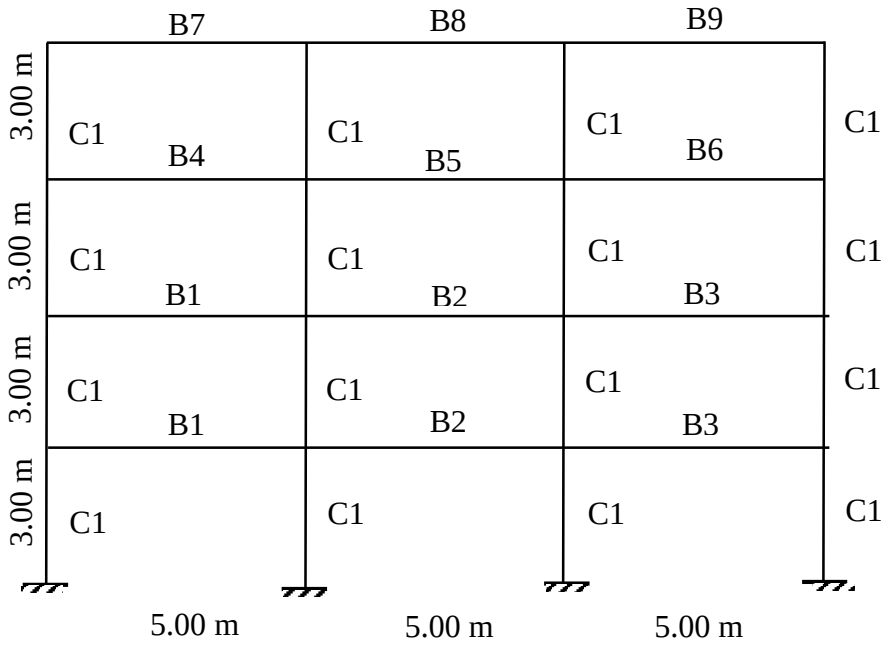

Figure D.4 Frame F4-4S3B

Table D.5 Sectional properties of frame F5-4S3B

Structural Member	Section	Width (mm)	Depth (mm)	Clear Cover (mm)	Total Reinforcing Rebar Area (mm^2)	
Beams	B1	200	500	50	700 (top)	500 (bottom)
Columns	C1	300	800	50	2000	

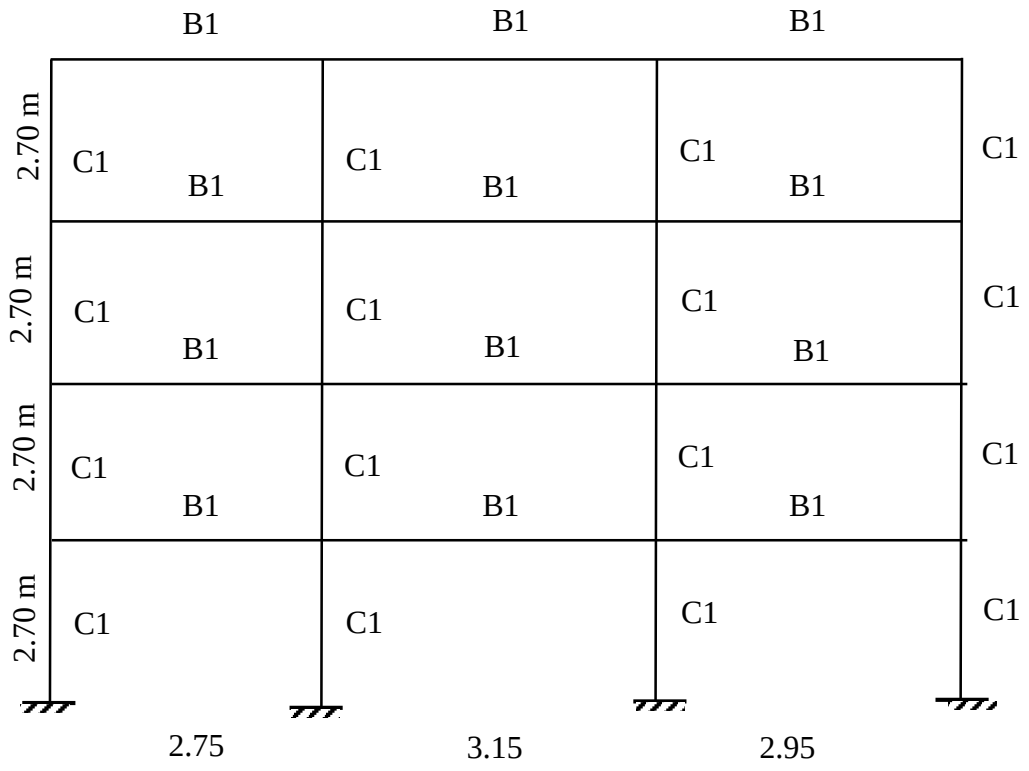

Figure D.5 Frame F5-4S

Table D.6 Sectional properties of frame F6-5S2B

Structural Member	Section	Width (mm)	Depth (mm)	Clear Cover (mm)	Total Reinforcing Rebar Area (mm^2)	
Beams	B1	250	600	50	2500 (top)	1650 (bottom)
Columns	C1	500	500	50	4064	

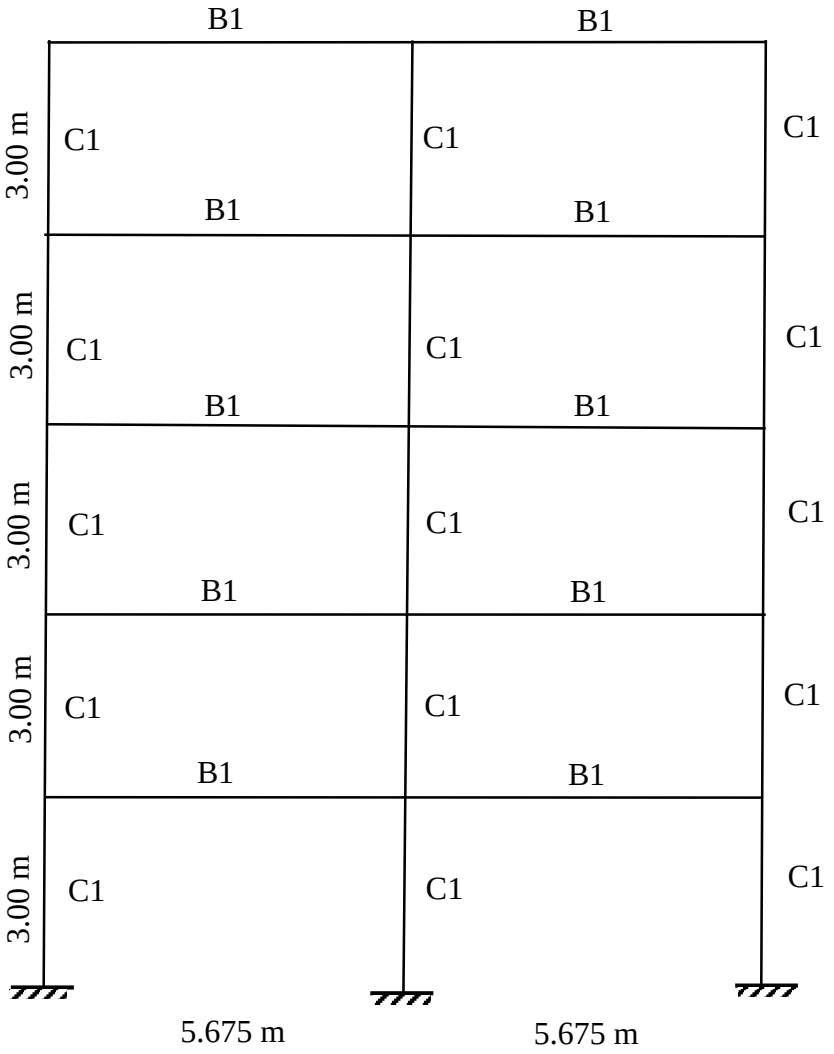

Figure D.6 Frame F6-5S2B

Table D.7 Sectional properties of frame F7-5S4B

Structural Member	Section	Width (mm)	Depth (mm)	Clear Cover (mm)	Total Reinforcing Rebar Area (mm^2)	
Beams	B1	200	600	50	761 (top)	571 (bottom)
	B2	200	600	50	677 (top)	484 (bottom)
	B3	200	600	50	677 (top)	548.5 (bottom)
	B4	200	600	50	1061 (top)	896.5 (bottom)
	B5	200	600	50	725.5 (top)	500 (bottom)
	B6	200	600	50	677 (top)	483.5 (bottom)
	B7	200	600	50	677 (top)	593.5 (bottom)
	B8	200	600	50	903.5 (top)	774 (bottom)
	B9	200	600	50	677 (top)	400 (bottom)
	B10	200	600	50	677 (top)	364.5 (bottom)
	B11	200	600	50	667.5 (top)	461.5 (bottom)
	B12	200	600	50	677 (top)	606 (bottom)
	B13	200	600	50	622.5 (top)	309.5 (bottom)
	B14	200	600	50	551.5 (top)	271 (bottom)
	B15	200	600	50	532.5 (top)	306.5 (bottom)
	B16	200	600	50	567.5 (top)	380.5 (bottom)
	B17	200	600	50	364.5 (top)	181 (bottom)
	B18	200	600	50	335.5 (top)	164.5 (bottom)
	B19	200	600	50	297 (top)	148.5 (bottom)
	B20	200	600	50	329 (top)	164.5 (bottom)
Columns	C1	700	300	50	2100	
	C2	350	700	50	2100	

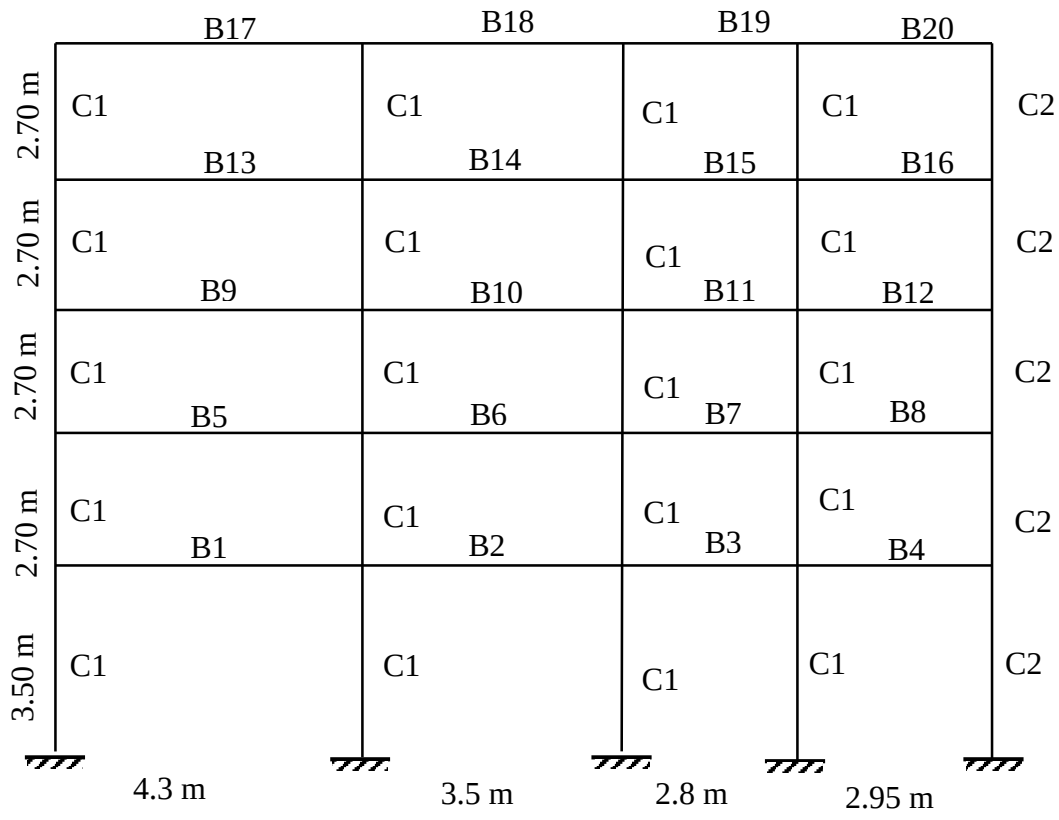

Figure D.7 Frame F7-5S4B

Table D.8 Sectional properties of frame F8-7S3B

Structural Member	Section	Width (mm)	Depth (mm)	Clear Cover (mm)	Total Reinforcing Rebar Area (mm^2)	
Beams	B1	300	550	50	1606.5 (top)	942 (bottom)
	B2	300	550	50	1529 (top)	
	B3	300	550	50	1732 (top)	942 (bottom)
	B4	300	550	50	1677 (top)	942 (bottom)
	B5	300	550	50	1655 (top)	942 (bottom)
	B6	300	550	50	1600 (top)	942 (bottom)
	B7	300	500	50	1622.5 (top)	845 (bottom)
	B8	300	500	50	1594 (top)	845 (bottom)
	B9	300	500	50	1416.5 (top)	845 (bottom)
	B10	300	500	50	1400 (top)	845 (bottom)
	B11	300	500	50	1129 (top)	732.5(bottom)
	B12	300	500	50	1142 (top)	735 (bottom)
	B13	300	500	50	845 (top)	458 (bottom)
	B14	300	500	50	845 (top)	523 (bottom)
Columns	C1	500	500	50	3161	
	C2	500	500	50	2503	
	C3	450	450	50	2026	
	C4	400	400	50	1897	
	C5	400	400	50	1600	

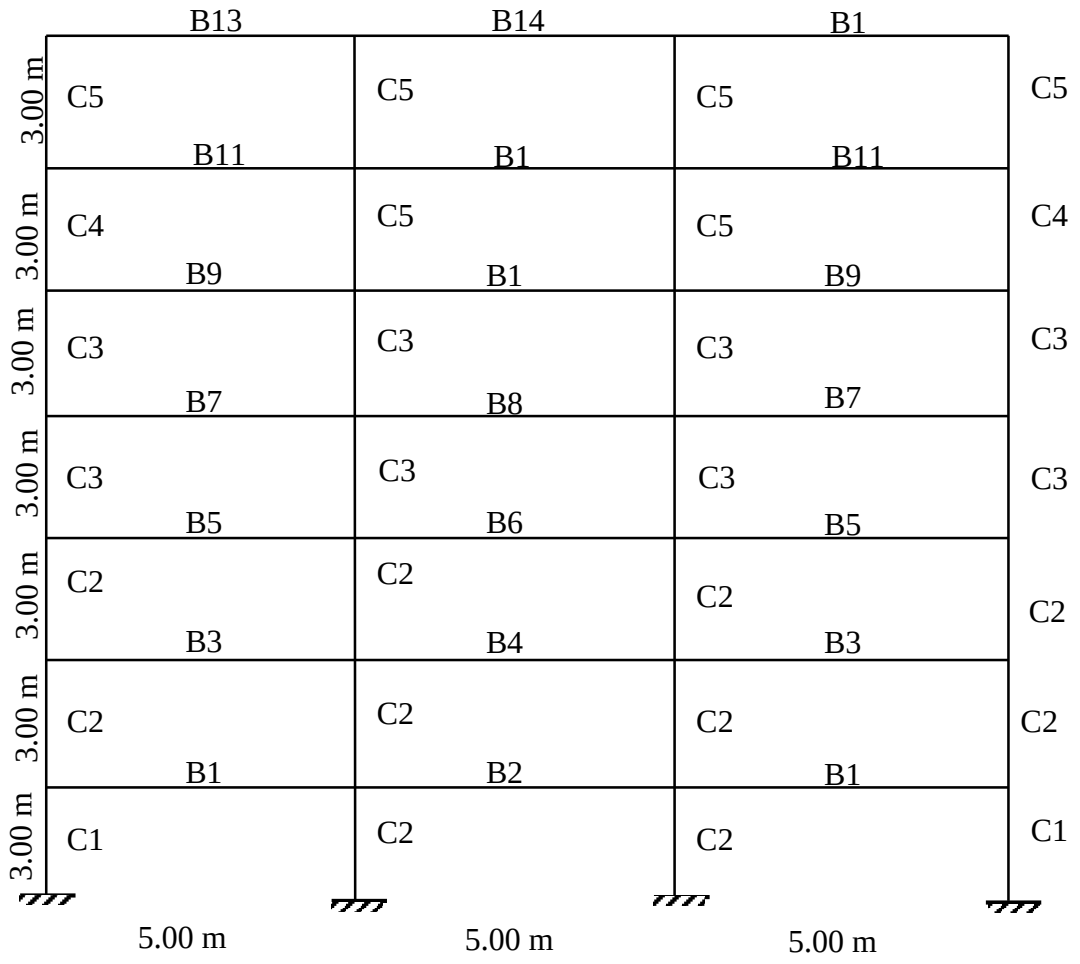

Figure D.8 Frame F8-7S3B

Table D.9 Sectional properties of frame F9-8S3B

Structural Member	**Section**	**Width (mm)**	**Depth (mm)**	**Clear Cover (mm)**	**Total Reinforcing Rebar Area (mm^2)**	
Beams	B1	500	900	50	5400 (top)	4800 (bottom)
	B2	400	750	50	4500 (top)	3600 (bottom)
	B3	300	600	50	1800 (top)	1125 (bottom)
Columns	C1	1100	1100	50	18360	
	C2	1000	1000	50	14280	
	C3	920	920	50	10200	

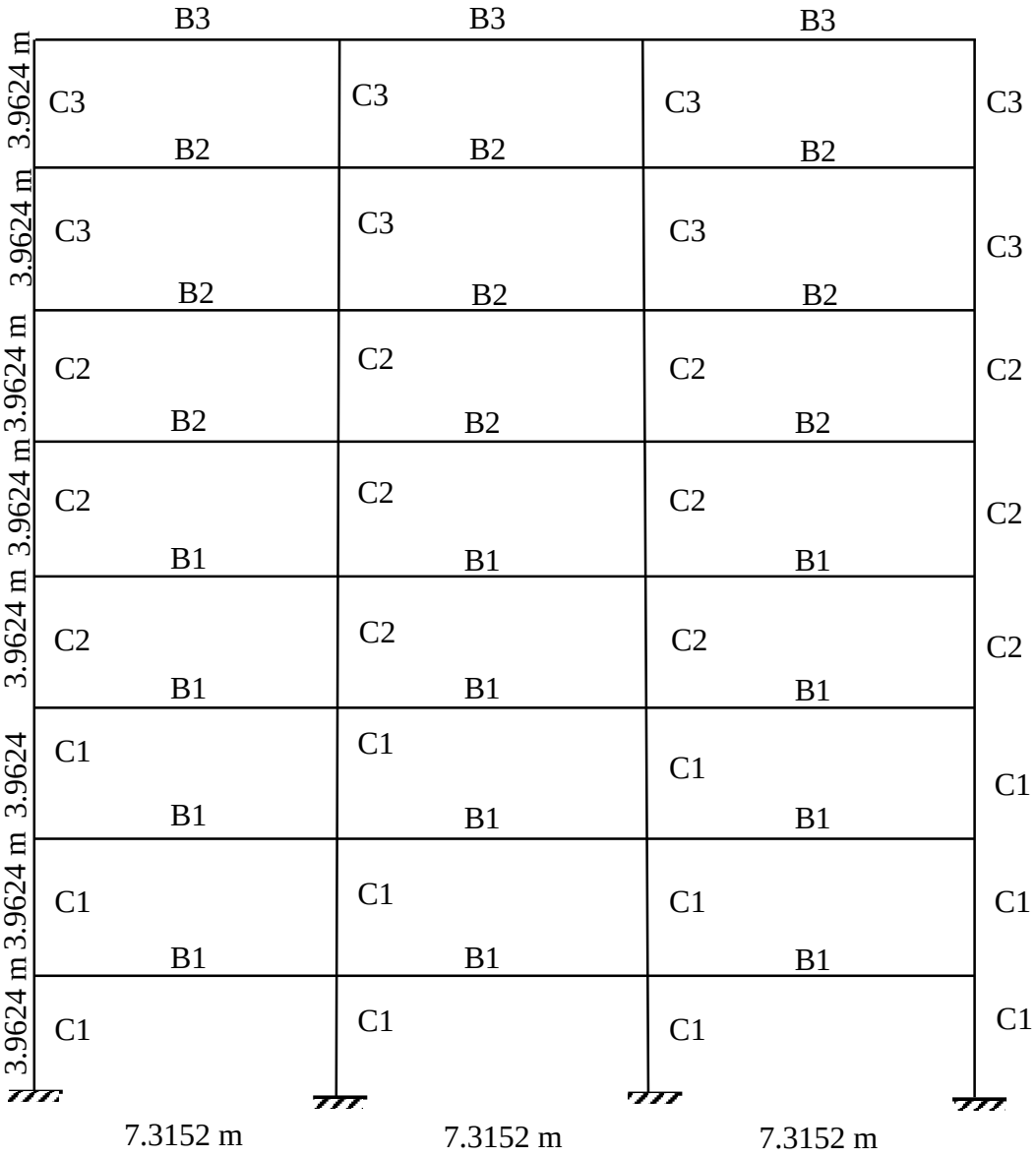

Figure D.9 Frame F9-8S3B

Table D.10 Material properties of concrete

Frame ID	Type of Concrete	Section	f_c (MPa)	ε_{c0}	f_{cu} (MPa)	ε_{cu}
F1-3S2B	Unconfined concrete properties	All	26	0.002	0.001	0.0057
	Confined concrete properties	Beams	30.522	0.0024	6.11	0.018
		Columns	33.422	0.0026	6.684	0.045
F2-3S2B	Unconfined concrete properties	All	18.5714	0.002	0.0007	0.0057
	Confined concrete properties	Beams	21.8014	0.0024	4.3643	0.018
		Columns	23.8729	0.0026	4.7743	0.045
F3-3S3B	Unconfined concrete properties	All	20	0.002	4	0.0063
	Confined concrete properties	Beams	24.9564	0.0024	4	0.0272
		Columns	25.937	0.0025	4	0.042
F4-4S3B	Unconfined concrete properties	All	20	0.002	4	0.0063
	Confined concrete properties	Beams	25.8742	0.0025	4	0.0279
		Columns	26.3842	0.0026	4	0.0063
F5-4S3B	Unconfined concrete properties	All	18	0.002	0.001	0.0075
	Confined concrete properties	Beams	20	0.0024	4.732	0.019
		Columns	20	0.0027	5.338	0.049

Table D.10 Continued

Frame ID	Type of Concrete	Section	f_c (MPa)	ε_{c0}	f_{cu} (MPa)	ε_{cu}
F6-5S2B	Unconfined concrete properties	All	20	0.002	0.001	0.0075
	Confined concrete properties	Beams	23.659	0.0024	4.732	0.019
		Columns	26.692	0.0027	5.338	0.049
F7-5S4B	Unconfined concrete properties	All	20	0.002	4	0.0063
	Confined concrete properties	Beams	21.3846	0.0021	4	0.0107
		C1	21.1533	0.0021	4	0.0173
		C2	21.5684	0.0022	4	0.0186
F8-7S3B	Unconfined concrete properties	All	20	0.002	4	0.0063
	Confined concrete properties	B(6-11)	24.7722	0.0024	4	0.0264
		B(12-19)	24.9564	0.0024	4	0.0272
		C1-C2	24.7881	0.0024	4	0.0349
		C3-C4	26.2555	0.0026	4	0.044
		C5-C6	28.5173	0.0028	4	0.0583
F9-8S3B	Unconfined concrete properties	All	28	0.002	0.001	0.0054
	Confined concrete properties	B1	30.704	0.0022	6.141	0.019
		B2	31.513	0.0023	6.303	0.02
		B3	33.047	0.0024	6.609	0.023
		C1	33.88	0.0024	6.776	0.053
		C2	35.008	0.0025	7.002	0.059
		C3	38.367	0.0027	7.673	0.082

Table D.11 Material properties of reinforcing steel

Frame ID	Section	f_y(MPa)	f_{yw}(MPa)	Hardening Ratio	E(MPa)
F1-3S2B	All	494	494	0.005	200000
F2-3S2B	All	494	494	0.005	200000
F3-3S3B	All	420	420	0.005	200000
F4-4S3B	All	420	420	0.005	200000
F5-4S3B	All	220	220	0.005	200000
F6-5S2B	All	420	420	0.005	200000
F7-5S4B	All	220	220	0.005	200000
F8-7S3B	All	420	420	0.005	200000
F9-8S3B	All	459	459	0.005	200000

Table D.12 Story masses

Frame ID	Story Masses (ton)							
	First Story	**Second Story**	**Third Story**	**Fourth Story**	**Fifth Story**	**Sixth Story**	**Seventh Story**	**Eighth Story**
F1-3S2B	88.851	88.851	48.777	-	-	-	-	-
F2-3S2B	88.851	88.851	48.777	-	-	-	-	-
F3-3S3B	61.47	61.47	30.73	-	-	-	-	-
F4-4S3B	60.63	60.63	60.63	30.31	-	-	-	-
F5-4S3B	19.98	19.98	19.98	15.3	-	-	-	-
F6-5S2B	47.505	52.177	52.177	52.177	56.14	-	-	-
F7-5S4B	36.89	36.89	36.89	36.89	18.45	-	-	-
F8-7S3B	56.245	56.245	56.245	56.245	56.245	56.245	28.123	-
F9-8S3B	230.45	230.45	230.45	230.45	230.45	230.45	230.45	202.92

Table D.13 Beam loading of the frames

Frame ID	Section	Dead Load (KN/m)	Live Load (KN/m)
F1-3S2B	B1	12.36	0.98
	B2	9.62	0.49
F2-3S2B	B1	12.36	0.98
	B2	9.62	0.49
F3-3S3B	B1-B4	12.36	0.98
	B5-B6	9.62	0.49
F4-4S3B	B1-B6	12.36	0.98
	B7-B9	9.62	0.49
F5-4S3B	B1	12.36	0.98
	B1-Top Floor	9.62	0.49
F6-5S2B	B1	12.36	0.98
	B1-Top Floor	9.62	0.49
F7-5S4B	B1-B16	20.49	1.31
	B17-B19	15.64	0.53
F8-7S3B	B1-B12	18.64	1.21
	B13-B14	14.55	0.49
F9-8S3B	B1	18.64	1.21
	B2	18.64	1.21
	B3	14.55	0.49

Table D.14 Modal properties

Frame ID	Modal Properties							
	T_1 (s)	**T_2 (s)**	**T_3 (s)**	**T_4 (s)**	**T_5 (s)**	**T_6 (s)**	**T_7 (s)**	**T_8 (s)**
F1-3S2B	0.4718	0.1223	0.0607	-	-	-	-	-
F2-3S2B	0.7177	0.2189	0.1242	-	-	-	-	-
F3-3S3B	0.5348	0.1723	0.0983	-	-	-	-	-
F4-4S3B	0.6925	0.2010	0.0952	0.0808	-	-	-	-
F5-4S3B	0.4940	0.1580	0.0893	0.0628	-	-	-	-
F6-5S2B	0.7807	0.2316	0.1178	0.0984	0.0759	-	-	-
F7-5S4B	0.5198	0.1757	0.1045	0.0866	0.0788	-	-	-
F8-7S3B	1.0521	0.3634	0.2008	0.1306	0.0951	0.0856	0.0826	-
F9-8S3B	1.3064	0.5173	0.4250	0.3004	0.2874	0.2821	0.2231	0.2123

APPENDIX E

COMPARISON OF NONLINEAR STATIC PUSH OVER ANALYSES AGAINST NONLINEAR TIME HISTORY ANALYSES

To assess the capacity curve of the 9 frames, nonlinear static (push-over) analysis is performed. Push-over analysis is a static analysis that directly incorporates inelastic material properties to approximate a force-deformation curve of the structure. To assess the push-over curve, the structure is subjected to a monotonically increasing load in accordance with a certain predefined pattern until a target deformation is obtained. In this study, in order to estimate the load-deformation response of the structures, a triangular lateral load pattern which is distributed along the structural height is considered. In a triangular load pattern, the lateral force applied at each story level is proportional to its story number. Then, the lateral load capacities of the buildings are compared against the peak responses from the records which are the base shears corresponding to the maximum top story displacements from nonlinear time history analyses with both real and simulated records. Results are presented in Figures E.1-E.27. It is obvious from these figures that most the frames especially all weak frames response both in the linear and nonlinear ranges to the selected ground motion set. It must be noted that these frames display typical structures and are not hypothetical.

E.1 Comparison of Capacity Curve and Dynamic Responses for the 1992 Erzincan Earthquake (Mw=6.6)

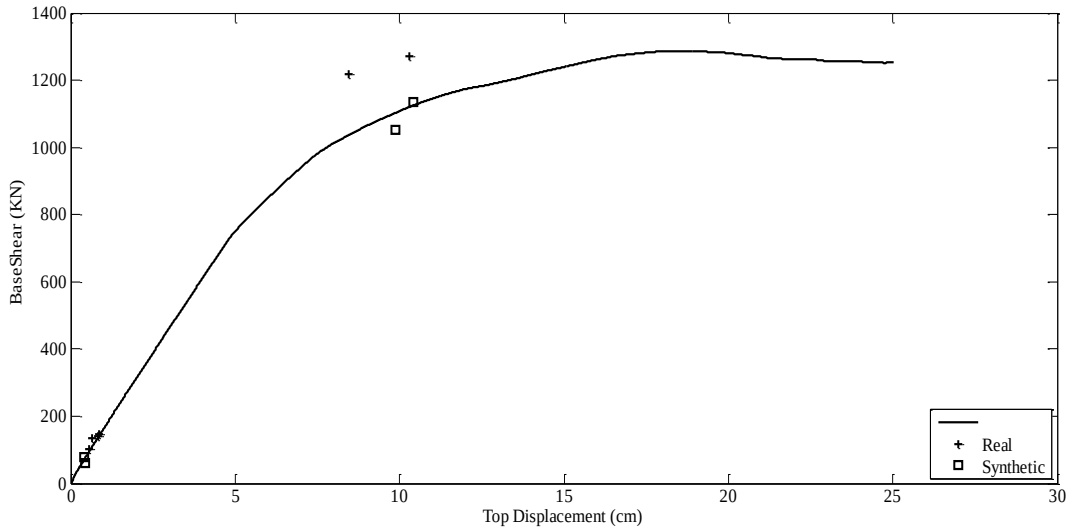

Figure E.1 Capacity Curve and Dynamic Responses of Erzincan Earthquake for F1-3S2B

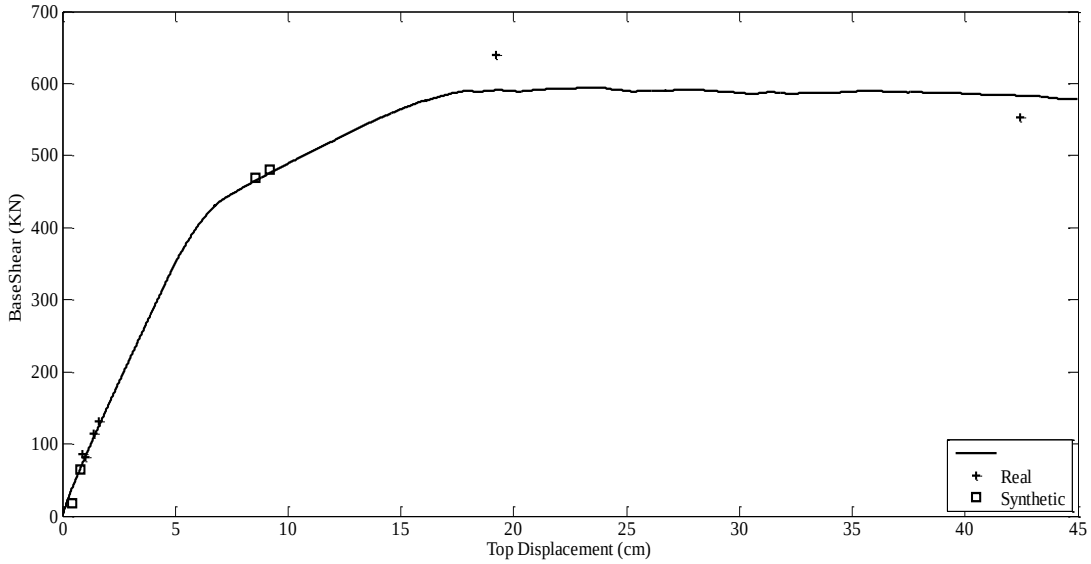

Figure E.2 Capacity Curve and Dynamic Responses of Erzincan Earthquake for F2-3S2B

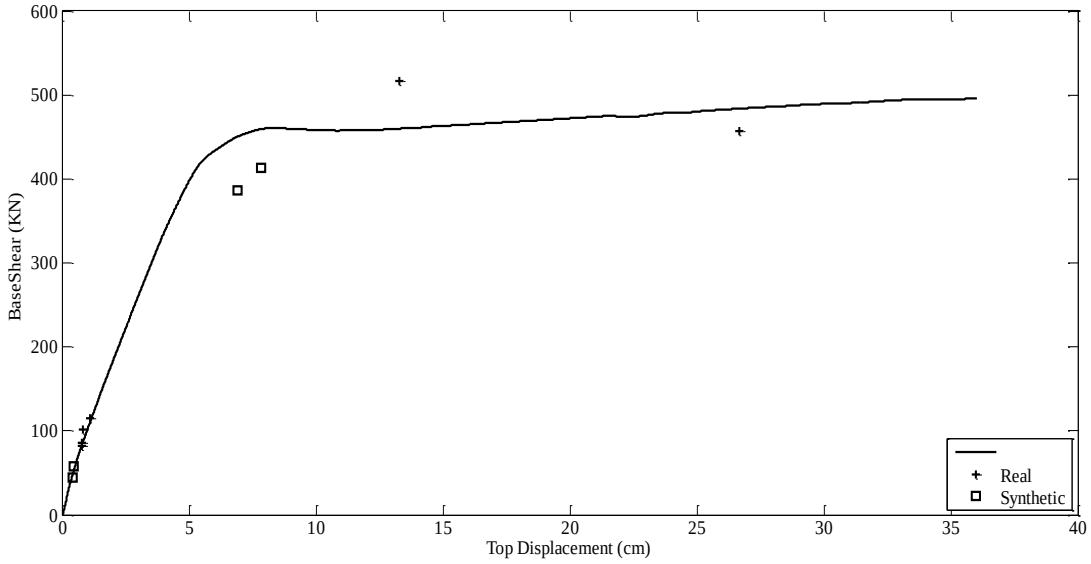

Figure E.3 Capacity Curve and Dynamic Responses of Erzincan Earthquake for F3-3S3B

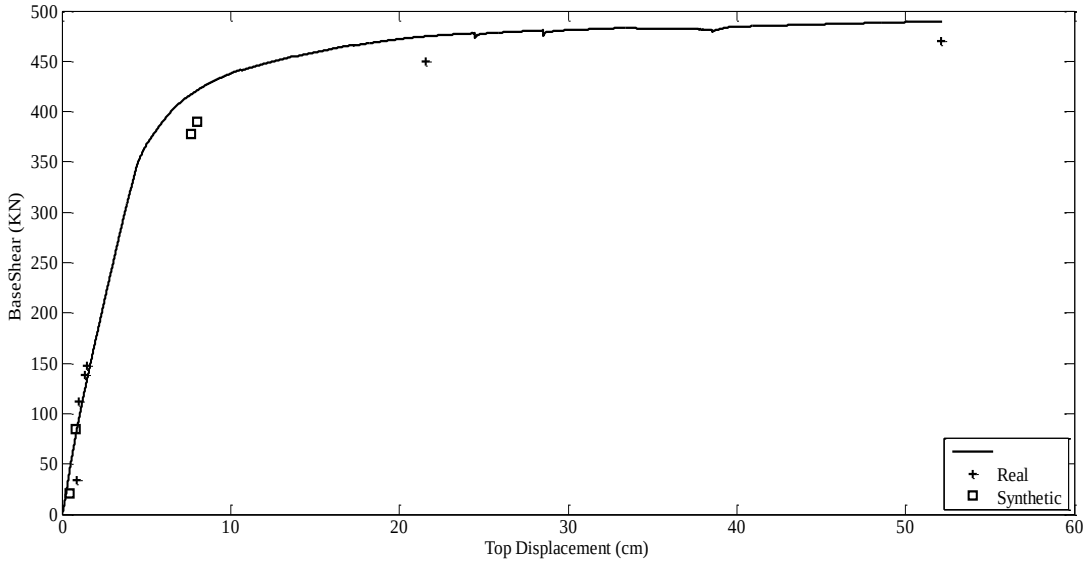

Figure E.4 Capacity Curve and Dynamic Responses of Erzincan Earthquake for F4-4S3B

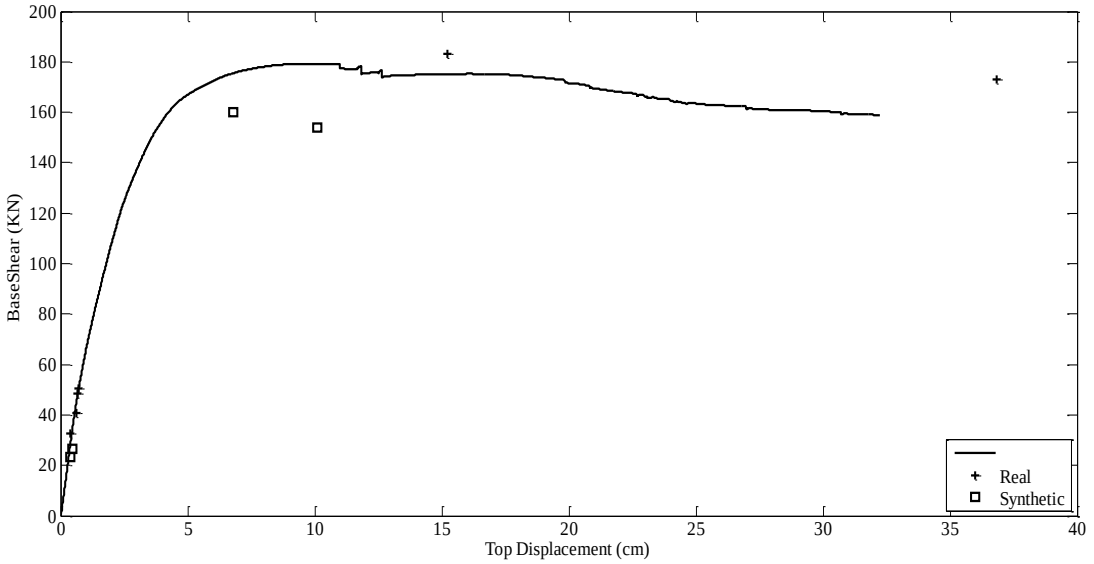

Figure E.5 Capacity Curve and Dynamic Responses of Erzincan Earthquake for F5-4S3B

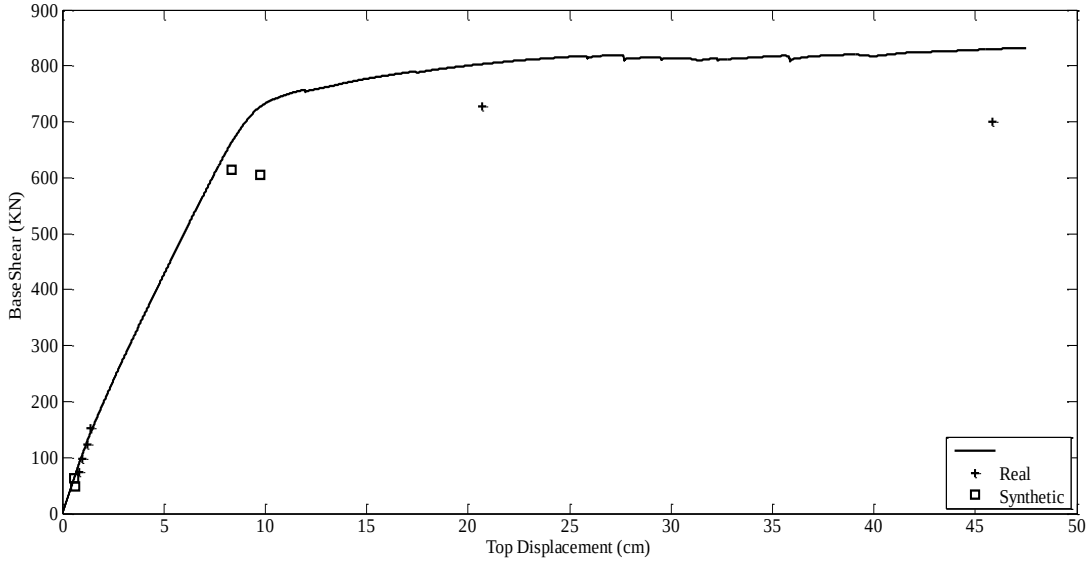

Figure E.6 Capacity Curve and Dynamic Responses of Erzincan Earthquake for F6-5S2B

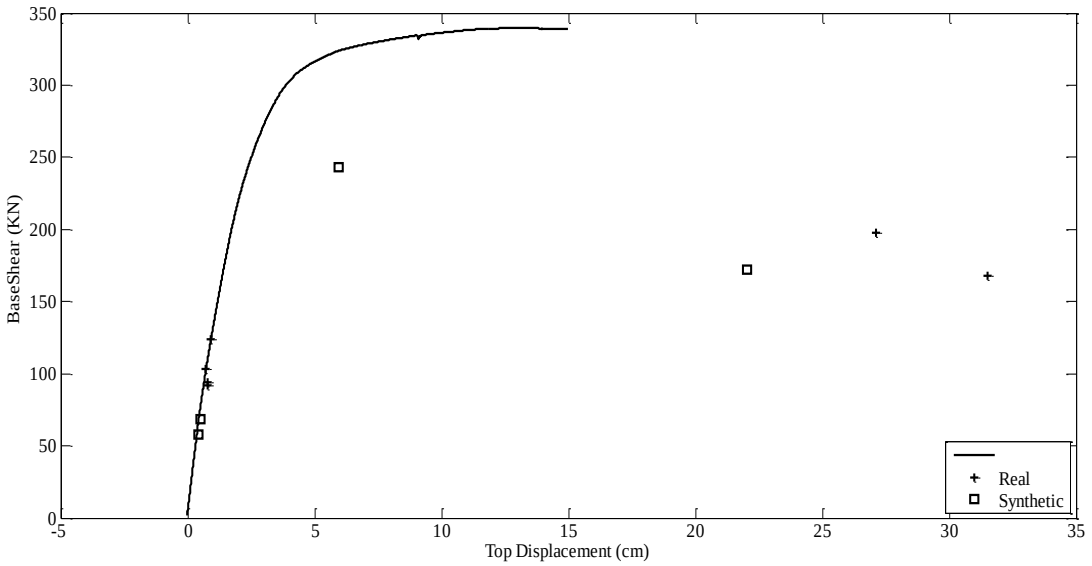

Figure E.7 Capacity Curve and Dynamic Responses of Erzincan Earthquake for F7-5S4B

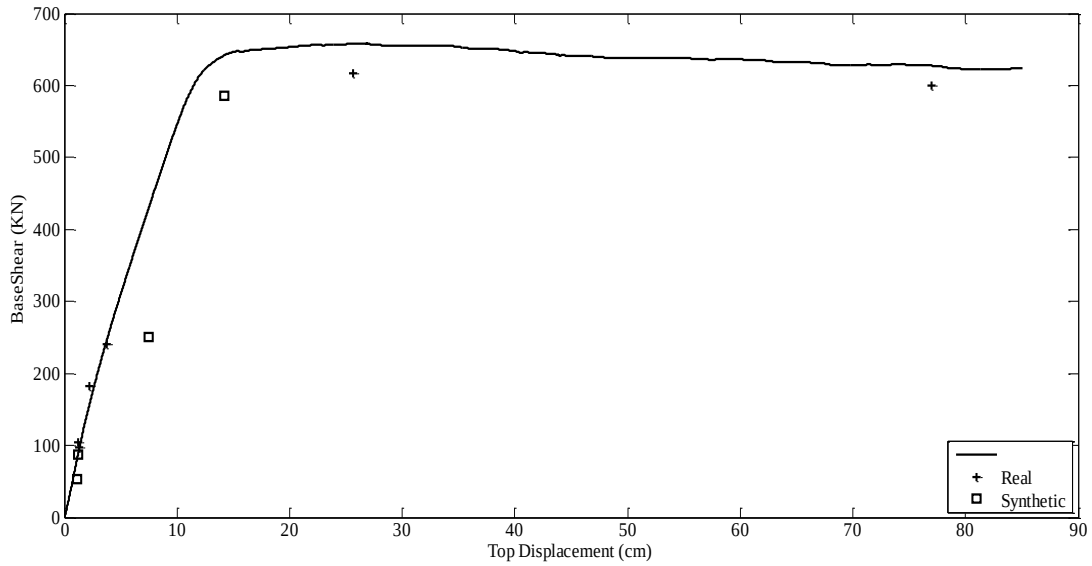

Figure E.8 Capacity Curve and Dynamic Responses of Erzincan Earthquake for F8-7S3B

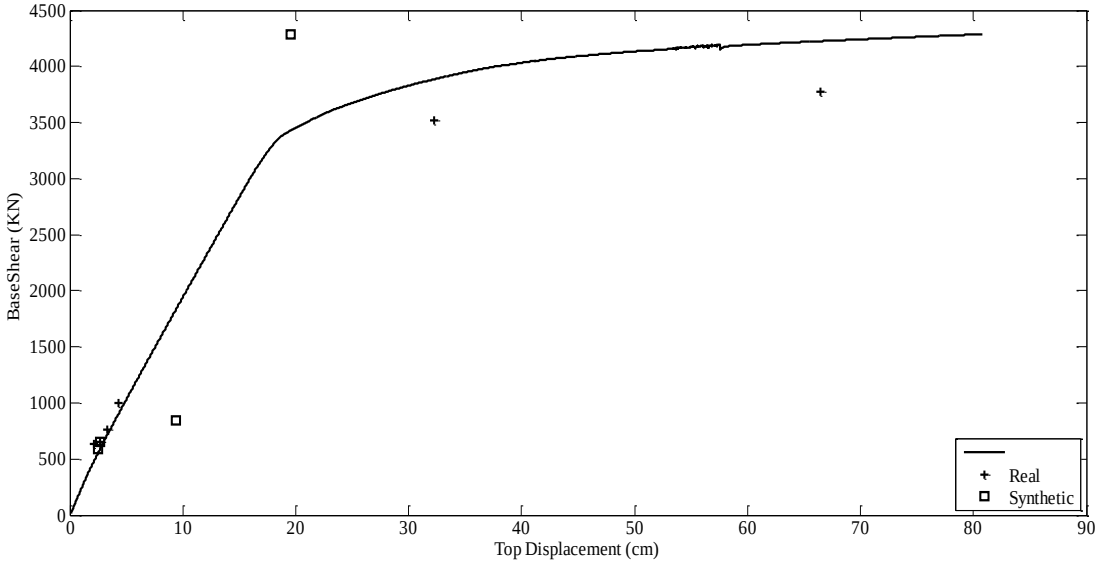

Figure E.9 Capacity Curve and Dynamic Responses of Erzincan Earthquake for F9-8S3B

E.2 Comparison of Capacity Curve and Dynamic Responses for the 1999 Düzce Earthquake (Mw=7.1)

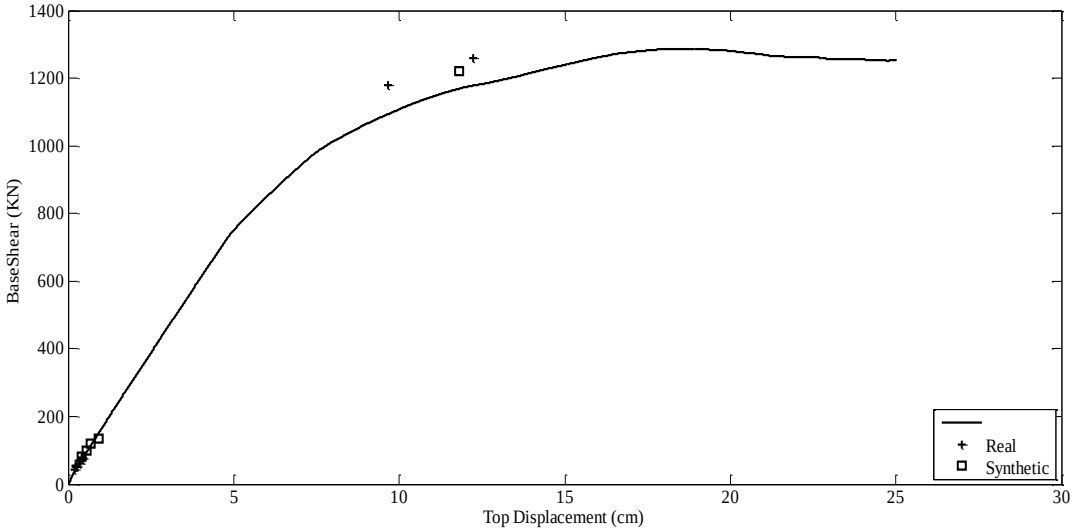

Figure E.10 Capacity Curve and Dynamic Responses of Düzce Earthquake for F1-3S2B

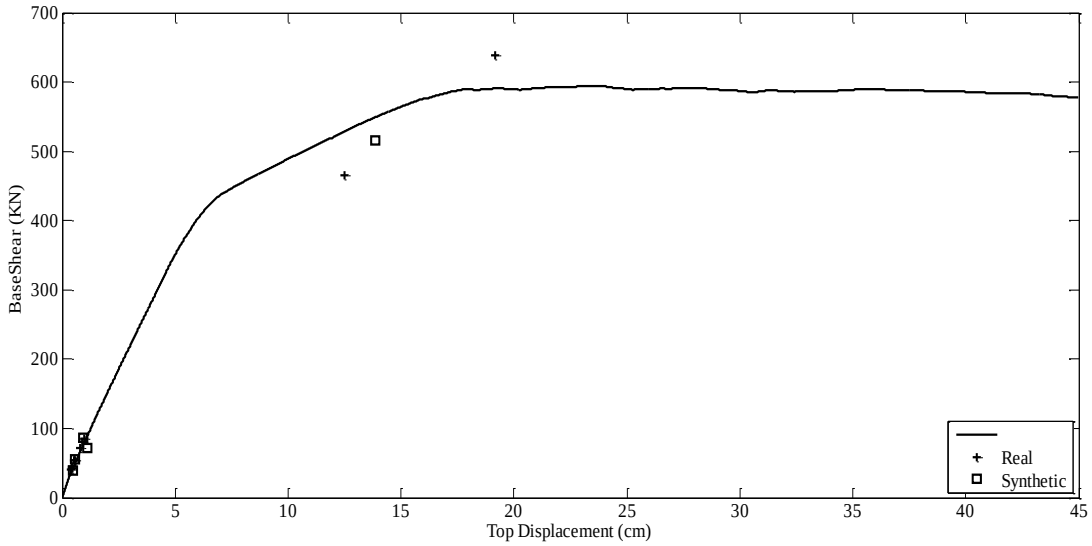

Figure E.11 Capacity Curve and Dynamic Responses of Düzce Earthquake for F2-3S2B

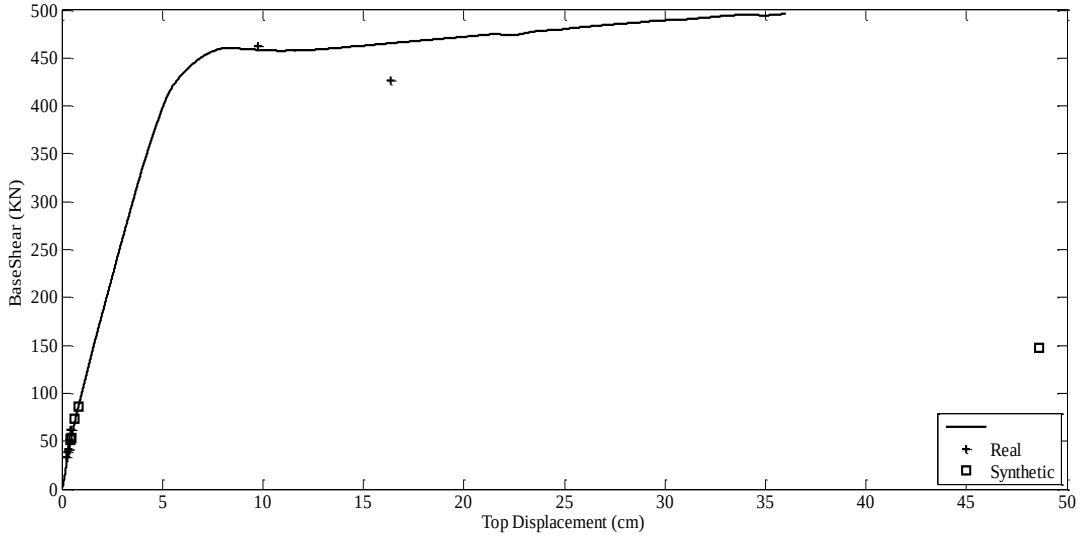

Figure E.12 Capacity Curve and Dynamic Responses of Düzce Earthquake for F3-3S3B

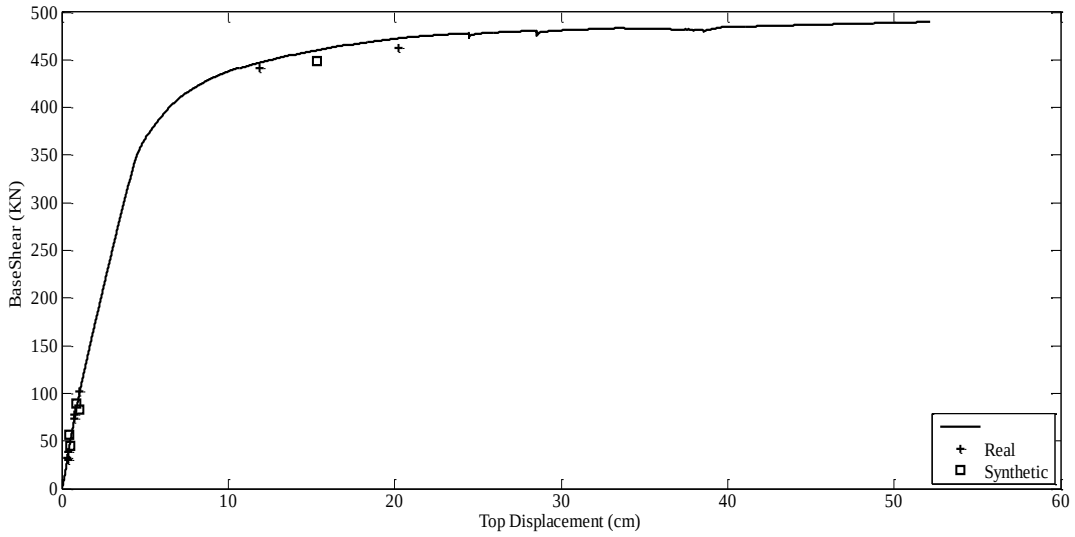

Figure E.13 Capacity Curve and Dynamic Responses of Düzce Earthquake for F4-4S3B

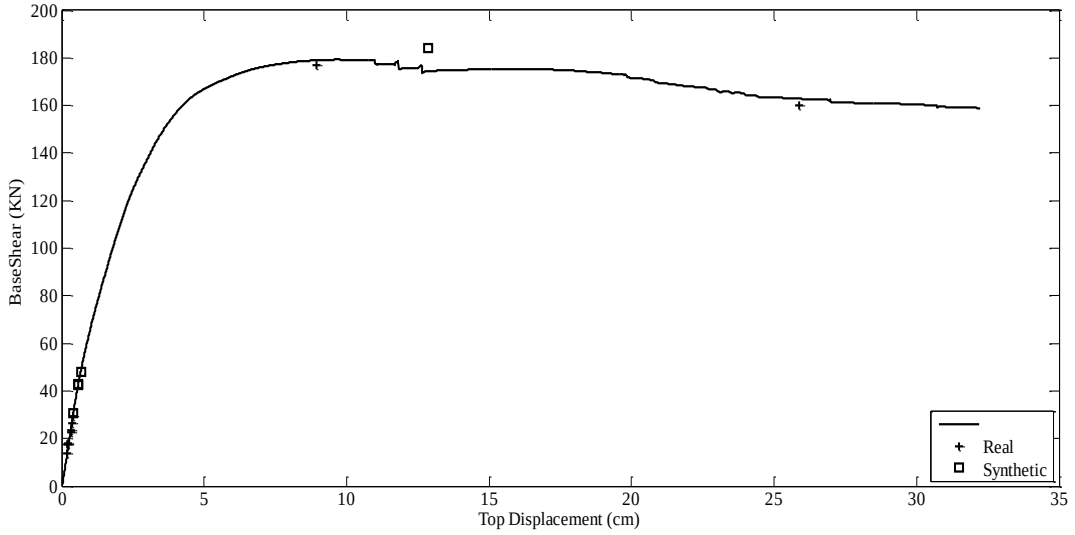

Figure E.14 Capacity Curve and Dynamic Responses of Düzce Earthquake for F5-4S3B

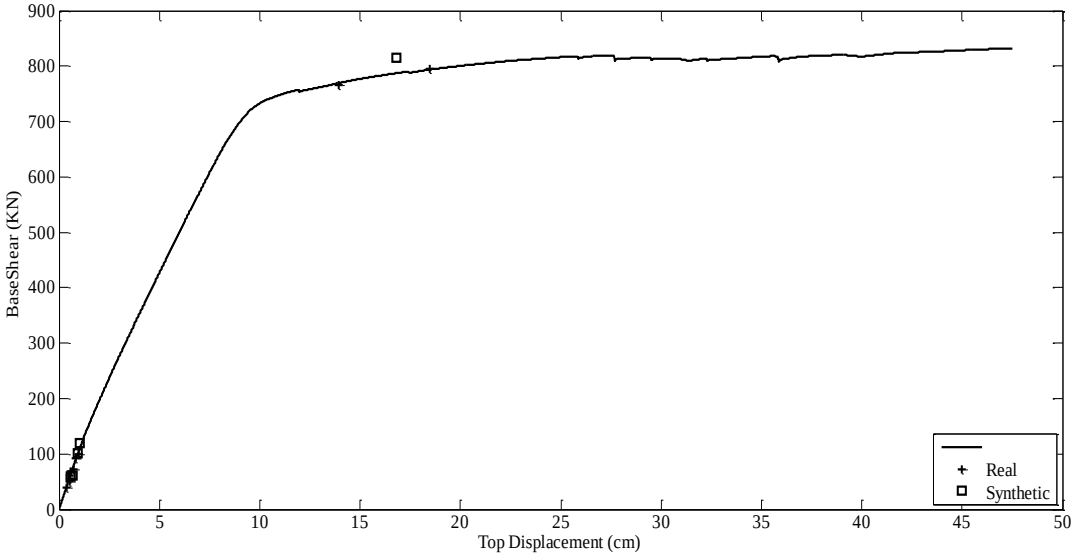

Figure E.15 Capacity Curve and Dynamic Responses of Düzce Earthquake for F6-5S2B

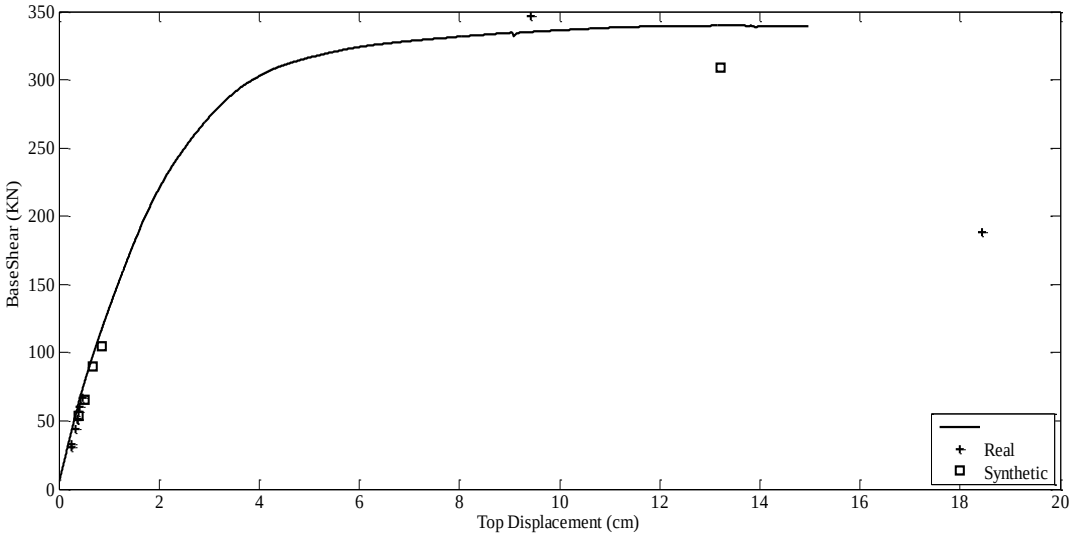

Figure E.16 Capacity Curve and Dynamic Responses of Düzce Earthquake for F7-5S4B

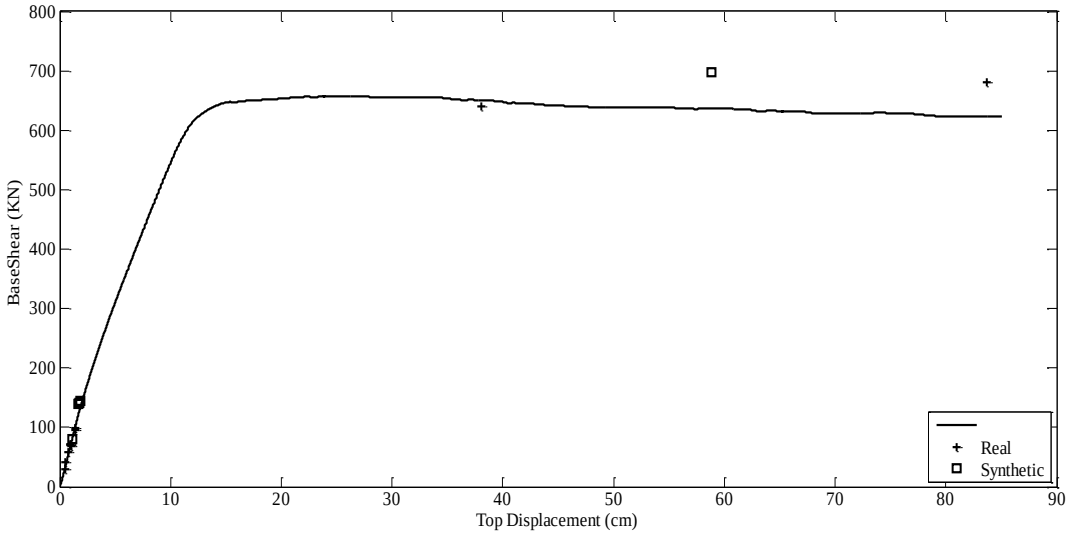

Figure E.17 Capacity Curve and Dynamic Responses of Düzce Earthquake for F8-7S4B

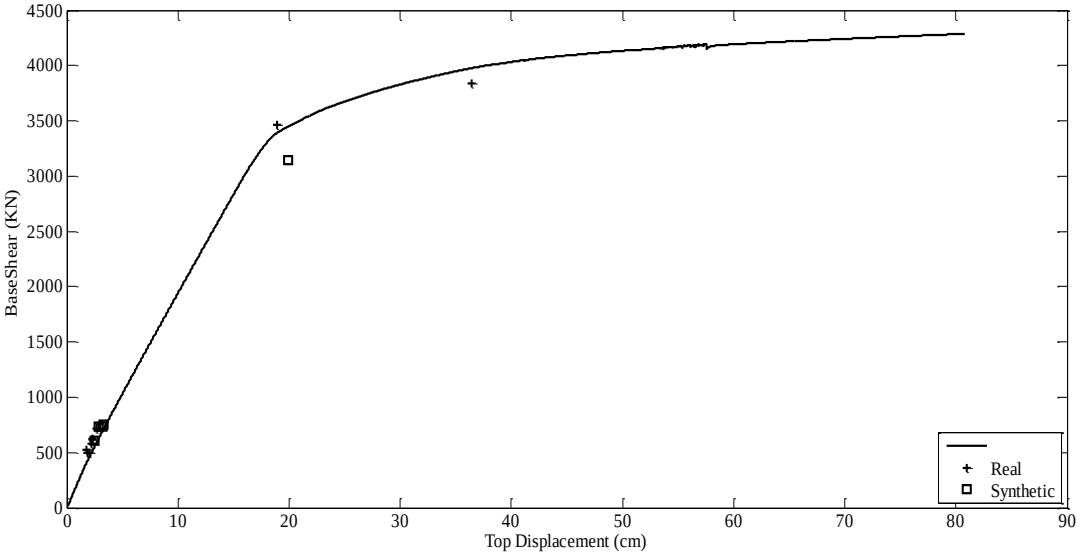

Figure E.18 Capacity Curve and Dynamic Responses of Düzce Earthquake for F9-8S3B

E.3 Comparison of Capacity Curve and Dynamic Responses for the 2009 L'Aquila Earthquake (Mw=6.3)

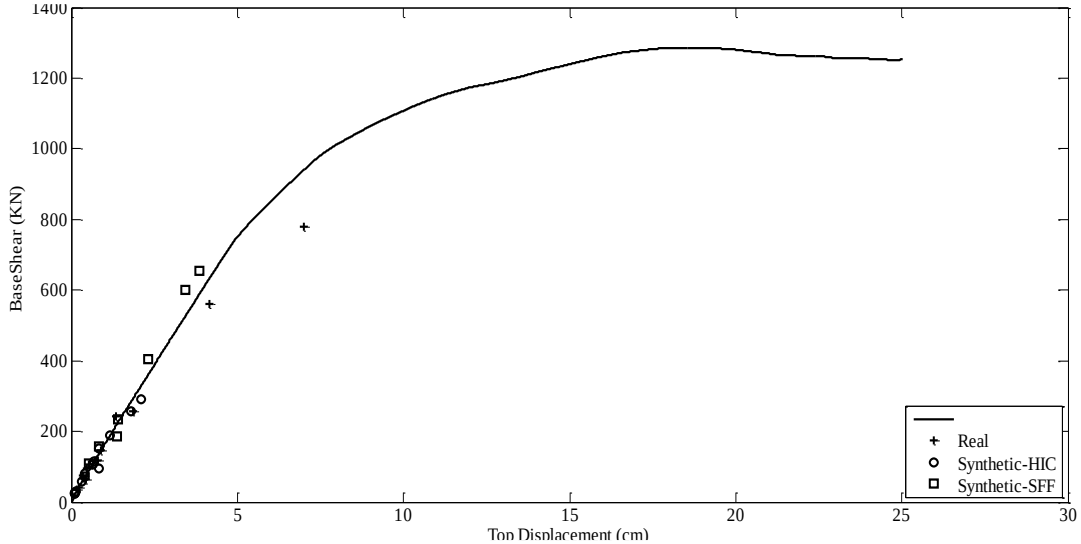

Figure E.19 Capacity Curve and Dynamic Responses of L'Aquila Earthquake for F1-3S2B

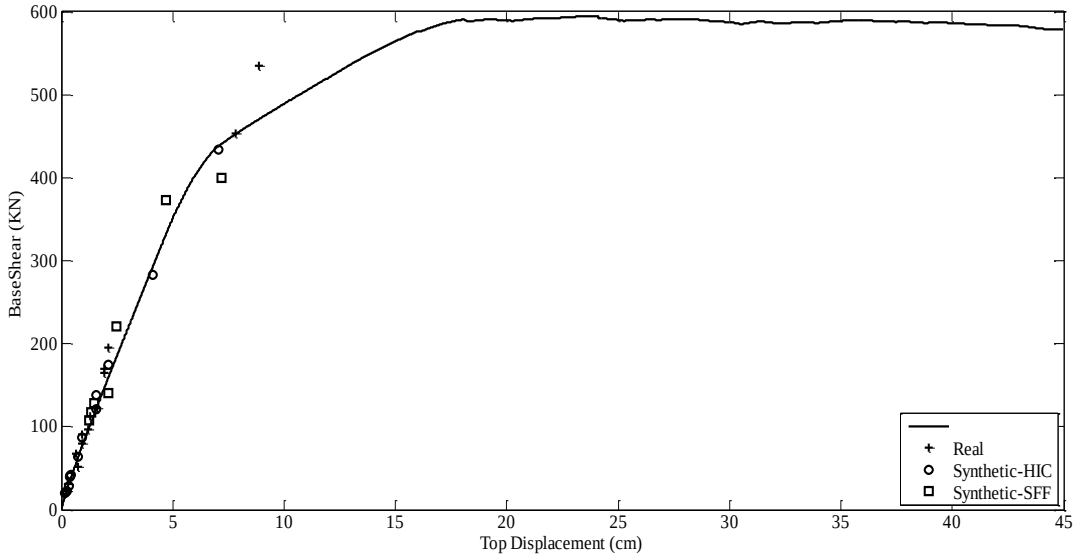

Figure E.20 Capacity Curve and Dynamic Responses of L'Aquila Earthquake for F2-3S2B

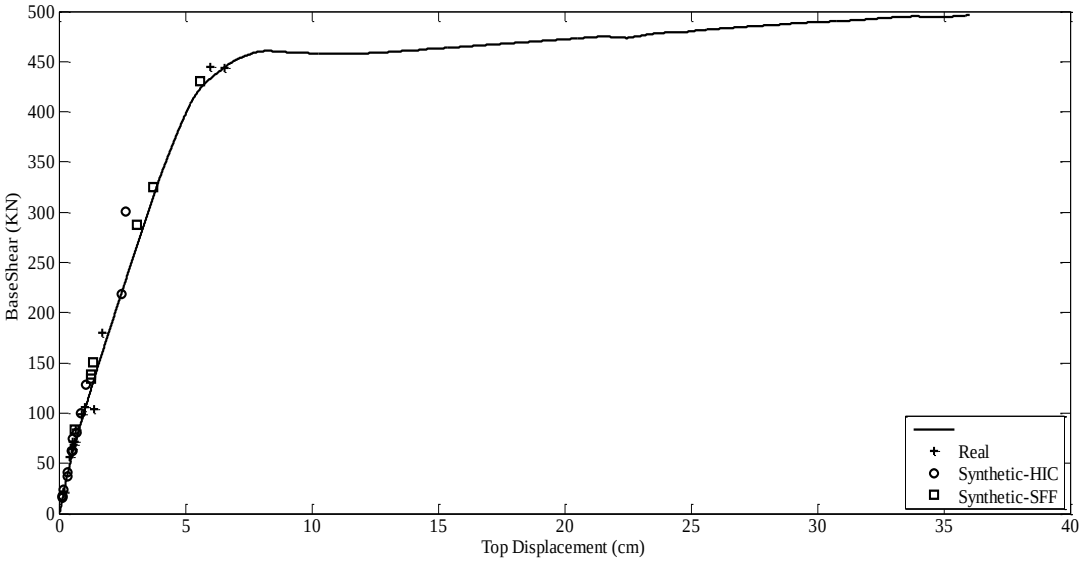

Figure E.21 Capacity Curve and Dynamic Responses of L'Aquila Earthquake for F3-3S3B

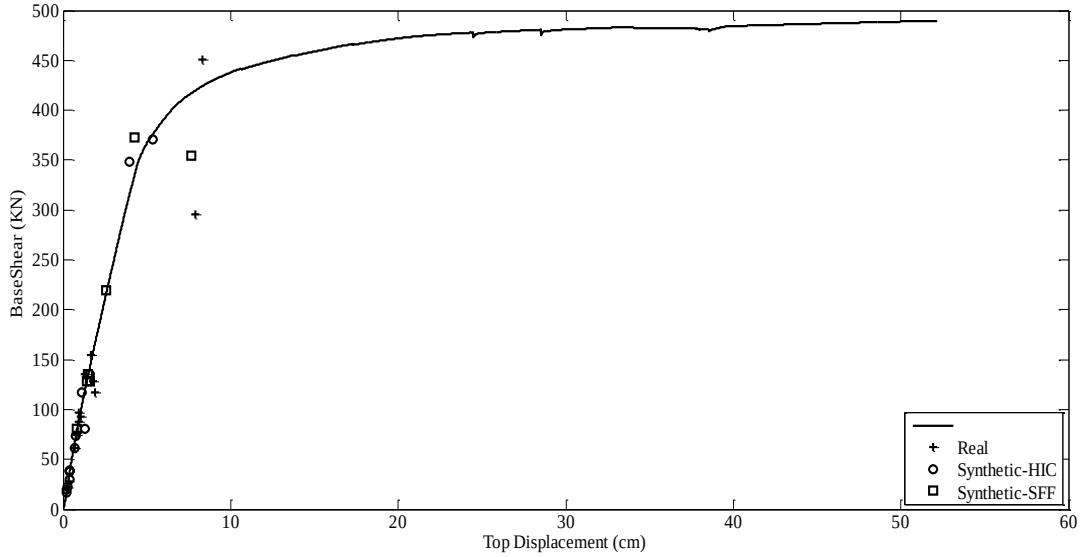

Figure E.22 Capacity Curve and Dynamic Responses of L'Aquila Earthquake for F4-4S3B

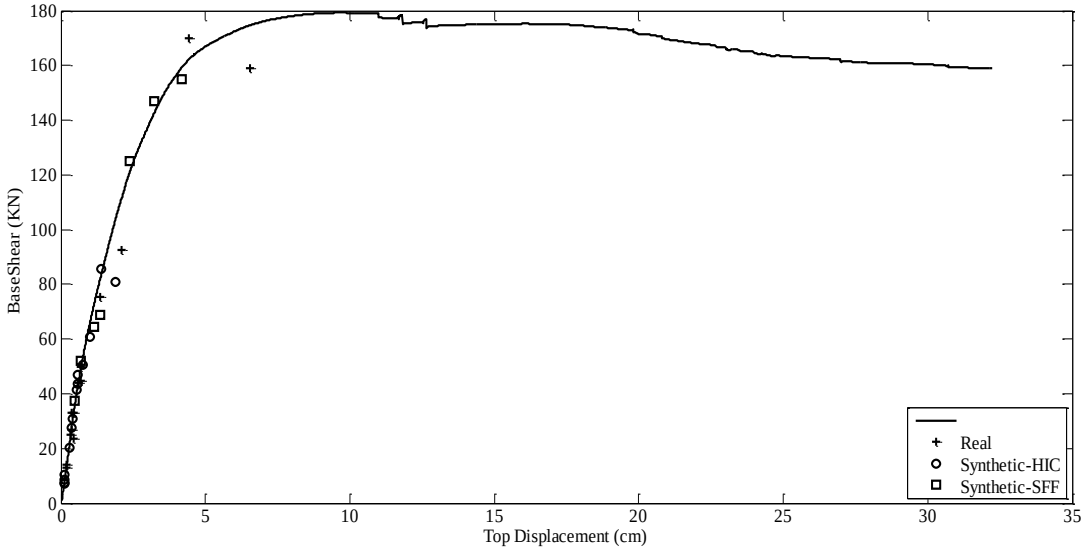

Figure E.23 Capacity Curve and Dynamic Responses of L'Aquila Earthquake for F5-4S3B

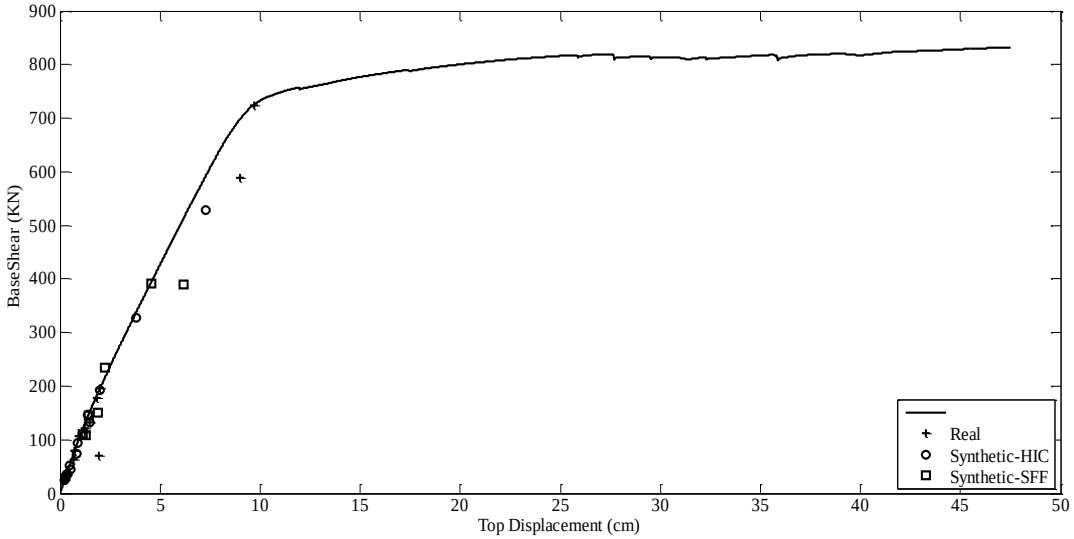

Figure E.24 Capacity Curve and Dynamic Responses of L'Aquila Earthquake for F6-5S2B

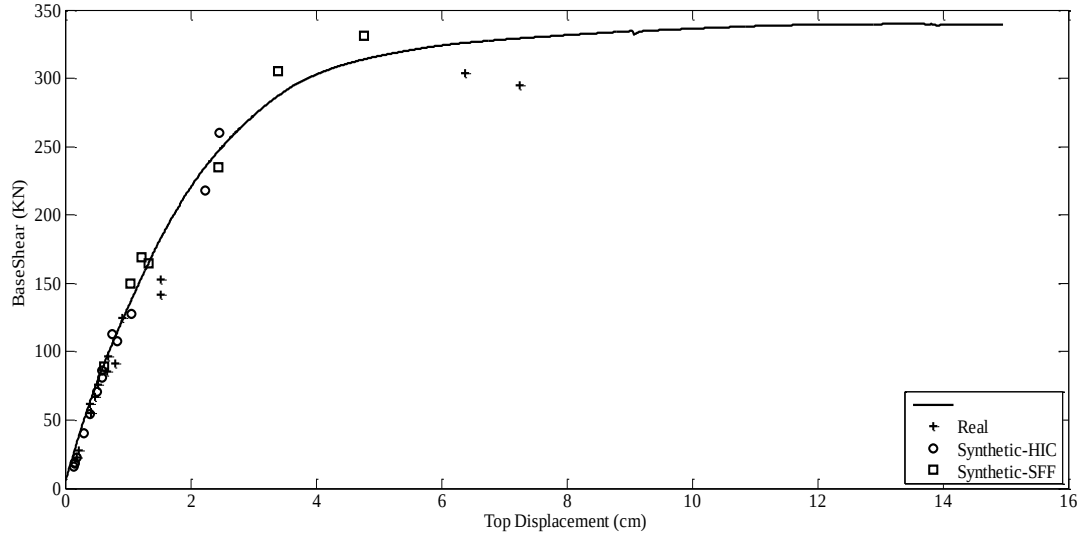

Figure E.25 Capacity Curve and Dynamic Responses of L'Aquila Earthquake for F7-5S4B

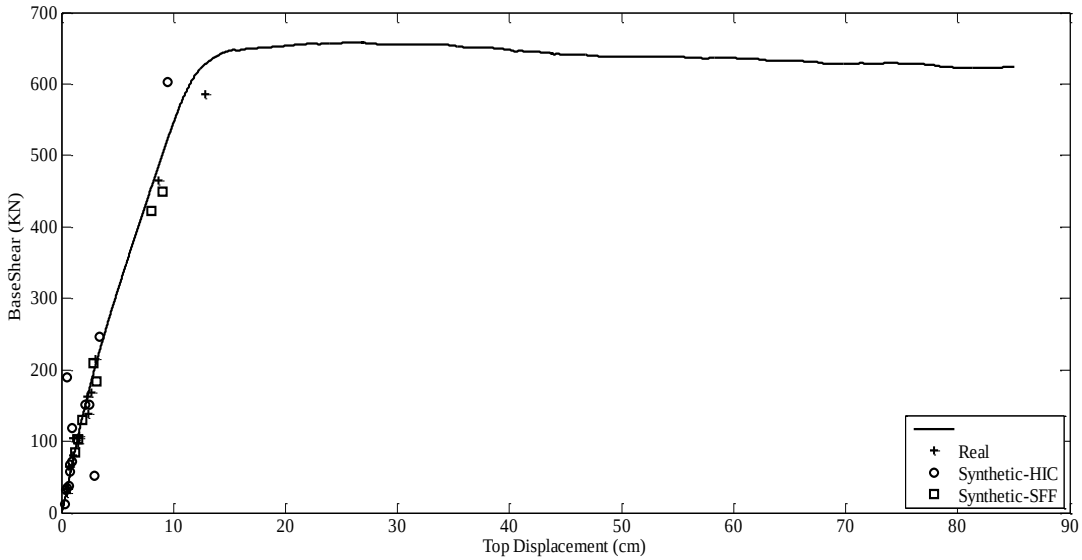

Figure E.26 Capacity Curve and Dynamic Responses of L'Aquila Earthquake for F8-7S3B

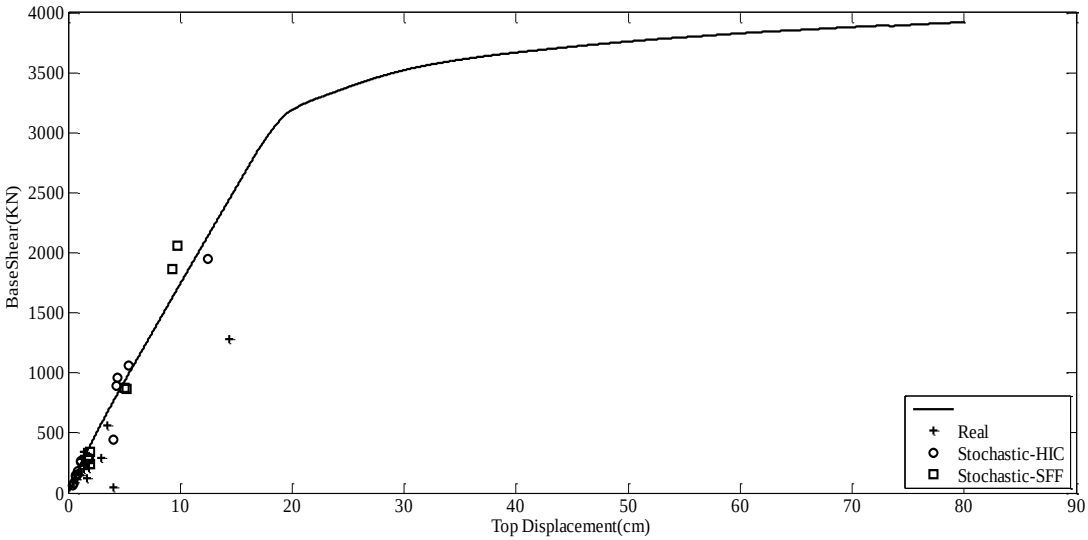

Figure E.27 Capacity Curve and Dynamic Responses of L'Aquila Earthquake for F9-8S3B

APPENDIX F

COMPARISON OF SEISMOLOGICAL MISFITS AGAINST NONLINEAR RESPONSE MISFITS

To have an overall understanding of the efficiency of synthetic records in simulation of real ground motions, for all case studies, residuals in terms of both FAS and RS at each station for each frequency or period are calculated. For this purpose, the residual is defined as log (predicted response) - log (observed response), where response can be either fast Fourier amplitude or the horizontal component of 5% damped pseudo acceleration. Then, the calculated residuals are averaged over all stations and all frequencies from 0.10 Hz to 10 Hz or all periods from 0.02 s to 4.00 s for each case study. Then, the standard deviation of the mean values which represents scatter of observations around the mean is obtained. To have a general idea about the capability of simulated records in predicting nonlinear responses of the MDOF frame structures, for all case studies, another type of residual is calculated. In addition to the residuals in terms of both FAS or RS, for each frame with a particular period, residual is calculated in terms of nonlinear response at each station using log (predicted response) - log (observed response). Here, response is considered to be the maximum top story displacement. Then, for each frame, the residuals are averaged over all stations and the standard deviation of the mean values is obtained. In the following sections the results for all case studies are obtained and then compared.

F.1 Comparison of the Seismological Misfits versus Nonlinear Response Misfits for the 1992 Erzincan (Mw=6.6) Earthquake

Figures F.1-F.3 show residuals corresponding to the 1992 Erzincan earthquake. In calculation process of this case study at station ERC, only residual corresponding to the simulated record with directivity effects is considered. It is observed that the average residuals are negative at lower frequencies or higher periods. This observation may be attributed to the effects of deep alluvial basin in producing long-period surface waves in Erzincan, which would affect the ground motion characteristics of the records. However, stochastic finite-fault methodology is incapable to model these effects. Also, the duration model applied for simulation of the 1992 Erzincan earthquake is not capable in simulation of the duration of surface wave portion of the observed time histories in the Erzincan region. As it is mentioned previously, Erzincan is placed on a deep sedimentary basin. The duration of observed ground motion records increase due to several reflections and reflections as the seismic waves pass through an alluvial basin. Therefore, real records of the 1992 Erzincan earthquake at three stations have larger duration compared to the simulated ones. To have a better estimate of duration of the observed records, a regional duration model may be preferred. At higher frequencies, the average residual has harmonic change with respect to the frequency or period either in positive or negative direction. When residuals corresponding to NR are studied, it is observed that all average residuals have negative values for the selected frames (Figure F.3). This observation verifies the underestimation of the real nonlinear responses with simulated records. For frames with fundamental period ranges in between 0.45 s to 0.7 s, as fundamental period of the frame increases, the average residual also increases from -0.1 to -0.35 log units. For frames with fundamental periods in between 0.7 s and 1 s, the average residual is constant and close to -0.35 log units. As fundamental period of the frame increases and becomes larger than 1 s, the average residual also decreases to -0.2 log units. The same trend is observed for the residuals in terms of either FAS or RS at the same frequencies of periods. Therefore, it can be concluded that, for this specific case, when there exist soil nonlinearity effects for the stations, stochastic finite-fault method is not conservative in prediction of nonlinear responses of MDOF frame structures.

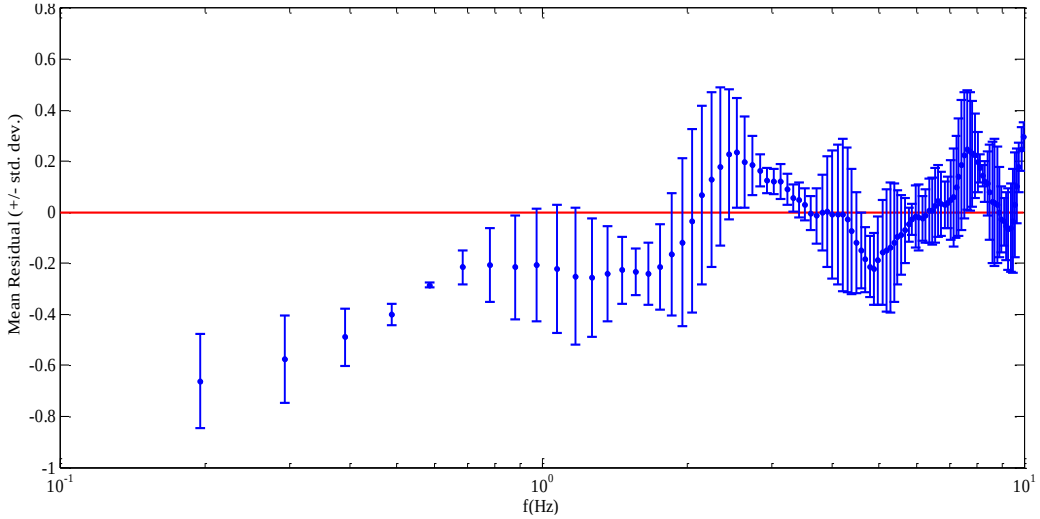

Figure F.1 Average of residuals over all simulated Erzincan records versus frequency, where residual = log(Predicted FAS) - log(Observed FAS). Standard deviation of residuals is depicted by error bars.

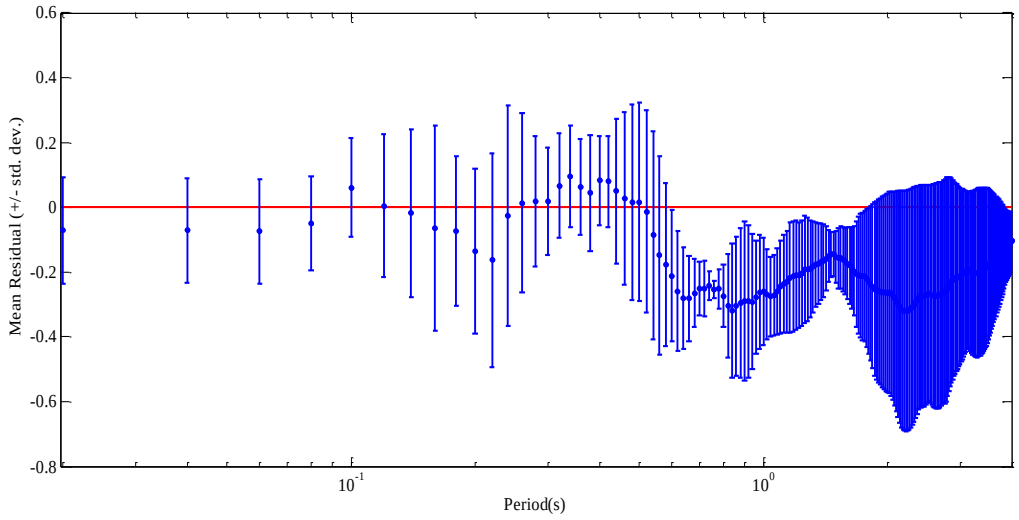

Figure F.2 Average of residuals over all simulated Erzincan records versus period, where residual = log(Predicted RS) - log(Observed RS). Standard deviation of residuals is depicted by error bars.

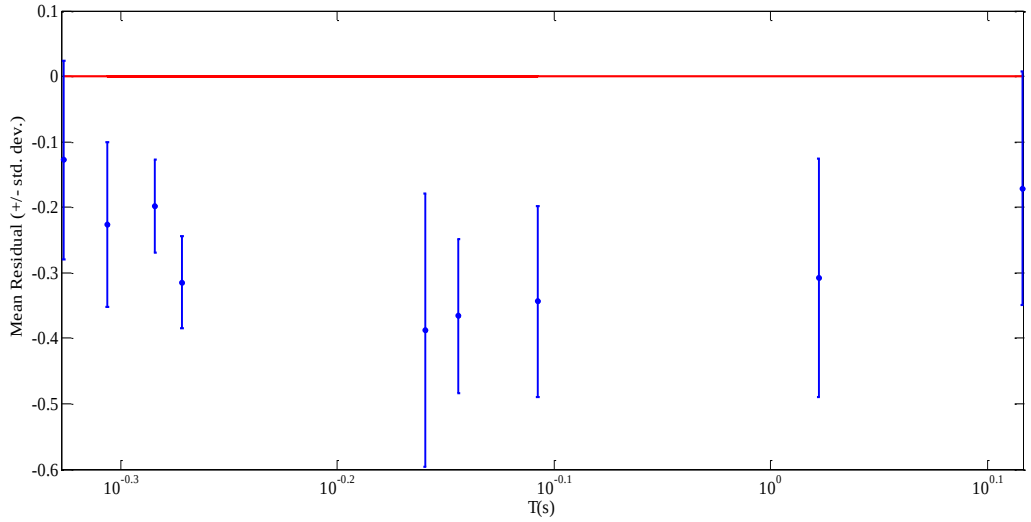

Figure F.3 Average of residuals over all simulated Erzincan records versus period of frames, where residual = log(Predicted NR) - log(Observed NR). Standard deviation of residuals is depicted by error bars.

F.2 Comparison of the Seismological Misfits versus Nonlinear Response Misfits for the 1999 Düzce (Mw=7.1) Earthquake

Figures F.4-F.6 illustrate residuals corresponding to the 1999 Düzce earthquake (Mw=7.1). It is observed that the average residual in terms of FAS is close to zero at all frequencies with the standard deviation ranging from 0.2 to 0.6 log units. This observation is also true for residual in terms of RS at all periods; however, the mean values are around 0.2 log units (Figures F.4 and F.5). For this case study, all frames have positive residuals in terms of NR with an average of 0.2 log units where both FAS and especially RS residuals are consistent with this trend (Figure F.6). Therefore, it can be concluded that for this specific case located on shallow alluvial basin, simulated records generated from stochastic finite-fault method can be safely used for seismic design and assessment purposes of MDOF structures. Therefore, the stochastic finite-fault method is capable of simulating the 1999 Düzce earthquake in the selected stations, where the ground motion parameters of the synthetic records are in good agreement with the observed ones.

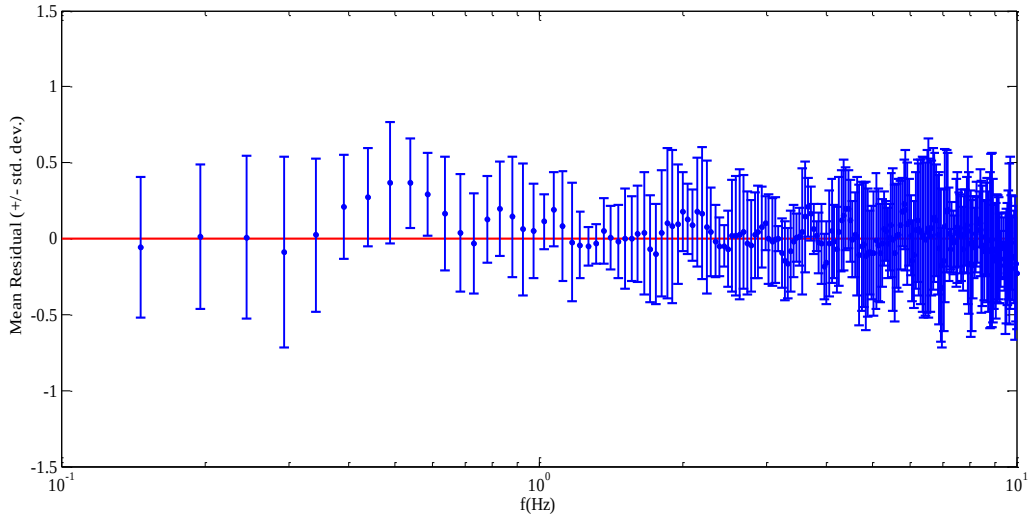

Figure F.4 Average of residuals over all simulated Düzce records versus frequency, where residual = log(Predicted FAS) - log(Observed FAS). Standard deviation of residuals is depicted by error bars.

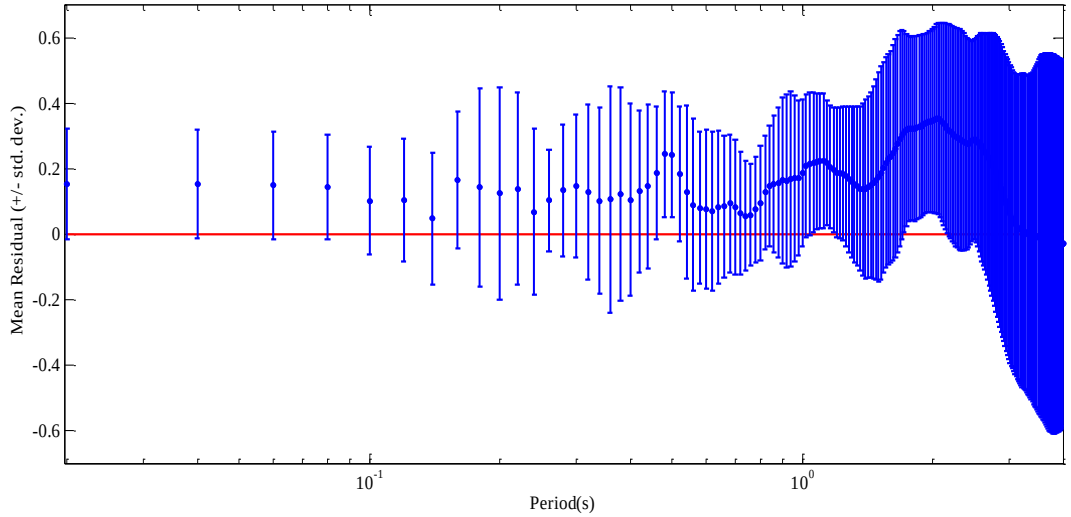

Figure F.5 Average of residuals over all simulated Düzce records versus period, where residual = log(Predicted RS) - log(Observed RS). Standard deviation of residuals is depicted by error bars.

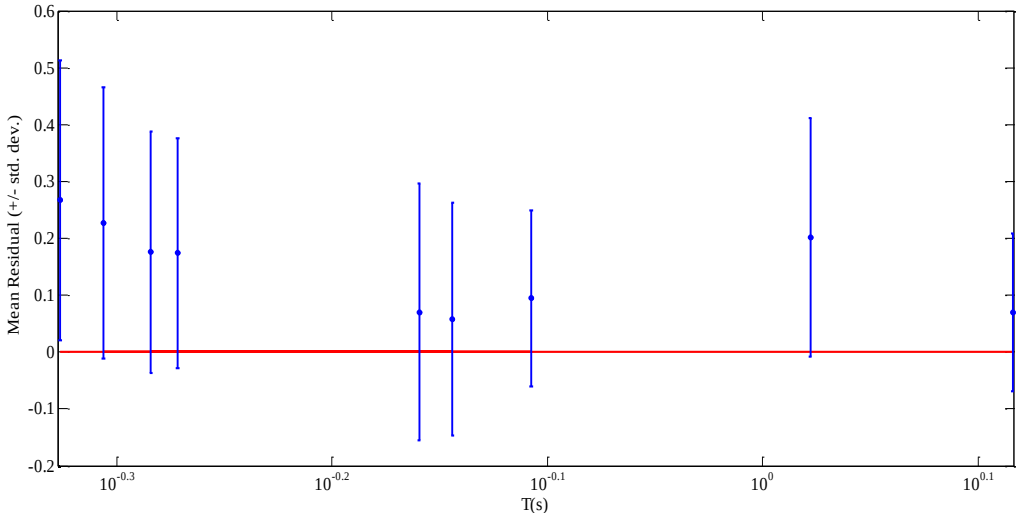

Figure F.6 Average of residuals over all simulated Düzce records versus period of frames, where residual = log(Predicted NR) - log(Observed NR). Standard deviation of residuals is depicted by error bars.

F.3 Comparison of the Seismological Misfits versus Nonlinear Response Misfits for the 2009 L'Aquila (Mw=6.3) Earthquake

Figures F.7-F.9 show residuals corresponding to the 2009 L'Aquila earthquake (Mw=6.3). It is observed that the average residual in terms of either FAS or RS has positive value at all frequencies when records are simulated with stochastic finite-fault methodology. On the other hand, the average residual in terms of FAS for the hybrid-integral-composite method is close to zero for low frequencies while it becomes negative as the frequency increases (Figure F.7). Figure F.8 presents that the average residual in terms of RS from stochastic finite-fault method has positive value (close to 0.2 log units) at all frequencies, whereas the hybrid-integral-composite method results in negative average residual (close to -0.2 log units). When the results corresponding to NR residuals are studied, it is observed that the average residuals from stochastic finite-fault methodology has positive values for all frames ranging from 0.2 to 0.3 log units (Figure F.9.a). Whereas, results corresponding to the hybrid-composite-method

reveals that for most of the frames the average residual is close to -0.2 log units; however, for frames with fundamental periods higher than 1 s, it slightly becomes close to zero (Figure F.9.b). These trends for residuals in terms of nonlinear responses obtained from two alternative simulation methods are consistent with those of the FAS and RS residuals. As a result, for this case specific, simulated records of stochastic finite-fault methodology overestimate the nonlinear response whereas simulated records of hybrid-integral-composite method underestimate. Therefore, stochastic finite-fault methodology for this case study could be conservatively used for seismic design and assessment purposes of MDOF structures in the studied period ranges compared to the hybrid-integral-composite technique.

(a)

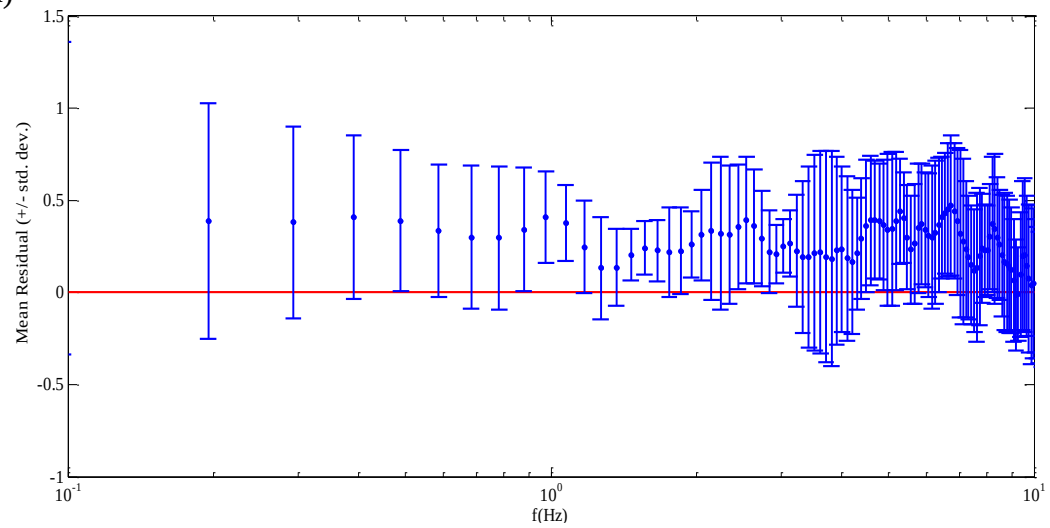

(b)

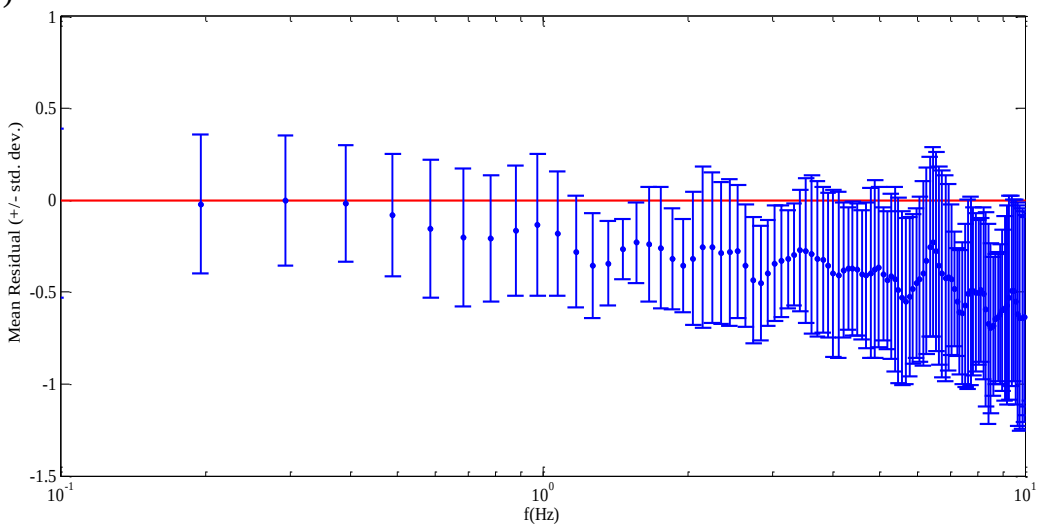

Figure F.7 Average of residuals using (a) Synthetic-SFF and (b) Synthetic-HIC methods over all simulated L'Aquila records versus frequency, where residual = log(Predicted FAS) - log(Observed FAS). Standard deviation of residuals is depicted by error bars.

(a)

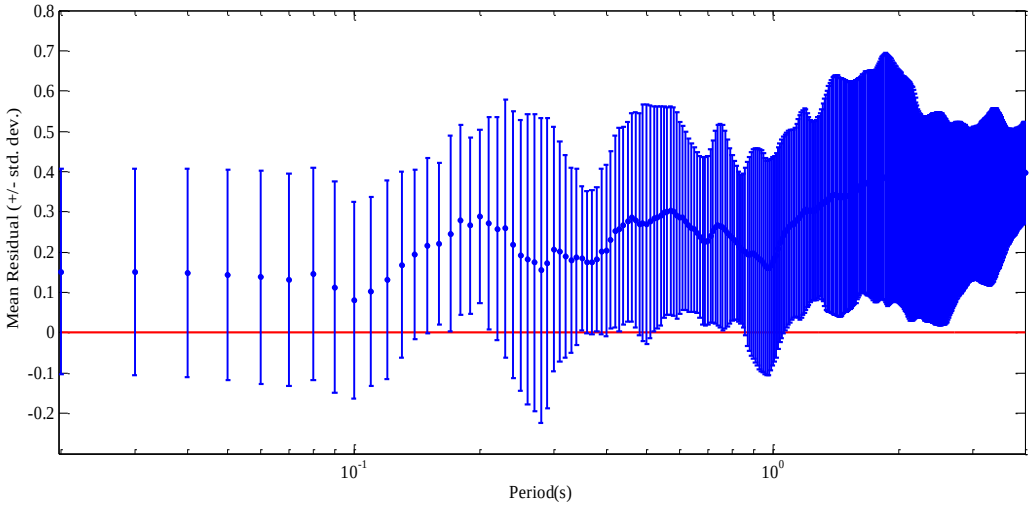

(b)

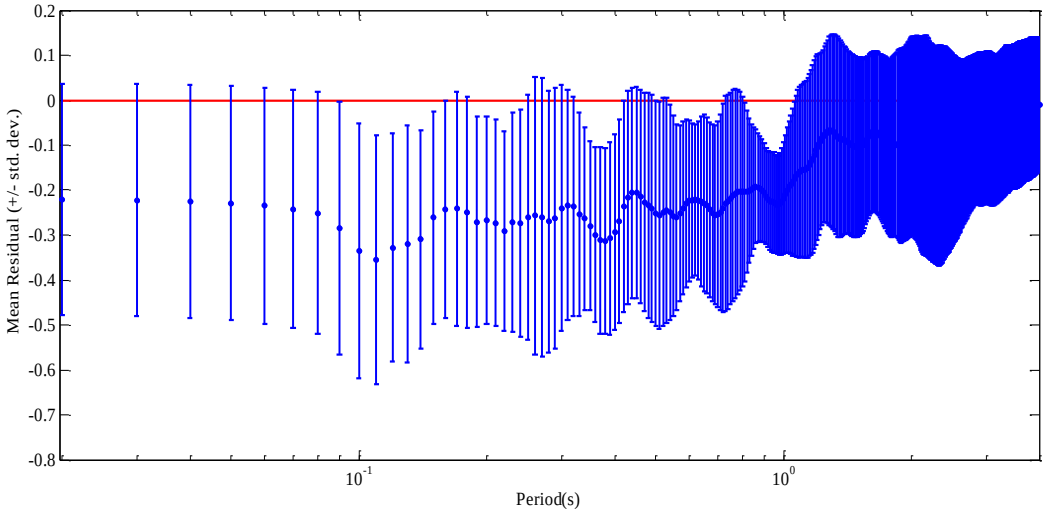

Figure F.8 Average of residuals using (a) Synthetic-SFF and (b) Synthetic-HIC methods over all simulated L'Aquila records versus period, where residual = log(Predicted RS) - log(Observed RS). Standard deviation of residuals is depicted by error bars.

(a)

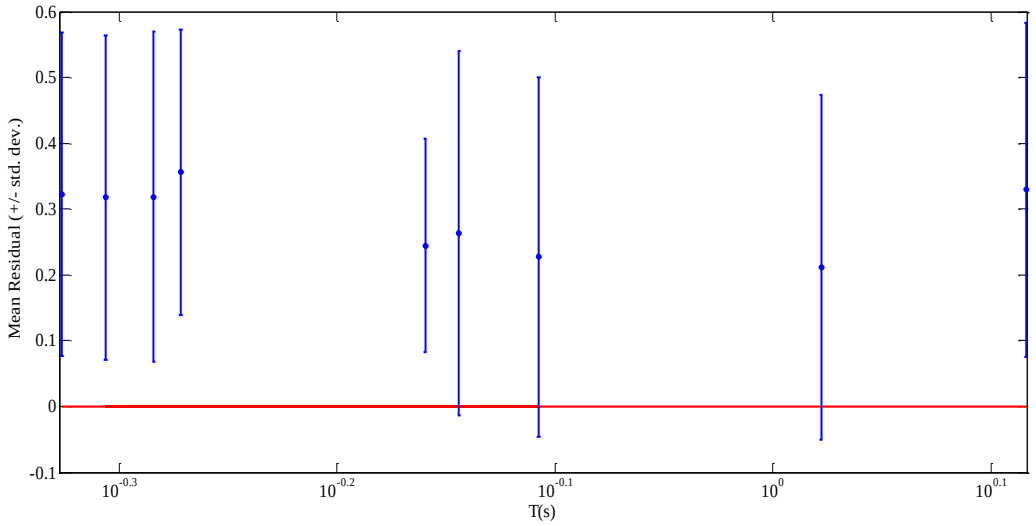

(b)

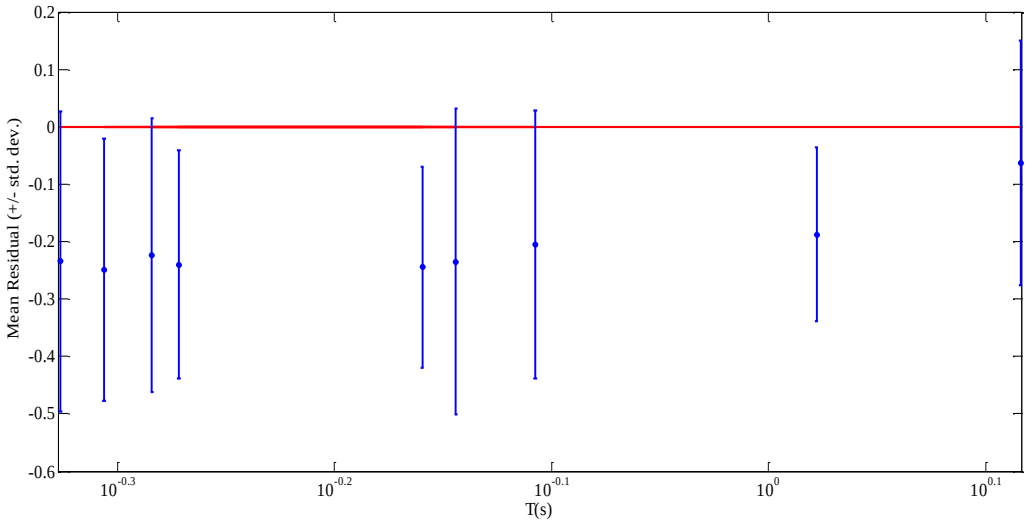

Figure F.9 Average of residuals using (a) Synthetic-SFF and (b) Synthetic-HIC methods over all simulated L'Aquila records versus period of frames, where residual = log(Predicted NR) - log(Observed NR). Standard deviation of residuals is depicted by error bars.

CURRICULUM VITAE

PERSONAL INFORMATION

Surname, Name: Karimzadeh Naghshineh, Shaghayegh
Nationality: Iranian
Date and Place of Birth: 15 September 1985, Tabriz
Marital Status: Married
Phone: +90 3122105424
email: shaghayegh.karimzadehnaghshineh@metu.edu.tr

EDUCATION

Degree	Institution	Year of Graduation
MS	Tabriz University, Civil Engineering	2009
BS	Tabriz University, Civil Engineering	2007
High School	Azadi High School, Tabriz	2003

WORK EXPERIENCE

Year	Place	Enrollment
2009- 2011	Structural design of apartment complex	Design Engineer
2012-2014	METU, TUJJB-UDP-01-12 Project	Project Assistant
2015-2016	METU, BAP-08-11-KB.2015K120470-2	Project Assistant

FOREIGN LANGUAGES

English, Azeri, Persian, Turkish

PUBLICATIONS

1. Askan A, Karimzadeh S, Asten M, Kılıç N, Şişman FN, Erkmen C. Assessment of seismic hazard in Erzincan (Turkey) region: construction of local velocity models and evaluation of potential ground motions, Turkish Journal of Earth Sciences, 24, 529-565, doi: 10.3906/yer-1503-8, (2015).

2. Askan A, Karimzadeh S, Bilal M. Seismic intensity maps for North Anatolian Fault Zone (Turkey) based on recorded and simulated ground motion data, Book Chapter, Neotectonics and Earthquake Potential of the Eastern Mediterranean Region, AGU Books, Wiley Online Library, In Press.

3. Karimzadeh S, Askan A, Yakut A, Ameri G. Assessment of Synthetic Ground Motion Records Obtained from Alternative Simulation Methods in Dynamic Analyses of Multi-Story frame Buildings, Seismological Research Letters, San Diego, California, 83, p. 372, 2012.

4. Karimzadeh S, Askan A, Yakut A, Ameri G. Assessment Of Synthetic Ground Motion Records Obtained From Alternative Simulation Techniques In Nonlinear Time History Analyses Of Multi-Storey Frame Buildings: A Case Study, 2nd Turkish conference on earthquake engineering and seismology , Hatay, Turkey, s.Paper No. 160, 2013.

5. Karimzadeh S, Askan A, Yakut A, Ameri G. Assessment of synthetic ground motion records from alternative simulation methods in dynamic response analysis of building structures. Seismological Research Letters, Salt Lake City, Utah, 84, 368, 2013.

6. Karimzadeh S, Askan A, Yakut A, Ameri G. Nonlinear time history analyses of structures under real and synthetic ground motions. Seismological Research Letters, Anchorage, Alaska, 85:2, Pg. 473, 2014.

7. Karimzadeh S, Askan A, Yakut A, Ameri G. Assessment of synthetic ground motion records obtained from alternative simulation techniques in nonlinear time history analyses of multi-storey frame buildings: A case study, the 9th International Conference on Structural Dynamics, EURODYN, Portugal, p. 351-358, 2014.

8. Askan A, Sisman FN, Karimzadeh S. Regional Kappa Models on North Anatolian Fault Zone (Turkey) and Their Use in Ground Motion Simulations, "American Geophysical Union", San Francisco, California, Paper No.: NH13B-1920, 2015.

9. Askan A, Erberik MA, Yakut A, Kilic N, Karimzadeh S, Sisman FN, Asten M. Estimation of seismic losses in urban regions within an interdisciplinary

framework; a case study, Seismological Research Letters, Anchorage, Alaska, 85:2, Pg. 511, 2014.

10. Karimzadeh S, Askan A, Bilal M. Seismic Intensity Maps for Scenario Events on the Eastern Segments of North Anatolian Fault Zone of Turkey based on Simulated Ground Motion Data, Pasadena, California, 86:2B, Pg. 686, 2015.

11. Karimzadeh S, Askan A, Erberik MA, Yakut A. Seismic damage assessment using synthetic ground motions: a case study for erzincan, "3rd Turkish conference on Earthquake Engineering and Seismology", Izmir, Turkey, 2015.

12. Askan A, Asten M, Erberik MA, Erkmen C, Karimzadeh S, Kılıç N, Şişman FN, Yakut A. Kentsel Alanlar için Bütünleşik Sismik Kayip Tahmin Yöntemi: Erzincan Pilot Uygulamasi, 3rd Turkish conference on Earthquake Engineering and Seismology, Izmir, Turkey, 2015, (In Turkish).

13. Karimzadeh S, Askan A, Erberik MA, Yakut A. Multicomponent seismic loss estimation on the North Anatolian Fault Zone (Turkey), "American Geophysical Union", San Francisco, US, Paper No.: NH13B-1920, 2015.